

Mapping Spatial Effects in CO2 Electrolysis

Iglesias van Montfort, H.P.

DOI

[10.4233/uuid:16cc1f44-7ca1-4bcd-a788-cb8e4b6ba80a](https://doi.org/10.4233/uuid:16cc1f44-7ca1-4bcd-a788-cb8e4b6ba80a)

Publication date

2024

Document Version

Final published version

Citation (APA)

Iglesias van Montfort, H. P. (2024). *Mapping Spatial Effects in CO2 Electrolysis*. [Dissertation (TU Delft), Delft University of Technology]. <https://doi.org/10.4233/uuid:16cc1f44-7ca1-4bcd-a788-cb8e4b6ba80a>

Important note

To cite this publication, please use the final published version (if applicable).
Please check the document version above.

Copyright

Other than for strictly personal use, it is not permitted to download, forward or distribute the text or part of it, without the consent of the author(s) and/or copyright holder(s), unless the work is under an open content license such as Creative Commons.

Takedown policy

Please contact us and provide details if you believe this document breaches copyrights.
We will remove access to the work immediately and investigate your claim.

Mapping Spatial Effects in CO₂ Electrolysis

Mapping Spatial Effects in CO₂ Electrolysis

Dissertatie

ter verkrijging van de graad van doctor
aan de Technische Universiteit Delft,
op gezag van de Rector Magnificus prof. dr. ir. T.H.J.J. van der Hagen,
voorzitter van het College voor Promoties,
in het openbaar te verdedigen
op vrijdag 13 September 2024 om 10:00 uur

door

Hugo-Pieter IGLESIAS VAN MONTFORT

Master of Science in Chemical Engineering,
Technische Universiteit Delft, Nederland,
geboren te Girona, Catalonië, Spanje

This dissertation has been approved by the promotor.

Promotor: Em. prof. dr. B. Dam

Promotor: Dr. T.E. Burdyny

Composition of the doctoral committee:

Rector Magnificus,

Em. prof. dr. B. Dam,

Dr. T.E. Burdyny,

chairperson

Delft University of Technology (NL, promotor)

Delft University of Technology (NL, promotor)

Independent members:

Em. prof. dr. J.J.C. Geerlings,

Prof. dr. D. Sinton,

Prof. dr. B. Seger,

Dr. M.C. Costa Figueiredo,

Dr. F. Pelayo García de Arquer,

Delft University of Technology (NL)

University of Toronto (CA)

Technical University of Denmark (DK)

Eindhoven University of Technology (NL)

Catalan Institute of Photonic Sciences (ES)

Reserve member:

Prof. dr. A. Urakawa,

Delft University of Technology (NL)



Front cover artwork by:

Uri Kaets

Printed by:

Ridderprint | ridderprint.nl

Copyright:

©2024 by H.P. Iglesias van Montfort

ISBN:

978-94-6384-612-7

An electronic version of this dissertation is available at
<http://repository.tudelft.nl/>

The work in this dissertation has been carried out in the Materials for Energy Conversion and Storage (MECS) section of the department of Chemical Engineering, at the Faculty of Applied Sciences of the Delft University of Technology in the Netherlands. This work is part of the *Towards large-scale electroconversion systems* (TOeLS) research programme, under the auspice of the e-Refinery Institute and financed by Shell Global Solutions, B.V. and the TKI Chemie consortium of ChemistryNL.

XXIX.

*Caminante, son tus huellas
el camino, y nada más;
caminante, no hay camino,
se hace camino al andar.
Al andar se hace camino,
y al volver la vista atrás
se ve la senda que nunca
se ha de volver a pisar.
Caminante, no hay camino,
sino estelas en la mar.*

XLIV.

*Todo pasa y todo queda,
pero lo nuestro es pasar,
pasar haciendo caminos,
caminos sobre la mar.*

Antonio Machado,
Proverbios y cantares,
in *Campos de Castilla* (1912)

CONTENTS

1	Introduction	1
1.1	Background & context	2
1.1.1	The role of carbon in our economy	2
1.1.2	Closing the carbon-cycle	3
1.2	CO ₂ electrolysis as a source of renewable carbon	5
1.2.1	Basic understanding of CO ₂ electrolysis	6
1.2.2	Recent advances: intensification and scale-up	10
1.3	Limitations of CO ₂ electrolysis	11
1.3.1	Utilization of CO ₂ at the cathodic interface	11
1.3.2	Formation of salt at the reaction interface	12
1.3.3	Gaps in current understanding of CO ₂ electrolysis	13
1.4	Outline of this dissertation	13
2	The influence of spatial effects on CO₂ electrolysis	25
2.1	Introduction	26
2.2	From 0D to 4D effects inside CO ₂ electrolyzers	27
2.3	Operando visualization of spatial effects	32
2.4	Looking further: the gas-diffusion electrode as a 3D region	34
2.5	Current distribution in gas-diffusion electrodes	36
2.6	Conclusions	37
3	Mapping electrochemical activity in electrolyzers using infrared thermography	47
3.1	Introduction	48
3.2	Heat as a proxy indicator for electrochemical activity	50
3.3	Infrared thermography: a proof-of-concept	51
3.4	Applications of spatial activity mapping	54
3.4.1	Catalyst screening through overpotential-dependent temperature changes	54
3.4.2	Detection of catalyst layer defects	55
3.4.3	Influence of flow-regimes on activity distribution	57
3.5	Exothermic homogeneous reactions during CO ₂ electrolysis	58
3.6	Materials and Methods	60
	Appendix	69

4	Current distribution on hydrophobic electrodes for CO₂ electrol- ysis	87
4.1	Introduction	88
4.2	Results	91
4.2.1	The role of local hydrophobicity in C ₂₊ selectivity of ePTFE electrodes	91
4.2.2	Operando observation of activity distribution on ePTFE electrodes	92
4.2.3	Deactivation mechanisms of copper on ePTFE electrodes . .	94
4.2.4	Improving current distribution on ePTFE electrodes: a non- invasive current collector	97
4.3	Discussion	101
4.4	Methods	102
	Appendix	113
5	A guide to assembly and operation of CO₂ electrolyzers	143
5.1	Introduction	144
5.2	Advanced electrolyzer design for CO ₂ electrolyzers	145
5.2.1	Background on the use of gas-diffusion layers	145
5.2.2	Flow-cells and MEA-cells: assembly and operation	146
5.3	Lab-scale setup for CO ₂ electrolysis	147
5.3.1	Regulation and measurement of gas and liquid streams . . .	147
5.3.2	Integration of in-line diagnostic systems	149
5.3.3	Additional detailed resources for various measurement as- pects	151
	Appendix	159
6	Reflection & outlook	197
	Summary	203
	Samenvatting	205
	Acknowledgments	207
	List of Publications	211
	Curriculum Vitæ	213

1

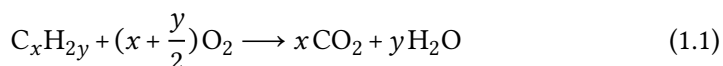
INTRODUCTION

“For our improvement we need a mirror.”

— Arthur Schopenhauer,
in *The Wisdom of Life* (1851)

1.1 Background & context

Ever since Prometheus stole fire from the Olympus and taught Humankind how to use it, we have been on the outlook of technological advancements to convert matter to energy. This is especially the case since the onset of the First Industrial Revolution.[1] The obtained energy is subsequently used in production processes of goods and utilities, that, with increasing automation, results in an added value to those consuming these products. It is no coincidence that this revolution began with the development of the steam machine: channeling the heat generated by combustion of a fuel, water is heated, evaporated, and the resulting steam is used to generate movement in an actionable element in the engine.[2] The source of the heat generated in the first step is the age-old combustion reaction of hydrocarbons:



The most popular sources of carbon atoms for this reaction have been, since the appearance of the steam engine, coal, petroleum, and natural gas; in that order. These sources – so called fossil fuels, due to their biogenic origin – are of limited quantity and require an extractivist economy that eventually results in their depletion.[3]

1.1.1 The role of carbon in our economy

Appliances, perfumes, detergents, textiles, toiletries, electronics, luggage, tires, fertilizers, bottles, food additives, food packaging, construction materials, insulation materials, solar panels, wind turbines, batteries... The large etcetera of products that sometimes do not come to mind when we ask ourselves is exactly the problem we face when we get the question: what do we use that carbon for? While energy and mobility are the most obvious answer (given their link to CO₂ emissions in popular imagery), the reality is that carbon is at the very core of a huge part of our manufacturing economy.

Of all carbon-based molecules processed by industry nowadays, roughly 60% have a petrochemical origin (oil, coal and gas), and 40% have a biologic or natural origin.[4] This distribution skews even more if we look at the carbon molecules processed to chemicals and materials (Fig. 1.1a). In this case, roughly 88% have a fossil origin, while only 8% are bio-based. The problem of these cycles, clearly, is the low rate of recycling loops in the ways we treat carbon. Only around 10% of molecules in the production stream (energy and materials) have previously been used (i.e. are of recycled origin). If we aim to reduce the extractive nature of our economy, we must turn our technical attention to ensuring recycling streams of carbon find their ways to market.

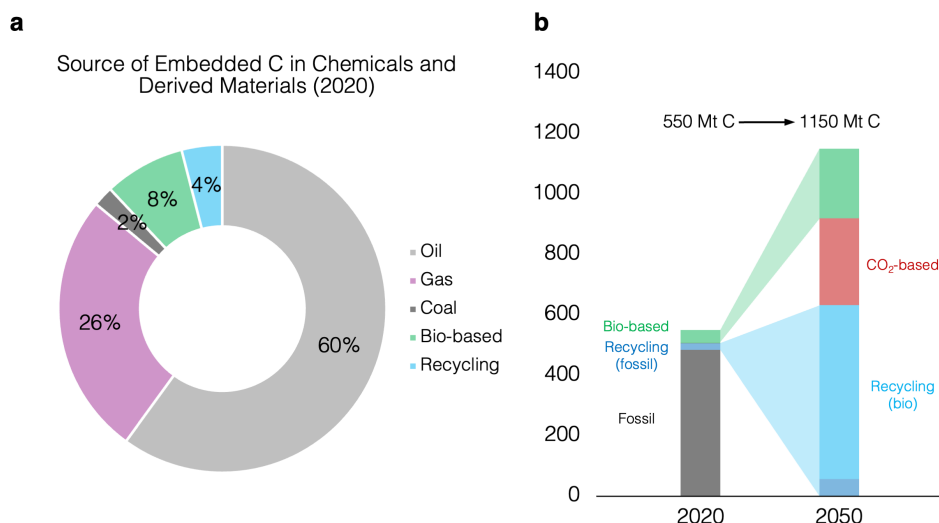


Figure 1.1: Current state and outlook of embedded carbon in the manufacture industry. (a) Physical source of used carbon atoms in chemicals and derived materials, year 2020. (b) Current volumes and origins and target metrics for 2050 at an assumed 5% annual growth rate of demand. Figures reproduced from [4]

As we will see, the first reflexes of technical and political leads in our society were to seek decoupling from the dependance on carbon by seeking alternative sources or assuming a reduction in economic capacity. The reality is, however, that we cannot paint an economic future without carbon value chains. Whereas the annual current production of C-based materials is 550 Mt (Fig. 1.1b), the demand is expected to grow to 1150 Mt. To do so sustainably, roughly 20% of these carbon atoms should be bio-based, 25% should stem from CO₂ utilization, and the rest should be a closed recycle loop. To achieve this, recent attention in chemical manufacturing research has been more and more dedicated to identifying and exploiting alternative carbon sources. These novel sources must be renewable and greenhouse gas (GHG) neutral to achieve a sustainable production chain.

1.1.2 Closing the carbon-cycle

Beyond the importance of carbon for the sustenance of our species, it is evident to assert that humankind has been treating carbon in the same extractivist way we are used to treating raw materials. After mining, processing, and combusting, the carbon molecules that drive the economic cycle are exhausted to the atmosphere, usually in the form of carbon dioxide. This largely explains the accumulation of this so-called GHG in our atmosphere, which in its turn drives climate change.[5]

We wouldn't, however, be humans if we hadn't come up with possible ways to solve this problem. On one hand, replacing energy and material streams to alternative materials would reduce our overall carbon footprint. In this light, the upcoming hydrogen economy aims to divert energy generation and storage from hydrocarbons to hydrogen molecules, through usage of renewable electricity.

On the other hand, more recent pleas in economic circles call for what is known as 'degrowth'. The idea behind this movement is to reduce our impact by shifting economic focus away from growth.[6–9] By collectively assuming a higher degree of poverty, defenders of this conviction pretend to address the current level of GHG emissions. This hypothesis, nonetheless, has many critics and undefined boundary conditions. Firstly, its proponents usually fail to define the degree of 'acquired poverty' needed to lower GHG emissions sufficiently – economists that oppose the idea speak of a 70% decline in income for Western countries while achieving little economic growth in developing countries (the world's GDP per capita was \$12,500 in 2022).[10] Secondly, critics point to the need of a planned economy to achieve these goals, and call on the proven failure of such systems to provide and compete with free-market economies throughout the 20th century and to uphold environmental standards.[11, 12] Thirdly, some are concerned by the authoritarian tone proponents of the most radical circles within this movement, whereas others highlight the necessity for a planned economy in order to achieve its goals.[12, 13]

An alternative, interesting way to decouple our economic activity from GHG emissions involves imposing a circularity on the carbon economy. If we achieve a sustainable product cycle, where every carbon atom processed can be ultimately reused, we can envision an economy with net-zero impact on our atmosphere. While hydrogen on its own will be needed in this transition (as an energy carrier), we have seen a myriad of industries that are hard if not impossible to decarbonize on the short term (at least not without involving some carbon-source).[14] Replacement of carbon sources for these industries are then the first step towards abatement of carbon-dioxide emissions. These technological possibilities have sparked interest by regulators as a way of achieving green growth and stimulating the productive economy of developed countries.[15]

As a first option, an alternative carbon source lies in direct, raw recycling of product streams by recollection and reprocessing. The reality of carbon products, however, is that they are linked with additives and other elements to achieve the materials desired properties, like the chemical resistance of fluor bonds in polytetrafluoroethylene (PTFE, better known as Teflon®) and the rigidity of chloride in polyvinyl chloride (PVC). These additives complicate the separation steps in the recycling chain and difficult the recycling process itself, which requires separate treatment of every embedded carbon product to achieve full recovery.[16, 17]

A second source for carbon atoms is biomass. Carbon atoms from natural

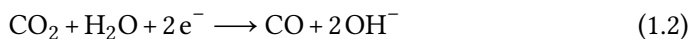
sources are usually embedded in cyclic olefin chains with a good carbon-density. Two major problems arise, however, in trying to synthesize products from these sources. On the one hand, agricultural biomass requires growth on arable land, which puts it in direct competition with food production, especially in underdeveloped countries (sources). In a world with ever-growing population, this is counter-productive at the least.[18] Secondly, refining sources that contain lignin requires energy-intensive steps under unfavorable conditions. The product further requires extensive separation steps to rinse it of hazardous organic compounds.[19]

A final solution, other than the two detailed above, lies in using nature's CO₂ deposits as a source to exploit. Most emitted carbon dioxide ends up either in the atmosphere in the form of gas or dissolves in the oceans in the form of a bicarbonate solution.[20] These deposits can be exploited through so-called direct-air capture (DAC) for atmospheric CO₂ and bipolar-membrane electrodialysis (BPMED) for seaborne CO₂. Of all carbon sources present, this technology would allow for collection of CO₂ without competing with food production and is less sensitive to contamination of the feed stream.[21] In addition, both DAC and BPMED are more easily integrated in downstream processing and conversion of CO₂, which renders them a superior option in terms of scalability.[22–24]

1.2 CO₂ electrolysis as a source of renewable carbon

A straightforward way of processing captured CO₂ is its electrochemical conversion into other compounds. The electrolysis of CO₂ (or the CO₂ reduction reaction, CO₂RR) involves the reduction of the carbon species in the carbon dioxide molecule to a higher oxidation – in other words, electrons are used to break the oxygen bonds to form carbon-based molecules. In this sense, CO₂ electrolysis holds promise in becoming a way to store sustainably sourced electrons in chemical bonds.[25] This is an opportunity to close the carbon cycle while producing the basic building blocks of the chemical industry in a GHG-neutral way, as we shall see.

The most elementary cathodic reduction reaction central to CO₂ electrolysis can be written as follows:



From this, the possible pathways of CO₂RR give way to a myriad of hydrocarbon compounds, like ethylene, formate, methane and higher oxygenates, besides the simpler carbon monoxide. The pathways towards each molecule are partially a source of academic debate, and the variety of products makes it difficult to fully picture a reaction-cascade overview. Some half-cell reactions towards these compounds are compiled in Table 1.1.[26]

Table 1.1: Overview of CO₂RR products. Number of electrons involved, reactions and half-cell potentials vs. RHE.

Product	z	Equation	E°, V vs. RHE
CO	2	$\text{CO}_2 + \text{H}_2\text{O} + 2\text{e}^- \longrightarrow \text{CO} + 2\text{OH}^-$	-0.11
HCOO ⁻	2	$\text{CO}_2 + \text{H}_2\text{O} + 2\text{e}^- \longrightarrow \text{HCOO}^- + \text{OH}^-$	-0.03 ¹
CH ₄	8	$\text{CO}_2 + 6\text{H}_2\text{O} + 8\text{e}^- \longrightarrow \text{CH}_4 + 8\text{OH}^-$	0.17
CH ₃ COO ⁻	8	$2\text{CO}_2 + 5\text{H}_2\text{O} + 8\text{e}^- \longrightarrow \text{CH}_3\text{COO}^- + 7\text{OH}^-$	0.11 ¹
C ₂ H ₄	12	$2\text{CO}_2 + 8\text{H}_2\text{O} + 12\text{e}^- \longrightarrow \text{C}_2\text{H}_4 + 12\text{OH}^-$	0.08
C ₂ H ₅ OH	12	$2\text{CO}_2 + 9\text{H}_2\text{O} + 12\text{e}^- \longrightarrow \text{C}_2\text{H}_5\text{OH} + 12\text{OH}^-$	0.09
C ₂ H ₆	14	$2\text{CO}_2 + 10\text{H}_2\text{O} + 14\text{e}^- \longrightarrow \text{C}_2\text{H}_6 + 14\text{OH}^-$	0.14
C ₃ H ₇ OH	18	$3\text{CO}_2 + 13\text{H}_2\text{O} + 18\text{e}^- \longrightarrow \text{C}_3\text{H}_7\text{OH} + 18\text{OH}^-$	0.10

Establishing a medium to carry out these reactions can be more complex than it seems. For this, we need a series of technologies and materials described in the sections below. Beyond the basics of CO₂RR, we shall present the most significant recent advances and research directions in the field and disclose the shortcomings in literature we aim to cover in this dissertation.

1.2.1 Basic understanding of CO₂ electrolysis

Electrolyzers

The study of CO₂ electrolysis initiated in the late ‘80s and early ‘90s, thanks to the groundbreaking work by Yoshio Hori.[27–32] In the first decades of developments in this field, H-cells dominated the landscape of cell technology. In this setup, the cathodic electrode, usually a metallic plate, evolves the reactants in an electrolyte solution, supported by a reference electrode and a counter electrode (anode) that carries out an oxidation reaction (Fig. 1.2a and b). This architecture runs, however, into limitations when carrying out CO₂ electrolysis. For one, the considerable overpotential due to ohmic losses limits its industrial applicability. Secondly, and most importantly, the system develops ponderous mass-transport limitations at high current densities. This is the consequence of the low availability of the main reactant, CO₂, in aqueous environments.[33, 34]

The move away from this architecture was motivated by a drive for industrial scalability, which required support of higher currents at equal or better product selectivities. Central to this advancement is the application of so-called gas-diffusion electrodes (GDEs), a technology mimicked from the water electrolysis and fuel-cell fields (Fig. 1.2c). GDEs tackle the shortcomings of H-cells by: i.) separating the gas

¹For formate and acetate, the equivalent pH-independent potential for pH > pK_{a,i} is equivalent to E° + 0.059 · n_{OH⁻} / z · ΔpH

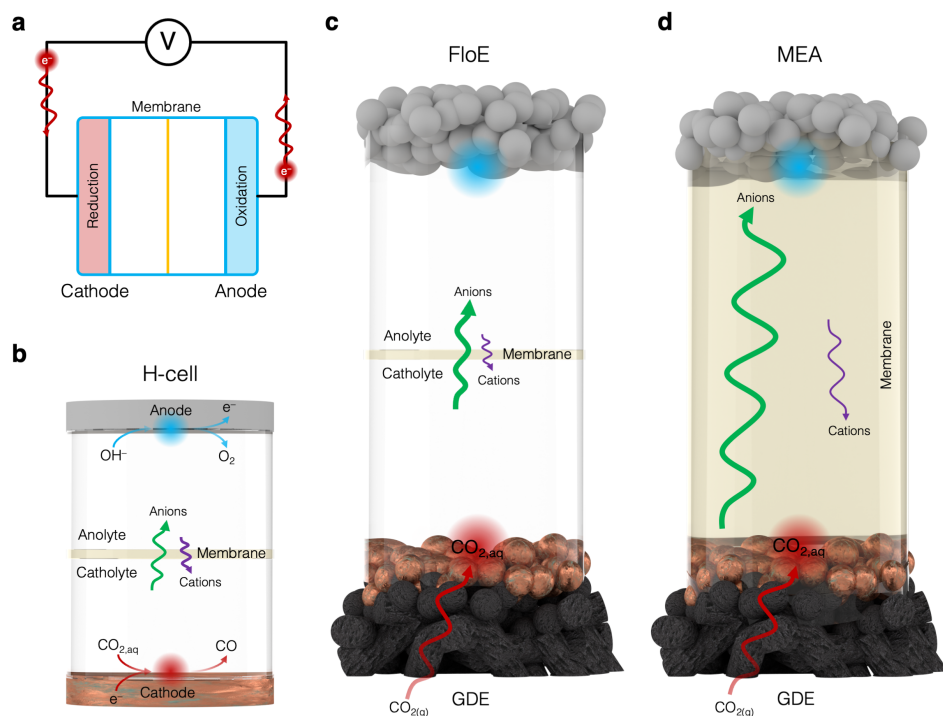


Figure 1.2: Most commonly used electrolyzer architectures (sketches not to scale). (a) Basic sketch of an electrolyzer: at the anode, the oxidation reaction releases electrons. When the potential is high enough, this drives the cathodic reduction reaction. (b) H-cell for aqueous reduction of CO₂. (c) GDE-based FloE, CO₂ diffuses through the GDE and reacts at the catalyst aqueous environment. (d) Zero-gap MEA design for alkaline CO₂ electrolysis. The membrane-thickness is exaggerated, this is usually the same thickness as that of FloE cells, which results in lower ohmic drops for this design.

and liquid environments, dividing the two main reactants (CO₂(g) and water), and ii.) introducing a porous interface between the two regimes – this allows CO₂ to dissolve very close to the reaction interface, reducing mass-transfer strain.[35–38] This advancement in electrolyzer design is central to all recent reports on metrics improvement in the CO₂ electrolysis field, as the bulk of the catalyst layer has access to CO₂.

Application of these gas-diffusion electrodes has found its way to the field in the form of two distinct electrolyzer designs. The first, known as a flow electrolyzer (FloE, Fig. 1.2c), is most similar to H-cells, in the sense that it retains a liquid electrolyte domain (divided into catholyte and anolyte by an ionic exchange membrane), and adds a gas compartment behind the cathode as a supply of reactant and exhaust of produced gasses.[39] The second, more heavily inspired

by fuel-cell designs, is a so-called zero-gap membrane-electrode assembly (MEA, Fig. 1.2d). In this electrolyzer, the liquid catholyte layer is replaced by a polymeric ion exchange membrane. This reduces the ionic pathway of species involved in the reaction and enables the cell to operate at a lower total voltage due to reduced ohmic resistance.

Catalysts

The determinant factor on which product (or products) are being formed from the myriad of possibilities (see table 1.1) lies mainly in the catalyst used. This (usually) metallic layer, placed at the cathode-electrolyte interface, performs the reaction by binding dissolved CO_2 ,^[40] supplying the electrons to the active site, and releasing the product compound at one stage of the reduction reaction.

The reality is, however, that most transition metals are not active for this reaction. At CO_2RR conditions (that is, in a suitable electrolyte saturated with aqueous CO_2), most metals show no CO_2RR products. The cause for this the stabilization of the intermediate CO^\bullet (CO bound to the surface). The energetics of this bound state are so favorable that this species is unable to leave, effectively poisoning the surface.^[41] Given this process, most metals display selectivity towards hydrogen, through the hydrogen-evolution reaction (HER) mechanism (Fig. 1.3, left column).

Metals that, on the other hand, bind very weakly to CO^\bullet and have an affinity for CO_2 , result in the formation of carbon monoxide (CO). These metals reduce CO_2 and, as soon as CO is formed, immediately expel it from the surface due to the unfavorable energetic state this creates. Such metals are displayed in the second column in Fig. 1.3. Of these, the most widely used catalyst for CO production in literature is silver.^[42]

Similarly to CO^\bullet -stabilizing metals, there's a group of metals that binds intermediates of the reaction well enough until it forms an adsorbed COOH^\bullet group. The resulting product for these metals is formic acid (or, in alkaline conditions, a formate salt). In addition, these metals show an unfavorable adsorption-strength for H^\bullet , which means their selectivity under CO_2RR conditions is almost exclusively towards formic acid/formate.^[43] Of this group, the most occurring catalysts are tin and bismuth (and their oxide forms).^[44, 45]

A special case that merits attention is that of copper. The unique electronic structure of copper allows it to stabilize CO^\bullet with intermediate strength while having no underpotential adsorbed H^\bullet . In layman's language, this means Cu stabilizes CO^\bullet sufficiently so that its residence time allows it to evolve to longer hydrocarbons.^[43] This, in effect, results in copper showing selectivity towards longer chain hydrocarbons like ethylene (C_2H_4) and propane (C_3H_8) and also less-reduced alcohols, like ethanol ($\text{C}_2\text{H}_5\text{OH}$) and propanol ($\text{C}_3\text{H}_7\text{OH}$). The added eco-

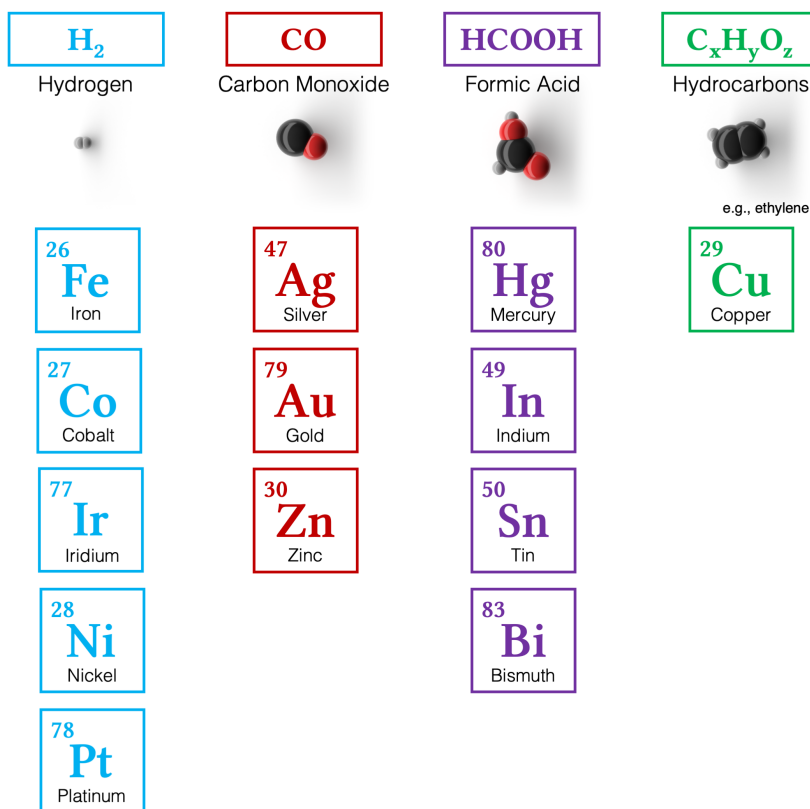


Figure 1.3: Main selectivity for some transition metals at CO₂RR conditions. Metals are depicted in increasing period and atomic number.

nomic value of these heavier compounds make copper into a valuable catalyst to study and scale towards industrial hydrocarbon production processes.[46–48]

Electrolytes

As the ionic support for the reaction, the electrolyte influences the CO₂RR in many different dimensions. An example of these is the local pH of the solution. Most research on CO₂RR reports uses neutral bicarbonate or alkaline hydroxide solutions. While bicarbonate buffers the production of hydroxide ions to a degree, more alkaline solutions do not, resulting in the formation of carbonate close to the dissolution interface.[49] The acidity of an electrolyte has also been shown to directly affect electron-transfer processes at an electrode.[50]

In addition to the effect on electron transfer, the cations employed in the solution have been shown to have a direct influence on the electrosynthesis in

CO₂RR.[51, 52] While the exact influence is still under debate, it is argued that cations in the inner Helmholtz-plane close to the catalyst enhance the local electrical field and help stabilize adsorbed CO₂. [53] In line with this hypothesis, bigger cations like cesium (Cs), which have a smaller hydration shell, have been shown to have a bigger enhancing effect than smaller cations with big hydration shells, like lithium (Li). Finally, cations have been shown to have a direct influence on local CO₂(aq) concentration, increasing threefold for ions like K⁺ and Cs⁺. [54]

1.2.2 Recent advances: intensification and scale-up

All these insights have, in recent years, been used extensively to test and showcase improvements towards intensification and scale-up of CO₂ electrolysis. Among these, three distinct development pathways merit attention: interface design of the catalyst, physical scale-up of the electrolyzer, and steering of product selectivity and stability.

As the first of these, design and tuning of the catalyst interface has been a way of improving understanding of the electrochemical synthesis routes in the cathode.[55, 56] By applying super-hydrophobic gas-diffusion layers (GDLs), the field has seen the rise of current density metrics in the order of -500 mA cm^{-2} , which had long been considered unattainable.[57] Combining this design with a catalyst environment that improves diffusion of the dissolved CO₂ further resulted in current densities of over -1 A cm^{-2} , well beyond what is considered to be an industrially attractive current density.[58–60] Functionalization of attractive catalysts like copper to tune the selectivity towards high-value products like ethylene and ethanol has further contributed to understanding the effects of meso-scale tuning on selectivity of the catalysts.[61, 62] Interface design efforts like the ones mentioned here have shown extended operational life-spans, breaking the 100h mark repeatedly, albeit at limited current densities.

A second relevant trend has been the push to achieve bigger scales and, with these, higher throughput of CO₂RR products. The crux of scale-up of electrochemical devices is, however, that one of the dimensions is barely scalable: the depth direction imposes an intrinsic resistance to transport of ions, so most industrial solutions aim to reduce the thickness of this direction by scaling up in the x-y-direction and stacking multiple reactor units (i.e., electrolyzers).[63] Steps towards expanding in the x-y direction have made appearances in literature in the last years,[64, 65] although most of the corpus still employs geometric surface areas in the 1-10 cm² range. On the other hand, though little works exploit as a research objective in itself, CO₂ electrolyzer stacks are starting to make an appearance.[66, 67]

As a final note it is important to realize the influence of selectivities on the integration of this process in industrial environments. This technology cannot

be implemented if it results in a product stream that requires extensive separation costs for chemicals towards $\geq 99\%$ purity. An option to overcome this is the integration of a CO₂RR electrolyzer into dimerization technology. This way, longer (C₄) hydrocarbons can be formed with considerable selectivity using widely-studied thermocatalysts.[68] Similar results can be achieved by integrating a CO₂ to CO electrolyzer into the up-stream of a Fischer-Tropsch process.[69]

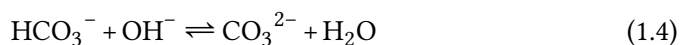
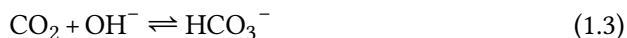
1.3 Limitations of CO₂ electrolysis

Despite this list of advances, CO₂ electrolysis is still hampered by intrinsic limitations due to the chemical nature of the reaction environment and cell design choices. This section discusses the consequences of said barriers and wades into possible solutions to them.

1.3.1 Utilization of CO₂ at the cathodic interface

Most applications of CO₂RR in literature employ an alkaline environment. The main reason for this is avoiding the competing hydrogen formation in acidic media: note the potentials of most CO₂ electrolysis reactions (see Table 1.1) are very close to the 0V vs. RHE of HER.

The alkaline nature of most electrolytes used for this reaction transform CO₂ electrolyzers in natural fuel-wasting electrolyzers. Carbon dioxide experiences, in basic and neutral environments, a quick reaction that buffers it to bicarbonate first, and then carbonate, following the reactions:



The ease of this reaction condemns CO₂ electrolyzers to a maximum fuel efficiency of 50% (see eq. 1.2, for every CO₂ molecule consumed, 2 OH[−] anions are produced, which in their turn buffer an additional CO₂ molecule following eqs. 1.3 and 1.4). For C₂₊-products, this efficiency further reduces, thus, to 25%. This shortcoming has, however, several workarounds. The first of these is to reduce CO₂ to CO in a high-temperature electrolyzer (so-called solid-oxide electrolyzer cells, SOECs) and then reduce CO to hydrocarbons in a separate, low-temperature electrolyzer. CO does not evolve to carbonates, although its solubility in aqueous media is lower and the product mix of CO electrolysis is notably different to that of CO₂ electrolysis. On the other hand, one may employ bipolar membrane electrolyzers. These bipolar membranes (BPMs) consist of a junction of an anion- and a cation-exchange membrane. Herein, the carbonate produced from buffering CO₂

is protonated again to CO_2 , so the loss in reactant is recovered by the transport nature of the membrane (or by separation from the anode off-stream).[70, 71]

1.3.2 Formation of salt at the reaction interface

The progressive buffering of more and more CO_2 to (bi-)carbonate species leads to an accumulation of these anions close to the cathode. In addition, the poor specificity of anion-exchange membranes used in alkaline electrolyzers causes the accumulation of the cations used in the electrolyte (most commonly potassium, K^+ , or cesium, Cs^+). This accumulation of both cations and anions at the reaction interface results in the precipitation of a salt if critical solubility limits or solubility products are exceeded. For potassium carbonate (K_2CO_3), this limit is 15.96M for K^+ -cations and 7.98M for carbonate anions.

The formation of salt presents a problem for many processes occurring in the electrolyzer. For once, it can block the gas-channels at the back of the GDE, especially so for zero-gap designs. This blocks gas-flow and results in pressure spikes that can rupture the assembly. On the other hand, salt precipitation at the micro-scale can block the pores of the gas-diffusion layer in the GDE and limit the availability of CO_2 , which in its turn results in a loss of selectivity and increased HER-rate.[42] Finally, carbonate salts may block specific catalytic sites of the cathode, which also results in a loss of overall activity.[72, 73]

Avoiding accumulation of the cations and anions responsible for this precipitation is, then, a crucial step in ensuring long-term operation of CO_2 electrolyzers. As it stands, solutions to this problem can be achieved by either tweaking the operational parameters of the electrolyzer, or by actively engineering alternative components. As most obvious examples of operational improvement we can distinguish the periodic rinsing of the backbone of the GDE.[65, 66] Another possibility reported is periodically switching the polarity of the cell from highly cathodic to mildly anodic. This creates periods of time where the positively charged K^+ -ions are drawn to the anolyte and flushed from the vicinity of the cathode. By studying transport models, the ideal off-duty length can be calculated. The main drawback of this approach, however, is the increase in operational costs that this means in an industrial setting, seeing as the electrolyzer has a lower average duty cycle.[74, 75]

On the other hand, active engineering of alternative components holds promise for breakthrough stability metrics. One such example is the usage of bipolar membrane electrode assemblies (BPMEAs). By providing a mildly acidic environment to the cathode, carbonate ions are regenerated to CO_2 ; the alkaline environment at the anode means usage of non-platinum group metal (non-PGM) catalysts is possible, which greatly reduces the capital costs of the electrolyzer. The drawback, however, is the increased operating cell potential, as the interface of the

BPM needs to split water into hydronium and hydroxide ions (which implies an added minimum potential of 0.83 V, the potential drop of the water dissociation reaction). Looking beyond the development of BPMEAs, engineering the cathodic interface to reduce the amount of cations present is a different promising approach. While it is generally accepted that heavy alkali metal cations improve the conditions for CO₂RR,[52] alternative positively charged ionomers have already been used in pure-water fed electrolyzers which show adequate selectivity and stability metrics.[76]

1.3.3 Gaps in current understanding of CO₂ electrolysis

Given the current developments and limitations described in this chapter, we can outline a set of gaps present in the understanding, development, and analysis of CO₂ electrolyzers in current literature. While the field has developed at an outstanding rate (and still is), there are a set of ingrained blind-spots that may become relevant in further upscaling of this technology.

The first of these blind spots is the lack of spatial awareness in reporting. While the lack of consideration of local conditions is acceptable when reporting on, say, an electrolyzer with an active area of 1 cm², this is not acceptable upon increasing dimensions. The local reactant concentration, pH, current density, overpotential and humidity of the gas stream all play a role in the efficiency and selectivity of the reaction, and should be considered (or, at least, homogenized where possible) to guarantee honest metric reporting. Adding to this, most developments and boundary-breaking research is reported using complex designs of catalyst interfaces. Without a proper understanding of process conditions in all 3 dimensions, efforts to scale-up any solution will be greatly hampered.

Secondly, the reliance on technology initially intended for other technologies, like water electrolysis and PEM fuel-cells has rooted issues in CO₂ electrolyzers that seem very hard to overcome. One example of this is the flooding of porous carbon-based GDE's.[77] While this is detrimental for CO₂RR, it is exactly what is needed in vapor-fed hydrogen PEM systems, as accumulation of water results in a degradation of performance. By relying on off-the-shelf solutions for a long time, these phenomena seem impossible to overcome. The answer to this problem lies, however, in usage of alternative designs and technologies for these GDLs.

1.4 Outline of this dissertation

This dissertation aims to increase knowledge and insight into spatial effects in CO₂ electrolyzers. More specifically, it presents novel insights into current distribution, physical effects, and heat development at the cathode interface of these novel devices. To do so, we detail a state-of-the-art measurement system based on infrared thermography that uses heat generation as a proxy for electrochemical activity.

Chapter 2 provides insights into the state of literature concerning the scale-up of CO₂ electrolyzers. After consideration of spatial variations and technologies developed to scope these effects, we proceed to identify common pitfalls and the necessity for standardization of reporting metrics to advance in the development of technological workarounds to intrinsic problems of CO₂ electrolysis. A publication based on this work is currently under review.

Chapter 3 presents a novel infrared thermography measurement technique that provides insight in the activity distribution on a cathodic surface. By decoupling heat generation sources, we can accurately represent current density distributions and study the effect of the changing fluid media over the interface. After presenting cases for possible applications, we proceed to study the applications on CO₂ electrolysis and possible limitations of infrared thermography. This work has been published in ACS Energy Letters and formed the basis for a Dutch patent.[78, 79]

Chapter 4 includes a study on novel, super-hydrophobic electrodes for CO₂ electrolysis to C₂₊-hydrocarbons. These electrodes have been used increasingly in this field, without ever accounting for the reduced current collection capabilities of their substrate. In this light, we use our infrared thermography technique to detail these limitations and develop novel non-invasive current collectors for copper electrocatalysts. These new designs result in a chemically more stable catalyst interface and improved current density and product distributions. This work has been published in Nature Communications.[80]

Chapter 5 is a synthesis of the acquired know-how of our lab in the last 5 years. After intensification of electrolyzer designs, increased awareness of the balance-of-plant for the lab scale is needed to report accurate metrics. In this chapter we detail novel cell designs, our back-pressure regulator device and novel characterization and measurement techniques to further advance the field. The chapter includes an equipment guide, assembly tutorials and troubleshooting guides to help starting researchers. This work has been published in ACS Energy Letters.[81]

References

- [1] N. Crafts. Explaining the first Industrial Revolution: two views. *European Review of Economic History*, 15(1):153–168, April 2011.
- [2] Kristine Bruland and Keith Smith. Assessing the role of steam power in the first industrial revolution: The early work of Nick von Tunzelmann. *Research Policy*, 42(10):1716–1723, December 2013.
- [3] John O. Browder. The Limits of Extractivism. *BioScience*, 42(3):174–182, March 1992.
- [4] Ferdinand Kähler, Olaf Porc, and Michael Carus. RCI Carbon Flows Report: Compilation of supply and demand of fossil and renewable carbon on a global and European level. Technical report, nova-Institut, October 2023.
- [5] S. Arrhenius. On the Influence of Carbonic Acid in the Air upon the Temperature of the Earth. *Publications of the Astronomical Society of the Pacific*, 9:14, February 1897.
- [6] Eleanor Finley. Beyond the Limits of Nature: A Social-ecological Perspective on Degrowth as a Political Ideology. *Capitalism Nature Socialism*, 30(2):244–250, April 2019.
- [7] Martin Weiss and Claudio Cattaneo. Degrowth – Taking Stock and Reviewing an Emerging Academic Paradigm. *Ecological Economics*, 137:220–230, July 2017.
- [8] Ying Chen. Degrowth — What’s in a Name?: Assessing Degrowth’s Political Implications. *Monthly review*, 75(3):160–170, 2023. 160.
- [9] Huber, Matt. The Problem With Degrowth. *Jacobin*, 2023.
- [10] World Bank. *The World Bank Annual Report 2022*. The World Bank, 2022.
- [11] Philip Micklin. The Aral Sea Disaster. *Annual Review of Earth and Planetary Sciences*, 35(1):47–72, May 2007.
- [12] Michael J. Albert. Ecosocialism for Realists: Transitions, Trade-Offs, and Authoritarian Dangers. *Capitalism Nature Socialism*, 34(1):11–30, January 2023.
- [13] Terzi, Alessio. *Growth for good: Reshaping capitalism to save humanity from climate catastrophe*. Harvard University Press, 2022.

- [14] Nina Khanna, Hongyou Lu, David Fridley, and Nan Zhou. Near and long-term perspectives on strategies to decarbonize China's heavy-duty trucks through 2050. *Scientific Reports*, 11(1):20414, October 2021.
- [15] David Kleimann, Niclas Poitiers, André Sapir, Simone Tagliapietra, Nicolas Véron, Reinhilde Veugelers, and Jeromin Zettermeyer. Green tech race? The US Inflation Reduction Act and the EU Net Zero Industry Act. *The World Economy*, 46(12):3420–3434, December 2023.
- [16] Xinyao Jiang, Bing Zhu, and Maiyong Zhu. An overview on the recycling of waste poly(vinyl chloride). *Green Chemistry*, 25(18):6971–7025, 2023.
- [17] Naohisa Yanagihara and Takahiro Katoh. Mineralization of poly(tetrafluoroethylene) and other fluoropolymers using molten sodium hydroxide. *Green Chemistry*, 24(16):6255–6263, 2022.
- [18] A. Muscat, E.M. De Olde, I.J.M. De Boer, and R. Ripoll-Bosch. The battle for biomass: A systematic review of food-feed-fuel competition. *Global Food Security*, 25:100330, June 2020.
- [19] Braz De Souza Marotti and Valdeir Arantes. Ultra-refining for the production of long-term highly pH-stable lignin nanoparticles in high yield with high uniformity. *Green Chemistry*, 24(3):1238–1258, 2022.
- [20] R. Sharifian, R. M. Wagterveld, I. A. Digdaya, C. Xiang, and D. A. Vermaas. Electrochemical carbon dioxide capture to close the carbon cycle. *Energy & Environmental Science*, 14(2):781–814, 2021.
- [21] Mahdi Fasihi, Olga Efimova, and Christian Breyer. Techno-economic assessment of CO₂ direct air capture plants. *Journal of Cleaner Production*, 224:957–980, July 2019.
- [22] Ibadillah A. Digdaya, Ian Sullivan, Meng Lin, Lihao Han, Wen-Hui Cheng, Harry A. Atwater, and Chengxiang Xiang. A direct coupled electrochemical system for capture and conversion of CO₂ from oceanwater. *Nature Communications*, 11(1):4412, September 2020.
- [23] Mengran Li, Erdem Irtem, Hugo-Pieter Iglesias van Montfort, Maryam Ab-dinejad, and Thomas Burdyny. Energy comparison of sequential and integrated CO₂ capture and electrochemical conversion. *Nature Communications*, 13(1):5398, September 2022.
- [24] Saptak Rarotra, Amit Kumar Singh, Tapas Kumar Mandal, and Dipankar Bandyopadhyay. Co-electrolysis of seawater and carbon dioxide inside

a microfluidic reactor to synthesize speciality organics. *Scientific Reports*, 13(1):10298, June 2023.

- [25] Ifan E L Stephens, Karen Chan, Alexander Bagger, Shannon W Boettcher, Julien Bonin, Etienne Boutin, Aya K Buckley, Raffaella Buonsanti, Etosha R Cave, Xiaoxia Chang, See Wee Chee, Alisson H M Da Silva, Phil De Luna, Oliver Einsle, Balázs Endrődi, Maria Escudero-Escribano, Jorge V Ferreira De Araujo, Marta C Figueiredo, Christopher Hahn, Kentaro U Hansen, Sophia Haussener, Sara Hunegnaw, Ziyang Huo, Yun Jeong Hwang, Csaba Janáky, Buddhinie S Jayatilake, Feng Jiao, Zarko P Jovanov, Parisa Karimi, Marc T M Koper, Kendra P Kuhl, Woong Hee Lee, Zhiqin Liang, Xuan Liu, Sichao Ma, Ming Ma, Hyung-Suk Oh, Marc Robert, Beatriz Roldan Cuenya, Jan Rossmeisl, Claudie Roy, Mary P Ryan, Edward H Sargent, Paula Sebastián-Pascual, Brian Seger, Ludmilla Steier, Peter Strasser, Ana Sofia Varela, Rafaël E Vos, Xue Wang, Bingjun Xu, Hossein Yadegari, and Yuxiang Zhou. 2022 roadmap on low temperature electrochemical CO₂ reduction. *Journal of Physics: Energy*, 4(4):042003, October 2022.
- [26] Allen J. Bard, Roger. Parsons, Joseph 1919-1992. Jordan, and International Union of Pure and Applied Chemistry. *Standard potentials in aqueous solution*. Monographs in electroanalytical chemistry and electrochemistry. M. Dekker, New York, 1st ed. edition, 1985. Section: xii, 834 pages : illustrations ; 26 cm.
- [27] Yoshio Hori, Akira Murata, and Yuzuru Yoshinami. Adsorption of CO, immediately formed in electrochemical reduction of CO₂, at a copper electrode. *Journal of the Chemical Society, Faraday Transactions*, 87(1):125, 1991.
- [28] Y. Hori, H. Wakebe, T. Tsukamoto, and O. Koga. Adsorption of CO accompanied with simultaneous charge transfer on copper single crystal electrodes related with electrochemical reduction of CO₂ to hydrocarbons. *Surface Science*, 335:258–263, July 1995.
- [29] Yoshio Hori, Hidetoshi Wakebe, Toshio Tsukamoto, and Osamu Koga. Electrocatalytic process of CO selectivity in electrochemical reduction of CO₂ at metal electrodes in aqueous media. *Electrochimica Acta*, 39(11-12):1833–1839, August 1994.
- [30] Yoshio Hori, Akira Murata, and Ryutaro Takahashi. Formation of hydrocarbons in the electrochemical reduction of carbon dioxide at a copper electrode in aqueous solution. *Journal of the Chemical Society, Faraday Transactions 1: Physical Chemistry in Condensed Phases*, 85(8):2309, 1989.

- [31] Yoshio Hori, Osamu Koga, Akiko Aramata, and Michio Enyo. Infrared Spectroscopic Observation of Adsorbed CO Intermediately Formed in the Electrochemical Reduction of CO₂ at a Nickel Electrode. *Bulletin of the Chemical Society of Japan*, 65(11):3008–3010, November 1992.
- [32] Y. Hori. Electrochemical CO₂ Reduction on Metal Electrodes. In Constantinos G. Vayenas, Ralph E. White, and Maria E. Gamboa-Aldeco, editors, *Modern Aspects of Electrochemistry*, volume 42, pages 89–189. Springer New York, New York, NY, 2008. Series Title: Modern Aspects of Electrochemistry.
- [33] S. Weisenberger and A. Schumpe. Estimation of gas solubilities in salt solutions at temperatures from 273 K to 363 K. *AIChE Journal*, 42(1):298–300, January 1996.
- [34] Denis A. Wiesenburg and Norman L Guinasso. Equilibrium solubilities of methane, carbon monoxide, and hydrogen in water and sea water. *Journal of Chemical & Engineering Data*, 24(4):356–360, October 1979.
- [35] Thao T. H. Hoang, Sumit Verma, Sichao Ma, Tim T. Fister, Janis Timoshenko, Anatoly I. Frenkel, Paul J. A. Kenis, and Andrew A. Gewirth. Nanoporous Copper–Silver Alloys by Additive-Controlled Electrodeposition for the Selective Electroreduction of CO₂ to Ethylene and Ethanol. *Journal of the American Chemical Society*, 140(17):5791–5797, May 2018.
- [36] Attila Kormányos, Balázs Endrődi, Zheng Zhang, Angelika Samu, László Mérai, Gergely F. Samu, László Janovák, and Csaba Janáky. Local hydrophobicity allows high-performance electrochemical carbon monoxide reduction to C₂₊ products. *EES Catalysis*, page 10.1039.D3EY00006K, 2023.
- [37] Uzoma O. Nwabara, Emiliana R. Cofell, Sumit Verma, Emanuela Negro, and Paul J. A. Kenis. Durable Cathodes and Electrolyzers for the Efficient Aqueous Electrochemical Reduction of CO₂. *ChemSusChem*, 13(5):855–875, March 2020.
- [38] Angelika Anita Samu, Imre Szenti, Ákos Kukovecz, Balázs Endrődi, and Csaba Janáky. Systematic screening of gas diffusion layers for high performance CO₂ electrolysis. *Communications Chemistry*, 6(1):41, February 2023.
- [39] Kai Liu, Wilson A Smith, and Thomas Burdyny. Introductory Guide to Assembling and Operating Gas Diffusion Electrodes for Electrochemical CO₂ Reduction. *ACS Energy Letters*, 2019.

- [40] Nathan T. Nesbitt, Thomas Burdyny, Hunter Simonson, Danielle Salvatore, Divya Bohra, Recep Kas, and Wilson A. Smith. Liquid-Solid Boundaries Dominate Activity of CO₂ Reduction on Gas-Diffusion Electrodes. *ACS Catalysis*, 10(23):14093–14106, December 2020. Publisher: American Chemical Society.
- [41] Marek Gajdo, Andreas Eichler, and Jürgen Hafner. CO adsorption on close-packed transition and noble metal surfaces: trends from *ab initio* calculations. *Journal of Physics: Condensed Matter*, 16(8):1141–1164, March 2004.
- [42] Mark Sassenburg, Reinier de Rooij, Nathan T. Nesbitt, Recep Kas, Sanjana Chandrashekar, Nienke J. Firet, Kailun Yang, Kai Liu, Marijn A. Blommaert, Martin Kolen, Davide Ripepi, Wilson A. Smith, and Thomas Burdyny. Characterizing CO₂ Reduction Catalysts on Gas Diffusion Electrodes: Comparing Activity, Selectivity, and Stability of Transition Metal Catalysts. *ACS Applied Energy Materials*, 5(5):5983–5994, May 2022. Publisher: American Chemical Society.
- [43] Alexander Bagger, Wen Ju, Ana Sofia Varela, Peter Strasser, and Jan Rossmeisl. Electrochemical CO₂ Reduction: A Classification Problem. *ChemPhysChem*, 18(22):3266–3273, November 2017.
- [44] Thuy-Duong Nguyen-Phan, Leiming Hu, Bret H. Howard, Wenqian Xu, Eli Stavitski, Denis Leshchev, August Rothenberger, Kenneth C. Neyerlin, and Douglas R. Kauffman. High current density electroreduction of CO₂ into formate with tin oxide nanospheres. *Scientific Reports*, 12(1):8420, May 2022.
- [45] Fa Yang, Ahmed O. Elnabawy, Roberto Schimmenti, Ping Song, Jiawei Wang, Zhangquan Peng, Shuang Yao, Ruiping Deng, Shuyan Song, Yue Lin, Manos Mavrikakis, and Weilin Xu. Bismuthene for highly efficient carbon dioxide electroreduction reaction. *Nature Communications*, 11(1):1088, February 2020.
- [46] Oleksandr S. Bushuyev, Phil De Luna, Cao Thang Dinh, Ling Tao, Genevieve Saur, Jao Van De Lagemaat, Shana O. Kelley, and Edward H. Sargent. What Should We Make with CO₂ and How Can We Make It? *Joule*, 2(5):825–832, May 2018.
- [47] Phil De Luna, Christopher Hahn, Drew Higgins, Shaffiq A. Jaffer, Thomas F. Jaramillo, and Edward H. Sargent. What would it take for renewably powered electrosynthesis to displace petrochemical processes? *Science*, 364(6438):eaav3506, April 2019.

- [48] Jared Sisler, Shaihzor Khan, Alexander H. Ip, Moritz W. Schreiber, Shaffiq A. Jaffer, Erin R. Bobicki, Cao-Thang Dinh, and Edward H. Sargent. Ethylene Electrosynthesis: A Comparative Techno-economic Analysis of Alkaline vs Membrane Electrode Assembly vs CO_2 -CO- C_2H_4 Tandems. *ACS Energy Letters*, 6(3):997–1002, March 2021.
- [49] N. Gupta, M. Gattrell, and B. MacDougall. Calculation for the cathode surface concentrations in the electrochemical reduction of CO_2 in KHCO_3 solutions. *Journal of Applied Electrochemistry*, 36(2):161–172, January 2006.
- [50] Marc T. M. Koper. Theory of multiple proton–electron transfer reactions and its implications for electrocatalysis. *Chemical Science*, 4(7):2710, 2013.
- [51] Giulia Marcandalli, Mariana C. O. Monteiro, Akansha Goyal, and Marc T. M. Koper. Electrolyte Effects on CO_2 Electrochemical Reduction to CO. *Accounts of Chemical Research*, 55(14):1900–1911, July 2022.
- [52] Mariana C. O. Monteiro, Federico Dattila, Bellenod Hagedoorn, Rodrigo García-Muelas, Núria López, and Marc T. M. Koper. Absence of CO_2 electroreduction on copper, gold and silver electrodes without metal cations in solution. *Nature Catalysis*, 4(8):654–662, July 2021.
- [53] Federico Dattila, Mariana C. O. Monteiro, Marc T. M. Koper, and Núria López. Reply to: On the role of metal cations in CO_2 electrocatalytic reduction. *Nature Catalysis*, 5(11):979–981, November 2022.
- [54] Arnav S. Malkani, Jacob Anibal, and Bingjun Xu. Cation Effect on Interfacial CO_2 Concentration in the Electrochemical CO_2 Reduction Reaction. *ACS Catalysis*, 10(24):14871–14876, December 2020.
- [55] Md Golam Kibria, Jonathan P. Edwards, Christine M. Gabardo, Cao-Thang Dinh, Ali Seifitokaldani, David Sinton, and Edward H. Sargent. Electrochemical CO_2 Reduction into Chemical Feedstocks: From Mechanistic Electrocatalysis Models to System Design. *Advanced Materials*, 31(31):1807166, August 2019.
- [56] Xingli Wang, Jorge Ferreira de Araújo, Wen Ju, Alexander Bagger, Henrike Schmies, Stefanie Kühl, Jan Rossmesl, and Peter Strasser. Mechanistic reaction pathways of enhanced ethylene yields during electroreduction of CO_2 -CO co-feeds on Cu and Cu-tandem electrocatalysts. *Nature Nanotechnology*, 14(11):1063–1070, November 2019.

- [57] Cao Thang Dinh, Thomas Burdyny, Golam Kibria, Ali Seifitokaldani, Christine M Gabardo, F Pelayo García De Arquer, Amirreza Kiani, Jonathan P Edwards, Phil De Luna, Oleksandr S Bushuyev, Chengqin Zou, Rafael Quintero-Bermudez, Yuanjie Pang, David Sinton, and Edward H Sargent. CO₂ electroreduction to ethylene via hydroxide-mediated copper catalysis at an abrupt interface. *Science*, 360:783–787, 2018.
- [58] Thomas Burdyny and Wilson A Smith. CO₂ reduction on gas-diffusion electrodes and why catalytic performance must be assessed at commercially-relevant conditions. *Energy and Environmental Science*, 2019.
- [59] F Pelayo García de Arquer, Cao Thang Dinh, Adnan Ozden, Joshua Wicks, Christopher McCallum, Ahmad R Kirmani, Dae Hyun Nam, Christine Gabardo, Ali Seifitokaldani, Xue Wang, Yuguang C Li, Fengwang Li, Jonathan Edwards, Lee J Richter, Steven J Thorpe, David Sinton, and Edward H Sargent. CO₂ electrolysis to multicarbon products at activities greater than 1 A cm⁻². *Science*, 367:661–666, 2020.
- [60] Doris Segets, Corina Andronesco, and Ulf-Peter Apfel. Accelerating CO₂ electrochemical conversion towards industrial implementation. *Nature Communications*, 14(1):7950, December 2023.
- [61] Wenchao Ma, Shunji Xie, Tongtong Liu, Qiyuan Fan, Jinyu Ye, Fanfei Sun, Zheng Jiang, Qinghong Zhang, Jun Cheng, and Ye Wang. Electrocatalytic reduction of CO₂ to ethylene and ethanol through hydrogen-assisted C–C coupling over fluorine-modified copper. *Nature Catalysis*, 3(6):478–487, April 2020.
- [62] Xue Wang, Ziyun Wang, F. Pelayo García De Arquer, Cao-Thang Dinh, Adnan Ozden, Yuguang C. Li, Dae-Hyun Nam, Jun Li, Yi-Sheng Liu, Joshua Wicks, Zitao Chen, Miaofang Chi, Bin Chen, Ying Wang, Jason Tam, Jane Y. Howe, Andrew Proppe, Petar Todorović, Fengwang Li, Tao-Tao Zhuang, Christine M. Gabardo, Ahmad R. Kirmani, Christopher McCallum, Sung-Fu Hung, Yanwei Lum, Mingchuan Luo, Yimeng Min, Aoni Xu, Colin P. O’Brien, Bello Stephen, Bin Sun, Alexander H. Ip, Lee J. Richter, Shana O. Kelley, David Sinton, and Edward H. Sargent. Efficient electrically powered CO₂-to-ethanol via suppression of deoxygenation. *Nature Energy*, 5(6):478–486, May 2020.
- [63] Geoffrey Prentice. *Electrochemical engineering principles*, volume 1. Prentice Hall, New Jersey, 1990. Publication Title: P.
- [64] B Endrődi, E Kecsenovity, A Samu, T Halmágyi, S Rojas-Carbonell, L Wang, Y Yan, and C Janáky. High carbonate ion conductance of a robust PiperION

membrane allows industrial current density and conversion in a zero-gap carbon dioxide electrolyzer cell. *Energy & Environmental Science*, 2020.

- [65] B. Endrődi, A. Samu, E. Kecsenvity, T. Halmágyi, D. Sebők, and C. Janáky. Operando cathode activation with alkali metal cations for high current density operation of water-fed zero-gap carbon dioxide electrolyzers. *Nature Energy*, 6(4):439–448, April 2021.
- [66] B. Endrődi, E. Kecsenvity, A. Samu, F. Darvas, R. V. Jones, V. Török, A. Danyi, and C. Janáky. Multilayer Electrolyzer Stack Converts Carbon Dioxide to Gas Products at High Pressure with High Efficiency. *ACS Energy Letters*, 4(7):1770–1777, July 2019.
- [67] Xiaojie She, Lingling Zhai, Yifei Wang, Pei Xiong, Molly Meng-Jung Li, Tai-Sing Wu, Man Chung Wong, Xuyun Guo, Zhihang Xu, Huaming Li, Hui Xu, Ye Zhu, Shik Chi Edman Tsang, and Shu Ping Lau. Pure-water-fed, electrocatalytic CO₂ reduction to ethylene beyond 1,000 h stability at 10 A. *Nature Energy*, January 2024.
- [68] Mi Gyoung Lee, Xiao-Yan Li, Adnan Ozden, Joshua Wicks, Pengfei Ou, Yuhang Li, Roham Dorakhan, Jaekyoung Lee, Hoon Kee Park, Jin Wook Yang, Bin Chen, Jehad Abed, Roberto Dos Reis, Geonhui Lee, Jianan Erick Huang, Tao Peng, Ya-Huei Chin, David Sinton, and Edward H. Sargent. Selective synthesis of butane from carbon monoxide using cascade electrolysis and thermocatalysis at ambient conditions. *Nature Catalysis*, 6(4):310–318, April 2023.
- [69] Svetlana Van Bavel, Sumit Verma, Emanuela Negro, and Maarten Bracht. Integrating CO₂ Electrolysis into the Gas-to-Liquids–Power-to-Liquids Process. *ACS Energy Letters*, 5(8):2597–2601, August 2020.
- [70] Marijn A. Blommaert, David Aili, Ramato Ashu Tufa, Qingfeng Li, Wilson A. Smith, and David A. Vermaas. Insights and Challenges for Applying Bipolar Membranes in Advanced Electrochemical Energy Systems. *ACS Energy Letters*, 6(7):2539–2548, July 2021.
- [71] Kailun Yang, Mengran Li, Siddhartha Subramanian, Marijn A. Blommaert, Wilson A. Smith, and Thomas Burdyny. Cation-Driven Increases of CO₂ Utilization in a Bipolar Membrane Electrode Assembly for CO₂ Electrolysis. *ACS Energy Letters*, 6(12):4291–4298, December 2021.
- [72] Sahil Garg, Qiucheng Xu, Asger B. Moss, Marta Mirolo, Wanyu Deng, Ib Chorkendorff, Jakub Drnec, and Brian Seger. How alkali cations affect salt

- precipitation and CO₂ electrolysis performance in membrane electrode assembly electrolyzers. *Energy & Environmental Science*, 16(4):1631–1643, 2023.
- [73] Asger B. Moss, Sahil Garg, Marta Mirolo, Carlos A. Giron Rodriguez, Roosa Ilvonen, Ib Chorkendorff, Jakub Drnec, and Brian Seger. In operando investigations of oscillatory water and carbonate effects in MEA-based CO₂ electrolysis devices. *Joule*, 7(2):350–365, February 2023.
- [74] Tu N. Nguyen, Zhu Chen, Ali Shayesteh Zeraati, Hadi Shaker Shiran, Sharif Md. Sadaf, Md Golam Kibria, Edward H. Sargent, and Cao-Thang Dinh. Catalyst Regeneration via Chemical Oxidation Enables Long-Term Electrochemical Carbon Dioxide Reduction. *Journal of the American Chemical Society*, 144(29):13254–13265, July 2022.
- [75] Yi Xu, Jonathan P. Edwards, Shijie Liu, Rui Kai Miao, Jianan Erick Huang, Christine M. Gabardo, Colin P. O’Brien, Jun Li, Edward H. Sargent, and David Sinton. Self-Cleaning CO₂ Reduction Systems: Unsteady Electrochemical Forcing Enables Stability. *ACS Energy Letters*, 6(2):809–815, February 2021.
- [76] Zhenglei Yin, Hanqing Peng, Xing Wei, Huan Zhou, Jun Gong, Mingming Huai, Li Xiao, Gongwei Wang, Juntao Lu, and Lin Zhuang. An alkaline polymer electrolyte CO₂ electrolyzer operated with pure water. *Energy & Environmental Science*, 12(8):2455–2462, 2019.
- [77] Kailun Yang, Recep Kas, Wilson A. Smith, and Thomas Burdyny. Role of the Carbon-Based Gas Diffusion Layer on Flooding in a Gas Diffusion Electrode Cell for Electrochemical CO₂ Reduction. *ACS Energy Letters*, 6(1):33–40, January 2021.
- [78] Hugo-Pieter Iglesias van Montfort and Thomas Edward Burdyny. Plane-resolved activity mapping at a gas-diffusion electrode through infrared thermography, February 2023.
- [79] Hugo-Pieter Iglesias van Montfort and Thomas Burdyny. Mapping Spatial and Temporal Electrochemical Activity of Water and CO₂ Electrolysis on Gas-Diffusion Electrodes Using Infrared Thermography. *ACS Energy Letters*, 7(8):2410–2419, August 2022. Publisher: American Chemical Society.
- [80] Hugo-Pieter Iglesias van Montfort, Mengran Li, Erdem Irtem, Maryam Abidinejad, Yuming Wu, Santosh K. Pal, Mark Sassenburg, Davide Ripepi, Sidhartha Subramanian, Jasper Biemolt, Thomas E. Rufford, and Thomas Burdyny. Non-invasive current collectors for improved current-density distribution during CO₂ electrolysis on super-hydrophobic electrodes. *Nature Communications*, 14(1):6579, October 2023.

- [81] Hugo-Pieter Iglesias van Montfort, Siddhartha Subramanian, Erdem Irtem, Mark Sassenburg, Mengran Li, Jesse Kok, Joost Middelkoop, and Thomas Burdyny. An Advanced Guide to Assembly and Operation of CO₂ Electrolyzers. *ACS Energy Letters*, 8(10):4156–4161, October 2023.

2

THE INFLUENCE OF SPATIAL EFFECTS ON CO₂ ELECTROLYSIS

*“He is a thinker, that is to say:
he knows how to make things simpler than they are.”*

— Friedrich Nietzsche,
in *The Gay Science* (1882)

CO₂ electrolyzers show promise as a clean conversion technology to produce value-added chemicals. Over the past decade research has shifted from classifying CO₂ reduction activity and selectivity as a catalytic property (0D) to one that includes the complex interactions of gas, liquid, and solid species taking place between the cathode and anode (1D). To scale up these electrolyzers, however, 2D and 3D spatial variations in product selectivity, activity and stability arise due to interactions of reactor components, and variations in concentrations of reactants, intermediates, and products. Conventional ‘black box’ measurement protocols are then by themselves insufficient to characterize CO₂ electrolyzers. In this perspective, we discuss the multi-dimensional spatial phenomena occurring inside these systems that can impact performance. We use recent works to demonstrate how a 2D/3D spatial perspective is essential for proper data interpretation, design of effective catalysts, prolonging the lifetime of CO₂ electrolyzers, and accelerating scale up efforts.

This chapter is based on a manuscript currently under review at *Chem Catalysis*, titled “Going beyond one dimension: how spatial effects define CO₂ electrolysis systems”, by S. Subramanian, H.P. Iglesias van Montfort and T. Burdyny.

2.1 Introduction

Low temperature CO₂ electrolysis using renewable energy sources is an attractive route to generate fossil-free fuels and base chemicals.[1–3] After years of rapid advancements in high-performing catalysts, component integration and efficient interface and reactor designs, the electrochemical CO₂ reduction (CO₂RR) has been scaled to >100 cm² cells and stacks for products such as carbon monoxide, formate, acetate and ethylene.[4–6] At the core of these developments is the use of gas-diffusion electrodes (GDEs) as catalyst supports which are then assembled in a membrane-electrode assembly (MEA) configuration. In a MEA the cathode, membrane and anode are within ~ 0.5 mm of each other. The combination of GDE's and MEA's then enables (i) high CO₂ access to all cathode sites allowing for current densities upwards of 200 mA cm⁻², (ii) substantial extrinsic gains in catalytic performance through a 3D porous catalyst layer, and (iii) low ohmic losses providing a pathway to full-cell voltages below 2.5 V.

A consequence of highly confined electrochemical regions and industrially viable reaction rates, however, is the formation of enormous spatial variations in CO₂, products, charge carriers, water and temperature in the one-dimensional (1D) direction from the cathode to the anode.[7–10] These spatial variations also extend to the 2D and 3D domain of a cell and stack, implying that the reactivity, selectivity, and efficiency of a CO₂ electrolyzer are not the same everywhere. When we upscale our systems, we then risk that the performance of our 5 cm² cells will not match a 100 or 1000 cm² cell due to differences in local concentrations, temperature, pressure, and component stability. Such concerns extend to the different cells within a stack. Translating performance to larger scales then requires understanding the importance and sensitivity of each parameter, and how they may vary spatially.

Notably, despite the existence of such 3D effects, the research field primarily uses 0D data to measure performance metrics.[11] Specifically, our standard electrochemical characterization techniques and gas/liquid product quantification almost explicitly are done using inlet and outlet measurements at periodic time intervals, providing only a 'black box' perspective of a highly-variable microenvironment. These 'device averaged' metrics are valuable and currently accepted in the field. Given the 3D operation of CO₂ electrolyzers (and 4D including time), however, the 'black box' measurement approach can lead to an incomplete understanding of the underlying behavior of our systems. The consequences of measurement uncertainty is also most pronounced in the operational domain of high CO₂ conversions, reactive products and larger cell/stack sizes[12, 13], specifically the conditions that the fast-moving field is heading towards. An appreciation and understanding of these spatial effects and their impact on performance metrics is then needed now, combined with approaches to approximate or measure spatial

effects.

In this chapter, we seek to shed light on the criticality of spatial variations in CO₂ electrolyzers, highlighting a body of recent studies employing operando techniques and multi-physics modeling tools that have identified these effects and their importance. We then provide instances where spatial effects can be used effectively for enhancing performance and mitigating instability for increasing the lifetime of an electrolyzer.

2.2 From 0D to 4D effects inside CO₂ electrolyzers

The electrochemical performance (activity, selectivity, efficiency, stability) of CO₂ electrolyzers is known to be governed by several factors. For example, we can tailor performance through our choice of components. These include the type, deposition and loading of cathode and anode catalysts, the type and dimensions of membrane/ionomers, and the choice of electrolyte and its concentration. The assembly and component configuration further plays a substantial role, as does the compression and gasketing of the system. And lastly operating parameters such as CO₂ flow rate, temperature, pressure, current density, and voltage will directly impact our measured performance. Each of these choices by themselves alter the initial ($t = 0$) measurable performance. However, as electrochemical reactions occur ($t > 0$) and species begin being transported throughout the system, the above factors will also separately cause an initially homogeneous reaction environment to evolve into a temporally and spatially varying one. Within this section we discuss spatial effects from the perspective of 0D (catalyst particle), 1D (cathode to anode direction), 2D (planar catalyst surface), 3D (multi-layer stack cells) and 4D (time).

At the core of our CO₂ electrolyzers is undoubtedly the atomistic catalyst surface with the domain being roughly a nanoparticle, here what we describe as 0D from a macroscopic perspective (Figure 2.1a). The rate of electrochemical CO₂RR is governed by the catalyst, applied potential and local microenvironment surrounding the catalyst surface.[14–16] The intrinsic catalytic activity of a single catalyst particle is, in principle, determined by the turnover number (TON) and turnover frequencies (TOF).[17] However, we are unable to easily characterize the activity of individual particles and precisely resolve the local electrochemical environment, meaning that we must estimate performance through device-average metrics (e.g. current density and Faradaic efficiency) normalized by the electrochemically active surface area.[18] By using precisely controlled catalyst layers (e.g. single crystals) and well-controlled conditions (e.g. excess CO₂ access, highly buffered solutions) we can use in operando techniques (e.g., X-ray Absorption Spectroscopy, Online Electrochemical Mass Spectroscopy, In-situ Raman and Infrared spectroscopy, neutron diffraction, etc.) to more closely link ob-

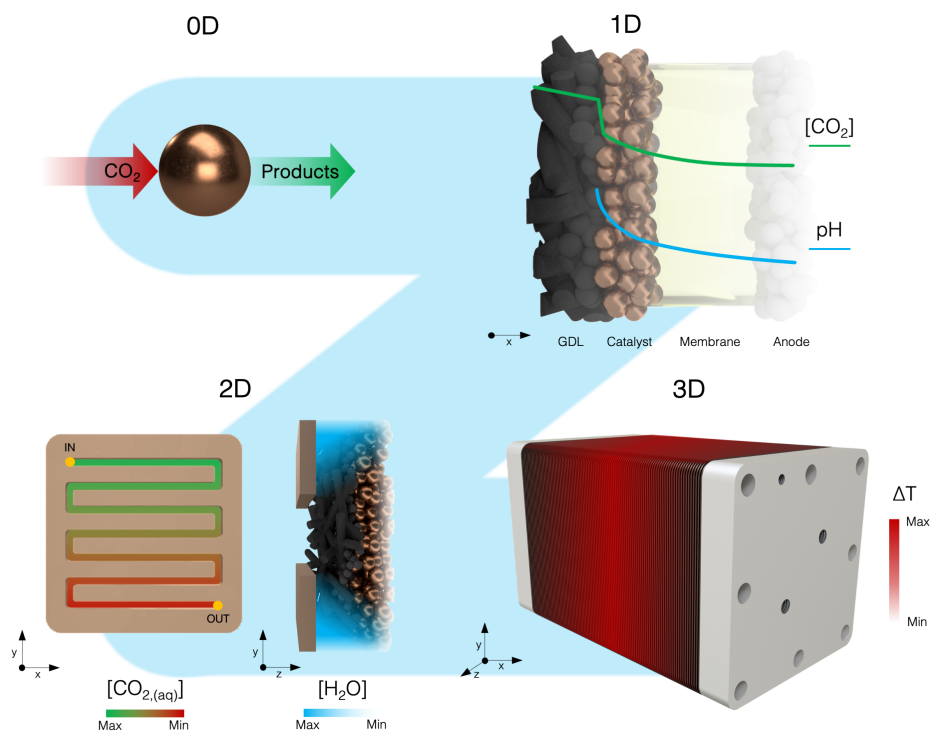


Figure 2.1: Study of CO₂RR electrolyzers requires a focus shift. Where in recent years the attention has been devoted to dimension-independent (0D) metrics, like faradaic efficiencies of specific catalyst species, modeling studies have recently picked up on depth-profiles of species (1D). To further advance knowledge in our field, more attention is required on 2D metrics, like special reactant distribution, and 3D aspects like heat production and accumulation.

served device-averaged performance to 0D surfaces. However, these studies are less representative of systems operating at elevated current densities.

The next dimensional direction of interest is the 1D regions between the cathode and anode which for a MEA system encompasses the gas-diffusion and microporous layers, the catalyst layer, ion exchange membrane, anode and anolyte (Figure 2.1b). This region, constituting less than 1 mm in distance, has extremely high variations in concentrations of CO₂, products, ions and water as evidenced through continuum transport modeling and observed experimental effects such as flooding and salt precipitation.[9, 10, 19] Without accounting for 1D effects in choosing components and system design, the achievable current densities, selectivity, and stability are substantially reduced. A deep understanding of the transport phenomena of this region has directly led to the development of new anion exchange membranes, the use of Cs⁺ as a cation, the lowering of anolyte concentra-

tions, appropriate catalyst deposition procedures and optimum cell compression.[20, 21] While much greater detail can be discussed regarding the critical 1D domain, these considerations are well accepted in the research field and covered elsewhere. For this perspective we then put greater emphasis on the 2D-3D spatial effects which are more under-explored, but critical for scale-up efforts of the technology.

Zooming out from the dominant 1D profile, we can consider a large variety of 2D planes. The 2D plane of most spatial importance and performance criticality, however, is assuredly the in-plane dimension of an individual cell that is perpendicular to the aforementioned 1D region. Slices of this region include the CO₂ gas channel, the gas-diffusion electrode (GDE), catalyst layer, membrane, and anode. For example in the anode compartment, pure liquid anolyte typically enters a cell, but this quickly becomes a two-phase mixture of anolyte and CO₂/O₂ gas as products evolve and carbonate crosses over the membrane. Near the latter part of the cell these gases can block active sites on the anode, as well as spatially influence the ohmic drops within a system. Combined the anode effects can then cause CO₂RR local current densities and applied voltages to vary, which impact the observed performance metrics. In small cell research we then typically overflow anolyte (e.g. 20 mL min⁻¹ for a 5 cm²) to avoid void fraction issues and boost performance. At very large cell areas though, pressure drop and pumping work become importance considerations, and excess anolyte flow may not be a viable option. We then must begin to form non-dimensional relationships and consider increasing pressure to lower void fractions as systems are scaled.

We would like to center most of our discussion, however, on the CO₂ gas channel, GDL and catalyst layer spatial variations as there are clear reports of how spatial effects impact the measured performance metrics. Within these three components from the inlet to the outlet of the reactor we have CO₂ being consumed and products being produced, resulting in a concentration gradient across a singular cell. Additionally, our systems use flow fields of various patterns to supply gas, remove products, and compress of cell together, all of which adds additional spatial complexities. Here we briefly discuss three dominant spatial considerations of the 2D planes of the cathodic side.

Firstly, due to CO₂ and product gradients across even small 5 cm² cells, the cathodic Faradaic efficiency can vary greatly from the inlet to the outlet of the reactor, particularly for CO₂ λ values (also called CO₂ excess) of 2-5. Such local FE values were first shown in our work for CO₂ to CO on a silver (Ag) catalyst where we noticed there were regions of the catalyst layer that were deplete of CO₂, even though the gas channel still contained abundant reactant.[13] In this work we discuss the implications of local FE versus device averaged FE's. We then followed up this work utilizing different flow field patterns (FFP's) which showed even greater spatial variations in concentrations, as well as discussed resistance to blockages of

different FFP's due to single versus multiple gas pathways.[22] Recently, further considerations were applied for a copper (Cu) catalyst where the residence time of intermediate CO was considered.[23] Lastly, in a case of direct CO electrolysis, Simonson et al. measured faradaic efficiencies at different locations using a copper and a segmented cell reactor.[24] Here spatial differences in ethylene and H₂ partial current densities were observed at various inlet flow rates and CO partial pressures. Collectively each of these examples provides motivation to contrast 2D FE's versus 0D measured FE's to sufficiently characterize the phenomena happening within systems.

A second conclusion resulting from acknowledging 2D concentration gradients across the gas channel is that there can be selectivity benefits by varying the composition of the catalyst layer spatially, which in turn can tune CO₂/CO ratios and shift C₂₊ production. This strategy has been shown widely in a number of studies employing tandem Ag/Cu or Zn/Cu catalyst systems to tune CO coverage and enhance C₂₊ or oxygenate production.[25–27] For instance, Zhang et al. designed a segmented Cu/Ag GDE (s-GDE) and found that a CO selective catalyst near the inlet (Ag) of the reactor and a Cu catalyst at subsequent segments maximizes C₂₊ partial current densities to > 1A/cm². [28] The strategy of controlling spatial management of by-products like CO shows how having a spatial perspective of electrochemical systems can be beneficial in designing effective catalyst layers for enhanced product formation rates.

A third 2D factor to consider on the cathode side is the water management. Too much or too little water in the membrane, catalyst layer and GDE are all problematic. In early work on humidification Wheeler et al. showed that the water concentration at the catalyst-membrane interface remained a constant in a MEA electrolyzer employing a Ag catalyst and humidity at the cathode feed was found to affect the production of CO significantly.[29] Using humidity sensors in the reactor and a numerical transport model, they showed that humidity at the cathode inlet feed modulated the flux of water transport and potassium cations crossover from the anode to cathode. Further work by Disch et al. also showed the variations in hydration using neutron imaging and compared water content in a flow field's land vs channel areas.[30] Due to the flow field both supplying gases and provides cell compression, large water differences were found between the two regions. This specific example is discussed further in the next section. Overall water management in MEA reactors is important due to two common failure mechanisms: flooding of the carbon GDE and (bi)-carbonate precipitation at the cathode. A proper understanding of water management and associated trade-offs in water concentrations at the cathode side are then essential for improving lifetime of these electrolyzers. In addition to concentrations of reactants (CO₂, H₂O), it is important to emphasize here that a variation in concentration of ions (K⁺,

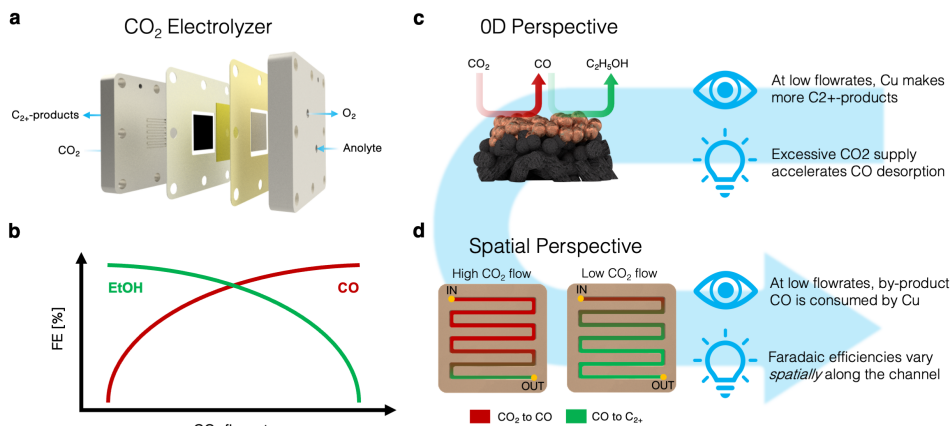


Figure 2.2: A spatial perspective on phenomena observed during operation sheds new light on the complexity of CO₂RR electrolyzers. (a) In a zero-gap MEA, the cathode evolves CO₂ and water to, e.g., C₂+ products. (b) A common effect observed in these electrolyzers is the shift in selectivity from ethanol to CO at higher flow-rates. (c) If we read this observation as independent of space-coordinates, we can be tempted to couple selectivity with convection effects. (d) The reality is, however, that flow-rates change concentration of species in an unequal way along the channel, and so do selectivities with it.

OH⁻, HCO₃⁻ and CO₃²⁻) at the catalyst microenvironment also alter reaction rates. For example, higher local cation concentration around the catalyst surface is known to increase C-C coupling and C₂+ product formation rates in Cu based MEA reactors in both alkaline and acidic conditions.

To illustrate how spatial dimensions can lead to differing hypotheses, we take CO₂RR on a copper (Cu) catalyst as an example (see Fig. 2.2). Experiments show that Cu produces the highest FE towards C₂+ products and lowest FE towards CO at lower inlet CO₂ flow-rates. Since CO is the intermediate for the formation of C₂+ products, interpreting this from a '0D perspective' (as shown in Fig. 2.1a) might lead to a possible conclusion that an excessive CO₂ supply helps to remove aqueous CO faster, reducing C-C coupling.[31] For example, a previous study by Sandberg et al. showed that adsorbate-adsorbate repulsion on Cu can facilitate *CO desorption and CO evolution.[32] In contrast, taking a spatial perspective might reveal an alternate hypothesis of a higher reactant residence time inside the electrolyzer (GDE and gas channel) as an alternate explanation for the observed increases in C₂+ selectivity at lower flow-rates. This means that as electrolyzers are scaled up (>1 cm²), spatial FE distributions arise inside the reactor, with the regions near the inlet feed predominantly producing CO₂ to CO and those down the channel producing CO to C₂+ products (See Figure 2.2).

For 3D systems we primarily think of an electrolyzer containing multiple cells within a larger stack. There are then considerations of how to feed CO₂ into all cells to prevent transport issues, as well as ensuring that each cell within a stack performs similarly or close to their optimal conditions. While assembly and design (e.g. gas headers, sealing, parallel/series power supply, shunt currents, etc.) is a critical factor to have a well-functioning stack, there will still be spatial variations that can impact behavior. A clear example of this is spatial temperature and pressure variations that will be unavoidable as a result of heat evolution and gas evolution, respectively. Controlling for these factors is needed as we move to large cell areas and numbers of cells that are typically only powered in a singular series connection. Current then flows through each cell equally, while the voltage requirements of each cell can differ. Means of in-line temperature management and system control by varying ramp rates and fluid flow are then ways of ensuring optimal and stable performance, emphasizing the necessity of 4D considerations if we begin to commercialize these technologies.

2.3 Operando visualization of spatial effects

While spatial variations can be inferred from ‘black box’ data and numerical models or probed with in-cell measurement points using humidity sensors or in-channel product quantification, these approaches still approximate or infer spatial effects. Direct measurement of spatial effects both in-plane and through the catalyst layer remains essential. Here operando techniques such as in-situ X-ray diffraction (XRD), Neutron diffraction, Raman spectroscopy and Infrared Thermography have just begun to probe CO₂ electrolyzers despite their usage in adjacent electrochemical fields. Here we will discuss these techniques and encourage their adopted use.

As an example of the application of such techniques, Moss et al. used in-situ XRD studies in a Cu based anion exchange membrane (AEM) electrolyzer and observed the evolution of bicarbonate formation within the GDE, which leads to salt precipitation and an oscillatory decline in the rates of CO₂RR (Fig. 2.3a).[33] These results not only provide insights into flooding of the GDE and subsequent decline in the performance, but also help in understanding ion transport mechanisms in AEMs under CO₂RR conditions, which are beneficial for designing AEMs specifically suited for CO₂ electrolyzers. Disch et al. used a neutron-diffraction technique in a zero gap MEA reactor and revealed that areas under the rib/land regions showed higher CO₂RR activity than at the gas flow field regions, due to higher water concentrations at the rib regions (Fig. 2.3b).[34] Our previous work on the influence of gas flow field pattern on CO production also showed that a higher pressure drop at the cathode side generated by a serpentine flow pattern resists electrolyte flooding the GDE, prolonging the lifetime of the electrolyzer.[22]

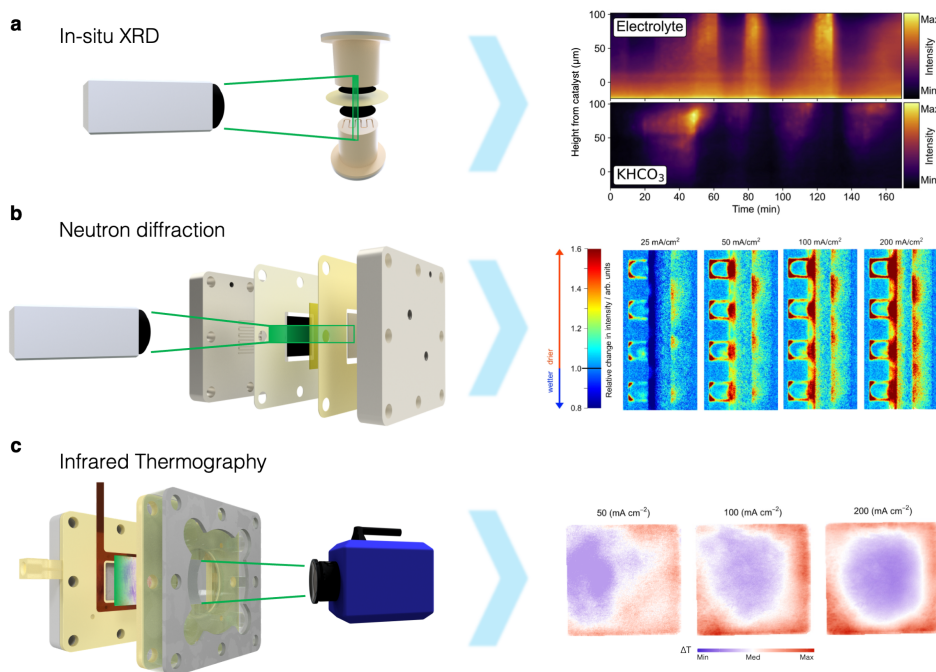


Figure 2.3: Recent developments in the field have enabled 2D visualization of phenomena occurring in CO₂RR-electrolyzers. (a) In-situ XRD reveals the species dynamics in and around the catalyst layer of an MEA.[33] (b) A neutron-diffraction analysis enables to visualize accumulation of water and salts between the membrane and the cathode at relevant current densities.[30] (c) Infrared-imaging of the cathode's backbone is a valid proxy for activity distribution of the catalyst in an x-y plane.[35, 36]

Design of proper gas flow field designs, rib spacing and humidification are then crucial considerations for the development of stable CO₂ electrolyzers.

In addition to these spatial variation in species concentrations, proper quantification of pH gradients around the catalyst coated GDL are essential as the competing HER and products like CH₄ are known to be pH dependent. This is where 1D reaction diffusion models have greatly enabled researchers to estimate pH gradients at various operating conditions and reactor configurations.[8, 37–39] A few studies have used operando techniques to estimate pH gradients around the catalyst surface in GDE flow cells. A study by Lu et al. using operando Raman spectroscopy in a GDE flow cell showed direct observation of pH gradients and the results were in good agreements with their reaction diffusion models.[40] As electrolyzers are scaled up, however, some operando pH measurement techniques may be challenging but not impossible to apply. For example: a similar study by Böhme

et al. showed maps of local pOH around the catalyst surface using confocal laser scanning microscopy (CLSM) and observed a higher pH in the micro-trenches of the GDE.[41] While each of these techniques come with its own advantages and limitations in terms of cell designs and spatial resolutions in space and time, we posit that one of these techniques might greatly benefit from combining it with a reaction diffusion model for proper estimation of pH gradients around the catalyst surface.

Additional means of probing local electrochemical activity are, for example, through infrared thermography (Fig. 2.3c) where thermal responses in time are a proportional result of electrochemical activity. In our previous work, we used infrared thermography to probe the local heat generated in a catalyst coated GDL during operation under various conditions.[35] At higher current densities during CO₂RR at ambient temperature, we found a Ag catalyst to be > 10 K hotter than the comparable electrolyte temperature. Such an observation has implications for modeling and kinetic interpretation whose properties (CO₂ solubility, reaction rates, diffusion, etc.) are strongly tied to temperature. As industrial CO₂ electrolyzers are likely to be operated at much higher current densities, it is important to understand that a catalyst during operation might be significantly hotter than the electrolyzer itself. Once again, this study shows why considering electrochemical reactions in multiple dimensions are beneficial for proper data interpretation and understanding of the phenomena occurring inside the electrolyzer.

2.4 Looking further: the gas-diffusion electrode as a 3D region

An important realization, in addition to the variation of the nature of catalyst in the 2D-plane, is the intrinsic complexity of the catalyst layer in the third dimension. The plethora of deposition methods reported in literature result in an equally complex landscape of electrode topologies. In a system that is very sensitive to local concentration of reactants,[42], tortuosity of the fluid phase,[43] and basicity, this leads to a blurred understanding of observed effects at play during CO₂RR. For added complexity, some catalysts, like copper, show an inherent instability that results in shifting product selectivities in time. These issues highlight the importance of understanding the role of our catalyst layer in the reaction system and the influence the deposition technique has on the performance metrics.

In a drive to tackle the instability of some catalysts, it can be enticing to ‘over-load’ the electrode with active particles. This prevents the catalyst activity from being a bottleneck in bench-top tests in a lab environment. Since catalyst loading is often overlooked as a variable in electrode development for CO₂RR, this practice goes mostly unnoticed. If one imagines a catalyst layer as a region with a

progressively deactivating regime, a thicker catalyst layer benefits the stability of the system overall. This comes at a cost of a thicker catalyst layer, but the reduced increase in this dimension relative to the overall cathode size seems a valid compromise. For context: Cu-catalysts are diverse in literature, and reported loadings are in the range of $0.1 \sim 3 \text{ mg cm}^{-2}$, spanning two orders of magnitude.[44–59] The main impacts of this practice are, for one, a skewed representation of partial current density towards a certain product; and two, a misleading reporting on stability of the catalyst, as the active region is allowed to progress through the layer during the experiments.

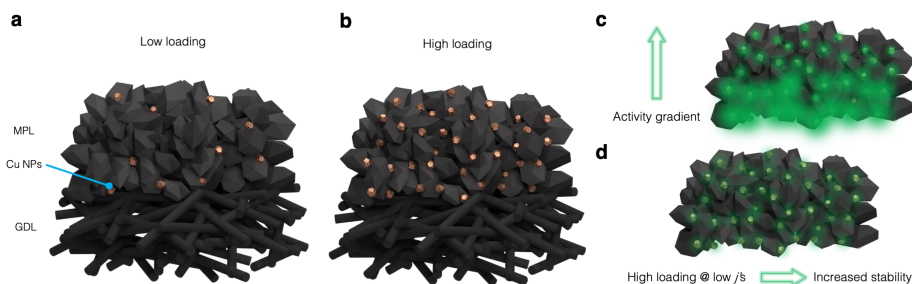


Figure 2.4: Catalyst loading directly affects the performance metrics of a CO_2RR GDE. (a) Sketch of the proximity of the catalyst layer in a low-loading GDE. (b) Same sketch for a high catalyst-loaded GDE. (c) A high loading enables a high presence of active species at the regions with highest CO_2 concentrations. (d) During stability tests, GDEs with a high loading show increased stability.

The problem of this blind-spot in literature comes when constant-potential tests are performed. Two electrodes with the same active catalyst but dissimilar loadings will display different current densities when subjected to the same polarization. The reason for this is simply that there are more electrochemical active sites per unit area (Fig. 2.4a and b). In addition, the common practice in the CO_2RR field is to condense current densities to a 2D-geometric area, disregarding the active electrochemical surface area. This draws unrealistic performance metrics of catalytic materials by ignoring the third depth dimension in electrode development. A richly-loaded catalyst layer allows for an appropriate level of activity at the gas-liquid interface, where CO_2 dissolves and reacts in the solid-liquid reaction (Fig. 2.4c).[42] Conversely, operating at lower current densities boosts the stability at high loadings by reducing intrinsic activities and the degradation mechanisms associated with this phenomenon (Fig. 2.4d).[60]

As a separate issue, catalyst layer thickness directly impacts local availability

and penetration depth of aqueous CO₂. While CO₂ solubility is generally high enough for industrially relevant current densities,[37] this metric is considerably affected by environmental factors like presence of ions, temperature and pressure of the gas-phase.[61, 62] CO₂ availability and average concentration in the aqueous phase of a thin catalyst layer of, say, 50 nm, then, is much more uniform than that of a 5 µm catalyst layer.[45, 63] This phenomenon is even more influential considering the dependance of certain catalysts like copper to the local ratio between reactant CO₂ and other intermediates like CO.[64] Furthermore, the tortuosity and complex structure of the active region of the GDE might result in varying pH conditions: a region with less convective or diffusive transport will result in the accumulation of carbonate species. Besides affecting the structural integrity of the catalyst,[65] this can result in a shift in the product selectivities.[66]

2.5 Current distribution in gas-diffusion electrodes

An often overlooked factor, besides that of catalyst loading, is that of current collection in gas-diffusion electrodes.[36] Assumed is that the carbonous substrate of most gas-diffusion layers is sufficiently conductive. The state of the CO₂RR field has not yet triggered output that could be confronted with poor current collection, since most output is performed on electrodes with a total surface area in the range of 1 – 5 cm² or current densities that do not challenge the capabilities of carbonous supports.

These assumptions may however soon be challenged by two separate developments. On the one hand, the move towards high current-density and surface area systems is moving the bottleneck of current-flow from the catalyst to the supporting interface (in this case, the GDE) and its anisotropy of current collection. On the other hand, irruption of alternative GDL-materials like expanded polytetrafluoroethylene (ePTFE) might complicate current collection and form a bottleneck at even smaller scales.

Carbonous electrodes have a long standing history of usage in the CO₂RR field, as their conductive backbone provides a solid base of conductivity, porosity and (combined with hydrophobic particles) an acceptable resistance to flooding. The latter, however, has been increasingly put under pressure as reports of flooding and its limitation to CO₂RR surfaced.[30, 67] Under cathodic circumstances, flooding of the porous layers is certain when reaching a certain potential threshold. This ultimately means conditions at the catalyst layer are heavily dependent on the local current density and potential, since, for example, a flooded carbonous electrode presents a considerable mass-transfer resistance to CO₂(aq).[36] A portion of the GDE at high potential, then, experiences more rapid flooding and thus a faster reduction in selectivity towards CO₂ products than a relatively drier portion. Imaging of these phenomena, especially that of spatial distribution of flooding, is

a valuable proxy to study current distribution.

In this regard, it may be attractive for the field of CO₂RR to collect the current at the posterior side of the catalyst – that is, using a front-contact current collector. This ensures variability of the collected current is not dependent on the gas-channel design and opens up the opportunity of designing a spatially variable current density to match local reactant conditions. This also relieves the carbonous back-layer of any variations in local potential or current density, so that flooding does not become an interface problem. Alternatively, a less conducting GDL might be compensated by a robust anterior current collection system, for example using flexible nickel meshes.[68]

A different strategy to avoiding microporous flooding involves using superhydrophobic MPLs insensitive to the interface potential. The most widespread application of this is the appearance of expanded polytetrafluoroethylene (ePTFE) GDEs in the CO₂RR field. These meshes of PTFE avoid macroscopic flooding by the intrinsic properties of the polymer, with the obvious caveat that they are non-conductive. This means every form of current collection must proceed through the front, active part of the electrode, in an in-plane geometry. Supplying electrons in this manner greatly strains the conductivity of the electrode, and induces great current distribution inequalities, especially so for thin catalyst layers.[36] Different strategies to tackle this have been proposed, from a non-active graphitic sandwich layer,[45] woven current collecting wires,[69] to insulated conductive plates[70] and non-invasive busbar electrodes.[36] The challenge for this architecture, overall, lies in engineering a technique that is scalable to industrial, meter-scale electrodes.

2.6 Conclusions

The vast array of overlapping phenomena occurring in CO₂ electrolyzers will make it an interesting research field for years to come. For the technology to be reliably scaled further, however, greater efforts are required to understand and optimize the 2D, 3D and 4D effects occurring in CO₂RR. Without such an appreciation, we are likely to continuously run into bottlenecks that then need to be solved on a case-by-case basis. Here, traditional chemical engineering principles should be applied to electrochemical systems to foresee problems ahead of time, which requires a mixture of older and newer approaches. We hope this perspective provides a basis for the multi-dimensional effects occurring, and spurs innovations as researchers and industry attempt to scale CO₂RR.

References

- [1] Rainer Küngas. Review—Electrochemical CO₂ Reduction for CO Production: Comparison of Low- and High-Temperature Electrolysis Technologies. *Journal of The Electrochemical Society*, 167(4):044508, January 2020.
- [2] Richard I. Masel, Zengcai Liu, Hongzhou Yang, Jerry J. Kaczur, Daniel Carrillo, Shaoxuan Ren, Danielle Salvatore, and Curtis P. Berlinguette. An industrial perspective on catalysts for low-temperature CO₂ electrolysis. *Nature Nanotechnology*, 16(2):118–128, February 2021.
- [3] David Wakerley, Sarah Lamaison, Joshua Wicks, Auston Clemens, Jeremy Feaster, Daniel Corral, Shaffiq A. Jaffer, Amitava Sarkar, Marc Fontecave, Eric B. Duoss, Sarah Baker, Edward H. Sargent, Thomas F. Jaramillo, and Christopher Hahn. Gas diffusion electrodes, reactor designs and key metrics of low-temperature CO₂ electrolyzers. *Nature Energy*, 7(2):130–143, February 2022.
- [4] B. Endrődi, E. Kecsenvity, A. Samu, F. Darvas, R. V. Jones, V. Török, A. Danyi, and C. Janáky. Multilayer Electrolyzer Stack Converts Carbon Dioxide to Gas Products at High Pressure with High Efficiency. *ACS Energy Letters*, 4(7):1770–1777, July 2019.
- [5] Woong Hee Lee, Chulwan Lim, Si Young Lee, Keun Hwa Chae, Chang Hyuck Choi, Ung Lee, Byoung Koun Min, Yun Jeong Hwang, and Hyung-Suk Oh. Highly selective and stackable electrode design for gaseous CO₂ electroreduction to ethylene in a zero-gap configuration. *Nano Energy*, 84:105859, June 2021.
- [6] Pengfei Wei, Dunfeng Gao, Tianfu Liu, Hefei Li, Jiaqi Sang, Chao Wang, Rui Cai, Guoxiong Wang, and Xinhe Bao. Coverage-driven selectivity switch from ethylene to acetate in high-rate CO₂/CO electrolysis. *Nature Nanotechnology*, 18(3):299–306, March 2023.
- [7] Matteo Agliuzza, Candido Fabrizio Pirri, and Adriano Sacco. A comprehensive modeling for the CO₂ electroreduction to CO. *Journal of Physics: Energy*, 6(1):015004, January 2024.
- [8] Lien-Chun Weng, Alexis T. Bell, and Adam Z. Weber. Modeling gas-diffusion electrodes for CO₂ reduction. *Physical Chemistry Chemical Physics*, 20(25):16973–16984, 2018.
- [9] Lien-Chun Weng, Alexis T. Bell, and Adam Z. Weber. A systematic analysis of Cu-based membrane-electrode assemblies for CO₂ reduction through

- multiphysics simulation. *Energy & Environmental Science*, 13(10):3592–3606, 2020.
- [10] Lien-Chun Weng, Alexis T. Bell, and Adam Z. Weber. Towards membrane-electrode assembly systems for CO₂ reduction: a modeling study. *Energy & Environmental Science*, 12(6):1950–1968, 2019.
- [11] Hugo-Pieter Iglesias Van Montfort, Siddhartha Subramanian, Erdem Irtem, Mark Sassenburg, Mengran Li, Jesse Kok, Joost Middelkoop, and Thomas Burdyny. An Advanced Guide to Assembly and Operation of CO₂ Electrolyzers. *ACS Energy Letters*, 8(10):4156–4161, October 2023.
- [12] Recep Kas, Andrew G. Star, Kailun Yang, Tim Van Cleve, Kenneth C. Neyerlin, and Wilson A. Smith. Along the Channel Gradients Impact on the Spatioactivity of Gas Diffusion Electrodes at High Conversions during CO₂ Electroreduction. *ACS Sustainable Chemistry and Engineering*, 9(3):1286–1296, January 2021. Publisher: American Chemical Society.
- [13] Siddhartha Subramanian, Joost Middelkoop, and Thomas Burdyny. Spatial reactant distribution in CO₂ electrolysis: balancing CO₂ utilization and faradaic efficiency. *Sustainable Energy & Fuels*, 5(23):6040–6048, 2021.
- [14] Stephanie Nitopi, Erlend Bertheussen, Soren B. Scott, Xinyan Liu, Albert K. Engstfeld, Sebastian Horch, Brian Seger, Ifan E. L. Stephens, Karen Chan, Christopher Hahn, Jens K. Nørskov, Thomas F. Jaramillo, and Ib Chorkendorff. Progress and Perspectives of Electrochemical CO₂ Reduction on Copper in Aqueous Electrolyte. *Chemical Reviews*, 119(12):7610–7672, June 2019. Publisher: American Chemical Society.
- [15] Uzoma O. Nwabara, Emiliana R. Cofell, Sumit Verma, Emanuela Negro, and Paul J. A. Kenis. Durable Cathodes and Electrolyzers for the Efficient Aqueous Electrochemical Reduction of CO₂. *ChemSusChem*, 13(5):855–875, March 2020.
- [16] Ifan E L Stephens, Karen Chan, Alexander Bagger, Shannon W Boettcher, Julien Bonin, Etienne Boutin, Aya K Buckley, Raffaella Buonsanti, Etosha R Cave, Xiaoxia Chang, See Wee Chee, Alisson H M Da Silva, Phil De Luna, Oliver Einsle, Balázs Endrődi, Maria Escudero-Escribano, Jorge V Ferreira De Araujo, Marta C Figueiredo, Christopher Hahn, Kentaro U Hansen, Sophia Haussener, Sara Hunegnaw, Ziyang Huo, Yun Jeong Hwang, Csaba Janáky, Buddhinie S Jayatilake, Feng Jiao, Zarko P Jovanov, Parisa Karimi, Marc T M Koper, Kendra P Kuhl, Woong Hee Lee, Zhiqin Liang, Xuan Liu, Sichao

- Ma, Ming Ma, Hyung-Suk Oh, Marc Robert, Beatriz Roldan Cuenya, Jan Rossmeisl, Claudie Roy, Mary P Ryan, Edward H Sargent, Paula Sebastián-Pascual, Brian Seger, Ludmilla Steier, Peter Strasser, Ana Sofia Varela, Rafaël E Vos, Xue Wang, Bingjun Xu, Hossein Yadegari, and Yuxiang Zhou. 2022 roadmap on low temperature electrochemical CO₂ reduction. *Journal of Physics: Energy*, 4(4):042003, October 2022.
- [17] Robert B. Kutz, Qingmei Chen, Hongzhou Yang, Syed D. Sajjad, Zengcai Liu, and I. Richard Masel. Sustainion Imidazolium-Functionalized Polymers for Carbon Dioxide Electrolysis. *Energy Technology*, 5(6):929–936, June 2017.
- [18] Ward Van Der Stam. The Necessity for Multiscale *In Situ* Characterization of Tailored Electrocatalyst Nanoparticle Stability. *Chemistry of Materials*, 35(2):386–394, January 2023.
- [19] Eric W. Lees, Justin C. Bui, Oyinkansola Romiluyi, Alexis T. Bell, and Adam Z. Weber. Exploring CO₂ reduction and crossover in membrane electrode assemblies. *Nature Chemical Engineering*, 1(5):340–353, May 2024.
- [20] Dong Un Lee, Bjørnt Joensen, Joel Jenny, Victoria M. Ehlinger, Sang-Won Lee, Kabir Abiose, Yi Xu, Amitava Sarkar, Tiras Y. Lin, Christopher Hahn, and Thomas F. Jaramillo. Controlling Mass Transport in Direct Carbon Dioxide Zero-Gap Electrolyzers via Cell Compression. *ACS Sustainable Chemistry & Engineering*, 11(46):16661–16668, November 2023.
- [21] Danielle A. Salvatore, Christine M. Gabardo, Angelica Reyes, Colin P. O’Brien, Steven Holdcroft, Peter Pintauro, Bamdad Bahar, Michael Hickner, Chulsung Bae, David Sinton, Edward H. Sargent, and Curtis P. Berlinguette. Designing anion exchange membranes for CO₂ electrolyzers. *Nature Energy*, 6(4):339–348, February 2021.
- [22] Siddhartha Subramanian, Kailun Yang, Mengran Li, Mark Sassenburg, Maryam Abdinejad, Erdem Irtem, Joost Middelkoop, and Thomas Burdyny. Geometric Catalyst Utilization in Zero-Gap CO₂ Electrolyzers. *ACS Energy Letters*, pages 222–229, November 2022. Publisher: American Chemical Society.
- [23] Siddhartha Subramanian, Jesse Kok, Pratik Gholkar, Asvin Sajeew Kumar, Hugo-Pieter Iglesias van Montfort, Ruud Kortlever, Atsushi Urakawa, Bernard Dam, and Burdyny, Thomas. CO residence time modulates multi-carbon formation rates in a zero-gap Cu based CO₂ electrolyzer. *Under Review*, November 2023.

- [24] Hunter Simonson, Walter Ellis Klein, Danielle Henckel, Sumit Verma, K. C. Neyerlin, and Wilson A. Smith. Direct Measurement of Electrochemical Selectivity Gradients over a 25 cm² Copper Gas Diffusion Electrode. *ACS Energy Letters*, pages 3811–3819, August 2023.
- [25] Carlos G. Morales-Guio, Etosha R. Cave, Stephanie A. Nitopi, Jeremy T. Feaster, Lei Wang, Kendra P. Kuhl, Ariel Jackson, Natalie C. Johnson, David N. Abram, Toru Hatsukade, Christopher Hahn, and Thomas F. Jaramillo. Improved CO₂ reduction activity towards C₂₊ alcohols on a tandem gold on copper electrocatalyst. *Nature Catalysis*, 1(10):764–771, October 2018.
- [26] Tianyu Zhang, Zhengyuan Li, Jianfang Zhang, and Jingjie Wu. Enhance CO₂-to-C₂₊ products yield through spatial management of CO transport in Cu/ZnO tandem electrodes. *Journal of Catalysis*, 387:163–169, July 2020.
- [27] Bing Zhang, Linlin Wang, Di Li, Zongmiao Li, Ran Bu, and Yingying Lu. Tandem strategy for electrochemical CO₂ reduction reaction. *Chem Catalysis*, 2(12):3395–3429, December 2022.
- [28] Tianyu Zhang, Justin C. Bui, Zhengyuan Li, Alexis T. Bell, Adam Z. Weber, and Jingjie Wu. Highly selective and productive reduction of carbon dioxide to multicarbon products via in situ CO management using segmented tandem electrodes. *Nature Catalysis*, 5(3):202–211, March 2022.
- [29] Danika G. Wheeler, Benjamin A. W. Mowbray, Angelica Reyes, Faezeh Habibzadeh, Jingfu He, and Curtis P. Berlinguette. Quantification of water transport in a CO₂ electrolyzer. *Energy & Environmental Science*, 13(12):5126–5134, 2020.
- [30] Joey Disch, Luca Bohn, Susanne Koch, Michael Schulz, Yiyong Han, Alessandro Tengattini, Lukas Helfen, Matthias Breitwieser, and Severin Vierrath. High-resolution neutron imaging of salt precipitation and water transport in zero-gap CO₂ electrolysis. *Nature Communications*, 13(1):6099, October 2022.
- [31] Yun Huang, Albertus D. Handoko, Pussana Hirunsit, and Boon Siang Yeo. Electrochemical Reduction of CO₂ Using Copper Single-Crystal Surfaces: Effects of CO* Coverage on the Selective Formation of Ethylene. *ACS Catalysis*, 7(3):1749–1756, March 2017.
- [32] Robert B. Sandberg, Joseph H. Montoya, Karen Chan, and Jens K. Nørskov. CO-CO coupling on Cu facets: Coverage, strain and field effects. *Surface Science*, 654:56–62, December 2016.

- [33] Asger B. Moss, Sahil Garg, Marta Mirolo, Carlos A. Giron Rodriguez, Roosa Ilvonen, Ib Chorkendorff, Jakub Drnec, and Brian Seger. In operando investigations of oscillatory water and carbonate effects in MEA-based CO₂ electrolysis devices. *Joule*, 7(2):350–365, February 2023.
- [34] Joey Disch, Luca Bohn, Lukas Metzler, and Severin Vierrath. Strategies for the mitigation of salt precipitation in zero-gap CO₂ electrolyzers producing CO. *Journal of Materials Chemistry A*, 11(14):7344–7357, 2023.
- [35] Hugo-Pieter Iglesias van Montfort and Thomas Burdyny. Mapping Spatial and Temporal Electrochemical Activity of Water and CO₂ Electrolysis on Gas-Diffusion Electrodes Using Infrared Thermography. *ACS Energy Letters*, 7(8):2410–2419, August 2022. Publisher: American Chemical Society.
- [36] Hugo-Pieter Iglesias van Montfort, Mengran Li, Erdem Irtem, Maryam Abidinejad, Yuming Wu, Santosh K. Pal, Mark Sassenburg, Davide Ripepi, Siddhartha Subramanian, Jasper Biemolt, Thomas E. Rufford, and Thomas Burdyny. Non-invasive current collectors for improved current-density distribution during CO₂ electrolysis on super-hydrophobic electrodes. *Nature Communications*, 14(1):6579, October 2023.
- [37] Thomas Burdyny and Wilson A Smith. CO₂ reduction on gas-diffusion electrodes and why catalytic performance must be assessed at commercially-relevant conditions. *Energy and Environmental Science*, 2019.
- [38] Thomas Moore, Xiaoxing Xia, Sarah E. Baker, Eric B. Duoss, and Victor A. Beck. Elucidating Mass Transport Regimes in Gas Diffusion Electrodes for CO₂ Electroreduction. *ACS Energy Letters*, 6(10):3600–3606, October 2021.
- [39] David Raciti, Mark Mao, and Chao Wang. Mass transport modelling for the electroreduction of CO₂ on Cu nanowires. *Nanotechnology*, 29(4):044001, January 2018.
- [40] Xu Lu, Chongqin Zhu, Zishan Wu, Jin Xuan, Joseph S. Francisco, and Hailiang Wang. In Situ Observation of the pH Gradient near the Gas Diffusion Electrode of CO₂ Reduction in Alkaline Electrolyte. *Journal of the American Chemical Society*, 142(36):15438–15444, September 2020.
- [41] Annette Böhme, Justin C. Bui, Aidan Q. Fenwick, Rohit Bhide, Cassidy N. Feltenberger, Alexandra J. Welch, Alex J. King, Alexis T. Bell, Adam Z. Weber, Shane Ardo, and Harry A. Atwater. Direct observation of the local microenvironment in inhomogeneous CO₂ reduction gas diffusion electrodes via versatile pOH imaging. *Energy & Environmental Science*, 16(4):1783–1795, 2023.

- [42] Nathan T. Nesbitt, Thomas Burdyny, Hunter Simonson, Danielle Salvatore, Divya Bohra, Recep Kas, and Wilson A. Smith. Liquid-Solid Boundaries Dominate Activity of CO₂ Reduction on Gas-Diffusion Electrodes. *ACS Catalysis*, 10(23):14093–14106, December 2020. Publisher: American Chemical Society.
- [43] Divya Bohra, Jehanzeb H. Chaudhry, Thomas Burdyny, Evgeny A. Pidko, and Wilson A. Smith. Modeling the electrical double layer to understand the reaction environment in a CO₂ electrocatalytic system. *Energy and Environmental Science*, 12(11):3380–3389, November 2019. Publisher: Royal Society of Chemistry.
- [44] Gian Luca De Gregorio, Thomas Burdyny, Anna Loiudice, Pranit Iyengar, Wilson A. Smith, and Raffaella Buonsanti. Facet-Dependent Selectivity of Cu Catalysts in Electrochemical CO₂ Reduction at Commercially Viable Current Densities. *ACS Catalysis*, 10(9):4854–4862, May 2020.
- [45] Cao Thang Dinh, Thomas Burdyny, Golam Kibria, Ali Seifitokaldani, Christine M Gabardo, F Pelayo García De Arquer, Amirreza Kiani, Jonathan P Edwards, Phil De Luna, Oleksandr S Bushuyev, Chengqin Zou, Rafael Quintero-Bermudez, Yuanjie Pang, David Sinton, and Edward H Sargent. CO₂ electroreduction to ethylene via hydroxide-mediated copper catalysis at an abrupt interface. *Science*, 360:783–787, 2018.
- [46] Mengyang Fan, Jianan Erick Huang, Rui Kai Miao, Yu Mao, Pengfei Ou, Feng Li, Xiao-Yan Li, Yufei Cao, Zishuai Zhang, Jinqiang Zhang, Yu Yan, Adnan Ozden, Weiyan Ni, Ying Wang, Yong Zhao, Zhu Chen, Behrooz Khatir, Colin P. O'Brien, Yi Xu, Yurou Celine Xiao, Geoffrey I. N. Waterhouse, Kevin Golovin, Ziyun Wang, Edward H. Sargent, and David Sinton. Cationic-group-functionalized electrocatalysts enable stable acidic CO₂ electrolysis. *Nature Catalysis*, 6(9):763–772, August 2023.
- [47] F Pelayo García de Arquer, Cao Thang Dinh, Adnan Ozden, Joshua Wicks, Christopher McCallum, Ahmad R Kirmani, Dae Hyun Nam, Christine Gabardo, Ali Seifitokaldani, Xue Wang, Yuguang C Li, Fengwang Li, Jonathan Edwards, Lee J Richter, Steven J Thorpe, David Sinton, and Edward H Sargent. CO₂ electrolysis to multicarbon products at activities greater than 1 A cm⁻². *Science*, 367:661–666, 2020.
- [48] Zhengxiang Gu, Hao Shen, Zheng Chen, Yaoyue Yang, Chao Yang, Yali Ji, Yuhang Wang, Chan Zhu, Junlang Liu, Jun Li, Tsun-Kong Sham, Xin Xu, and Gengfeng Zheng. Efficient Electrocatalytic CO₂ Reduction to C₂₊ Alcohols at Defect-Site-Rich Cu Surface. *Joule*, 5(2):429–440, February 2021.

- [49] Attila Kormányos, Balázs Endrődi, Zheng Zhang, Angelika Samu, László Mérai, Gergely F. Samu, László Janovák, and Csaba Janáky. Local hydrophobicity allows high-performance electrochemical carbon monoxide reduction to C₂₊ products. *EES Catalysis*, 1(3):263–273, 2023.
- [50] Hefei Li, Tianfu Liu, Pengfei Wei, Long Lin, Dunfeng Gao, Guoxiong Wang, and Xinhe Bao. High-Rate CO₂ Electroreduction to C₂₊ Products over a Copper-Copper Iodide Catalyst. *Angewandte Chemie*, 133(26):14450–14454, June 2021.
- [51] Jun Li, Adnan Ozden, Mingyu Wan, Yongfeng Hu, Fengwang Li, Yuhang Wang, Reza R. Zamani, Dan Ren, Ziyun Wang, Yi Xu, Dae-Hyun Nam, Joshua Wicks, Bin Chen, Xue Wang, Mingchuan Luo, Michael Graetzel, Fanglin Che, Edward H. Sargent, and David Sinton. Silica-copper catalyst interfaces enable carbon-carbon coupling towards ethylene electrosynthesis. *Nature Communications*, 12(1):2808, May 2021.
- [52] Wenchao Ma, Shunji Xie, Tongtong Liu, Qiyuan Fan, Jinyu Ye, Fanfei Sun, Zheng Jiang, Qinghong Zhang, Jun Cheng, and Ye Wang. Electrocatalytic reduction of CO₂ to ethylene and ethanol through hydrogen-assisted C–C coupling over fluorine-modified copper. *Nature Catalysis*, 3(6):478–487, April 2020.
- [53] Zesong Ma, Zhilong Yang, Wenchuan Lai, Qiyou Wang, Yan Qiao, Haolan Tao, Cheng Lian, Min Liu, Chao Ma, Anlian Pan, and Hongwen Huang. CO₂ electroreduction to multicarbon products in strongly acidic electrolyte via synergistically modulating the local microenvironment. *Nature Communications*, 13(1):7596, December 2022.
- [54] Adnan Ozden, Fengwang Li, F. Pelayo García De Arquer, Alonso Rosas-Hernández, Arnaud Thevenon, Yuhang Wang, Sung-Fu Hung, Xue Wang, Bin Chen, Jun Li, Joshua Wicks, Mingchuan Luo, Ziyun Wang, Theodor Agapie, Jonas C. Peters, Edward H. Sargent, and David Sinton. High-Rate and Efficient Ethylene Electrosynthesis Using a Catalyst/Promoter/Transport Layer. *ACS Energy Letters*, 5(9):2811–2818, September 2020.
- [55] Xue Wang, Ziyun Wang, F. Pelayo García De Arquer, Cao-Thang Dinh, Adnan Ozden, Yuguang C. Li, Dae-Hyun Nam, Jun Li, Yi-Sheng Liu, Joshua Wicks, Zitao Chen, Miaofang Chi, Bin Chen, Ying Wang, Jason Tam, Jane Y. Howe, Andrew Proppe, Petar Todorović, Fengwang Li, Tao-Tao Zhuang, Christine M. Gabardo, Ahmad R. Kirmani, Christopher McCallum, Sung-Fu Hung, Yanwei Lum, Mingchuan Luo, Yimeng Min, Aoni Xu, Colin P. O’Brien,

- Bello Stephen, Bin Sun, Alexander H. Ip, Lee J. Richter, Shana O. Kelley, David Sinton, and Edward H. Sargent. Efficient electrically powered CO₂-to-ethanol via suppression of deoxygenation. *Nature Energy*, 5(6):478–486, May 2020.
- [56] Yuxuan Wang, Hao Shen, Ken J. T. Livi, David Raciti, Han Zong, John Gregg, Mofopofoluwa Onadeko, Yidong Wan, Adam Watson, and Chao Wang. Copper Nanocubes for C₂₊ Reduction in Gas Diffusion Electrodes. *Nano Letters*, 19(12):8461–8468, December 2019.
- [57] Qiqi Wu, Ruian Du, Peng Wang, Geoffrey I. N. Waterhouse, Jia Li, Yongcai Qiu, Keyou Yan, Yun Zhao, Wei-Wei Zhao, Hsin-Jung Tsai, Meng-Cheng Chen, Sung-Fu Hung, Xue Wang, and Guangxu Chen. Nanograin-Boundary-Abundant CuO-Cu Nanocubes with High C₂₊ Selectivity and Good Stability during Electrochemical CO₂ Reduction at a Current Density of 500 mA/cm². *ACS Nano*, 17(13):12884–12894, July 2023.
- [58] Gong Zhang, Zhi-Jian Zhao, Dongfang Cheng, Huimin Li, Jia Yu, Qingzhen Wang, Hui Gao, Jinyu Guo, Huaiyuan Wang, Geoffrey A. Ozin, Tuo Wang, and Jinlong Gong. Efficient CO₂ electroreduction on facet-selective copper films with high conversion rate. *Nature Communications*, 12(1):5745, September 2021.
- [59] Min Zheng, Pengtang Wang, Xing Zhi, Kang Yang, Yan Jiao, Jingjing Duan, Yao Zheng, and Shi-Zhang Qiao. Electrocatalytic CO₂-to-C₂₊ with Ampere-Level Current on Heteroatom-Engineered Copper via Tuning *CO Intermediate Coverage. *Journal of the American Chemical Society*, 144(32):14936–14944, August 2022.
- [60] Stefan Popović, Milutin Smiljanić, Primož Jovanovič, Jan Vavra, Raffaella Buonsanti, and Nejc Hodnik. Stability and Degradation Mechanisms of Copper-Based Catalysts for Electrochemical CO₂ Reduction. *Angewandte Chemie*, 132(35):14844–14854, August 2020.
- [61] S. Weisenberger and A. Schumpe. Estimation of gas solubilities in salt solutions at temperatures from 273 K to 363 K. *AIChE Journal*, 42(1):298–300, January 1996.
- [62] Denis A. Wiesenburg and Norman L Guinasso. Equilibrium solubilities of methane, carbon monoxide, and hydrogen in water and sea water. *Journal of Chemical & Engineering Data*, 24(4):356–360, October 1979.
- [63] Ying Chuan Tan, Kelvin Berm Lee, Hakhyeon Song, and Jihun Oh. Modulating Local CO₂ Concentration as a General Strategy for Enhancing C–C Coupling in CO₂ Electroreduction. *Joule*, 4(5):1104–1120, May 2020.

- [64] Xingli Wang, Jorge Ferreira de Araújo, Wen Ju, Alexander Bagger, Henrike Schmies, Stefanie Kühl, Jan Rossmeisl, and Peter Strasser. Mechanistic reaction pathways of enhanced ethylene yields during electroreduction of CO₂–CO co-feeds on Cu and Cu-tandem electrocatalysts. *Nature Nanotechnology*, 14(11):1063–1070, November 2019.
- [65] Danielle A. Henckel, Michael J. Counihan, Hannah E. Holmes, Xinyi Chen, Uzoma O. Nwabara, Sumit Verma, Joaquín Rodríguez-López, Paul J. A. Kenis, and Andrew A. Gewirth. Potential Dependence of the Local pH in a CO₂ Reduction Electrolyzer. *ACS Catalysis*, 11(1):255–263, January 2021.
- [66] Ana Sofia Varela, Matthias Kroschel, Nathaniel D. Leonard, Wen Ju, Julian Steinberg, Alexander Bagger, Jan Rossmeisl, and Peter Strasser. pH Effects on the Selectivity of the Electrocatalytic CO₂ Reduction on Graphene-Embedded Fe–N–C Motifs: Bridging Concepts between Molecular Homogeneous and Solid-State Heterogeneous Catalysis. *ACS Energy Letters*, 3(4):812–817, April 2018.
- [67] Kailun Yang, Recep Kas, Wilson A. Smith, and Thomas Burdyny. Role of the Carbon-Based Gas Diffusion Layer on Flooding in a Gas Diffusion Electrode Cell for Electrochemical CO₂ Reduction. *ACS Energy Letters*, 6(1):33–40, January 2021.
- [68] Michele Perego, Dario Oldani, and Angelo Ottaviani. US Patent 8372255: Elastic Current Collector for Electrochemical Cells.
- [69] Simon Rufer, Michael Nitzsche, Sanjay Garimella, Jack Lake, and Kripa K. Varanasi. Hierarchically Conductive Electrodes Unlock Stable and Scalable CO₂ Electrolysis. *ChemRxiv*, November 2023.
- [70] Michael Filippi, Tim Möller, Remigiusz Pastusiak, Erhard Magori, Benjamin Paul, and Peter Strasser. Scale-Up of PTFE-Based Gas Diffusion Electrodes Using an Electrolyte-Integrated Polymer-Coated Current Collector Approach. *ACS Energy Letters*, pages 1361–1368, March 2024.

3

3

MAPPING ELECTROCHEMICAL ACTIVITY IN ELECTROLYZERS USING INFRARED THERMOGRAPHY

*“Equipped with his five senses, man explores the universe around him
and calls the adventure ‘Science’.”*

— Edwin P. Hubble

Electrolysis of water, CO₂ and nitrogen-based compounds presents the opportunity of generating fossil-free fuels and feedstocks at an industrial scale. Devices are complex in operation, and their performance metrics are usually reported as electrode-averaged quantities. In this work, we report the usage of infrared thermography to map the electrochemical activity of a gas-diffusion electrode performing water and CO₂ reduction. By associating the heat map to a characteristic catalytic activity, the presented system can capture electrochemical and physical phenomena as they occur in electrolyzers for large-scale energy applications. We demonstrate applications for catalyst screening, catalyst-degradation measurements and spatial activity mapping for water and CO₂ electrolysis at current densities up to 0.2 A cm⁻². At these current densities we report catalyst temperature increases (>10K for 0.2 A cm⁻²) not apparent otherwise. Further, substantial localized current density fluctuations are present. These observations challenge assumed local conditions, providing new fundamental and applied perspectives.

3.1 Introduction

In the critical drive to find solutions for sustainable energy storage, electrochemical technologies which can be operated at global energy scales using fossil-free electricity offer promise. Research activities range broadly from the development of catalysts for novel reactions in nitrogen-based electrochemistry, steady improvement in C2 and C3 product selectivity for CO₂ reduction, to the fine-tuning of well-understood reactions such as water-splitting.[2–5] Performance metrics such as current density, efficiency/overpotential, selectivity and stability provide the central foundation for evaluating electrochemical advancements and comparing systems.[6–8]

Despite electrochemical performance metrics being spatial and temporal properties (4D in space and time) which vary throughout a catalyst layer, these foundational metrics are measured as black box averaged quantities by potentiostats and bulk product quantification methods. All spatial information is then distilled to 1D resolutions in time. Not only are spatial resolutions in activity and selectivity lost, which results in phenomena and system behavior being indirectly evaluated, but electrochemistry is then faced with a one potentiostat – one data point problem. Catalyst screening efforts and mass data production for machine learning algorithms then subsequently suffer from insufficient or oversimplified data. Further, the dominant factors contributing to observed performance must be determined through multiple experiments and post-electrolysis analysis to properly disambiguate overlapping contributions of the catalyst, system and operating parameters. With electrochemical behavior governed by phenomena spanning broad physical scales (angstroms to meters) and scientific domains, a more direct link between electrochemical activity - and how we measure that activity - is necessary.

Efforts towards the measurement of temporal-spatial electrochemical activity, as well as combinatorial setups, have been introduced to partially address these shortfalls, with an emphasis on catalyst activity.[9–15] However, most approaches still require the sequential testing of miniaturized reactors or cell segmentation, both of which have spatial resolutions set by physical limitations.[16–20] Multi-well dye-based techniques allow for parallelization but provide only indirect indicators of electrochemical activity over a small catalyst, with tested current densities up to 50 mA cm⁻². [14, 21] Dye techniques further rely on an observable liquid electrolyte resulting in cell configurations distanced from standard operation. Separately, thermographic approaches have been demonstrated in ‘quasi in-situ’ operation for fuel cell applications using membrane-electrode assemblies.[22–25] Here an infrared camera observes the cathodic chamber where ambient oxygen may react with hydrogen that has crossed over from the anodic chamber. The exothermic reaction between hydrogen and oxygen then allows thermography to detect hydrogen crossover, and subsequently pinholes in the ion exchange mem-

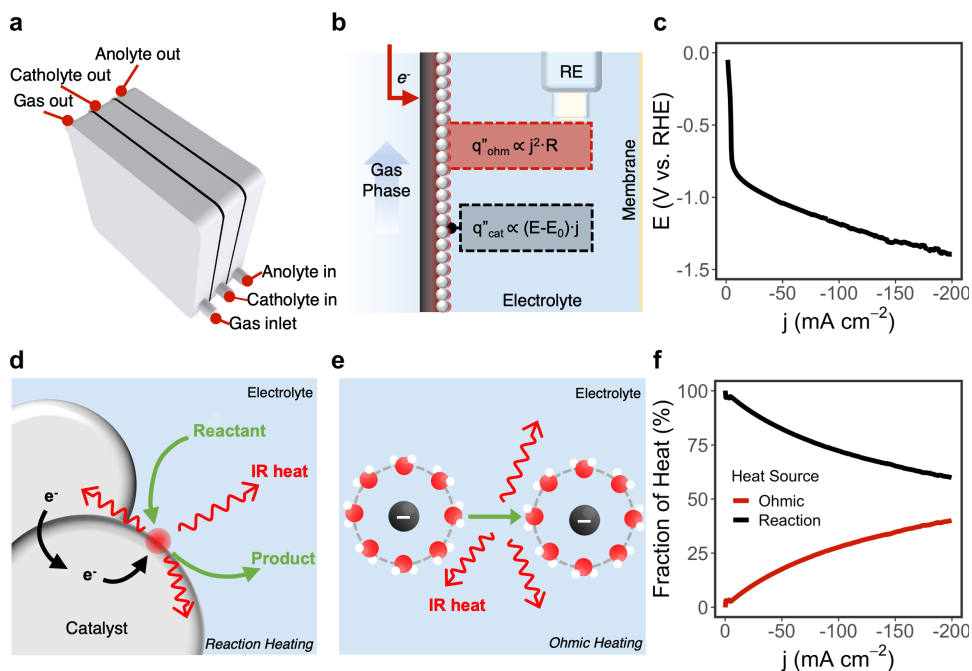


Figure 3.1: Heat production in a lab-scale electrolyzer is controlled mainly by catalytic and resistive overpotentials. (a) Schematic representation of a representative 3-compartment electrolyzer cell. (b) Half-cell view of an electrochemical cell using a catalyst deposited onto the liquid side of a gas-diffusion electrode. Heat generation locations and formula of ohmic heating (q''_{ohm}) and reaction-driven heating (q''_{cat}) are shown. (c) Polarization curve (uncompensated) of a 100nm Pt GDE during HER in the reported electrolyzer (1M KOH catholyte, sweep rate of $-1\text{ mA cm}^{-2} \text{ s}^{-1}$). (d) Heat is produced at the catalyst-electrolyte interface due to the overpotential required to drive the reaction. (e) Ohmic heating as a result of ion transport in an electrolyte. (f) Relative source of heating at the interface as a function of applied current density for a 15 mm thick 1 M KOH electrolyte.

brane and the effect of preparing membrane electrode assemblies. If an operando and accessible technique provided optical-level resolution of electrochemical activity under representative conditions, it would not only be valuable for catalyst testing, but broadly beneficial for both fundamental and applied analyses of the many rapidly advancing electrochemical fields.

In this study we exploit the typically undesired energy inefficiencies inherent in electrochemical reactions to observe location-specific catalytic activity via infrared thermography on gas-diffusion electrodes (GDE) for water and CO_2 electrolysis applications. After testing the operating principles of the system, we proceed to display its functionality on a lab-scale electrolyzer (Fig. 3.1a). We first demonstrate temperature deviations from ambient conditions as a function of applied

current densities up to 0.2 A cm^{-2} , followed by a proof-of-concept set of experiments for spatial catalyst screening applications. The remainder of the work then highlights the substantial spatial and temporal variability in current density that exist during electrolysis on GDEs during water and CO_2 electrolysis, contradicting assumed steady state behavior.

3.2 Heat as a proxy indicator for electrochemical activity

In considering a means of directly probing localized reactions, we reflected that all electrochemical reactions are a result of charge transport. Subsequently the current density (j) measured in our external circuits is the cumulative sum of all localized charge transport over an electrode's surface, and the voltage (V) represents the overpotentials needed to drive this transport. By nature, however, charge transfer and transport are fundamentally inefficient; a by-product of inefficient transfer and transport is heat generation. It is important to note that the quantity of heat (q) produced at a catalyst's surface due to charge transfer scales linearly with current density ($q \propto j$), whereas heat produced by ohmic resistances in the electrolyte, for example, scale quadratically with the applied current density ($q \propto j^2$).^[26] Thus, for an individual nanoparticle or region of an electrode, the local activity occurring should result in a proportional local heat generation. A characterization system capable of observing local heating can then in principle act as an indicator for electrochemical activity itself, opening the door for spatial and temporal mapping of catalytic activity with optical resolutions.

As shown in Fig. 3.1a and b, a commonly utilized GDE-based electrolyzer will generate heat in different cell locations during operation. We can estimate the quantity and location of heating that will occur in the cathodic chamber due to the catalyst heating (Fig. 3.1d) and ohmic heating (Fig. 3.1e) using known relations for heat generation (Eq. 3.1 and 3.2). To quantify this heat generation for a representative experiment, we performed a linear voltammetry scan (LSV) (Fig. 3.1c) of hydrogen evolution on a silver (Ag) electrocatalyst deposited onto a carbon GDE. Using the LSV data, the cell geometry and Eqs. 3.3 and 3.4, we can predict the heat generated as a function of current density (Fig. 3.A.1 and 3.A.2). As shown in Fig. 3.1f, most of the heat generation for a 15 mm catholyte chamber occurs due to the overpotentials of the electrocatalyst at low current densities, with increasing contributions from ohmic heating at increased current densities. At 0.2 A cm^{-2} , overpotential and ohmic heating become similar. In cases where the catholyte chamber is only 1 mm, however, heat coming from the cathodic electrochemical reaction accounts for up to 95% of all heat generation at the cathode (Fig. 3.A.4 and 3.A.5).

From the above analysis we then posit that any temperature change of the catalyst, particularly at lower current densities, is primarily due to the heat generated

from the electrochemical reactions on the cathode (e.g. $2\text{H}_2\text{O} + 2\text{e}^- \longrightarrow \text{H}_2 + 2\text{OH}^-$). Observing the temperature changes of the catalyst during operation then acts as a measure of electrochemical activity, meaning that spatial and temporal variations in temperature can be linked to changes in the local quantity of reaction occurring. We then designed an experimental system capable of observing these temperature changes spatially and temporally and relating our observations to the reactions occurring on the catalyst.

3.3 Infrared thermography: a proof-of-concept

The calculations in the previous section indicated that catalyst temperature changes can be linked to the quantity of reactions occurring. Measuring the temperature of the catalyst with high spatial resolutions in operando is practically challenging, however, as physical instrumentation is intrusive. Here we applied infrared thermography to record the temperature at the back of the GDE with spatial resolution (Fig. 3.2a, 3.A.6 - 3.A.9). The operation and configuration of the original electrochemical cell remains unaltered through the use of a gas tight IR transparent window positioned in the gas channel, providing data representative of standard high performance metrics works in applications such as CO_2 electrolysis.[3, 27]

Notably the temperature at the back of the GDE is not the same as the temperature of the catalyst embedded in the liquid electrolyte. However, through control experiments described here, and calculations presented in the SI we have confirmed that the temperature at the back of the GDE is representative of the catalyst temperature (see Figure 3.A.3 and the Supplementary Notes in the SI).

During cell operation the temperatures recorded by the infrared camera are coupled to a potentiostat to display the dynamics of our electrolyzer in an operando mode. Shown in Fig. 3.2b is an example case where we measured the GDE temperature of a sputtered 200 nm Pt electrode in 1 M KOH during a current density ramp rate of $0.45 \text{ mA cm}^{-2} \text{ s}^{-1}$. Over a current density range of 0 to -40 mA cm^{-2} , relatively large temperature changes of $\sim 1.5 \text{ K}$ are observed compared to the camera's sensitivity ($< 0.02 \text{ K}$). Further, chronopotentiometry tests performed with the Pt electrode at 20 and 200 mA cm^{-2} with elevated catholyte flow rates (20 sccm) show a rapid GDE temperature change within 10 s of operation (Figs. 3.A.10 - 3.A.12). The catholyte and anolyte temperatures, however, only gradually increase despite the high flow rates. These curves confirm that substantial heating occurs in the catalyst layer and that elevated temperatures are reached before heat production in the catalyst layer is balanced by heat dissipation from the gas and electrolyte convective flows. Importantly, upon the removal of an applied potential, the GDE temperature quickly decays back to that of the electrolyte temperature providing an indication to the system's response time (Fig. 3.A.13). The rapid decrease highlights the system's ability to measure both increasing and decreasing activity

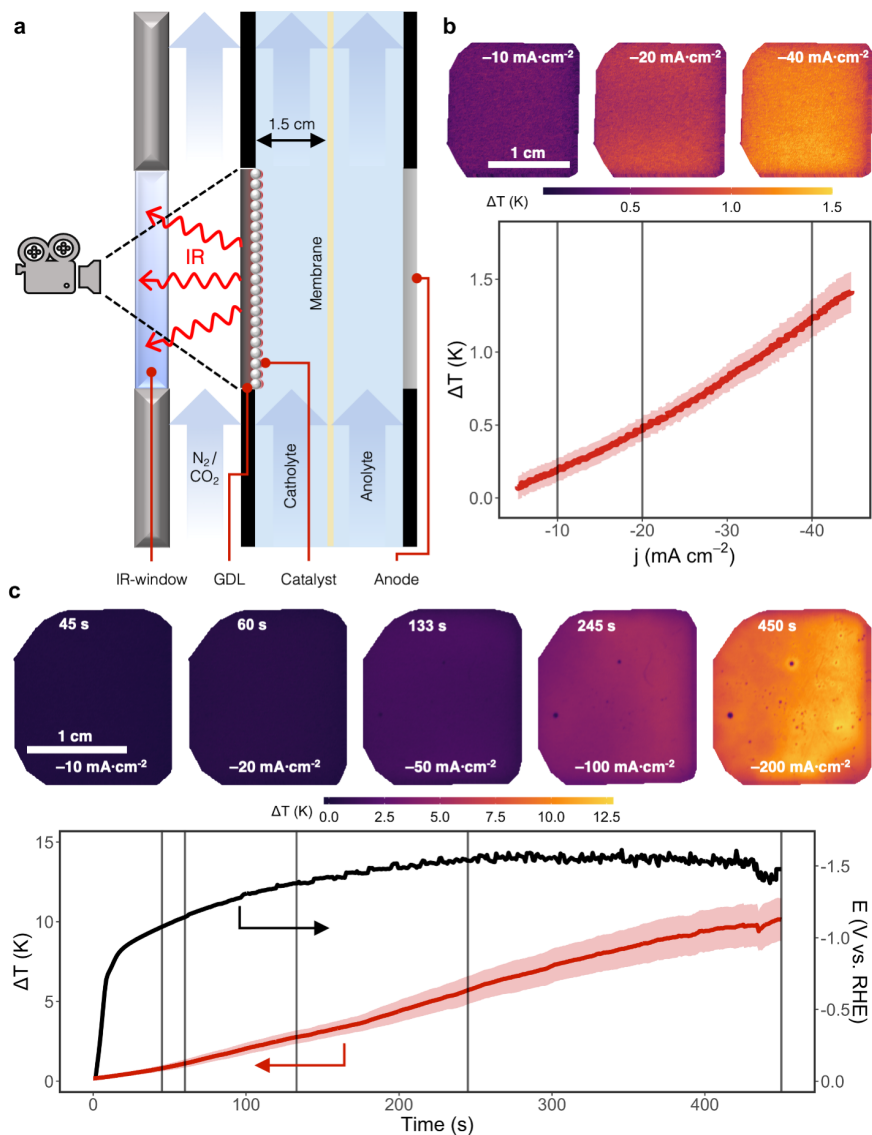


Figure 3.2: A windowed electrolyzer design allows sensing of catalytic activity on a gas-diffusion electrode (GDE). (a) Schematic depiction of the windowed electrolyzer and infrared (IR) imaging. (b) Thermographic stills of the back of the GDE with a 100nm platinum catalyst layer and a stagnant electrolyte layer (1M KOH). (c) Average and standard deviation of temperatures across the back of the GDE during a 0 to -200 mA cm^{-2} polarization curve using a 100nm silver catalyst layer and a 1 M KOH electrolyte flowing at 6 sccm. Vertical black lines indicate thermographic stills at various times and current densities of the polarization curve.

fluctuations during operation providing an avenue for spatial and temporal current density approximations. We can then confirm that infrared thermography can measure temperature changes, and thus electrochemical activity, at low reaction rates. Further, as calculated in the Supplementary Notes, we confirm that the GDEs heat conduction is dominant versus the electrolyte. These results act as a proof-of-concept that electrochemical activity, and its fluctuations in time, can be observed through infrared thermography.

We then turned to a 100 nm thick Ag sputtered catalyst deposited onto a GDE (see appendix for details) to demonstrate the spatial-temporal capabilities of our system under conditions known to cause failure via flooding of the GDE.[28] Here N₂ gas is passed through the gas channel at the back of the GDE, and hydrogen evolution via water electrolysis takes place on the Ag catalyst. In Fig. 3.2c the current density is ramped from 0 to -200 mA cm⁻² at a rate of 0.45 mA cm⁻² s⁻¹. Thermographic stills corresponding to timestamps of -10, -20, -50, -100 and 200 mA cm⁻² highlight the rapid change in temperature as reaction rate increases, as well as the spatial effects occurring across the electrode. Near the end of the experiment, for example, perspiration of the electrolyte is observed. The lower temperatures of these droplets can be explained by evaporation of the water droplets by the non humidified N₂ stream. We note that the actual droplet temperatures are overestimated from those presented in Fig. 3.2c, however, due to the different emissivity of water (0.98) versus the corrected carbon emissivity (0.81).

A critical takeaway from the Ag linear sweep, however, is that by the end of the <8 min experiment the temperature of the non-wetted portions of the GDE had already increased by 10 K. Such a large temperature change influences the ongoing electrochemical reaction kinetics. For example, kinetic studies on a Pt electrode in 0.1 M KOH showed an exchange current density change of almost 2-fold for temperature changes from just 298 K to 308 K.[29] In electrochemical systems with competing reactions, large temperature changes would then also impact the relative reaction rates, influencing Faradaic efficiencies. For fields such as CO₂ electrocatalysis, where current densities of >1 A cm⁻² are reported for single and multi-carbon products, our findings indicate that 10–30 K catalyst temperature swings are not unfathomable depending on the system configuration. These demonstrations highlight just how quickly and by how much electrocatalyst temperatures are elevated during operation, which is critical for mass transport, thermodynamic and kinetic models where temperatures are traditionally assumed as fixed quantities.

With the concept and response of the thermography system proven, we now provide a series of applications to both demonstrate the capabilities of the technique for comparing catalysts, spatial activity mapping and for different electrochemical reactions.

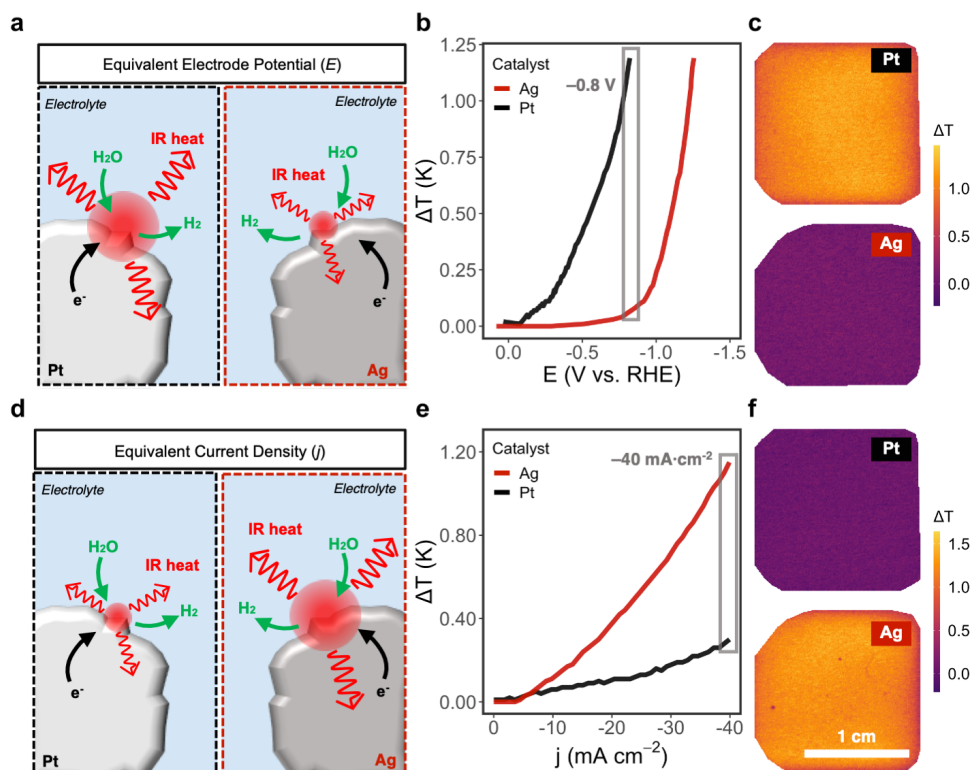


Figure 3.3: Electrode activity can be visualized using the spatial thermal-electric potentiostat. (a) At equal applied potentials, a more active catalyst will result in greater heat generation for the same reaction. (b) Combined thermal imaging and potentiostatic data showing a potential dependence of the average temperature observed on Pt and Ag GDE's. The electrolyte is 1M KHCO₃ flowing at 6 sccm. (c) Thermographic stills of the Pt and Ag GDE's at -0.8 V vs. RHE. (d) At equal current density, a less active catalyst will result in greater heat generation for the same reaction. (e) Combined thermal imaging and potentiostatic data showing a current density dependence of the average temperature observed on Pt and Ag GDE's. The electrolyte is 1M KHCO₃ flowing at 6 sccm. (f) Thermographic stills of the Pt and Ag GDE's at -40 mA cm⁻².

3.4 Applications of spatial activity mapping

3.4.1 Catalyst screening through overpotential-dependent temperature changes

Thus far we have focused on the link between heat and reaction rates. If our method can sense activity occurring in the catalyst layer, the overpotential of the reaction should also be discernible through temperature measurements. Specifically, we asked if the technique can be a useful means of measuring both the onset potential of a given catalyst and comparing the activities of different materials when coupling the thermal data from the IR camera and electric data from the

potentiostat.

Using the previously described Pt and Ag catalyst layers on GDE's, we observed temperature changes with the camera system under increasing current densities of $0.45 \text{ mA cm}^{-2} \text{ s}^{-1}$ (Fig. 3.A.14). As an established catalyst for hydrogen evolution, Pt should generate more heat than the poor HER Ag catalyst at a fixed electrode potential due to greater charge transfer (Fig. 3.3a). These assumptions are confirmed by comparing the thermal signal against the electrode potential, where at a fixed potential of 0.8 V vs a reversible hydrogen electrode (RHE) the Pt catalyst has increased in temperature by 1 K, while the relatively inactive Ag catalyst shows minimal increases (Fig. 3.3b and c). The combination of thermal-electric data further shows the vast difference in onset potential of the two catalysts, demonstrating a means to use DELTAT vs overpotential for numerous catalysts on the same electrode. The reversed scenario where temperature evolution is instead compared at fixed reaction rates has the opposite effect (Fig. 3.3d). Here the more efficient Pt catalyst shows a lower temperature change than Ag at a comparable reaction rate (Fig. 3.3e and f).

The catalyst comparisons between Ag and Pt in Fig. 3.3 demonstrate the potential for screening catalysts in a combinatorial fashion on a singular GDE, using local temperature as an indicator of spatial reaction rate (Fig. 3.3b) or overpotential (Fig. 3.3e). Using our acquisition system the temperature of individual groups of pixels can be analyzed during a reaction, allowing for temperature vs. reaction rate or overpotential curves to be plotted for multiple catalysts on the same GDE at once. Such an approach can overcome the one potentiostat – one data point challenge for single product reactions.

3.4.2 Detection of catalyst layer defects

Beyond catalytic screening applications, spatial mapping of catalyst activity provides an additional means of examining key transport phenomena, limiting chemical reactions, and changes in behavior over time. In electrochemical systems uneven current distributions across a catalyst will result from poor catalyst deposition, differently ageing portions of the electrode, and spatially varying operating conditions (reactant concentrations, pressure, etc.), all of which are undesired. Defining a non-invasive probing mechanism to assess activity distribution is thus attractive, for both laboratory and scale-up efforts. Here we identify applications for spatial mapping, as well as fundamental resolution limitations of the approach.

To simulate a catalyst region which may have been removed or deactivated during operation, we partially masked a portion of a GDE's microporous layer (MPL) prior to depositing a 100 nm thick copper (Cu) catalyst (Fig. 3.4a). After a linear current density ramp to -50 mA cm^{-2} , the current density was kept constant. Here distinctive heating patterns corresponding to the catalyst layer formed as a

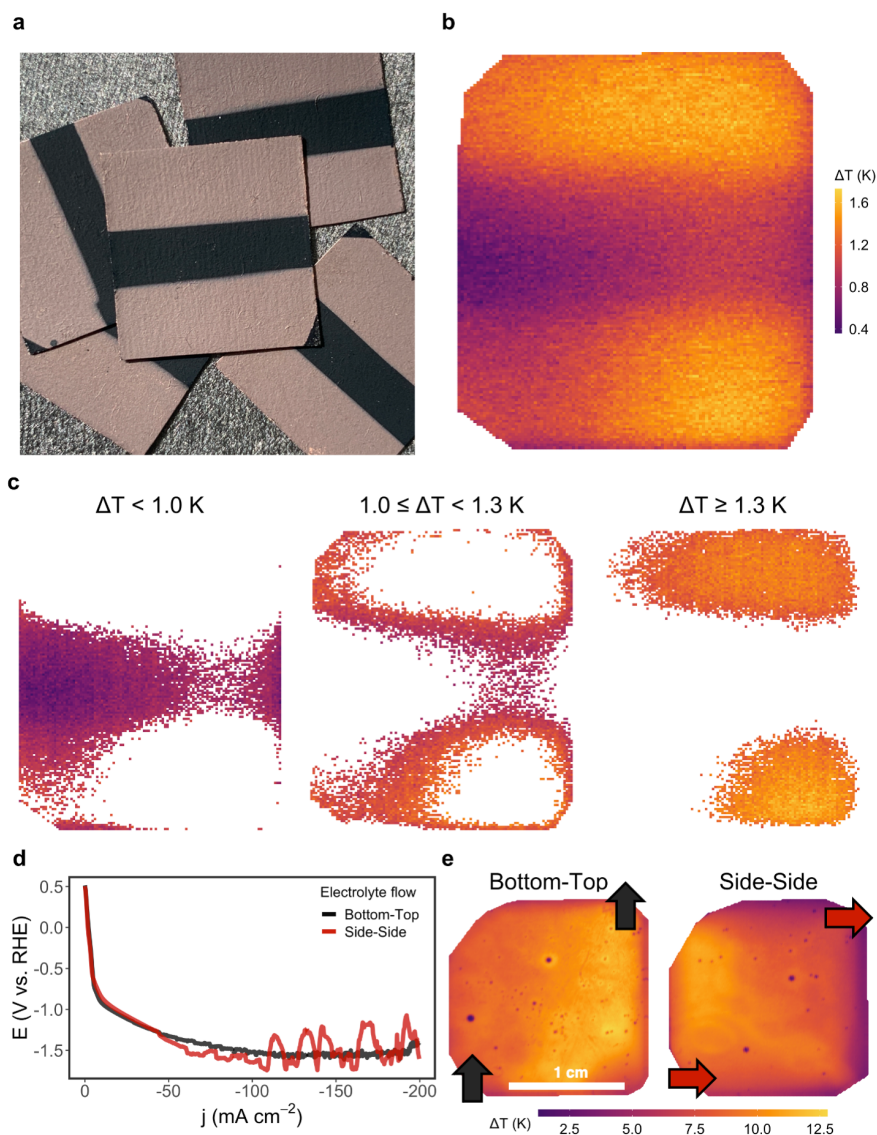


Figure 3.4: The spatial thermal-electric potentiostat is effective for defect detection and sensing of current density distribution over an electrocatalyst's surface. (a) Gas-diffusion electrodes (GDE) with a surface copper layer and catalyst-free defects applied by masking during deposition. (b) Thermographic still of a defected copper GDE at 50 mA cm^{-2} with 1M KOH flowing at 6 sccm. (c) Binned individual pixels of the still image in (b) as a function of temperature increase. (d) Polarization curves under the same electrolyte flow directions in (e), where the influence of bubble accumulation is observed at voltage fluctuations. (e) Thermographic stills of a 100 nm Ag electrode with different electrolyte flow configurations at 200 mA cm^{-2} .

result of the electrochemical reactions occurring (Fig. 3.4b). The upper and lower hotter bands correspond to the coated sections of the GDE, while the cooler central region is the bare carbon MPL which has lower HER activity.[28] It can then be deduced that the static -50 mA cm^{-2} applied to the system (112.5 mA total) is not equally distributed over the electrode, with the Cu regions experiencing much higher reaction rates than the average value imposed by the potentiostat.

The probing technique further allows for individual analysis per pixel, which means an image can be binned based on the individual value of each dot and tracked over time. Binning the readings results in a clearer picture (Fig. 3.4c), where we can see the central part of the GDE reading considerably lower temperatures than the other two bins. In this experiment the temperature distribution effects linked to the electrolyte flow patterns in the system can also be observed. Higher overall temperatures are binned at the exit side of the reactor (top-right), and in the stagnant electrolyte regions (bottom-right and top-left).

The spatial resolution of the presented technique is mainly influenced by two distinct factors. On one hand, the (an)isotropy of the electrode support material: for anisotropic carbon GDE's with better in-plane heat conduction than through-plane conduction, the resolution can be expected to be affected more heavily by the thickness of the electrode. On the other hand, excessive heat retention or evacuation by the device also influence measurements. These could in turn influence response times of the system, which we expect to be dependent on the temperature difference between the GDE and the electrolyte. Thus, a small temperature difference would result in a longer cooling time, whereas a high temperature difference would decrease this.

3.4.3 Influence of flow-regimes on activity distribution

Following from the observations of the defected catalyst layer, we wanted to better understand how the catholyte and anolyte can influence the reaction rate distribution across a catalyst layer. To this end we varied the flow direction of the anolyte and catholyte flow from a bottom-to-top direction to a side-to-side direction. While in the cathode chamber product gases diffuse into the gas channel prior to nucleating, the anodic reaction performed here is the oxygen evolution reaction (OER) which results in substantial generation of O_2 bubbles. In the side-to-side configuration gas bubbles become trapped in anode compartment, resulting in a noticeably less stable linear sweep voltammetry measurement (Fig. 3.4d). Such disturbances in the anode compartment are further shown to cause rapidly changing temperature profiles of the cathode GDE, implying that the shielding of O_2 bubbles impacts the current density distribution of the cathode. During operation cloud-like heating patterns are observed to move across the cathode even though no bubbles are present in the catholyte (Fig. 3.4e and Fig. 3.A.15), which

is not observed during bottom-to-top flow. These variations are best viewed in supplementary videos attached to the original publication.

As no gas evolution is present in the cathode chamber, we suspect that the build-up of gas in the anode chamber is partially shielding the nickel mesh anode. Any portion of the anode that is shielded will then impact the anodic current density distribution, and we suspect that the temperature variations observed on the cathode are a result of this uneven current density distribution. Such increases and decreases in activity would not only result in faster catalyst aging, but also indicate that voltage and current density of an electrocatalyst is highly variable.

The collective spatial observations presented in this section point to many experimental systems having a less homogenous reaction environment than indicated through purely potentiostatic data. These considerations are particularly important within elevated current density experiments where large reaction rate changes occur with minimal changes in overpotential, implying a higher variance across the electrode's surface.

3.5 Exothermic homogeneous reactions during CO₂ electrolysis

A known unwanted side-reaction in CO₂ electrolyzers is the reaction of reactant CO₂ with by-product hydroxide, which lowers device utilization and represents one of the technology's largest practical barriers.[8, 30, 31] The parasitic reaction which forms carbonates and precipitates is highly exothermic in nature and occurs within the liquid-immersed catalyst layer (Fig. 3.5a). The generated heat then should be discernible with our camera.

Using a Ag catalyst that is adept at CO₂ conversion to CO, we compared the thermal-electric data of the catalyst in both a CO₂ and N₂ environment. A CO₂ feed will produce primarily CO, while an N₂ feed only produced H₂. First observing the electrical data, a lower overpotential is shown for the CO₂ gas-flow, which can be explained by Ag being a better CO₂ reduction catalyst than HER catalyst (Fig. 3.5b). When observing the thermal data (Fig. 3.5c), however, 1-2 K greater temperatures are observed in the CO₂ gas flow case. As CO₂ reduction to CO and HER have similar thermoneutral half-cell potentials (see appendix), these temperature changes are ascribed to the exothermic interaction between CO₂ and hydroxide.

Importantly, a control experiment where the gaseous CO₂ feed was stopped at 0 mA cm⁻² showed a temperature decrease of only around 0.2 K (Fig. 3.A.16). Such a result is reasonable as the absolute moles of neutralized hydroxide in a stagnant electrolyte film is substantially lower than is generated at -200 mA cm⁻².

Another interesting observation can be made from the electrode's average tem-

perature (Fig. 3.5c) after 60 s. Here the electrode's temperature rapidly increased to values 10K above room temperature. Much like in the HER case above, these increased surface temperatures have implications for mass transport and density-functional theory models which presently do not consider activity-temperature relationships.[32–34] For example the solubility of CO₂ in water decreases by 30% from 298 K to 308 K, while solubility limits for salts will increase.

Besides the average temperature of the electrode, it is also worth noting the deviation in observed temperature changes. The electrode performing CO₂RR displayed, under the same conditions, a much wider temperature distribution than the one performing HER. This could be blamed on entrance effects of the gas-feed resulting in increased CO₂ dissolution in the entrance region of the GDE. However, seeing as the feed of CO₂ (20 sccm) is considerably higher than its consumption in the electrocatalytic process (at 200 mA cm⁻², 2 orders of magnitude difference), it is safe to assume that the increased variance in temperatures is an indicator of at least some degree of poorer current-density distribution upon performing CO₂RR on these electrodes. This highlights the blind-spot in CO₂RR literature when it comes to spatial distribution effects on catalytic performance of showcased electrolyzer solutions.

For complex catalytic pathways observed in CO₂ reduction, heat effects are also of noticeable influence on the selectivity of the catalyst. For example copper electrodes have been shown to vary selectivity with changes in temperature.[35–37] Additionally, improved mass transfer of reactants can be expected at hot-spots, as viscosity of water and diffusion of gases in the interface are affected by temperature.[38, 39] For scale-up purposes, maintaining similarity of electrochemical activity across a surface is necessary to ensure understanding of the behavior of system.[40, 41] The ability of thermography to indirectly scope activity over a surface during operation presents a chance to gain more information from experiments, aiding in catalyst and system advancements.

The concept of utilizing infrared emissions as a direct indicator of catalytic activity provides a broad set of potential applications for the ever-growing set of novel electrochemical reactions under investigation. The high emissivity of common carbon provides an operando time and location specific measure of activity at backbones optical resolutions, which can be coupled with electrical data analysis. Through a series of demonstrative applications, we show the propensity for infrared thermography to link measured changes in the gas-diffusion layer temperature to reaction overpotentials, catalyst type, defect sites on the catalyst layer, and dissolution of CO₂ into the electrolyte during CO₂ electrolysis. The substantial catalytic temperatures observed during regular operation highlight the need to reinterpret assumed kinetic data and reaction environments for these important electrochemical reactions.

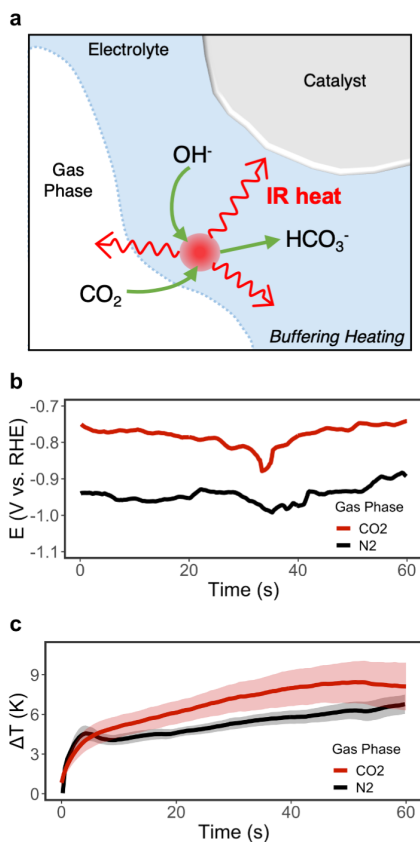


Figure 3.5: The heat effects of CO_2 dissolution are comparable to reaction-driven heating at elevated current densities. (a) CO_2 dissolves in alkaline media to form (bi)carbonates in an exothermic reaction. (b) Reaction potentials under a N_2 and CO_2 gas flow at a 100nm Ag GDE using 1M KOH at a fixed current density of 200 mA cm^{-2} . Under N_2 the primary reaction is hydrogen evolution. Under CO_2 gas flow the primary reaction is CO_2 reduction. (c) Temperature increases over the GDE surface for the sequences in b, where the CO_2 reduction case displays a noticeably higher overall temperature despite lower applied potentials.

3.6 Materials and Methods

Infrared Imaging

The camera system used consisted of a FLIR SC7650 with a 25 mm fixed-focal length objective and a $f/2.5$ aperture. The manufacturer's software AltaIR software was used to control the camera and pre-process the acquired data. All images we include in the report are taken at a quarter-size resolution (320 by 256 pixels of the maximum 640 by 512 possible), at a refresh rate of 25Hz and sub-sampling of 1/10 frames. This means, ultimately, that the acquisition frequency of the system is 2.5

fps. This allowed us to keep the footage from exceeding 1GB per file.

We performed all experiments in an enclosed box (a repurposed faraday-cage, Fig. 3.A.7) to avoid any reflections from the lab in interfering in the measurements. The endplate of the electrolyzer was covered using scotch-tape to ensure no reflections from the metallic surface would interfere with the irradiation of the GDE.

The camera records thermal images at spectral wavelengths between 3.0 and 5.0 μ m. At these wavelengths, the transmittance values of the sapphire window were approximated to be 90%. In order to translate the recorded emittance from the GDE backbone to a true temperature value, we compared the irradiation at room temperature of the GDE through the window and a piece of carbon tape with emissivity values of 0.8-0.9, which we approximated as 0.85.[42] The results from this calibration measurement are displayed in Fig. 3.A.8. The value of the corrected GDE emissivity of 0.81 coincides with the irradiation reading of the carbon tape, whereas the uncorrected GDE irradiation value is above the latter. These measurements were performed by comparing an identical number of pixels of the GDE and the carbon tape, as can be seen in Fig. 3.A.9.

Electrochemical Testing

Electrolyte was pumped through the anolyte and catholyte chambers using a peristaltic pump, with a minimum rate of 6 sccm. The gas-phase stream used was either N₂ (for all water-splitting runs) or CO₂ (for all CO₂RR runs), which we controlled using a mass-flow controller (MFC, Bronkhorst EL-FLOW Select). The pressure of the gas and liquid channels were controlled using three back-pressure regulators (BPR), one after each flow channel. A mass-flow meter (MFM) was connected to the effluent gas-stream which subsequently flowed to a liquid trap and then an in-line gas chromatograph (GC). The full instrumentation and flow setup is sketched in Fig. 3.A.6.

Electrochemical experiments were performed using a Versastat MC-1000 potentiostat. All potentials reported are corrected for ohmic drops (85% correction applied) with resistances measured by electrochemical impedance spectroscopy (EIS) in a frequency range of 12550 Hz to 1.5 Hz at OCV and the maximum current applied. These routines were performed in sync with the camera system, to obtain thermographs that could be coupled to the time stamps of the potentiostat readings. Experiments were performed in both stepped current mode and chronopotentiometry as detailed for the experiments in the main text.

Materials

For all tests detailed in this study we used a modular electrolyzer, based on three separate flow chambers of PTFE with spacing gaskets in between. Metal endplates were added to ensure even cell compression. To enable IR filming of the gas diffusion electrode (GDE), the PTFE gas compartment was fully cut through and a

sapphire window was integrated in the design in place of the PTFE wall (see Fig. 3.2a and Fig. 3.A.7). The device was tested for leaking during operation using a mass-flow controller on the gas-inlet stream and a mass-flow meter on the gas-outlet stream to ensure the mass flow in was equivalent to the mass flow out. The catholyte used was either 1M KOH (Sigma-Aldrich 99.99% semiconductor grade) or 1M KHCO₃ (Sigma-Aldrich 99.7% ACS reagent). Anolyte was always 1M KOH to reduce total cell potential. The catholyte and anolyte compartments in the electrolyzer were separated by a Nafion 115 cation-exchange membrane.

3

Freudenberg H14C10 gas-diffusion layers were used as GDE's in all experiments with a manufacturer reported thickness of 175 μ m ($\delta_{GDE} = 175\text{ }\mu\text{m}$). Catalyst layers of a nominal thickness of 100 nm were deposited using DC magnetron sputtering pressure at 3 μ bar. Introduction of defects on these layers was achieved by shielding a region of the hydrophobic micro-porous layer with titanium masks during deposition.

The infrared imaging camera (FLIR SC7650) was equipped with a fixed focal length concave lens of 25 mm (FLIR) and controlled using ALTAIR software. The window in the PTFE cell was an Edmund Optics uncoated sapphire ($\delta = 1\text{mm}$ and $\varnothing = 23.75\text{mm}$). All measurements were performed in a dark box (see Fig. 3.A.7) to avoid infrared contamination by external sources and unwanted reflections.

References

- [1] Hugo-Pieter Iglesias van Montfort and Thomas Burdyny. Mapping Spatial and Temporal Electrochemical Activity of Water and CO₂ Electrolysis on Gas-Diffusion Electrodes Using Infrared Thermography. *ACS Energy Letters*, 7(8):2410–2419, August 2022.
- [2] Gao Feng Chen, Yifei Yuan, Haifeng Jiang, Shi Yu Ren, Liang Xin Ding, Lu Ma, Tianpin Wu, Jun Lu, and Haihui Wang. Electrochemical reduction of nitrate to ammonia via direct eight-electron transfer using a copper–molecular solid catalyst. *Nature Energy*, 5(8):605–613, August 2020.
- [3] F Pelayo García de Arquer, Cao Thang Dinh, Adnan Ozden, Joshua Wicks, Christopher McCallum, Ahmad R Kirmani, Dae Hyun Nam, Christine Gabardo, Ali Seifitokaldani, Xue Wang, Yuguang C Li, Fengwang Li, Jonathan Edwards, Lee J Richter, Steven J Thorpe, David Sinton, and Edward H Sargent. CO₂ electrolysis to multicarbon products at activities greater than 1 A cm⁻². *Science*, 367:661–666, 2020.
- [4] Taehee Kim and G. Tayhas R. Palmore. A scalable method for preparing Cu electrocatalysts that convert CO₂ into C₂₊ products. *Nature Communications*, 11(1):1–11, December 2020.
- [5] Zhen Yu Wu, Mohammadreza Karamad, Xue Yong, Qizheng Huang, David A. Cullen, Peng Zhu, Chuan Xia, Qunfeng Xiao, Mohsen Shakouri, Feng Yang Chen, Jung Yoon (Timothy) Kim, Yang Xia, Kimberly Heck, Yongfeng Hu, Michael S. Wong, Qilin Li, Ian Gates, Samira Siahrostami, and Haotian Wang. Electrochemical ammonia synthesis via nitrate reduction on Fe single atom catalyst. *Nature Communications*, 12(1):1–10, December 2021.
- [6] Karen Chan. A few basic concepts in electrochemical carbon dioxide reduction. *Nature Communications*, 11(1):1–4, December 2020.
- [7] Uzoma O. Nwabara, Emiliana R. Cofell, Sumit Verma, Emanuela Negro, and Paul J. A. Kenis. Durable Cathodes and Electrolyzers for the Efficient Aqueous Electrochemical Reduction of CO₂. *ChemSusChem*, 13(5):855–875, March 2020.
- [8] Joshua A. Rabinowitz and Matthew W. Kanan. The future of low-temperature carbon dioxide electrolysis depends on solving one basic problem. *Nature Communications*, 11(1):1–3, December 2020.
- [9] José L. Fernández, Vadari Raghuveer, Arumugam Manthiram, and Allen J. Bard. Pd-Ti and Pd-Co-Au electrocatalysts as a replacement for platinum for

oxygen reduction in proton exchange membrane fuel cells. *Journal of the American Chemical Society*, 127(38):13100–13101, September 2005.

- [10] Stephen E. Fosdick, Sean P. Berglund, C. Buddie Mullins, and Richard M. Crooks. Evaluating electrocatalysts for the hydrogen evolution reaction using bipolar electrode arrays: Bi- and trimetallic combinations of Co, Fe, Ni, Mo, and W. *ACS Catalysis*, 4(5):1332–1339, May 2014.
- [11] James B. Gerken, Sarah E. Shaner, Robert C. Massé, Nicholas J. Porubsky, and Shannon S. Stahl. A survey of diverse earth abundant oxygen evolution electrocatalysts showing enhanced activity from Ni-Fe oxides containing a third metal. *Energy and Environmental Science*, 7(7):2376–2382, 2014.
- [12] D. Guevarra, A. Shinde, S. K. Suram, I. D. Sharp, F. M. Toma, J. A. Haber, and J. M. Gregoire. Development of solar fuels photoanodes through combinatorial integration of Ni-La-Co-Ce oxide catalysts on BiVO₄. *Energy and Environmental Science*, 9(2):565–580, February 2016.
- [13] Do Kyoung Kim and Wilhelm F. Maier. Combinatorial discovery of new autoredox catalysts for the CO₂ reforming of methane. *Journal of Catalysis*, 238(1):142–152, February 2006.
- [14] Erik Reddington, Anthony Sapienza, Bogdan Gurau, Rameshkrishnan Viswanathan, S Sarangapani, Eugene S Smotkin, and Thomas E Malouk. Combinatorial Electrochemistry: A Highly Parallel, Optical Screening Method for Discovery of Better Electrocatalysts. *J. Electron Spectrosc. Relat. Phenom.*, 280:1735–1737, 1986.
- [15] Heechang Ye, Hyun S. Park, and Allen J. Bard. Screening of electrocatalysts for photoelectrochemical water oxidation on W-doped BiVO₄ photocatalysts by scanning electrochemical microscopy. *Journal of Physical Chemistry C*, 115(25):12464–12470, June 2011.
- [16] P. C. Ghosh, T. Wüster, H. Dohle, N. Kimiaie, J. Mergel, and D. Stolten. In situ approach for current distribution measurement in fuel cells. *Journal of Power Sources*, 154(1):184–191, March 2006.
- [17] John M. Gregoire, Michele E. Tague, Sophie Cahen, Sahr Khan, Héctor D. Abruña, Francis J. DiSalvo, and R. Bruce van Dover. Improved Fuel Cell Oxidation Catalysis in Pt_{1-x}Ta_x. *Chemistry of Materials*, 22(3):1080–1087, February 2010.

- [18] Rui Lin, Heinz Sander, Erich Gülzow, and Andreas Friedrich. Investigation of Locally Resolved Current Density Distribution of Segmented PEM Fuel Cells to Detect Malfunctions. *ECS Transactions*, 26(1):229–236, 2010.
- [19] Luigi Osmieri, Scott Mauger, Michael Ulsh, K.C. Neyerlin, and Guido Bender. Use of a segmented cell for the combinatorial development of platinum group metal-free electrodes for polymer electrolyte fuel cells. *Journal of Power Sources*, 452:227829, March 2020.
- [20] Tatyana V. Reshetenko, Guido Bender, Keith Bethune, and Richard Rocheleau. A segmented cell approach for studying the effects of serpentine flow field parameters on PEMFC current distribution. *Electrochimica Acta*, 88:571–579, January 2013.
- [21] Jeremy L. Hitt, Yuguang C. Li, Songsheng Tao, Zhifei Yan, Yue Gao, Simon J.L. Billinge, and Thomas E. Mallouk. A high throughput optical method for studying compositional effects in electrocatalysts for CO₂ reduction. *Nature Communications*, 12(1):1–10, December 2021.
- [22] Niccolo V. Aieta, Prodig K. Das, Andrew Perdue, Guido Bender, Andrew M. Herring, Adam Z. Weber, and Michael J. Ulsh. Applying infrared thermography as a quality-control tool for the rapid detection of polymer-electrolyte-membrane-fuel-cell catalyst-layer-thickness variations. *Journal of Power Sources*, 211:4–11, August 2012.
- [23] Prodig K Das, Adam Z Weber, Guido Bender, Austin Manak, Daniel Bittinat, Andrew M Herring, and Michael Ulsh. Rapid detection of defects in fuel-cell electrodes using infrared reactive-flow-through technique. *Journal of Power Sources*, 261:401–411, 2014.
- [24] Adam Phillips, Michael Ulsh, K. C. Neyerlin, Jason Porter, and Guido Bender. Impacts of electrode coating irregularities on polymer electrolyte membrane fuel cell lifetime using quasi in-situ infrared thermography and accelerated stress testing. *International Journal of Hydrogen Energy*, 43(12):6390–6399, March 2018.
- [25] Min Wang, Samantha Medina, Josias Ochoa-Lozano, Scott Mauger, Svitlana Pylypenko, Michael Ulsh, and Guido Bender. Visualization, understanding, and mitigation of process-induced-membrane irregularities in gas diffusion electrode-based polymer electrolyte membrane fuel cells. *International Journal of Hydrogen Energy*, 46(27):14699–14712, April 2021.
- [26] Henry A Catherino. Estimation of the heat generation rates in electrochemical cells. *Journal of Power Sources*, 239:505–512, 2013.

- [27] Cao Thang Dinh, Thomas Burdyny, Golam Kibria, Ali Seifitokaldani, Christine M Gabardo, F Pelayo García De Arquer, Amirreza Kiani, Jonathan P Edwards, Phil De Luna, Oleksandr S Bushuyev, Chengqin Zou, Rafael Quintero-Bermudez, Yuanjie Pang, David Sinton, and Edward H Sargent. CO₂ electroreduction to ethylene via hydroxide-mediated copper catalysis at an abrupt interface. *Science*, 360:783–787, 2018.
- [28] Kailun Yang, Recep Kas, Wilson A. Smith, and Thomas Burdyny. Role of the Carbon-Based Gas Diffusion Layer on Flooding in a Gas Diffusion Electrode Cell for Electrochemical CO₂ Reduction. *ACS Energy Letters*, 6(1):33–40, January 2021.
- [29] Daoping Tang, Juntao Lu, Lin Zhuang, and Peifang Liu. Calculations of the exchange current density for hydrogen electrode reactions: A short review and a new equation. *Journal of Electroanalytical Chemistry*, 644(2):144–149, June 2010.
- [30] Jianan Erick Huang, Fengwang Li, Adnan Ozden, Armin Sedighian Rasouli, F. Pelayo García de Arquer, Shijie Liu, Shuzhen Zhang, Mingchuan Luo, Xue Wang, Yanwei Lum, Yi Xu, Koen Bertens, Rui Kai Miao, Cao-Thang Dinh, David Sinton, and Edward H. Sargent. CO₂ electrolysis to multicarbon products in strong acid. *Science*, 372(6546):1074–1078, June 2021.
- [31] Adnan Ozden, Yuhang Wang, Fengwang Li, Mingchuan Luo, Jared Sisler, Arnaud Thevenon, Alonso Rosas-Hernández, Thomas Burdyny, Yanwei Lum, Hossein Yadegari, Theodor Agapie, Jonas C. Peters, Edward H. Sargent, and David Sinton. Cascade CO₂ electroreduction enables efficient carbonate-free production of ethylene. *Joule*, 5(3):706–719, March 2021.
- [32] Divya Bohra, Jehanzeb H. Chaudhry, Thomas Burdyny, Evgeny A. Pidko, and Wilson A. Smith. Modeling the electrical double layer to understand the reaction environment in a CO₂ electrocatalytic system. *Energy and Environmental Science*, 12(11):3380–3389, November 2019.
- [33] Recep Kas, Andrew G. Star, Kailun Yang, Tim Van Cleve, Kenneth C. Neyerlin, and Wilson A. Smith. Along the Channel Gradients Impact on the Spatioactivity of Gas Diffusion Electrodes at High Conversions during CO₂ Electroreduction. *ACS Sustainable Chemistry and Engineering*, 9(3):1286–1296, January 2021.
- [34] Nathan T. Nesbitt, Thomas Burdyny, Hunter Simonson, Danielle Salvatore, Divya Bohra, Recep Kas, and Wilson A. Smith. Liquid-Solid Boundaries Dom-

- inate Activity of CO₂ Reduction on Gas-Diffusion Electrodes. *ACS Catalysis*, 10(23):14093–14106, December 2020.
- [35] Steven T. Ahn, Ismael Abu-Baker, and G.Tayhas R. Palmore. Electroreduction of CO₂ on polycrystalline copper: Effect of temperature on product selectivity. *Catalysis Today*, 288:24–29, June 2017.
- [36] Yoshio Hori, Katsuhei Kikuchi, Akira Murata, and Shin Suzuki. Production of Methane and Ethylene in Electrochemical Reduction of Carbon Dioxide at Copper Electrode in Aqueous Hydrogencarbonate Solution. *Chemistry Letters*, 15(6):897–898, 1986.
- [37] Baopeng Yang, Kang Liu, HuangJingWei Li, Changxu Liu, Junwei Fu, Hongmei Li, Jianan Erick Huang, Pengfei Ou, Tartela Alkayyali, Chao Cai, Yuxia Duan, Hui Liu, Pengda An, Ning Zhang, Wenzhang Li, Xiaoqing Qiu, Chuankun Jia, Junhua Hu, Liyuan Chai, Zhang Lin, Yongli Gao, Masahiro Miyauchi, Emiliano Cortés, Stefan A. Maier, and Min Liu. Accelerating CO₂ Electroreduction to Multicarbon Products via Synergistic Electric–Thermal Field on Copper Nanoneedles. *Journal of the American Chemical Society*, 144(7):3039–3049, February 2022.
- [38] Edward N Fuller, Paul D Schettler, and J Calvin Giddings. New method for prediction of binary gas-phase diffusion coefficients. *Industrial and Engineering Chemistry*, 58(5):18–27, 1966.
- [39] Joseph Kestin, Mordechai Sokolov, and William A. Wakeham. Viscosity of liquid water in the range -8 °C to 150 °C. *Journal of Physical and Chemical Reference Data*, 7(3):941–948, 1978.
- [40] F Goodridge and K Scott. *Electrochemical process engineering: a guide to the design of electrolytic plant*, volume 1. Plenum Press, New York, 1995.
- [41] Geoffrey Prentice. *Electrochemical engineering principles*, volume 1. Prentice Hall, New Jersey, 1990.
- [42] Fluke Process Instruments. Emissivity - Non-Metals, 2019.
- [43] Allen J Bard, György Inzelt, and Fritz Scholz. *Electrochemical Dictionary*. Springer, 2012.
- [44] Nada Zamel, Efim Litovsky, Saher Shakhshir, Xianguo Li, and Jacob Kleiman. Measurement of in-plane thermal conductivity of carbon paper diffusion media in the temperature range of -20 °C to +120 °C. *Applied Energy*, 88(9):3042–3050, 2011.

- [45] William M Deen. *Analysis of transport phenomena*. Oxford University Press New York, 1998.
- [46] Masterton, W.L., Slowinski, E.J., and Stanitski, C.L. *Chemical Principles: Alternative Edition with a Qualitative Analysis Supplement*. Saunders College Pub., 1st edition, 1983.

APPENDIX

Supplementary Notes

Evaluating the expected working criteria for a functioning infrared thermography device

The usage of heat-measurements as proxies for electrochemical activity is mainly challenged by two facts: (i) heat is not an intrinsically measurable quantity, and (ii) associating heat with electrochemical activity requires disambiguating all heat sources present in electrochemical systems. Heating occurs across a device due to charge transport resistances in the electrode, electrolyte, and membrane for example. An operando analysis technique is then required to demonstrate the theoretical link between heat and activity under actual operating conditions. Providing such a link would provide real-time visualized activity of an electrocatalyst, opening a door to new insights and experimental techniques.

The following subsections are used to evaluate the criteria proposed in the main text for being able to use catalytic heating as a means of observing catalytic activity. The criteria are then assessed one by one in the text below.

- i. Heat production is sufficient such that activity can be evaluated at low potentials and current densities
- ii. Heat generation is translatable to temperature
- iii. The location of temperature measurement is representative of the electrocatalyst
- iv. Measured temperature can be ascribed to various sources of heat generation

The first two criteria (i and ii) were assessed by evaluating the magnitude of heat that is generated at the surface of an electrocatalyst during a representative reaction, and determining what magnitudes of temperature changes this electrochemical heat production might induce. To determine the amount of heating we first note that the amount of power consumed across an element within an electric circuit (and, thus, also in an electrochemical cell) is governed by the total current passed through and the voltage drop across an interface or element,[43] by:

$$P = I \cdot \Delta E \quad (3.1)$$

Making use of Ohm's law for resistive elements (e.g. an electrolyte), the relation can also be expressed as:

$$P = I^2 \cdot R \quad (3.2)$$

At an electrocatalyst's surface (e.g. cathode or anode), some of this power will go to the formation of chemical products (e.g. H_2 , CO , etc.), while the rest will

be dissipated as heat if operating in an exothermic potential range. The power going to heat is determined by the difference between the applied potential (E_{app}) and the thermoneutral potential ($E_{tn,0}$). The heat generated at an electrocatalyst's surface (Q_{cat}) can then be expressed as:

$$Q_{cat} = E_{app} - E_{tn,0} \cdot I \quad (3.3)$$

We can also express this in a more useful form of the heat generated as a function of geometric catalyst surface area (q_{cat}'') using the current density (j):

$$q_{cat}'' = \frac{Q_{cat}}{A_{geo}} = (E_{app} - E_{tn,0}) \cdot j \quad (3.4)$$

Now using the above equations and the example data on a platinum electrode presented in Fig. 3.1c in the 3-electrode setup, the heat generation from the catalyst's surface can be determined as a function of current density (Fig. 3.A.2). For example, a current density of 10 mA cm^{-2} occurs at an approximate cathode potential of -0.85 V vs a reversible hydrogen electrode (RHE). For a half-cell thermoneutral voltage for hydrogen evolution of 0.249 V vs. RHE determined as described in the later appendix section, the heat generated within the platinum catalyst layer can then be calculated as below:

$$q_{Pt}'' @ 10 \text{ mA cm}^{-2} = (-0.85 - 0.249) \cdot (10 \text{ mA cm}^{-2}) = 10.99 \text{ mW cm}^{-2} \quad (3.5)$$

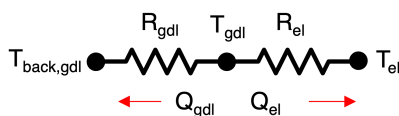
The heat production from the catalyst layer by itself is not informative until compared with the thermal capacitance of the carbon gas-diffusion layer supporting the platinum catalyst, where it can be translated into an expected temperature effect. In the absence of heat transport away from the platinum and carbon GDE, a heating rate is calculated from this heat generation. For this calculation we assume an area weight of the Freudenberg H14C10 GDE as 100 g m^{-2} (or $1 \cdot 10^{-5} \text{ kg cm}^{-2}$), and knowing that graphite in the GDE has a specific heat of approximately $840 \text{ J kg}^{-1} \cdot \text{K}^{-1}$. The heating rate is then determined from the thermal mass as:

$$\frac{\Delta T}{t} = \frac{Q_{cat}}{m \cdot C_{p,m}} = \frac{q_{cat}''}{m'' \cdot C_{p,m}} = \frac{0.01099}{(1 \cdot 10^{-5})(840)} = 1.31 \text{ K s}^{-1} \quad (3.6)$$

A heating rate on the order of 1.31 K s^{-1} is quite substantial and detectable. These calculations do not take into account heat loss from the catalyst and GDE, of course, but the calculated value at a low current density of 10 mA cm^{-2} is a magnitude which satisfies our criteria (i) and (ii) above.

iii. The location of temperature measurement is representative of the electrocatalyst Turning to criterium (iii), we ask whether the temperature measured at an externally visible location (e.g. the external side of a carbon GDE roughly 175 μm from an electrocatalyst) is representative of the temperature of the catalyst itself. While heat from catalytic activity and overpotentials is generated in the catalyst layer, direct measurement of this surface will affect the reaction itself. Thus direct observation of catalytic activity needs to be done from a proxy site that is not the catalyst layer. Here the back of the GDE is an optimal measurement point for both thermocouples and infrared imaging. To determine if the back of the GDE was a suitable proxy for the catalyst temperature, we assessed the heat flux away from the catalyst's surface to determine the expected difference in temperature of the GDE and the catalyst layer. For example, a low initial heat flux through the GDE as compared to the cathode compartment would indicate that the temperature of the GDE back and catalyst are quite different, and this measurement point is not representative of the catalyst.

To perform an analysis to determine this, we compared the heat flux through the GDE to the heat flux into a 15 mm catholyte channel that was used to create the polarization curve in Fig. 3.1c. The analysis in question can be visualized in Fig. 3.A.3 where the temperature of the GDE shows only a slight difference with the catalyst layer. The two 1D heat transfer mediums considered in the analysis are heat conduction in the porous graphite paper of the GDE, and heat conduction in the stagnant layer of electrolyte. These have their own specific heat transfer coefficients and distances to convective boundaries (e.g. gas flow and catholyte flow, respectively). From this analysis we can determine the dominant of the two conduction heat transfer mechanisms. This analysis makes use of an equivalent circuit model and Fourier's law of conduction (Eq. 3.7):



$$q' = k \nabla T \approx k \frac{\Delta T}{\Delta x} \quad (3.7)$$

where k is the thermal conductivity, $T_{back,gdl}$ is the temperature at the back of the GDE, R_{gdl} is the thermal equivalent resistance of the GDE, Q_{gdl} is the heat flux towards the back of the GDE, T_{cat} is the catalyst layer temperature, R_{el} is the thermal equivalent resistance of the electrolyte, Q_{el} is the heat flux towards the bulk electrolyte and T_{el} is the bulk electrolyte temperature.

Using the thermal model and Fourier's law, the approximation for the two conduction pathways are shown in Eq. 3.8 and 3.9, with their ratio in Eq. 3.10. Here the heat is equivalent to the cumulative 'current' in either direction, originating from a 'current' source at the catalyst layer:

$$Q_{gdl} = \frac{\Delta T}{R_{gdl}} = k_{gdl} \frac{\Delta T}{\Delta x} A = k_{gdl} \frac{(T_{cat} - T_{back,gdl})}{\delta_{gdl}} A \quad (3.8)$$

$$Q_{el} = \frac{\Delta T}{R_{el}} = k_{el} \frac{\Delta T}{\Delta x} A = k_{gdl} \frac{(T_{cat} - T_{el})}{\delta_{el}} A \quad (3.9)$$

$$\frac{Q_{gdl}}{Q_{el}} = \frac{q'_{gdl}}{q'_{el}} = \left| \frac{k_{gdl} (T_{cat} - T_{back,gdl})}{k_{el} (T_{cat} - T_{el})} \frac{\delta_{el}}{\delta_{gdl}} \right| \quad (3.10)$$

Where δ_{gde} and δ_{el} are, respectively, the thickness of the GDE and the thermal diffusion thickness in the electrolyte. The ratio in Eq. 3.10 can be evaluated for the system producing the data in Fig. 3.1. Here the comparative conductive heat transfer is assessed at $t = 0$ where $T_{back,GDL} = T_{el}$ as the entrance temperature of the convective gas and liquid phases are ambient temperature. Under longer operation both the back of the GDE and the stagnant electrolyte film will heat up at different rates, and heat flux will be dominated by the convective processes of the gas and liquid phases. The only variables in Eq. 3.10 are the thermal conductivities and the conduction lengths of the GDE and electrolyte layer.

For the GDE, these values are easy to determine. For a Freudenberg H14C10 GDE the thickness is 175 μm while the known through-plane thermal conductivity is 0.3 $\text{W m}^{-1} \text{K}^{-1}$ [44], which accounts for the porous and disordered structure of the GDE. The electrolyte thermal conductivity meanwhile is taken as 0.6 $\text{W m}^{-1} \text{K}^{-1}$. The thickness of the thermally-conductive electrolyte region is more challenging to determine as it depends on the hydrodynamics of the electrolyte channel flow. Here the thermal diffusion thickness is taken as the thermal boundary layer using the relation for flow over a flat plate (Eq. 3.11) and assuming that the Prandtl (Pr) number of water is of 7.5:[45]

$$\delta_{el} = 5.0 \sqrt{\frac{\nu x}{u_0}} Pr^{-1/3} \quad (3.11)$$

where ν represents the kinematic viscosity of water, x is the distance that the flow has travelled along the flat plate, and u_0 is the flow at the channel center.

For a commonly utilized electrolyte flowrate of 6 sccm, the velocity of the liquid at the center point is 0.044 cm/s. Filling in the relation above with the kinematic viscosity for water at 20°C (0.01 cm^2/s), the thermal diffusion thickness (δ_{elec}) is estimated to be 0.86 cm or 8600 μm after a flow distance of $x = 0.5$ cm.

Eq. 9 can then be numerically evaluated under these conditions, and, approximating the thermal conductivity of the electrolyte to be the same of pure water, results in a ratio of GDE to electrolyte heat flux of ~ 25 . This means that for an equivalent temperature drop, the GDE will conduct 25-fold more heat than the electrolyte. The conclusion from this analysis is that the temperature at the back of the GDE will be close to that of the catalyst layer, thus satisfying our criteria (iii) that the temperature at the back of the GDE can be used as a proxy for the catalyst layer temperature when observing catalytic activity.

From the above analysis it is important to note that entrance effects may be present as the thermal boundary layer thickness will be very small near the entrance. Near the electrolyte inlet the temperature of the GDE may then be less representative. For example, for values of $x = 0.25$ cm, the ratio of heat flux in Eq. 3.10 drops to ~ 17 .

iv. Measured temperature can be ascribed to various sources of heat generation The system, as depicted in Fig. 1B, is centered around the cathodic half-cell. Within this region three types of heating can occur: heating from the cathodic reaction, ohmic heating of the electrolyte, and resistive heating of the GDE itself due to the flow of electrons. Here we compare the order of magnitude of these cathodic heat sources and show that these can be ascribed to different heat sources through well-known equations. Further, we show that the heat from the cathodic reaction is dominant versus the other two forms of heating.

As described in Fig. 1b the power going to the catalyst and ohmic heating are proportional to the product of the voltage drop across the element, and the current density that is passed. For the catalyst heating (labelled as q''_{cat}), the heating as a function of current density was already calculated as described in Eq. 3.3 and 3.4 and is plotted in Fig. 3.A.2 for a 2.25 cm^2 cathode area using the potentiostatic data in Fig. 3.1c. The ohmic heating of the electrolyte in the system can be determined by the following equation:

$$q''_{ohm} = \frac{Q_{ohm}}{A_{geo}} = \frac{(V_{ohm} \cdot I)}{A_{geo}} = (R_u \cdot j) \cdot (j \cdot A_{geo}) = R_u j^2 A_{geo} \quad (3.12)$$

where R_u represents the ohmic resistance measured between the cathode and the reference electrode in the center of the catholyte channel (in Ω). Both potential and resistances can be measured analytically using a potentiostat and EIS over the region between the working electrode and the reference electrode.

For the utilized reaction configuration which uses a 15 mm electrolyte channel, an ohmic resistance of $R_u = 2.5 \Omega$ was measured for the 1 M KOH catholyte channel. Using Eq. 3.12 ohmic resistive heating can then be plotted as a function of current density as in Fig. 3.A.3. Here at -10 mA cm^{-2} the ohmic heating results in $\sim 1.27 \text{ mW}$

or (0.56 mW/cm^2) . This is roughly 20-fold lower than the 10.99 mW/cm^2 calculated from the heat generation at the catalyst layer, implying that catalyst heating is much more significant than ohmic heating at lower current densities. Even at elevated current densities cathode heating is shown to be dominant (Fig. 3.1f). For an even thinner electrolyte of 1 mm (see Fig. 3.A.4 and 3.A.5), heating in catalyst layer is two orders of magnitude larger than ohmic heating at -10 mA cm^{-2} .

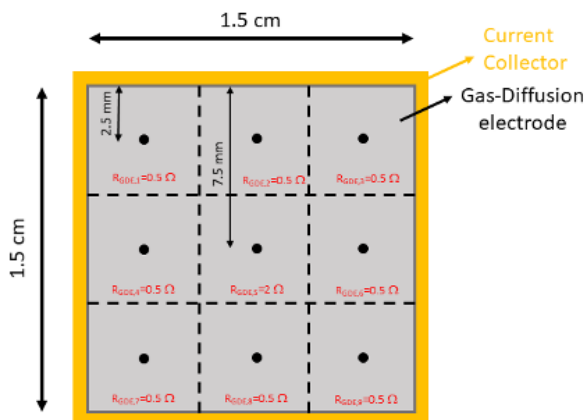
The last heating source present in the field of view of the infrared setup is due to the resisted electrical charge transport of electrons within the carbon GDE itself. To assess the possible influence on overall heat generation and energy consumption, the resistance over the full width of the GDE ($\sim 2 \text{ cm}$) was measured with a multimeter to be 4Ω . As the heat generated throughout the GDE also follows Ohm's law, we can write the relation as follows:

$$\frac{Q_{gde}}{A_{geo}} = q''_{gde} = \frac{V_{ohm} \cdot I}{A_{geo}} = (R_u \cdot j) \cdot (j \cdot A_{geo}) = R_u j^2 A_{geo} \quad (3.13)$$

Unfortunately the GDE resistance at any given location across the electrode depends on the distance between the reaction location $x = (0, 1.5 \text{ cm})$ and $y = (0, 1.5 \text{ cm})$ and the current collector. For example a catalyst around the perimeter of the electrode has a much lower electron pathway through the GDE than a catalyst particle in the centre of the electrode. If the voltage drops are large due to the resistance, then current density will also vary. However, without perform a full analysis of the system to determine the potentials and resistances across the GDE, we can provide an order-of-magnitude calculation that determines the rough magnitude of heat generation that is associated with the GDE resistance.

To perform this calculation, we can split the 1.5 cm by 1.5 cm GDE a number of equal squares and assume an even current distribution over the electrode. For the case of 9 equal squares as shown below for example, each region is then responsible for 1/9th of the total current passed in the reaction. For the 8 squares around the perimeter, they all have relatively similar access to the current collector and can thus be assumed to have a lower resistance than the center square. As the full GDE resistance across the GDE width of 2 cm is measured as 4Ω , we can estimate an approximate GDE resistance of $2 \Omega/\text{cm}$ of electrode width and assign a rough resistance to each square. For the perimeter squares the distance from the center to the current collector is $\sim 2.5 \text{ mm}$, which gives a resistance of 0.5Ω . From the central square the electrons must travel 7.5 mm through the GDE, giving an approximate resistance of 2Ω .

Making use of Eq. 3.13 for each of the 9 squares, we can then estimate the GDE heating, again at 10 mA cm^{-2} (total current of 0.0225 A):



$$q_{gde}'' = \sum \frac{I^2 R_{gde}}{A_{geo}} = \frac{8 \left[\left(\frac{0.0225}{9} \right)^2 \cdot 0.5 \right] + \left[\left(\frac{0.0225}{9} \right)^2 \cdot 2 \right]}{2.25} = 0.0167 \quad (3.14)$$

At this current density, where the power-term of the catalyst's overpotential is of about 10.99 mW/cm² as previously described (compared to a mere 0.017 mW/cm² of resistive origin), this ohmic resistance can then be disregarded as it is roughly 1/660th of the overpotential heating term. Logically we can confirm that this result makes sense as well. If substantial heating and therefore voltage loss occurred as a result of GDE heating, then cell potentials of such systems would also be much larger than what is typically observed.

Calculation of half-cell thermoneutral potentials

For the electrochemical reactions interesting for producing value-added chemicals (e.g. H₂, CO, ethylene, etc.), substantial overpotentials are required for the reaction to occur spontaneously beyond the equilibrium potential (E^0). Independently of this, every reaction at an electrode is further characterized by a thermoneutral potential ($E_{tn,0}$), i.e., the potential at which the reaction is energetically neutral. Applying a potential lower than this thermoneutral potential will result in the reaction drawing heat from the system, while operating at a potential higher than this value will result in the reaction supplying heat to the system. This thermoneutral potential is defined by:

$$E_{tn,0} = - \frac{\Delta H_r}{nF} \quad (3.15)$$

where ΔH_r is the enthalpy of the reaction, n is the number of electrons transferred and F is Faraday's constant.

Within this work the thermoneutral potential is critical parameter to understand as our instrumentation tool couples emitted heat to potentiostatic data via temperature changes, which only occurs at potentials beyond the thermoneutral potential. Here we calculate these potentials for the reactions for a number of reactions of interest in this work. To calculate these values we use the following values at 298 K for standard enthalpy and Gibbs free energy of formation shown in Table S1.

Table 3.A.1: Gibbs free energy and enthalpy of formation for relevant reaction species at 298 K.[46]

		CO ₂	H ₂ O	OH ⁻	CO	H ₂
$\Delta_f G^\circ$	[kJ/mol]	-394.39	-237.14	-157.2	-137.16	0
$\Delta_f H^\circ$	[kJ/mol]	-393.52	-285.83	-230.0	-110.53	0

Using the data in Table 3.A.1, the equilibrium and thermoneutral potentials can be calculated on both a standard hydrogen electrode (SHE) and reversible hydrogen electrode (RHE) scale. These are shown below in Table 3.A.2. Conversion from an SHE to RHE scale is done using the Nernst equation in the form of Eq. 3.16 below:

$$E_{RHE} = E_{SHE} + 0.0591 \cdot \Delta \text{pH} \quad (3.16)$$

Table 3.A.2: Calculated equilibrium (E°) and thermoneutral ($E_{tn,0}$) potentials at 298 K.

Reaction		E_{SHE}° (V)	E_{SHE}° (V)	$E_{tn,0,SHE}$ (V)	$E_{tn,0,RHE}$ (V)
$2\text{H}_2\text{O} \rightarrow 2\text{H}_2 + \text{O}_2$		1.229	1.229	1.481	1.481
$2\text{H}^+ + 2\text{e}^- \rightarrow \text{H}_2$	(pH = 0)	0	0	0	0
$2\text{H}_2\text{O} + 2\text{e}^- \rightarrow \text{H}_2 + 2\text{OH}^-$	(pH = 14)	-0.828	0	-0.579	0.249
$2\text{H}_2\text{O} \rightarrow \text{O}_2 + 4\text{e}^- + 4\text{H}^+$	(pH = 0)	1.229	1.229	1.481	1.481
$4\text{OH}^- \rightarrow \text{O}_2 + 4\text{e}^- + 2\text{H}_2\text{O}$	(pH = 14)	0.400	1.229	0.903	1.73
$\text{CO}_2 \rightarrow \text{CO} + 0.5\text{O}_2$		1.333	1.333	1.446	1.446
$\text{CO}_2 + 2\text{H}^+ + 2\text{e}^- \rightarrow \text{CO} + \text{H}_2\text{O}$	(pH = 0)	-0.104	-0.104	0.015	0.015
$\text{CO}_2 + \text{H}_2\text{O} + 2\text{e}^- \rightarrow \text{CO} + 2\text{OH}^-$	(pH = 14)	-0.933	-0.105	-0.564	0.264

The most relevant reactions for our results are the 2-electron half-reaction for CO₂ reduction to CO and HER in an alkaline medium (pH = 14), which are 0.264 V vs. RHE and 0.249 V vs. RHE respectively. This means that, at the equilibrium potential, both reactions are exothermic.

Supplementary Figures

3

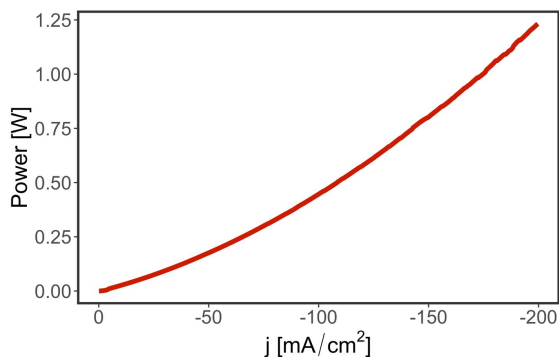


Figure 3.A.1: Total heat generation from cathodic and ohmic overpotentials between the working and reference electrodes in the studied electrolyzer, as calculated using the relation in Eq. 3.3. The half-cell resistance between working and reference electrodes was $\sim 2.5\Omega$ using a 1M KOH electrolyte.

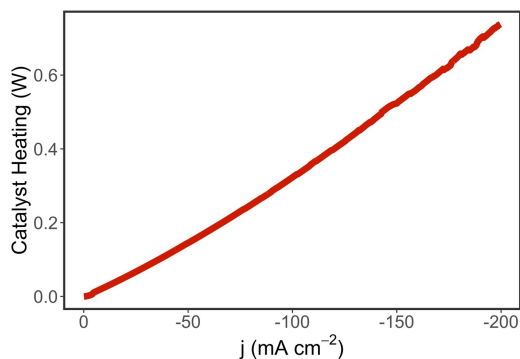


Figure 3.A.2: Total heating occurring at the catalyst, obtained by subtracting resistive heating in the electrolyte to the measured potential between the working and reference electrodes. The half-cell resistance between working and reference electrodes was $\sim 2.5\Omega$ using a 1M KOH electrolyte.

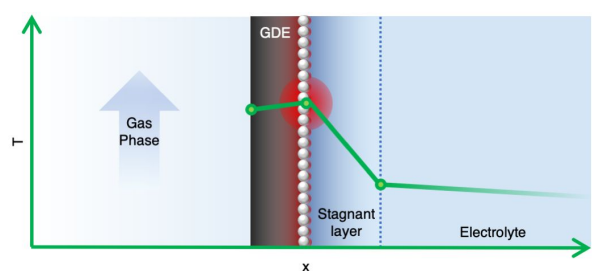


Figure 3.A.3: Heat development at the catalyst layer and distribution to the GDL backbone and electrolyte double-layer. According to our calculations, the GDE should absorb roughly 25 times more heat than the electrolyte.

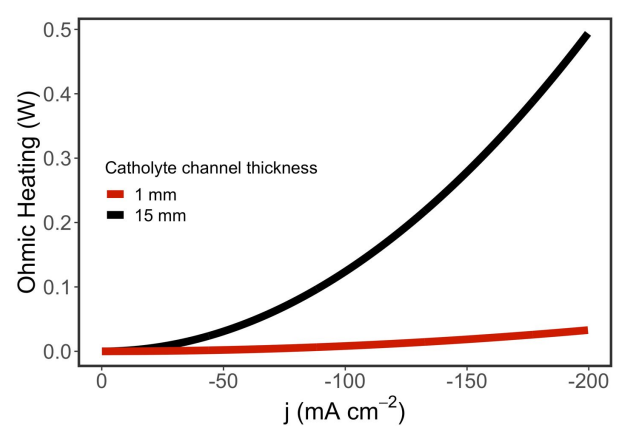


Figure 3.A.4: Virtual difference in ohmic heating in the catholyte channel as a function of electrolyte chamber thickness. Resistance of the 1 mm chamber taken to be exactly 1/15 of the registered resistance. Values for a 1M KOH catholyte in the cathodic half-cell (WE-RE).

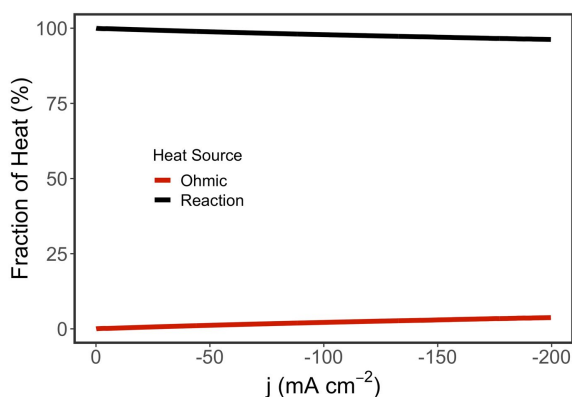


Figure 3.A.5: Relative source of heating at the interface as a function of applied current density for a 1 mm thick 1 M KOH electrolyte, obtained by multiplying the resistance recorded by 1/15.

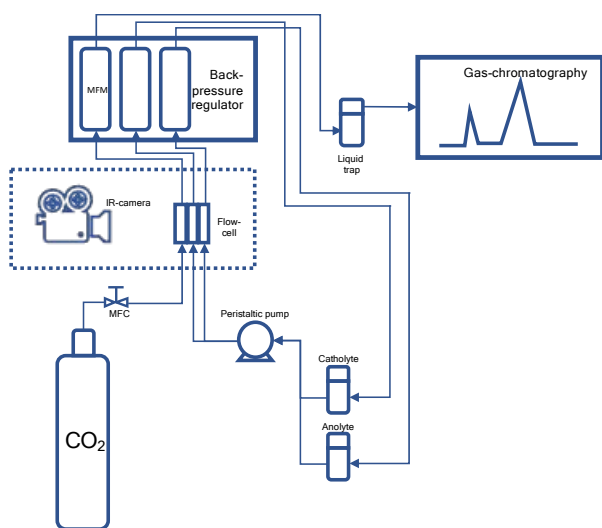


Figure 3.A.6: Setup diagram of the windowed flow electrolyzer. The IR camera and the flow-cell were placed in a dark box (see Fig. 3.A.7), the effluent electrolyte and gas-out streams were circulated through a back-pressure regulator (BPR) to ensure the gas-phase did not penetrate in the catholyte compartment due to pressure differences.

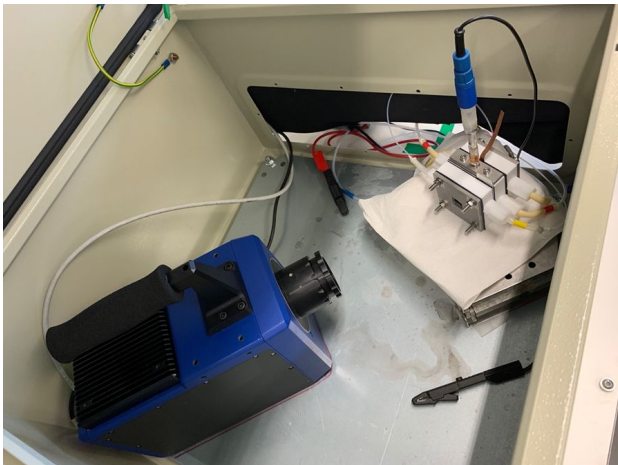


Figure 3.A.7: IR-camera and windowed electrolyzer in the dark box.

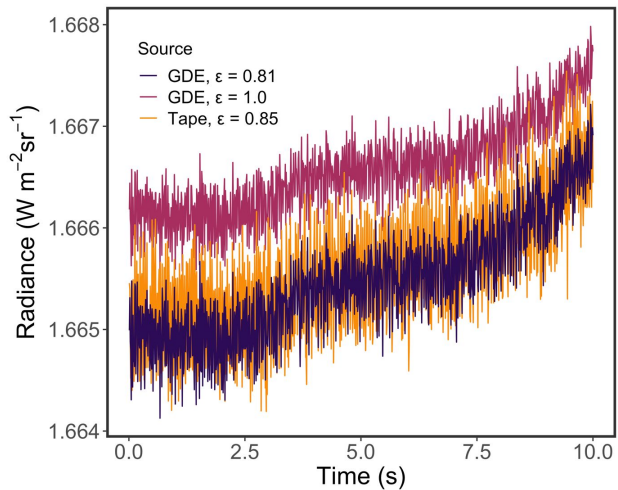


Figure 3.A.8: Calibration of the emissivity values of a GDE behind a sapphire window. See figure 3.A.9 for a depiction of the calibration setup.

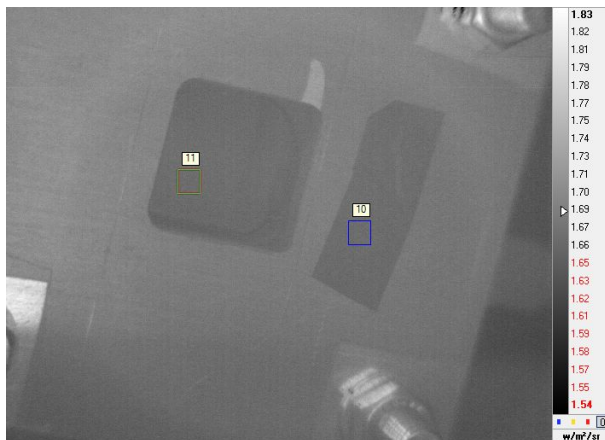


Figure 3.A.9: Calibration setup. Equal areas on the GDE (11) with different emissivity values were compared to carbon tape on the endplate (10) and recorded over a short period of time.

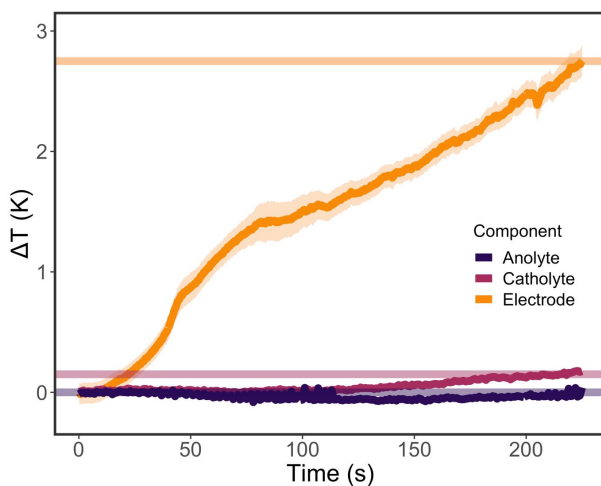


Figure 3.A.10: Heating of the GDE area under increasing current density ($t = 0 \rightarrow 0 \text{ mA cm}^{-2}$, $t = 200 \text{ s} \rightarrow 200 \text{ mA cm}^{-2}$) using a 1M KOH electrolyte at an increased flow-rate of 20 sccm. Temperatures for catholyte and anolyte were measured at the inlet of the electrolyte beaker (see figure 3.A.6). The shaded areas represent the standard deviation of temperatures across the electrode surface.

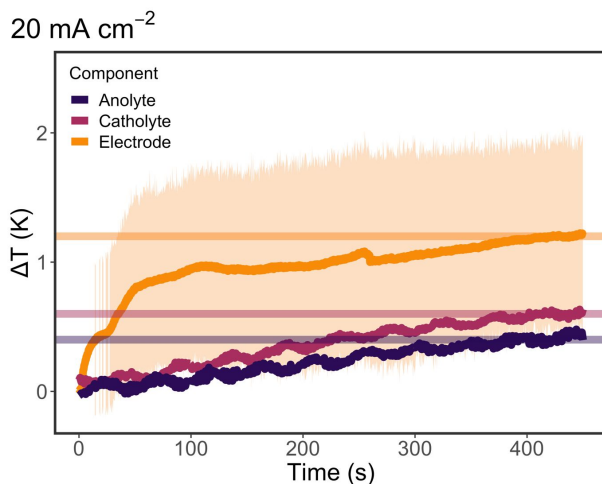


Figure 3.A.11: Heating of the GDE area under constant current density (-20 mA cm^{-2}) using a 1M KOH electrolyte at an increased flow-rate of 20 sccm. Temperatures for catholyte and anolyte were measured at the inlet of the electrolyte beaker (see figure 3.A.6). Solid horizontal lines represent the final temperature of each component after the 450 s experiment. The shaded areas represent the standard deviation of temperatures across the electrode surface.

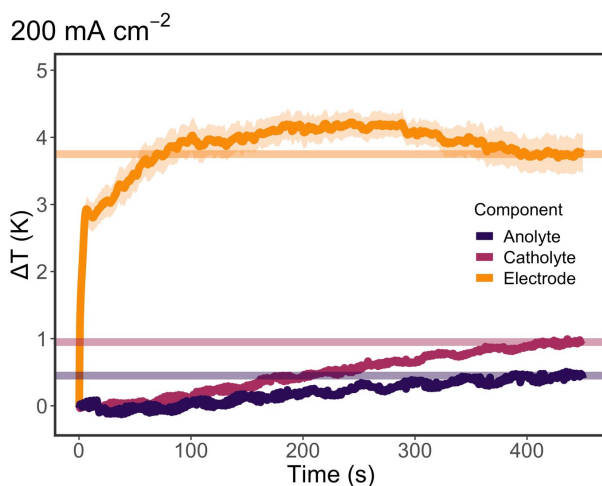


Figure 3.A.12: Heating of the GDE area under constant current density (-200 mA cm^{-2}) using a 1M KOH electrolyte at an increased flow-rate of 20 sccm. Temperatures for catholyte and anolyte were measured at the inlet of the electrolyte beaker (see figure 3.A.6). Solid horizontal lines represent the final temperature of each component after the 450 s experiment. The shaded areas represent the standard deviation of temperatures across the electrode surface.

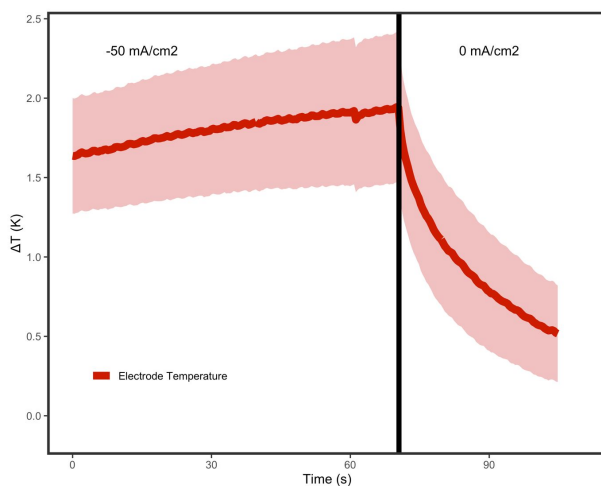


Figure 3.A.13: Cooling of an electrode after a current density ramp to -50 mA cm^{-2} .

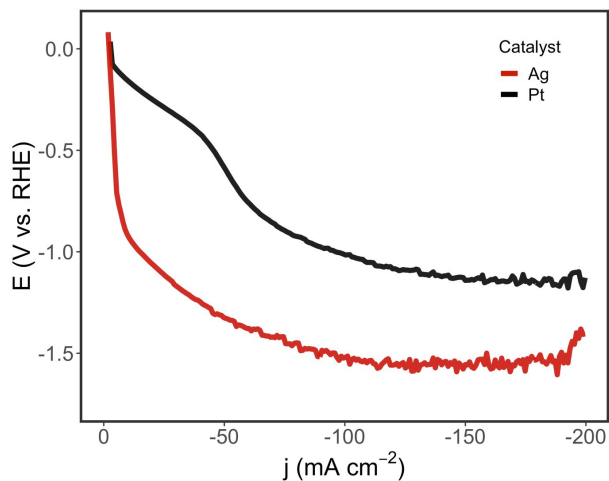


Figure 3.A.14: Polarization curves of silver and platinum coated-GDEs for increasing current densities using a 1 M KHCO_3 electrolyte.

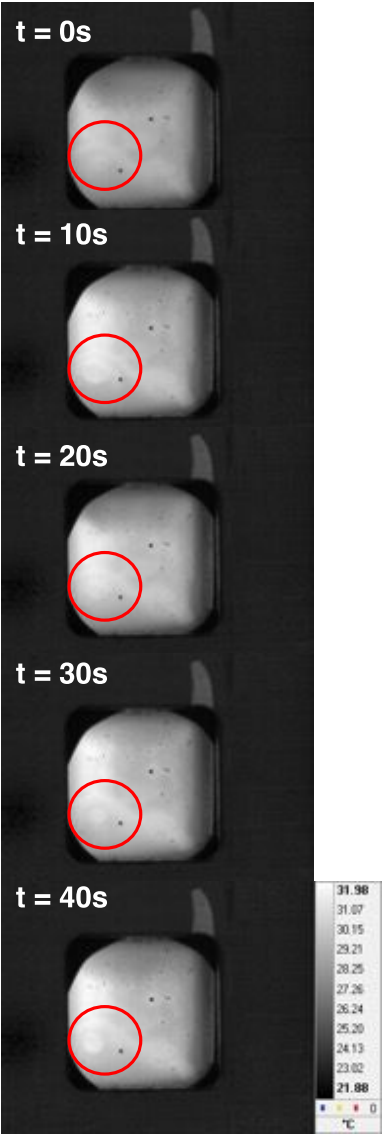


Figure 3.A.15: Sequence of the side-to-side fed electrolyzer presented in figure 3.4e. The feature circled can be seen to evolve quickly over time. The sequence can be observed in camera footage.

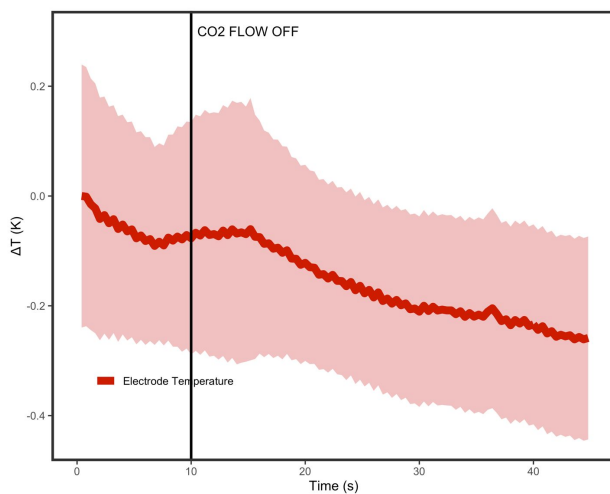


Figure 3.A.16: Effects of shutting of the CO_2 feed during at the end of a potentiostatic run on a 100nm Ag electrode using 1M KOH electrolyte.

4

4

CURRENT DISTRIBUTION ON HYDROPHOBIC ELECTRODES FOR CO₂ ELECTROLYSIS

*“Not everything that counts can be counted,
and not everything that can be counted counts.”*

— Sign hanging in A. Einstein’s office at Princeton

Electrochemical reduction of CO₂ presents an attractive way to store renewable energy in chemical bonds in a potentially carbon-neutral way. However, current electrolyzers suffer from intrinsic problems, like flooding and salt accumulation, that must be overcome to industrialize the technology. To resolve flooding and salt precipitation issues, researchers have used ultra-hydrophobic electrodes based on either polytetrafluoroethylene (PTFE) gas-diffusion layers (GDL’s), or carbon-based GDL’s with added PTFE. While the PTFE backbone is highly-resistant to flooding, the non-conductive nature of PTFE means that without additional current collection the catalyst layer itself is responsible for electron-dispersion, which penalizes system efficiency and stability. In this work, we present operando results that illustrate the poor current/potential distribution in thin catalyst layers (~50 nm) deposited onto PTFE GDL’s. We then compare the effects of thicker catalyst layers (~500 nm) and a newly developed non-interfering current collector (NICC). The NICC is able to maintain even current distribution with 10-fold thinner catalyst layers while improving stability towards ethylene (≥ 30%) by approximately two-fold.

4.1 Introduction

The electrochemical reduction of carbon dioxide (CO₂RR) has been gaining traction as a means of storing renewable energy in sustainable fuels and chemicals like carbon monoxide, ethylene, and ethanol. As a result, research and development efforts are shifting from understanding fundamental reaction mechanisms towards industrial scale-up and practical challenges of electrochemical conversion processes.[2, 3] Gas diffusion electrodes (GDEs) are now widely used to overcome mass-transport limitations at the cathode, where CO₂ is reduced, to perform CO₂RR at industrially relevant reaction rates, to yield value-added carbon products.[4, 5]

The electrochemical reduction of CO₂ using GDEs is however challenged by several problems that curb the upscaling of this technology to large industrial applications (Fig. 4.1a). First, the competing hydrogen evolution reaction (HER) forces CO₂ electrolysis towards alkaline environments, where HER has a higher overpotential than CO₂RR. This shift to alkaline environments, in turn, causes CO₂ to buffer in the alkaline reaction medium to form carbonates and bicarbonates.[6] Second, the accumulation of carbonates and cations close to the cathode catalyst causes the precipitation of carbonate salts that hamper transfer of reactant to the electrocatalytic phase.[7] Third, the hydrophobicity of the carbon gas-diffusion layer (GDL) of the GDE declines (i.e., the carbon becomes more hydrophilic) as current flows through the GDL,[8, 9] and together with precipitation of hygroscopic carbonate salts, enhances flooding of electrolyte into the GDE pore structure. The flooding of GDE pores with liquid electrolyte blocks gas diffusion pathways for CO₂, which reduces the availability of CO₂ at the electrocatalytic sites and allows the promotion of the HER.[10]

To avoid flooding issues during long-term CO₂RR operation, researchers have aimed to increase the hydrophobicity of gas-diffusion layers (Fig. 4.1a).[11] One successful approach to increase GDE hydrophobicity is using super-hydrophobic expanded polytetrafluoroethylene (PTFE) gas-diffusion layers.[12–16] These GDLs consist of a micro-porous layer (MPL) and backing layer (BL). The MPL is made from an expanded PTFE (ePTFE) with 250 – 500 nm fibrils stretched from 1 – 10 μ m nodes, whereas the BL is a polymeric support material formed by coarse laminates of polyethylene or polypropylene (PE, PP). In contrast to carbon-based GDE's which can quickly lose their ability to prevent flooding,[10, 17, 18] non-conducting PTFE GDE's maintain hydrophobicity when exposed to sustained electrochemical potentials and moderate hydrostatic pressures. With further modifications, like covering the catalyst layer with ionomers, electrolyzers using ePTFE type GDE's have then shown the ability to deliver both high stability (> 60 h) and selectivity (> 80 % FE at 1.17 A cm⁻²) towards multicarbon (C₂₊) products during CO₂RR (Fig. 4.1a).[19]

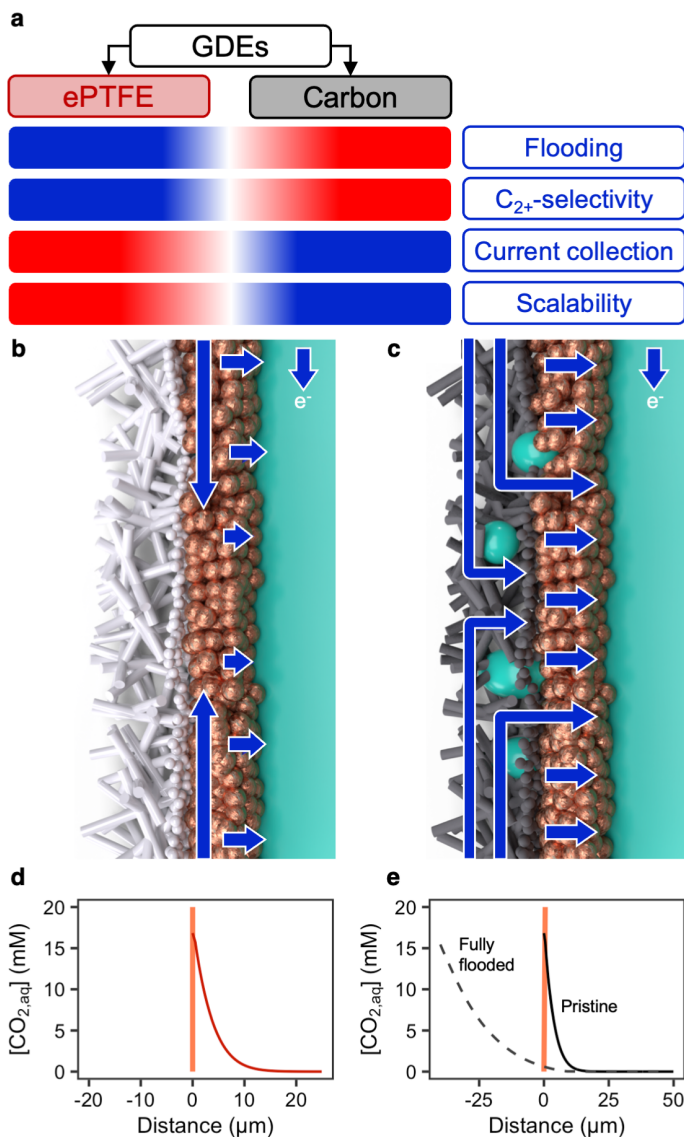


Figure 4.1: The local environment characteristics at an ePTFE and flooded carbon GDLs. (a) Advantages and disadvantages of super-hydrophobic ePTFE and carbon- based GDE architectures for CO₂ electrolysis. (b) Close-up sketch of an ePTFE electrode, current collection sketched in blue. (c) Sketch of a carbon-based GDE, current collection sketched in blue. (d) Modeled local CO_{2(aq)} concentration at steady-state close to the catalyst layer (coral) in the ePTFE electrode at -300 mA cm^{-2} . (e) Modeled local CO_{2(aq)} concentration at steady-state close to the catalyst layer (coral) for the carbon GDE, for non-flooded and fully flooded cases at -300 mA cm^{-2} .

4

However, a caveat of the excellent non-wetting and CO₂ diffusion properties of ePTFE GDE's is the non-conductive nature of the polymeric backbone. Upon electron flow from the anode to the cathode, electrons must then be conducted transversely through the catalyst layer rather than the GDL (Fig. 4.1b), which is contrary to the conductive backbone of carbon-based GDE's (Fig. 4.1c). As catalyst layer thicknesses (0.1 to 5 μm) are much thinner than carbon-GDE's (200 to 500 μm),^[20] current distribution through the catalyst layer results in much higher in-plane ohmic resistances than in carbon-GDE's, which deter the industrial scalability of electrolyzers with ePTFE GDE's. Even for a 5 cm² electrode area, large current density disparities would occur due to the increased in-plane resistance to electron-conduction, negatively impacting product selectivity towards CO₂RR. When the current distribution is constrained in a poorly conducting electrode, it can be expected that catalytic activity is concentrated close to the current collector, while the rest of the electrode surface operates at reduced potential/current density or is even inactive for CO₂RR – a problem that only worsens for increasing geometric catalyst areas. This current distribution disparity on the CO₂RR electrodes (ePTFE and carbon-GDE's) has, to our knowledge, never been studied in detail before.

In order to design and assess efficient electrode architecture designs for CO₂RR, we need to better understand the operando behavior of the electrode – even more so considering that local activity (and, thus, local overpotential) can have a critical influence on the product distribution observed.^[21–24] If current distribution is not uniform due to high conductivity resistance in the catalyst layer, the potential applied to the catalyst will vary spatially, jeopardizing the long-term stability and product selectivity. We have shown previously that local heat production (probed by temperature sensing of the electrode's GDL) is a valid and accurate proxy for an electrode's activity.^[25] Infrared (IR) thermography then provides a basis of understanding local conditions and electrode behavior during operation of a CO₂ electrolyzer.

Herein, we use infrared thermography to demonstrate the potential problems of current distribution in ePTFE-based electrodes with thin catalyst layers in a state-of-the-art flow cell CO₂RR electrolyzer. Using a 1D reaction-diffusion model of the gas-liquid interfaces in the ePTFE and carbon-based electrodes, we show how the GDE structure and operational stability affects the local availability of CO₂ in the catalyst layer and the C₂₊ product selectivity. Then we analyze the current distribution in ePTFE electrodes and examine the deterioration of the thin catalyst layers deposited on the expanded PTFE-layer. Infrared thermographs display poor current density distribution for 50 nm catalyst layers, where the active region is taxed with a current load around 5 times higher than the average. Finally, we showcase a non-invasive current collector (NICC) as an alternative catalyst

layer design to improve the current collection and distribution in ePTFE electrodes whilst maintaining C_{2+} product selectivity.

4.2 Results

4.2.1 The role of local hydrophobicity in C_{2+} selectivity of ePTFE electrodes

Contrary to ePTFE electrodes, carbon GDL's have the advantage of being conductive (albeit with a much higher through-plane conductivity than the in-plane conductivity)[26, 27]. The disadvantage of these electrodes, however, is the flooding of the micro-porous layer. Besides promoting unwanted HER at the micro-porous layer, flooding impedes CO_2 transport towards the catalyst layer. Whereas, on an ePTFE electrode, dissolved CO_2 reacts directly on the interface of dissolution. A fully flooded micro-porous layer (MPL) poses a considerable barrier of around 20–40 μm between the coordinate of dissolution and the reactive surface, as the alkaline electrolyte will start buffering the reactant before it reaches the catalyst.[20]

To illustrate the effect of a flooded MPL, we employed a simple reaction-diffusion model at steady-state for both architectures. Solving the model for current densities of -300 mA cm^{-2} along the gas-liquid phase-boundary, we see that the concentration of dissolved CO_2 is severely hampered in the flooded carbon MPL case compared to an ePTFE electrode (Fig. 4.1d, e, see Supplementary Notes for details on the model's parameters).

Comparing the product selectivity of a carbon-based electrode (Sigracet® 38BB) and an ePTFE electrode (Sterlitech® Aspire QL822) over time highlights the limitations of the carbon support which is more susceptible to flooding due to electrowetting of the carbon support. Here we used a three-chamber flow cell with 1 M KOH as both the catholyte and anolyte. The carbon-based GDE was sputtered with a 200 nm Cu layer, and the ePTFE electrode with a 500 nm one. For these two different electrodes we then ran constant current densities experiments from -10 mA cm^{-2} to -300 mA cm^{-2} . Here we observed that the ePTFE electrode exhibited a superior selectivity towards hydrocarbon C_{2+} products (ethylene, ethanol, acetate, propane and propanol) across the board (Fig. 4.A.1). While the copper catalysts on each electrode support are not identical in morphology or surface area, the disparity in selectivities towards the higher value C_{2+} products shows the influence that architecture design has on the performance of a GDE.

4.2.2 Operando observation of activity distribution on ePTFE electrodes

The dependence of product selectivity on local availability of CO₂ then raises questions on the requirements of a catalyst layer. Further, thicker catalyst layers may deplete dissolved CO₂ depending on the operating current density or spatial distribution of CO₂ under high single-pass conversion conditions.[13] If a thinner and thicker catalyst layer can achieve similar performance, then less material would be beneficial from a cost and resource perspective. The development of stable, thin catalytic layers would then enable a more efficient CO₂RR process. However, a drawback of these thin layers is the limited in-plane current collection in the absence of conductive gas-diffusion layers.

To study the effect of this limited in-plane current collection on thin copper films, we deposited two different thicknesses of catalyst on our ePTFE GDLs. Copper thin films deposited by direct-current (DC) magnetron sputtering (see “Methods”) show a considerably higher current resistivity compared to bulk metals (e.g. smooth thin-films below 500 nm is up to 20 times higher in electrical resistance).[28, 29] In the conditions at which these electrodes are operated, i.e. high polarization and high reactant availability, these thin films can then lead to disparity of the current distribution across the GDE. This is directly evidenced by an electrochemical impedance spectra (EIS) analysis which shows the comparatively higher ohmic resistance of 50 nm Cu layer (1.1 Ω) vs. 500 nm Cu layer (0.45 Ω) on ePTFE, as well as vs. the pristine carbon-based support (0.6 Ω) (EIS data in Fig. 4.A.2, two probes arrangement data in Table 4.A.3).

Then, using our IR thermography set-up (Fig. 4.2a, Supplementary Figs. 4.A.3–4.A.6), we characterized the evolution of temperature distribution during a linear polarization of the cathode. Infrared thermography is a suitable method to study the local activity on thin GDEs, with which one can relate the increase in temperature of the backbone to the local current density on the catalyst of the electrode.[25] The heat map directly relates to the current distribution profile, hence it offers a powerful proxy to track the current/voltage disparity by cross comparison of GDEs and differing catalyst layers (see the Supplementary Notes). Figure 4.2b, c shows that the thermographs, especially at higher current densities ($< -100 \text{ mA cm}^{-2}$), show a uniform temperature distribution on the backbone of catalyst layers for 500 nm and 1 μm thicknesses. The 50 nm layers, on the other hand, display an activity pattern that is centered around the edges of the electrode for -50 and -200 mA cm^{-2} , where the travel length for electrons from the current collector is much shorter than for the center of the electrode (Fig. 4.2b, c, right panels). While the surface-wide, averaged temperature increase for both electrodes is similar ($\Delta T \approx 4.5 \text{ K}$, see Supplementary Fig. 4.A.7), the variance of these temperatures across the surface is considerably more exaggerated for the thinner, less

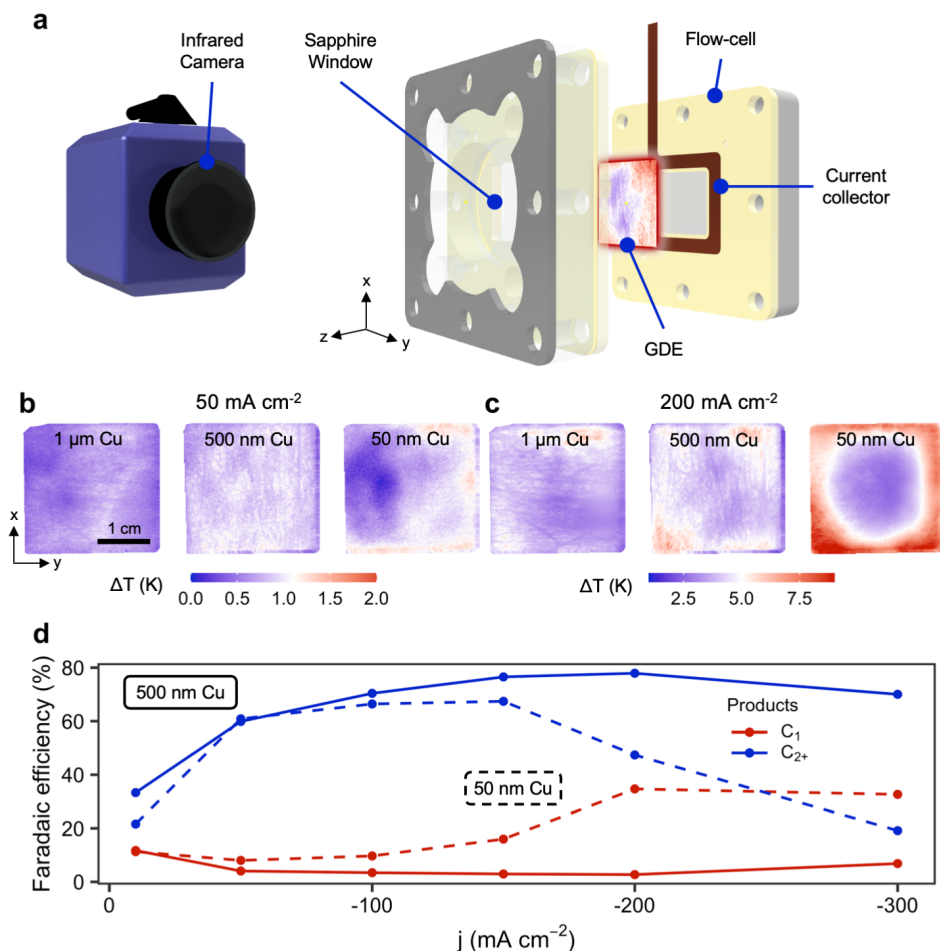


Figure 4.2: Current distribution in an ePTFE electrode strongly depends on catalyst thickness. (a) Infrared thermography setup for an electrochemical flow cell. (b) Space-dependent temperature increase on an ePTFE/1000 nm Cu electrode (left), an ePTFE/500 nm Cu electrode (center), and an ePTFE/50 nm Cu electrode (right) at -50 mA cm^{-2} . (c) Space-dependent temperature increase on the same electrodes at -200 mA cm^{-2} . (d) Impact of catalyst-layer thickness on the product selectivity of ePTFE electrodes at increasing current densities.

conductive 50 nm Cu layers. This observation implies that, while total activity is similar, as the applied current is the same, the distribution of this activity on the catalyst surface is very divergent.

This irregular electrochemical activity distribution has direct consequences for the observed product distribution. As mentioned before, since the product distribution on copper catalysts is highly dependent on local pH and overpotential, a non-

uniform activity pattern is likely to result in an altered product composition.[27] Looking at the selectivity towards C1-products (methane and formate) versus that of higher hydrocarbons, we see that the C1:C₂₊ selectivity ratio of the 50 nm layer results is close to 2: 3 at -200 mA cm^{-2} , whereas the thicker 500 nm layer has an approximate 1: 35 ratio (Fig. 4.2d, Supplementary Table 4.A.4).

The trend for the 50 nm catalyst layer, however, is contrary to reports in literature. Upon increasing local overpotential and current density, Cu layers have been observed to shift production to higher hydrocarbons, like ethylene and ethanol.[22, 30, 31] The observed shift in product distribution can then, at least partially, be explained as a consequence of changing CO_{2(aq)}:CO_(aq) ratios.[32, 33] If we translate the recorded temperatures to a current density value for the observed temperature increases (see Supplementary Fig. 4.A.8), local current densities in the thin catalyst layer are then as high as -1 A cm^{-2} at the electrode's perimeter, in contrast to the average applied current density of -200 mA cm^{-2} . The elevated local current density then consequently results in greater local depletion of reactant species, lower CO availability and increased overpotential that all play a role in shifting selectivity towards methane and hydrogen.[34, 35] In effect, if we use the local current density and temperature values to approximate a concentration for dissolved CO₂ using parameters detailed in the model (Equations S9 to S13 in the Supplementary Notes), a distribution ranging from 6 to 10 mM is observed for the 50 nm electrode (Supplementary Fig. 4.A.9), where high-activity areas have a clearly lower CO_{2(aq)} concentration compared to inactive areas.

4.2.3 Deactivation mechanisms of copper on ePTFE electrodes

A potential consequence of the high degree of spatial temperature variances described in Fig. 4.2 and the preceding section is that the non-uniformity could impact the stability of thin Cu catalyst layers during extended operation and through dynamic electrical loads on the system. Degradation of copper catalysts during CO₂RR is a broad concern because changes in the catalyst properties impact the selectivity, activity and stability of electrolysis.[36, 37] Several degradation mechanisms have been reported for metallic copper electrodes, like detachment and dissolution,[38] Ostwald-ripening,[39] reshaping[40] or agglomeration.[41] Restructuring of the copper surfaces has been shown to increase hydrogen production and loss of selectivity towards CO₂RR-products.[42] However, it is likely that many of the reported experiments were at conditions (e.g., low current density, H-cell reactors) that facilitated uniform current distributions, such that the effects of significant variations in current density across the electrode were not considered. Further, many prior studies used planar-type electrodes that do not represent the complexity of the three-dimensional, multi-layered porous GDE structures like the ePTFE electrodes presented in this study.

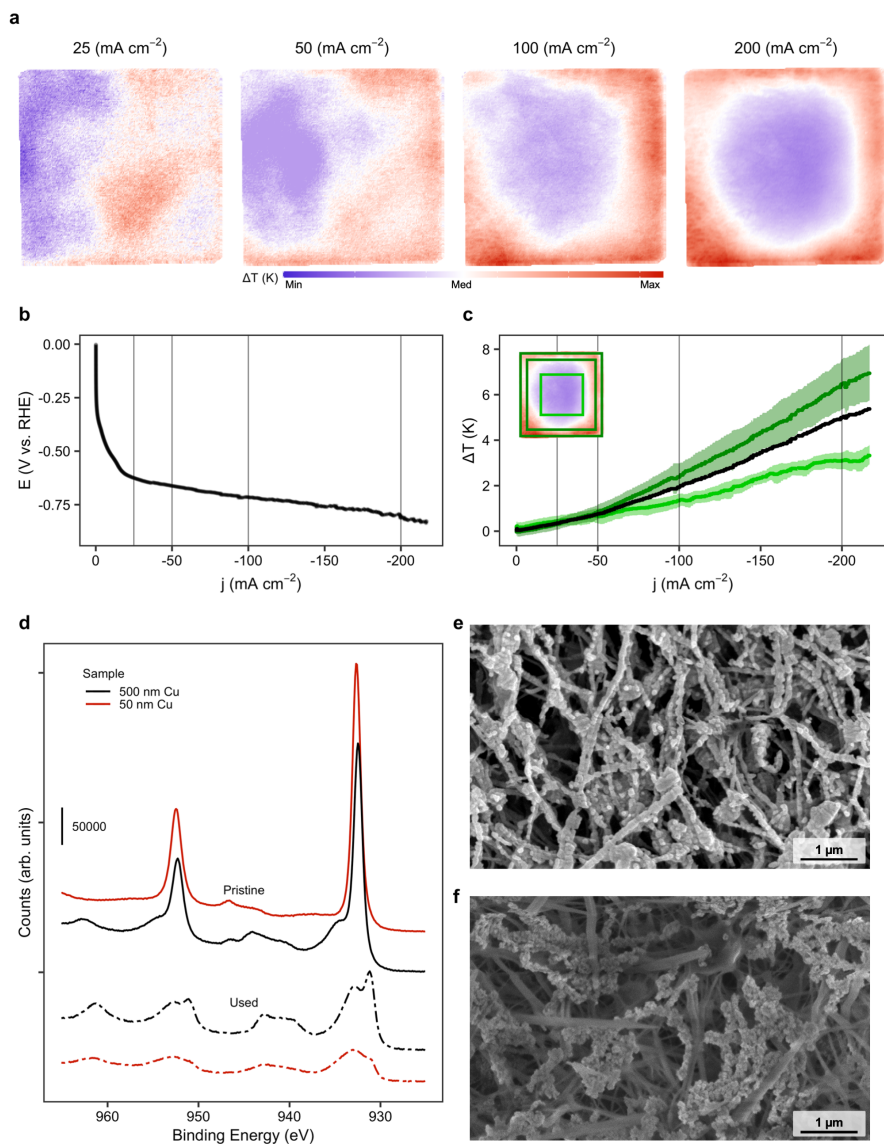


Figure 4.3: Degradation of ePTFE/Cu electrodes is highly dependent on local polarization. (a) Activity distribution in an ePTFE/50 nm Cu electrode at increasing current densities. (b) Polarization curve for the electrode in (a). (c) Observed average temperature increase and its deviation for the high and low activity zones in (a). Electrode average temperature in black. Insert depicts the thermograph at -200 mA cm^{-2} and the analyzed areas. (d) XPS spectrograms of pristine and used ePTFE/500 nm and ePTFE/50 nm samples. (e) SEM image of a pristine ePTFE/50 nm sample. (f) SEM image of a used ePTFE/50 nm sample after 2 h of operation.

We hypothesized that copper is exposed to spatially varying effects for more complex and larger surfaces at abrupt interfaces, like the ePTFE electrodes presented herein. Under the absence of polarization or reduced electrochemical potential, copper forms hydroxide species in basic conditions, as is the case for the electrodes described in this work.[43] Ultimately, this means degradation of the catalyst layer is accelerated under alkaline CO₂RR conditions. In effect, even the thicker 500 nm Cu layers in this work presented loss of selectivity for C₂₊-products and increased H₂-production rates in a short period (Supplementary Fig. 4.A.10).

To scope and assess the degradation mechanisms for the thin 50 nm Cu layers, we subjected our electrodes to a slow polarization increase. Combined with the IR thermography, this allowed us to determine an operando activity distribution (Fig. 4.3a and b). For low polarizations, like the -25 and -50 mA cm⁻² cases, the temperature increase compared to open-circuit voltage is evenly distributed over the surface, which indicates a homogeneous current-density distribution. Upon increasing this polarization to higher values, the activity quickly accumulates to those areas closest to the current collector, where the path of electric resistance is lowest. This effect starts manifesting beyond -50 mA cm⁻². Figure 4.3c shows that the area around the edges of the electrode has an increased temperature gradient (red), whereas the center part of the electrode stagnates (blue).

The lack of polarization at the center of the electrode presents an opportunity for copper to dissolve in the locally high alkaline environment. All sites subjected to a polarization of less than -0.5 V vs. SHE are prone to the formation of Cu(OH)₂ species, which easily transforms to CuO.[43, 44] In effect, optical examination of the catalyst layers before and after electrolysis shows an increased degradation for thinner films (see Supplementary Figs. 4.A.11 and 4.A.12). XPS-analysis of both 500 nm and 50 nm samples, before and after polarization as aforementioned are displayed in Fig. 4.3d. Pristine samples of both thicknesses show the characteristic Cu 2p_{3/2} peak at 933 eV and a Cu 2p_{1/2} one at 952 eV.[45] Meanwhile, the pristine 500 nm sample shows a distinctive shoulder peak at 935 eV. After polarization, on the other hand, both samples have a reduced Cu 2p_{3/2} peak and two shake-up peaks developed at 942 and 963 eV, similar to Cu(OH)₂ scans.[46] The lower intensity of copper-specific peaks and the presence of the soluble hydroxide species suggest that copper mainly detaches from the surface by dissolution in the basic electrolyte. This is further confirmed by Cu LMM scans, which show the presence of a metallic under-layer for pristine samples.[47] This metallic under-layer is preserved in the 500 nm Cu sample, but missing in the 50 nm sample (see Supplementary Fig. 4.A.13).

To strengthen this analysis, we proceeded to study both samples under SEM and AFM. Figure 4.3e, f depict the surface of the 50nm electrode before and after electrolysis, respectively. The conformal coating of the expanded PTFE fibers by

copper in Fig. 4.3e matches earlier reports in literature.[19] An analysis of the used sample showed little remnants of copper on the surface close to the center of the electrode, which could be fully oxidized. The increased difficulty in acquiring these later images also confirms the reduction in electrical conductivity of used 50 nm samples. While 500 nm samples show a minor degradation after running (see Supplementary Figs. 4.A.14–4.A.16), there seems to be little detachment of catalyst from the electrode (e.g. ~ 40 nm or 17% copper film thinning around a fiber calculated from measured average of 234 to 195 nm, before and after CO₂RR). This contrast in detachment is confirmed by AFM scans we performed on 50 nm Cu ePTFE electrodes and 200 nm Cu carbon electrodes (see Supplementary Figs. 4.A.17, 4.A.18).

On the other hand, selectivity figures for high current densities show a loss of selectivity and progressive deactivation of electrodes. The excessive equivalent current densities shown in Supplementary Fig. 4.A.8 point to cathodic corrosion and restructuring as a primary deactivation mechanism at areas close to the current collector.[48, 49] An increased local potential on copper nanoparticles is known to result in accelerated restructuring of the surface, resulting in stabilization of certain intermediates and increase in partial current densities towards hydrogen.[38, 50]

All in all, it appears that the physical stability of copper electrodes is highly dependent on its conductivity and exposure to a certain potential value to ensure that the catalyst would remain in a fully reduced, metallic state. Within 30 min, the 50 nm sample would develop areas that are or poorly connected (or even disconnected) from the current collector leading to chemical oxidation and dissolution of the copper species. Conversely, the areas that remain electrically connected near the perimeter of the electrode would experience accelerated deterioration due to the increased share of the local current density (Supplementary Fig. 4.A.19). This ultimately means that any solution that ambitions to stabilize copper electrocatalysts for CO₂RR must take the equalization of the current distribution across the surface into account.

4.2.4 Improving current distribution on ePTFE electrodes: a non-invasive current collector

Reports of using of ePTFE electrodes for CO₂RR generally involve a small catalytic surface area, in the order of 1–2 cm². [13, 19] On top of this, these catalyst layers are usually in the order of a couple of microns, instead of the much thinner hundreds of nanometers traditionally used in the deposition on carbon-based GDEs.[10, 51–54] As we have shown above, the stability of the copper in the reaction environment not only depends on previously mentioned degradation mechanisms, but also on its corrosion if the current collection is insufficient. Any solution to the stability

of copper catalysts on super-hydrophobic substrates goes, then, through solving the current collection issue.

Previously developed electrodes using these super-hydrophobic backbones have overcome current collection issues simply by applying a rather thick sandwiching layer consisting of carbon nanoparticles (C-NPs) and a graphite coating on top.[13] The use of carbon, however, implies the risk of promoting HER if sufficient potential is applied on the cathode. This solution seemed to stabilize electrode performance for operational times upwards of 100 h, but reported results are at rather low current densities and using highly conductive catholytes. While this solution was sufficient to achieve the metrics reported, it seems unfeasible to apply the same solution at a larger scale for high current densities and less concentrated electrolytes. Under these conditions, the applied potential is likely to surpass the -0.8 V vs. RHE required for HER promotion on the graphite and C-NPs at high rates.[10, 55, 56] On top of this, an added current collection layer between the cathode and anode is likely to result in longer ionic pathways, increasing ohmic resistances in the system and, in the case of CO₂RR, accumulating and precipitating (bi)carbonate salts.

In designing a remedy for the copper dissolution, we turned our attention to non-invasive solutions. This means a design that is intrinsically non-invasive and has minimal effect on the overall product distribution of our catalyst. As we highlighted before, thin copper catalyst layers have a limited conductivity when compared to the bulk metal. The usage of non-invasive bus-electrodes (or busbars) is widespread in the manufacture of photovoltaic semiconductors. Here, a thin busbar of (most commonly) silver collects current generated by the semi-conductor upon exposure to sunlight.[57, 58] By segmenting an area into smaller current collection channels, the ohmic resistance experienced by current traveling in-plane is greatly reduced. To illustrate the comparative conductance of different copper film thicknesses, we measured the ohmic drop of a $1\mu\text{m}$ Cu film using a 2-electrode probe showing a 9-fold reduced resistivity for the $1\mu\text{m}$ vs 50 nm thin films (see Supplementary Table 4.A.3).

Making use of deposition masks, we sputtered $1\mu\text{m}$ thick copper busbars on a 50nm Cu/ePTFE electrode to fabricate non-invasive current collectors (NICCs) for our electrode architecture (see Fig. 4.4a, Supplementary Figs. 4.A.22 to 4.A.24, and Supplementary Table 4.A.5). These busbars made electrical contact with the front-sided copper tape in the flow cell (while the copper tape is isolated from the catholyte, so it does not contribute to the catalyst area), functioning in practice as ‘highways’ for electrons to travel through before spreading out over the catalyst surface. The intention, in terms of system design, of deploying this solution is twofold: first, the low profile of these current collectors avoids any leakage of electrolyte between the gasket and the GDE and presents a facile, scalable design;

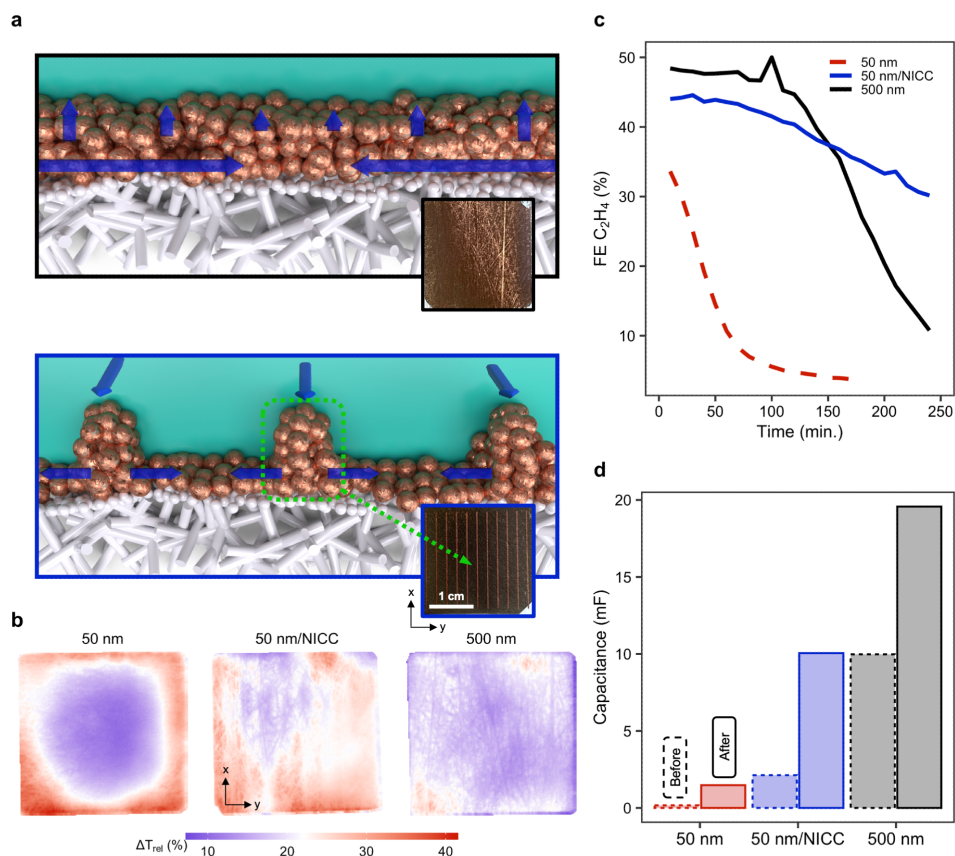


Figure 4.4: A non-invasive current collector extends stability and selectivity of ePTFE/Cu electrodes. (a) Sketches of a traditional ePTFE/Cu (top) and ePTFE/NICC/Cu electrode (bottom). Current collection lines depicted in blue. (b) Activity distribution for an ePTFE/50 nm, an ePTFE/50 nm/NICC and an ePTFE/500 nm electrode at -200 mA cm^{-2} . (c) Observed selectivity towards ethylene for the three designs at a constant potential of $\sim -0.55 \text{ V vs. RHE}$. (d) Change in capacitance for the three designs after 4h-long operation at constant potential of $\sim -0.55 \text{ V vs. RHE}$.

and second, the material acting as collector is the same deployed as catalyst, which should avoid excessive promotion of unwanted side-reactions, like HER. The goal of these NICCs is not to prevent electrochemical reactions on the $1 \mu\text{m}$ copper busbars, but to minimize their effect on product mixes while improving overall electrode current density distribution.

To test the efficacy of such an approach, we decided to compare to the previously benchmarked 50 and 500 nm catalyst interfaces. In effect, when comparing the latter two with a Cu/NICC sample, the thermal signature of the NICC enabled electrode is much more even than that of a bare 50 nm sample, much like that of

the 500 nm one, as shown in Fig. 4.4b. This means, in short, that our design results in an improved current collection when compared to traditionally deposited thin-films on ePTFE GDLs.

The current collection and distribution of activity over the catalytic area translates itself into an observable improvement of selectivity and stability for thin catalyst-layers. Comparing all three designs (500 nm, 50 nm and 50 nm/NICC on an ePTFE electrode) at constant potential during extended periods (4 hrs. max.), resulted in the ethylene selectivity displayed in Fig. 4.4c. Even though the onset selectivity of the NICC design is lower compared to the former 500 nm layer, a steep drop was observed for the films using the conventional method. To note, after 4-h of electrolysis, the NICC electrode can preserve 30% FE for ethylene whereas the conventional electrodes lose their selectivity, dropping below 10% FE.

While these reported stability durations are lower than state-of-the-art reports,[7, 19] the mass loadings of copper in this work are orders of magnitude lower ($0.112 \text{ mg}_{\text{Cu}} \text{ cm}^{-2}$ for a 50 nm Cu/NICC electrode versus $\sim 2 \text{ mg}_{\text{Cu}} \text{ cm}^{-2}$). This observation is supported by 7-h constant potential measurements comparing (i) a $1 \mu\text{m}$ Cu electrode, (ii) a 200 nm Cu/NICC electrodes, and (iii) a 500 nm Cu sample (Supplementary Fig. 4.A.24) indicating higher mass loadings are an enabling factor in stability studies. Our results however still demonstrate the added stability towards C₂H₄ of the 50 nm/NICC design versus the 500 nm and 50 nm counterparts (see Supplementary Table 4.A.6), though copper stability that plagues the CO₂ and CO reduction fields remains.

As the busbars themselves are made of copper, it is also interesting to examine if the electrochemical activity for the 50 nm/NICC case can be attributed to the $1 \mu\text{m}$ Cu busbars, as compared to the 50 nm Cu layer over the entire electrode. For instance, we model that sufficient dissolved CO₂ is expected to be present at $1 \mu\text{m}$ depths even at higher current densities (Fig. 4.1d). To understand this influence, we can compare the ethylene Faradaic efficiency for the 50 nm Cu case, the 50 nm/NICC Cu case, and an electrode only containing the $1 \mu\text{m}$ Cu busbars (e.g. ePTFE + NICC). As shown in Supplementary Table 4.A.5 and Supplementary Fig. 4.A.20, the $1 \mu\text{m}$ Cu busbars show a quick decline in ethylene selectivity with increasing current density, while the combined 50 nm/NICC Cu case maintains ethylene selectivity up to -200 mA cm^{-2} . We can then conclude that the greater performance of the 50 nm/NICC system over the 50 nm sample alone is not due to the additional mass loading of the $1 \mu\text{m}$ Cu busbars.

A way of monitoring the evolution of surface roughness during electrolysis is the measuring of double-layer capacitance in the used GDEs.[59] To do so, we performed cyclic voltammetry before and after long electrolysis runs ($\sim 4 \text{ h}$) at different scan rates between -0.3 and $0.3 \text{ V vs. Ag/AgCl}$. The capacitance analysis of the NICC design shows a noticeable increase against its 50nm counterpart

(Fig. 4.4d). The thicker, 500 nm electrode, however, still displays a bigger capacitance overall. The change in capacitance is relatively smaller for the 50 nm/ NICC and 500 nm designs than for the 50 nm one, indicating a dramatic increase in surface roughness. Compared to the 50 nm/NICC design, the 500 nm layer displays a lower capacitance change (around two-fold, 10 mF before and 19.5 mF after). This indicates that, while corrosion of the electrode can influence selectivity directly, it is not the main driver of selectivity changes, as the 50nm/NICC shows an improved selectivity towards ethylene over time. While the sharp disparity between before and after measurements can also be due to the presence of oxide species in the fresh samples tested before electrolysis, the noticeable increase for the 50 nm/NICC sample suggests a considerable larger area of the electrode is electrically connected. The improved current density distribution and more equal overpotential distribution, then, appears to also influence degradation of these electrodes directly.

4.3 Discussion

We will now briefly comment on the NICC approach more broadly for membrane electrode assembly systems, and the potential benefits of replacing the copper bus-bar structure with silver.

It is worthwhile to discuss the potential for the NICC in membrane-electrode assembly systems which still predominantly utilize carbon-based GDE's. Firstly, while carbon-based GDE's can maintain long term CO₂RR performance in MEA systems due to the lack of catholyte, operational wetting and flooding of the MPL layer is still occurring as evidenced by salt precipitation on the back of the GDE. Further, modeling studies in the fuel cell domain have shown the preference of previously wetted MPLs and GDLs to remain wetted, as removing water from nanopores is challenging.[60] These wetted areas then likely act as an impediment for CO₂ gas flow, even if not impeding it entirely. Additionally, flooded regions act as isolated liquid volumes susceptible to anion and cation concentration reaching precipitation levels, further hampering mass transport. Such periodic water volumes, salt deposits and condensate release within carbon GDL's are shown by X-ray experiments, and may be prevented using the NICC with an ePTFE backbone.[61–63] Overall, we hypothesize that the use of carbon-based GDE's in MEA systems may be one reason why the CO selectivity of many silver-based zero-gap MEA systems is pre- dominantly limited around -200 to -300 mA cm⁻² while the same GDE and catalyst in flowing catholyte systems reaches much higher CO₂ reduction current densities before HER becomes dominant.[19, 64] Efforts to utilize ePTFE electrodes and the NICC in an MEA systems can be of interest for future studies to overcome these limitations.

An interesting replacement for copper busbars in future studies would be the

use of silver busbars as used in photovoltaics. Silver provides the best conductivity of any pure metal, with 5% greater conductivity than copper, which would reduce voltage losses along the busbar. Any by-product carbon monoxide formed during CO₂ reduction on the silver would also likely be utilized as a reactant on the copper layers. Finally, silver is a more stable electrode material than copper, likely providing greater longevity. For these reasons future work should consider silver as a busbar material.

The demonstrations in this work were on a 2.25 cm by 2.25 cm (5 cm²) electrode. To examine the prospect of using the ePTFE and copper busbar approach for larger electrodes, we assessed the busbar dimensions required for a 20 cm by 20 cm (400 cm²) electrode to maintain an identical voltage drop from the exterior current collector to the center of the electrode. These calculations are shown in the Supplementary Notes and in Supplementary Fig. 4.A.21 which indicate the NICC approach is feasible for larger electrodes with a busbar spacing of 20 mm, a busbar height of 100 μ m, and a busbar width of 3 mm. These busbar dimensions could further be reduced using cross-hatched patterns or reduced busbar spacings.

In conclusion, we have shown spatial and temporal implications of current collection on the performance of thin catalyst layers for CO₂RR. Particularly in the case of non-conducting ePTFE gas-diffusion layers, targeted efforts are needed to provide current collection pathways across the entire catalyst layer, due to the conductivity limitation of <500 nm thick catalyst layers. By illustrating the spatial degradation of a 50 nm copper catalyst layer using infrared thermography, we built a better understanding of the effects of catalyst migration on spatial temperatures, current densities, and reactant availability. Further, by adding a non-invasive current collector to the 50 nm Cu-catalyst layer, we showed that the electrode's performance can approach and exceed 50 nm and 500 nm conventional films. This opens the pathway to further advancement of thin-layer catalysts on ultra-hydrophobic GDEs for CO₂-electrolysis.

Especially for ePTFE electrodes, which hold a potentially important role in advancing CO₂RR, current collection has long been an under-studied subject, mainly because of unobserved limitations in lab-scale electrolyzers. Without addressing issues surrounding current collection on ePTFE supports, these gas-diffusion layers are unlikely to be industrially applicable. Beyond this work, greater considerations about current collection in catholyte flow field channels, and how to connect ePTFE electrodes in stacked configurations are critical. This work begins these discussions, hopefully opening the door to future work.

4.4 Methods

Cathode fabrication Copper metallic layers were deposited directly on the ePTFE (Sterlitech® Aspire QL822, 0.45 μ m) or carbon-based GDLs (Sigracet® 38BB)

by DC magnetron sputtering at a pressure of 3 μ bar. By regulating the power applied and the time of exposure, we were able to regulate the thickness of the catalytic layer. After deposition, the electrodes were stored in a glovebox (<0.1 ppm O₂ and <0.1 ppm H₂O) and only taken out before assembly of the electrolyzer cell. NICCs were sputtered using a slit-mask with 0.3 mm wide, 1 μ m thick Cu slits along the entire width of the pre-sputtered 50 nm ePTFE GDE.

Flow-cell design We employed a proprietary flow-cell design that is based around a commercially available titanium anode block (Dioxide Materials®, 5 cm² Titanium Anode Block). Around this anode block, we designed and printed a catholyte flow-chamber with a reference electrode port (ϕ = 1.75 mm) and a similar gas-chamber, with matching gaskets as sealants (see Figs. 4.A.5 and 4.A.6). Current collectors for ePTFE cathodes were copper-tape based, precision-plotted using a Cricut® Maker 3. The assembly was completed with a gas/electrolyte end-block with an incorporated infrared window, and a metallic pressing plate. Experiments were performed using untreated nickel (Ni) foam as the anode, and Sustainion® X37-50 anionic exchange membranes (AEMs). Electrolyte was flown pumping the electrolyte and sucking the anolyte, as to generate a pressure delta across the membrane. This avoided expansion of the membrane in the catholyte compartment and accumulation of O₂-bubbles in the anolyte compartment.

IR-thermography setup Thermal images of the backbone of the electrode were acquired using a FLIR SC7650 camera system, using the windowed electrolyzer. The camera was equipped with a fixed focal length of 25 mm and acquired images at a frame-rate of 1 fps with a total resolution of 640 by 512 pixels, operated by commercial ALTAIR® software. The total scanned area of the electrode was 5 cm² (\pm 2.25 by 2.25 cm square), with an Edmund Optics® uncoated sapphire window (δ = 1 mm, ϕ = 32 mm). Temperature values acquired with the camera were corrected by the compound transmittance of the sapphire window and the emissivity of the polypropylene backing of the ePTFE electrodes. Measurements were performed under a light-shielding blanket to avoid contamination of signals with external reflections on the camera lens.

Electrochemical setup Electrochemical routines were applied using either a Princeton Applied Research® Parstat 4000 (\pm 48 V, 20 A) or MC-1000 (\pm 12 V, 2 A) in a three-electrode configuration. Gas-flow to the electrolyzer was controlled by a Bronkhorst® mass-flow controller. Electrolyte was pumped using two separate peristaltic pumps and two sets of pressure dampeners, to alleviate the cyclic pressure spikes of the peristaltic motion. All three fluid channels were regulated through a back-pressure regulator (BPR), which controlled pressure for each stream

independently, and measured live mass flow-rate for the gaseous product stream. This stream was circulated through a liquid trap and a proprietary liquid detector to avoid liquid injections to the in-line gas-chromatographer (GC, Global Analyser Solutions® CompactGC 4.0). Before reaching this GC, a valve regulated pressure spikes to avoid disruption of the back-pressure after each injection. Liquid product samples were collected periodically in duplicate from the catholyte beaker using a needle and were stored in air-tight vials at 5 °C to avoid evaporation of volatile species. These samples were then analyzed in batch using an Agilent Technologies® 1260 Infinity II HPLC.

Polarization curves were applied by a galvanodynamic swing from 0 to -300 mA cm⁻² at a rate of -1 mA cm⁻² s⁻¹. Product distribution studies were acquired either at increasing fixed current densities or at fixed working electrode potential (without i-R feedback correction). Capacitance measurements were performed on all three different architectures by cycling the electrodes from -0.3 to +0.3 V vs. Ag/AgCl, collecting the average charging current over a non-Nernstian region for the anodic swing at increasing scan-rates (5, 10, 15, 20 and 25 mV s⁻¹). The value for capacitance was extracted as the slope of the linearization of charging current over scan-rate.

Characterization Pristine and post-operation samples of both carbon and ePTFE GDE's were stored in a glovebox before characterization. Scanning electron microscopy (SEM) was performed on a JOEL JSM-7001F and FEI Nova NanoSEM 450 instruments. To improve image quality, the surfaces of GDE were cleaned using an Evactron 25 De-Contaminator RF Plasma Cleaning System, and the ePTFE GDEs were coated with a Pt film (5nm) using a Quorum Q150T Metal Coater. One more plasma cleaning was conducted after the coating process. In addition to this, a fresh cross-section of GDE was obtained by breaking the sample in liquid nitrogen before the general sample preparation.

XPS spectra were collected using a Thermo Scientific® K-alpha spectrometer using an Al K α monochromator. For all measurements (F1s, C1s, Cu LLM, Cu2p and valence-band scans) the spot size was 400 μ m, the pass energy 50 eV and the step-size 0.10 eV, while the base pressure of the analysis chamber was 2·10⁻⁹ mbar. Resulting scans were averaged after 10 measurements (valence bands required the averaging of 50 scans).

References

- [1] Hugo-Pieter Iglesias van Montfort, Mengran Li, Erdem Irtem, Maryam Ab-dinejad, Yuming Wu, Santosh K. Pal, Mark Sassenburg, Davide Ripepi, Sid-dhartha Subramanian, Jasper Biemolt, Thomas E. Rufford, and Thomas Bur-dyny. Non-invasive current collectors for improved current-density distribu-tion during CO₂ electrolysis on super-hydrophobic electrodes. *Nature Com-munications*, 14(1):6579, October 2023.
- [2] Thomas Burdyny and Wilson A Smith. CO₂ reduction on gas-diffusion elec-trodes and why catalytic performance must be assessed at commercially-relevant conditions. *Energy and Environmental Science*, 2019.
- [3] Wilson A Smith, Thomas Burdyny, David A Vermaas, and Hans Geerlings. Pathways to Industrial-Scale Fuel Out of Thin Air from CO₂ Electrolysis. *Joule*, 2019.
- [4] Eric W. Lees, Benjamin A. W. Mowbray, Fraser G. L. Parlane, and Curtis P. Berlinguette. Gas diffusion electrodes and membranes for CO₂ reduction electrolyzers. *Nature Reviews Materials*, 7(1):55–64, January 2022.
- [5] David Wakerley, Sarah Lamaison, Joshua Wicks, Auston Clemens, Jeremy Feaster, Daniel Corral, Shaffiq A. Jaffer, Amitava Sarkar, Marc Fontecave, Eric B. Duoss, Sarah Baker, Edward H. Sargent, Thomas F. Jaramillo, and Christopher Hahn. Gas diffusion electrodes, reactor designs and key metrics of low-temperature CO₂ electrolyzers. *Nature Energy*, 7(2):130–143, February 2022.
- [6] Joshua A. Rabinowitz and Matthew W. Kanan. The future of low-temperature carbon dioxide electrolysis depends on solving one basic problem. *Nature Communications*, 11(1):1–3, December 2020. Publisher: Nature Research.
- [7] Yi Xu, Jonathan P. Edwards, Shijie Liu, Rui Kai Miao, Jianan Erick Huang, Christine M. Gabardo, Colin P. O'Brien, Jun Li, Edward H. Sargent, and David Sinton. Self-Cleaning CO₂ Reduction Systems: Unsteady Electrochemical Forcing Enables Stability. *ACS Energy Letters*, 6(2):809–815, February 2021.
- [8] Fabian Bienen, Melanie C. Paulisch, Thorben Mager, Jens Osiewacz, Manigah Nazari, Markus Osenberg, Barbara Ellendorff, Thomas Turek, Ulrich Nieken, Ingo Manke, and K. Andreas Friedrich. Investigating the electrowetting of silver-based gas-diffusion electrodes during oxygen reduction reaction with electrochemical and optical methods. *Electrochemical Science Advances*, 3(1), February 2023.

- [9] Anna M. Kalde, Maren Grosseheide, Sebastian Brosch, Sharon V. Pape, Robert G. Keller, John Linkhorst, and Matthias Wessling. Micromodel of a Gas Diffusion Electrode Tracks In-Operando Pore-Scale Wetting Phenomena. *Small*, n/a(n/a):2204012, 2022. _eprint: <https://onlinelibrary.wiley.com/doi/pdf/10.1002/smll.202204012>.
- [10] Kailun Yang, Recep Kas, Wilson A. Smith, and Thomas Burdyny. Role of the Carbon-Based Gas Diffusion Layer on Flooding in a Gas Diffusion Electrode Cell for Electrochemical CO₂ Reduction. *ACS Energy Letters*, 6(1):33–40, January 2021.
- [11] Uzoma O. Nwabara, Emiliana R. Cofell, Sumit Verma, Emanuela Negro, and Paul J. A. Kenis. Durable Cathodes and Electrolyzers for the Efficient Aqueous Electrochemical Reduction of CO₂. *ChemSusChem*, 13(5):855–875, March 2020.
- [12] J.W. Blake, J.T. Padding, and J.W. Haverkort. Analytical modelling of CO₂ reduction in gas-diffusion electrode catalyst layers. *Electrochimica Acta*, 393:138987, October 2021.
- [13] Cao Thang Dinh, Thomas Burdyny, Golam Kibria, Ali Seifitokaldani, Christine M Gabardo, F Pelayo García De Arquer, Amirreza Kiani, Jonathan P Edwards, Phil De Luna, Oleksandr S Bushuyev, Chengqin Zou, Rafael Quintero-Bermudez, Yuanjie Pang, David Sinton, and Edward H Sargent. CO₂ electroreduction to ethylene via hydroxide-mediated copper catalysis at an abrupt interface. *Science*, 360:783–787, 2018.
- [14] Klaudia Wagner, Prerna Tiwari, Gerhard F. Swiegers, and Gordon G. Wallace. Alkaline Fuel Cells with Novel Gortex-Based Electrodes are Powered Remarkably Efficiently by Methane Containing 5% Hydrogen. *Advanced Energy Materials*, 8(7):1702285, March 2018.
- [15] Klaudia Wagner, Prerna Tiwari, Gerhard F. Swiegers, and Gordon G. Wallace. An electrochemical cell with Gortex-based electrodes capable of extracting pure hydrogen from highly dilute hydrogen–methane mixtures. *Energy & Environmental Science*, 11(1):172–184, 2018.
- [16] Joshua Wicks, Melinda L. Jue, Victor A. Beck, James S. Oakdale, Nikola A. Dudukovic, Auston L. Clemens, Siwei Liang, Megan E. Ellis, Geonhui Lee, Sarah E. Baker, Eric B. Duoss, and Edward H. Sargent. 3D-Printable Fluoropolymer Gas Diffusion Layers for CO₂ Electroreduction. *Advanced Materials*, 33(7):2003855, February 2021.

- [17] Lorenz M. Baumgartner, Christel I. Koopman, Antoni Forner-Cuenca, and David A. Vermaas. Narrow Pressure Stability Window of Gas Diffusion Electrodes Limits the Scale-Up of CO₂ Electrolyzers. *ACS Sustainable Chemistry & Engineering*, 10(14):4683–4693, April 2022.
- [18] McLain E. Leonard, Lauren E. Clarke, Antoni Forner-Cuenca, Steven M. Brown, and Fikile R. Brushett. Investigating Electrode Flooding in a Flowing Electrolyte, Gas-Fed Carbon Dioxide Electrolyzer. *ChemSusChem*, 13(2):400–411, January 2020.
- [19] F Pelayo García de Arquer, Cao Thang Dinh, Adnan Ozden, Joshua Wicks, Christopher McCallum, Ahmad R Kirmani, Dae Hyun Nam, Christine Gabardo, Ali Seifitokaldani, Xue Wang, Yuguang C Li, Fengwang Li, Jonathan Edwards, Lee J Richter, Steven J Thorpe, David Sinton, and Edward H Sargent. CO₂ electrolysis to multicarbon products at activities greater than 1 A cm⁻². *Science*, 367:661–666, 2020.
- [20] Angelika Anita Samu, Imre Szenti, Ákos Kukovecz, Balázs Endrődi, and Csaba Janáky. Systematic screening of gas diffusion layers for high performance CO₂ electrolysis. *Communications Chemistry*, 6(1):41, February 2023.
- [21] Ruud Kortlever, Jing Shen, Klaas Jan P. Schouten, Federico Calle-Vallejo, and Marc T. M. Koper. Catalysts and Reaction Pathways for the Electrochemical Reduction of Carbon Dioxide. *The Journal of Physical Chemistry Letters*, 6(20):4073–4082, October 2015.
- [22] Ming Ma, Kristina Djanashvili, and Wilson A. Smith. Controllable Hydrocarbon Formation from the Electrochemical Reduction of CO₂ over Cu Nanowire Arrays. *Angewandte Chemie International Edition*, 55(23):6680–6684, June 2016.
- [23] Mariana C. O. Monteiro, Stefan Dieckhöfer, Tim Bobrowski, Thomas Quast, Davide Pavesi, Marc T. M. Koper, and Wolfgang Schuhmann. Probing the local activity of CO₂ reduction on gold gas diffusion electrodes: effect of the catalyst loading and CO₂ pressure. *Chemical Science*, 12(47):15682–15690, 2021.
- [24] Carlos G. Morales-Guio, Etosha R. Cave, Stephanie A. Nitopi, Jeremy T. Feaster, Lei Wang, Kendra P. Kuhl, Ariel Jackson, Natalie C. Johnson, David N. Abram, Toru Hatsukade, Christopher Hahn, and Thomas F. Jaramillo. Improved CO₂ reduction activity towards C₂₊ alcohols on a tandem gold on copper electrocatalyst. *Nature Catalysis*, 1(10):764–771, October 2018.

- [25] Hugo-Pieter Iglesias van Montfort and Thomas Burdyny. Mapping Spatial and Temporal Electrochemical Activity of Water and CO₂ Electrolysis on Gas-Diffusion Electrodes Using Infrared Thermography. *ACS Energy Letters*, 7(8):2410–2419, August 2022. Publisher: American Chemical Society.
- [26] Nicholas Schwartz, Jason Harrington, Kirk J. Ziegler, and Philip Cox. Effects of Electrode Support Structure on Electrode Microstructure, Transport Properties, and Gas Diffusion within the Gas Diffusion Layer. *ACS Omega*, 7(34):29832–29839, August 2022.
- [27] Mohammad Zhiani, Saeedeh Kamali, and Somayeh Majidi. In-plane gas permeability and thought-plane resistivity of the gas diffusion layer influenced by homogenization technique and its effect on the proton exchange membrane fuel cell cathode performance. *International Journal of Hydrogen Energy*, 41(2):1112–1119, January 2016.
- [28] K. Mech, R. Kowalik, and P. Żabiński. Cu Thin Films Deposited by DC Magnetron Sputtering for Contact Surfaces on Electronic Components. *Archives of Metallurgy and Materials*, 56(4), January 2011.
- [29] Ernst Schmiedl, Peter Wissmann, and Hans-Ulrich Finzel. The Electrical Resistivity of Ultra-Thin Copper Films. *Zeitschrift für Naturforschung A*, 63(10-11):739–744, November 2008.
- [30] Dilan Karapinar, Charles E. Creissen, José Guillermo Rivera de la Cruz, Moritz W. Schreiber, and Marc Fontecave. Electrochemical CO₂ Reduction to Ethanol with Copper-Based Catalysts. *ACS Energy Letters*, 6(2):694–706, February 2021.
- [31] Yao Zheng, Anthony Vasileff, Xianlong Zhou, Yan Jiao, Mietek Jaroniec, and Shi-Zhang Qiao. Understanding the Roadmap for Electrochemical Reduction of CO₂ to Multi-Carbon Oxygenates and Hydrocarbons on Copper-Based Catalysts. *Journal of the American Chemical Society*, 141(19):7646–7659, May 2019.
- [32] Yifan Li and Peidong Yang. Co-feeding copper catalysts couple carbon. *Nature Nanotechnology*, 14(11):1002–1003, November 2019.
- [33] Xingli Wang, Jorge Ferreira de Araújo, Wen Ju, Alexander Bagger, Henrike Schmies, Stefanie Kühl, Jan Rossmeis, and Peter Strasser. Mechanistic reaction pathways of enhanced ethylene yields during electroreduction of CO₂–CO co-feeds on Cu and Cu-tandem electrocatalysts. *Nature Nanotechnology*, 14(11):1063–1070, November 2019.

- [34] Dan Ren, Jinhuan Fong, and Boon Siang Yeo. The effects of currents and potentials on the selectivities of copper toward carbon dioxide electroreduction. *Nature Communications*, 9(1):925, December 2018.
- [35] Haochen Zhang, Xiaoxia Chang, Jingguang G. Chen, William A. Goddard, Bingjun Xu, Mu-Jeng Cheng, and Qi Lu. Computational and experimental demonstrations of one-pot tandem catalysis for electrochemical carbon dioxide reduction to methane. *Nature Communications*, 10(1):3340, December 2019.
- [36] Antonio J. Martín, Sharon Mitchell, Cecilia Mondelli, Shibashish Jaydev, and Javier Pérez-Ramírez. Unifying views on catalyst deactivation. *Nature Catalysis*, 5(10):854–866, September 2022.
- [37] Stefan Popović, Milutin Smiljanić, Primož Jovanovič, Jan Vavra, Raffaella Buonsanti, and Nejc Hodnik. Stability and Degradation Mechanisms of Copper-Based Catalysts for Electrochemical CO₂ Reduction. *Angewandte Chemie*, 132(35):14844–14854, August 2020.
- [38] Philipp Grosse, Aram Yoon, Clara Rettenmaier, Antonia Herzog, See Wee Chee, and Beatriz Roldan Cuenya. Dynamic transformation of cubic copper catalysts during CO₂ electroreduction and its impact on catalytic selectivity. *Nature Communications*, 12(1):6736, November 2021.
- [39] Nejc Hodnik, Gerhard Dehm, and Karl J. J. Mayrhofer. Importance and Challenges of Electrochemical *in Situ* Liquid Cell Electron Microscopy for Energy Conversion Research. *Accounts of Chemical Research*, 49(9):2015–2022, September 2016.
- [40] Dohyung Kim, Christopher S. Kley, Yifan Li, and Peidong Yang. Copper nanoparticle ensembles for selective electroreduction of CO₂ to C₂–C₃ products. *Proceedings of the National Academy of Sciences*, 114(40):10560–10565, October 2017.
- [41] Jianfeng Huang, Nicolas Hörmann, Emad Oveisi, Anna Loiudice, Gian Luca De Gregorio, Oliviero Andreussi, Nicola Marzari, and Raffaella Buonsanti. Potential-induced nanoclustering of metallic catalysts during electrochemical CO₂ reduction. *Nature Communications*, 9(1):3117, December 2018.
- [42] Stefan J. Raaijman, Nakkiran Arulmozhi, and Marc T. M. Koper. Morphological Stability of Copper Surfaces under Reducing Conditions. *ACS Applied Materials & Interfaces*, 13(41):48730–48744, October 2021.

- [43] B Beverskog and I Puigdomenech. Revised Pourbaix Diagrams for Copper at 25 to 300 °C. *Journal of The Electrochemical Society*, 144(10):3476–3483, 1997.
- [44] Yannick Cudennec and André Lecerf. The transformation of Cu(OH)₂ into CuO, revisited. *Solid State Sciences*, 5(11-12):1471–1474, November 2003.
- [45] Jonas Deuermeier, Jürgen Gassmann, and Joachim Brötz. Reactive magnetron sputtering of Cu₂O: Dependence on oxygen pressure and interface formation with indium tin oxide. *J. Appl. Phys.*, 2011.
- [46] R. P. Vasquez. Cu(OH)₂ by XPS. *Surface Science Spectra*, 5(4):267–272, October 1998.
- [47] S. Poulston, P. M. Parlett, P. Stone, and M. Bowker. Surface Oxidation and Reduction of CuO and Cu₂O Studied Using XPS and XAES. *Surface and Interface Analysis*, 24(12):811–820, November 1996.
- [48] Thomas J. P. Hersbach, Alexei I. Yanson, and Marc T. M. Koper. Anisotropic etching of platinum electrodes at the onset of cathodic corrosion. *Nature Communications*, 7(1):12653, August 2016.
- [49] Alexei I. Yanson, Paramaconi Rodriguez, Nuria Garcia-Araez, Rik V. Mom, Frans D. Tichelaar, and Marc T. M. Koper. Cathodic Corrosion: A Quick, Clean, and Versatile Method for the Synthesis of Metallic Nanoparticles. *Angewandte Chemie International Edition*, 50(28):6346–6350, July 2011.
- [50] Reihaneh Amirbeigi, Jing Tian, Antonia Herzog, Canrong Qiu, Arno Bergmann, Beatriz Roldan Cuenya, and Olaf M. Magnussen. Atomic-scale surface restructuring of copper electrodes under CO₂ electroreduction conditions. *Nature Catalysis*, August 2023.
- [51] Mark Sassenburg, Reinier de Rooij, Nathan T. Nesbitt, Recep Kas, Sanjana Chandrashekar, Nienke J. Firet, Kailun Yang, Kai Liu, Marijn A. Blommaert, Martin Kolen, Davide Ripepi, Wilson A. Smith, and Thomas Burdyny. Characterizing CO₂ Reduction Catalysts on Gas Diffusion Electrodes: Comparing Activity, Selectivity, and Stability of Transition Metal Catalysts. *ACS Applied Energy Materials*, 5(5):5983–5994, May 2022. Publisher: American Chemical Society.
- [52] Mark Sassenburg, Maria Kelly, Siddhartha Subramanian, Wilson A. Smith, and Thomas Burdyny. Zero-Gap Electrochemical CO₂ Reduction Cells: Challenges and Operational Strategies for Prevention of Salt Precipitation. *ACS Energy Letters*, pages 321–331, December 2022. Publisher: American Chemical Society.

- [53] Siddhartha Subramanian, Kailun Yang, Mengran Li, Mark Sassenburg, Maryam Abdinejad, Erdem Irtem, Joost Middelkoop, and Thomas Burdyny. Geometric Catalyst Utilization in Zero-Gap CO₂ Electrolyzers. *ACS Energy Letters*, pages 222–229, November 2022. Publisher: American Chemical Society.
- [54] Kai Liu, Wilson A Smith, and Thomas Burdyny. Introductory Guide to Assembling and Operating Gas Diffusion Electrodes for Electrochemical CO₂ Reduction. *ACS Energy Letters*, 2019.
- [55] Christine M. Gabardo, Colin P. O'Brien, Jonathan P. Edwards, Christopher McCallum, Yi Xu, Cao-Thang Dinh, Jun Li, Edward H. Sargent, and David Sinton. Continuous Carbon Dioxide Electroreduction to Concentrated Multi-carbon Products Using a Membrane Electrode Assembly. *Joule*, 3(11):2777–2791, November 2019.
- [56] Xue Wang, Ziyun Wang, F. Pelayo García De Arquer, Cao-Thang Dinh, Adnan Ozden, Yuguang C. Li, Dae-Hyun Nam, Jun Li, Yi-Sheng Liu, Joshua Wicks, Zitao Chen, Miaofang Chi, Bin Chen, Ying Wang, Jason Tam, Jane Y. Howe, Andrew Proppe, Petar Todorović, Fengwang Li, Tao-Tao Zhuang, Christine M. Gabardo, Ahmad R. Kirmani, Christopher McCallum, Sung-Fu Hung, Yanwei Lum, Mingchuan Luo, Yimeng Min, Aoni Xu, Colin P. O'Brien, Bello Stephen, Bin Sun, Alexander H. Ip, Lee J. Richter, Shana O. Kelley, David Sinton, and Edward H. Sargent. Efficient electrically powered CO₂-to-ethanol via suppression of deoxygenation. *Nature Energy*, 5(6):478–486, May 2020.
- [57] Daniel L. Meier, Vinodh Chandrasekaran, Atul Gupta, Vijay Yelundur, and Ajeet Rohatgi. Silver Contact Grid: Inferred Contact Resistivity and Cost Minimization in 19% Silicon Solar Cells. *IEEE Journal of Photovoltaics*, 3(1):199–205, January 2013.
- [58] T. Panda, S. Sadhukhan, S. Acharyya, P Banerjee, A. Nandi, S. Bose, N. Mondal, G. Das, S. Maity, P. Chaudhuri, and H. Saha. Impact of multi-busbar front grid patterns on the performance of industrial type c-Si solar cell. *Solar Energy*, 236:790–801, April 2022.
- [59] G. A. Kolyagin and V. L. Kornienko. Double layer capacitance of gas-diffusion electrodes made of acetylene black and expanded natural graphites and evaluation of the surface area wetted by the electrolyte. *Russian Journal of Applied Chemistry*, 80(8):1341–1345, August 2007.

- [60] Adam Z. Weber. Improved modeling and understanding of diffusion-media wettability on polymer-electrolyte-fuel-cell performance. *Journal of Power Sources*, 195(16):5292–5304, August 2010.
- [61] Joey Disch, Luca Bohn, Susanne Koch, Michael Schulz, Yiyong Han, Alessandro Tengattini, Lukas Helfen, Matthias Breitwieser, and Severin Vierrath. High-resolution neutron imaging of salt precipitation and water transport in zero-gap CO₂ electrolysis. *Nature Communications*, 13(1):6099, October 2022.
- [62] Sahil Garg, Qiucheng Xu, Asger B. Moss, Marta Mirolo, Wanyu Deng, Ib Chorkendorff, Jakub Drnec, and Brian Seger. How alkali cations affect salt precipitation and CO₂ electrolysis performance in membrane electrode assembly electrolyzers. *Energy & Environmental Science*, 16(4):1631–1643, 2023.
- [63] Asger B. Moss, Sahil Garg, Marta Mirolo, Carlos A. Giron Rodriguez, Roosa Ilvonen, Ib Chorkendorff, Jakub Drnec, and Brian Seger. In operando investigations of oscillatory water and carbonate effects in MEA-based CO₂ electrolysis devices. *Joule*, 7(2):350–365, February 2023.
- [64] B. Endrődi, A. Samu, E. Kecsenvity, T. Halmágyi, D. Sebők, and C. Janáky. Operando cathode activation with alkali metal cations for high current density operation of water-fed zero-gap carbon dioxide electrolyzers. *Nature Energy*, 6(4):439–448, April 2021.
- [65] Jonathan E. Guyer, Daniel Wheeler, and James A. Warren. FiPy: Partial Differential Equations with Python. *Computing in Science & Engineering*, 11(3):6–15, May 2009.
- [66] Prerna Tiwari, George Tsekouras, Gerhard F. Swiegers, and Gordon G. Wallace. Gortex-Based Gas Diffusion Electrodes with Unprecedented Resistance to Flooding and Leaking. *ACS Applied Materials & Interfaces*, 10(33):28176–28186, August 2018.
- [67] S. Weisenberger and A. Schumpe. Estimation of gas solubilities in salt solutions at temperatures from 273 K to 363 K. *AIChE Journal*, 42(1):298–300, January 1996.
- [68] Denis A. Wiesenburg and Norman L Guinasso. Equilibrium solubilities of methane, carbon monoxide, and hydrogen in water and sea water. *Journal of Chemical & Engineering Data*, 24(4):356–360, October 1979.
- [69] William M Deen. Analysis of transport phenomena. 1998. Publisher: Oxford University Press New York.

APPENDIX

Supplementary Notes

Reaction-diffusion in a Finite Volume Partial-Differential Equation Solver

In wanting to calculate and represent the effect of the GDE architecture on local availability of [CO₂ in the catalyst layer, we constructed a 1-D reaction-diffusion model close to the gas-liquid interface of both ePTFE and carbon-based electrodes. To define and execute the solver, we used the FiPy solver package, in a Python environment.[65]

This model is focused on the catalytic interface in a porous GDE and is defined by three domains: (i) the micro-porous layer (MPL), (ii) the catalyst layer and (iii) the electrolyte, simulating the behavior of CO₂ in an alkaline flow-electrolyzer. The domain of the model is 500 μm thick, the nodal distance of the mesh is 1 nm. For these regions, (i) can be modelled as a flooded (i.e. liquid-phase) domain or a gaseous one, whereas (ii) and (iii) are considered to be wetted throughout. The MPL is assumed to be 20 μm thick for the ePTFE simulation and 40 μm in the case of a carbon GDL.[20, 66] The catalyst layer is 500 nm thick in both cases and the rest of the modelled domain is liquid-phase electrolyte as used in the experiments (1M KOH).

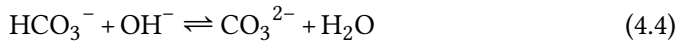
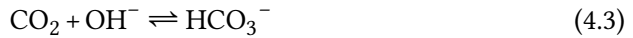
In the gaseous phase (i), gas-species (CO₂, CO and H₂) are governed by simple diffusion equations, in the form of:

$$\frac{\partial c_i}{\partial t} = D_i \frac{\partial^2 c_i}{\partial x^2} \quad (4.1)$$

With a convective transport boundary on the left boundary of the system and a phase-change (gas to liquid) on the right boundary. In the catalyst layer, dissolved species (CO_{2(aq)}, OH⁻, HCO₃⁻, CO₃²⁻ and H⁺) are governed by:

$$\frac{\partial c_i}{\partial t} = D_i \frac{\partial^2 c_i}{\partial x^2} + R_h + R_i \quad (4.2)$$

where R_h are the homogeneous CO₂-buffering reactions:



and R_i are the electrochemical production and consumption rates of CO₂, OH⁻, CO and H₂:

$$R_{\text{CO}_2} = -\frac{j_t}{F} \left(\frac{s_{\text{CO}}}{z_{\text{CO}}} \right) \frac{\varepsilon_{\text{cat}}}{L_{\text{cat}}} \quad (4.5)$$

$$R_{\text{CO}} = \frac{j_t}{F} \left(\frac{s_{\text{CO}}}{z_{\text{CO}}} \right) \frac{\varepsilon_{\text{cat}}}{L_{\text{cat}}} \quad (4.6)$$

$$R_{\text{OH}^-} = \frac{j_t}{F} \frac{\varepsilon_{\text{cat}}}{L_{\text{cat}}} \quad (4.7)$$

$$R_{\text{H}_2} = \frac{j_t}{F} \left(\frac{1 - s_{\text{CO}}}{z_{\text{H}_2}} \right) \frac{\varepsilon_{\text{cat}}}{L_{\text{cat}}} \quad (4.8)$$

where s_i are the selectivities (faradaic efficiencies) towards every product (assumed to be 80% CO and 20% H₂), ε_{cat} is the porosity of the catalyst layer, L_{cat} its length, F the Faraday constant, z_i the stoichiometric number of electrons involved in each reduction reaction, and j_t the total applied current (a scalar in the model). In the liquid phase of the model, (iii), only the homogeneous buffering reactions are involved.

A cornerstone of the modeled quantities lies in the amount of aqueous CO₂ at the gas-liquid interface. Solubility of CO₂ is heavily influenced by the presence of ions in the liquid phase.[67] In order to set the calculated CO_{2(aq)} at this interface, the Hessian of the model is disturbed at the nodes before and after the phase-change using a mask involving a large number (2⁶³). The CO_{2(aq)} concentration is set using the Séchenov constants on the classical Henry model of carbon dioxide dissolution.[13, 19] First, the Henry equation for CO₂ as a function of temperature:[68]

$$[\text{CO}_{2(\text{aq})}] = P_{\text{CO}_2} \cdot K_H \cdot K_c \quad (4.9)$$

With:

$$\ln K_H = 93.4517 \left(\frac{100}{T} \right) - 60.2409 + 23.3585 \ln \left(\frac{T}{100} \right) \quad (4.10)$$

The Henry equilibrium is corrected for the presence of ions in the solution, following:[12]

$$\log \left(\frac{[\text{CO}_{2(\text{aq}),0}]}{[\text{CO}_{2(\text{aq})}]} \right) = K_c c_i \quad (4.11)$$

where $[\text{CO}_{2(\text{aq}),0}]$ is the solubility of CO₂ in pure water at a given temperature. The correction factor for each ion, K_c is calculated using:

$$K_c = \sum (h_i + h_g) \quad (4.12)$$

$$h_g = h_{g,0} + h_T (T - 298.15) \quad (4.13)$$

The constants used in this case for each ionic species are taken from earlier reports in literature. The concentration of K⁺ is calculated imposing electronic neutrality at the boundary each solving loop, bicarbonate anions are disregarded since their concentration is residual.

Table 4.A.1: Séchenov constants for involved ionic species.

Species	h_i
K ⁺	0.0922
OH ⁻	0.0839
CO ₃ ²⁻	0.1423

4

Table 4.A.2: Correction factors for CO₂ dilution and temperature effects.

Magnitude	Value
$h_{g,0}$	-0.0172
h_T	-0.00338

The value of [CO_{2,aq}] is updated every computational loop of the model assuming a partial pressure of 1.1 bar for CO₂, and is the basis of the boundary value of the plots in Fig. 4.1d and e.

Working principle of IR thermography on gas-diffusion electrodes for CO₂RR

While we have detailed the working principles of infrared thermography for electrochemical activity mapping in previous works,[25] the text below reproduces the rationale behind it in order to illustrate the design considerations for this case.

For infrared thermography to be a valid technique for this use case, we lay 3 main conditions that must be met in order to couple temperature measurements to local electrochemical activity. These are:

i. Heat production must be sufficient so that activity can be mapped at relevant current densities Power consumed by an electrochemical system is defined as:

$$P = I \cdot \Delta E \quad (4.14)$$

Applying Ohm's law, this translates to:

$$P = I^2 \cdot R \quad (4.15)$$

At an electrode, a part of this power will be destined to driving the reaction, whereas parts of it will be translated into heating of the system's surrounding. This heating, in electrolysis, is mainly due to either ohmic resistances or reaction overpotential. For the latter, the heat stream is proportional to the reaction overpotential, which in its turn is the difference between the required potential (E_{app}) and the thermo-neutral potential of the reaction in question ($E_{tn,0}$), by:

$$Q_{cat} = E_{app} - E_{tn,0} \cdot I \quad (4.16)$$

$$q''_{cat} = \frac{Q_{cat}}{A_{geo}} = (E_{app} - E_{tn,0}) \cdot j \quad (4.17)$$

If we take, for example, reduction of CO_2 to CO (simplified process of the reactions at a copper electrode, with $E_{tn,0} = 0.264$ V vs. RHE) and compare it to the operational, $i \cdot R$ corrected potential of the tested ePTFE electrodes at 50 mA cm^{-2} (around -0.65 V vs. RHE), the total heat generation will be:

$$q''_{cat,Cu} = (E_{app} - E_{tn,0}) \cdot j = (-0.65 - 0.264) \cdot (-0.05) = 0.046 \text{ W cm}^{-2} \quad (4.18)$$

At the same current density, the contribution to heating of the other main source, ohmic resistance, is calculated by considering the measured resistance between the GDE and the RE (in this case, 0.48Ω):

$$q''_{ohm} = I^2 \cdot R = (j \cdot A)^2 \cdot R = (-0.05 \cdot 5)^2 \cdot 0.48 = 0.030 \text{ W cm}^{-2} \quad (4.19)$$

which is lower than the heating resulting from the reaction overpotential, thus fulfilling requirement i.

ii. Heat generation must be translatable to temperature The heat produced, will not translate itself to observational temperature increases if the specific heat of the GDE's backbone is too high. The $C_{p,m}$ value for ePTFE is around $1500 \text{ J kg}^{-1} \text{ K}^{-1}$. Assuming an area weight for our electrodes similar to that of a thick sheet of paper (120 g m^{-2} , or $1.2 \cdot 10^{-5} \text{ kg cm}^{-2}$), we can calculate a theoretical heating rate by:

$$\frac{\Delta T}{t} = \frac{Q_{cat}}{m \cdot C_{p,m}} = \frac{q''_{cat}}{m'' \cdot C_{p,m}} = \frac{0.046}{(1.2 \cdot 10^{-5})(1500)} = 2.55 \text{ K s}^{-1} \quad (4.20)$$

which constitutes a heating rate even higher to the one we previously reported.⁹ This second requirement is thus also met.

iii. The temperature of the electrode's backbone is representative of the catalyst's temperature The final topic to assess the viability of this technique is the representativity of the backbone's temperature with respect to the catalyst's temperature. In case not enough heat is transported through the GDE to its open back side and is otherwise advectively removed by the flowing electrolyte, the measured temperature is not representative of the activity at a certain location. To compare the two heat streams (towards the backbone of the GDE and towards the electrolyte layer), we can devise a simplified 1-D heat conduction problem based on Fourier's law of heat conduction:

In evaluating the ratio between the heat fluxes, we can quantify how much heat 'travels' to the back of the GDE, that is filmed by the camera, and how much is lost to the advective effect of the electrolyte. For each heat flux, we approximate the value by:

$$q' = k \nabla T \approx k \frac{\Delta T}{\Delta x} \quad (4.21)$$

Applying this approximation to the problem described in the sketch above, we obtain:

$$Q_{gdl} = \frac{\Delta T}{R_{gdl}} = k_{gdl} \frac{\Delta T}{\Delta x} A = k_{gdl} \frac{(T_{cat} - T_{back,gdl})}{\delta_{gdl}} A \quad (4.22)$$

$$Q_{el} = \frac{\Delta T}{R_{el}} = k_{el} \frac{\Delta T}{\Delta x} A = k_{el} \frac{(T_{cat} - T_{el})}{\delta_{el}} A \quad (4.23)$$

$$\frac{Q_{gdl}}{Q_{el}} = \frac{q'_{gdl}}{q'_{el}} = \left| \frac{k_{gdl} (T_{cat} - T_{back,gdl})}{k_{el} (T_{cat} - T_{el})} \frac{\delta_{el}}{\delta_{gdl}} \right| \quad (4.24)$$

Where δ is the thickness of each phase, T_{cat} the temperature of the catalyst layer, and k the heat-transfer constant of each phase.

For the solid, GDE-phase, the thermal conductivity can be taken as that of ePTFE, which is around $0.29 \text{ W m}^{-1} \text{ K}^{-1}$. The thickness of the GDE is around $220 \mu\text{m}$ total. For the electrolyte, on the other hand, thermal conductivity is assumed, for simplicity, to be equal to that of water ($\sim 0.6 \text{ W m}^{-1} \text{ K}^{-1}$), while the thermal diffusivity length requires further evaluation. If we assume the Prandtl number of the electrolyte to be close to that of water (~ 7.5), we know that:[69]

$$\delta_{el} = 5.0 \sqrt{\frac{\nu x}{u_0}} Pr^{-1/3} \quad (4.25)$$

where ν represents the kinematic viscosity of water, x is the distance that the flow has travelled along the flat plate, and u_0 is the flow at the channel center.

For the system we discuss, typical flow rates of catholyte used where in the order of 5 sccm. For an electrolyte chamber of dimensions 22 x 22 x 3 mm, this results in an average fluid velocity (u_0) of 0.13 cm s^{-1} . After an average travel distance of 1.1 cm in the catholyte chamber, the thermal boundary between the GDE and the flowing catholyte is around $7400 \text{ } \mu\text{m}$. Filling then out equation S23, we obtain that, in equilibrium ($\Delta T = 1$), the ratio of heat fluxes is 16:1 in the direction of the GDE backbone, which confirms that this value of temperature is relevant and representative for the temperature of the catalyst layer.

For further and more intensive analysis of the rationale behind IR thermography for electrochemical activity mapping in electrolysis devices, we kindly refer the reader to our previous work, which includes an intensive analysis in its supporting information.[25]

The rationale for a non-invasive current collector (NICC)

Scaling an electrode design to industrially relevant dimensions poses a challenge, as evidenced by the activity distribution measurements reported in this work. The high ohmic resistance posed by a thin catalyst layer only becomes more dramatic considering the high amounts of current this layer would have to conduct for big electrode sizes. This section outlines the rationale of using a non-invasive current collector (NICC) for scaling purposes.

Let's assume we compare a 2 cm by 2 cm electrode with area 4 cm^2 (whose busbars are the same as our experimental 2.25 cm by 2.25 cm electrodes) with a 100-fold larger electrode. This would be a 20 cm x 20 cm electrode with an area of 400 cm^2 (see below Fig. 4.A.21). By maintaining the same scaling factors as in our prototype reported in this manuscript and using a 2 cm x 2 cm electrode as the base case, we can expect the 100-fold larger electrode to have a busbar spacing of 20 mm, a busbar height of $100 \text{ } \mu\text{m}$, and a busbar width of 3 mm. The scaling principle we propose here is to scale the busbar dimensions based on the area increase of 100-fold, not the side length dimension increase of 10-fold. The approximate cross-sectional area of the busbars is then 0.3 mm^2 . The current that travels through each busbar from the outside to the centre would then $I = (10 \text{ cm}) \times (2 \text{ cm}) \times (0.2 \text{ A cm}^{-2}) = 4 \text{ A}$ (for $j = 0.2 \text{ A cm}^{-2}$). Segmenting the 10 cm pathway into 20 parts (because current decreases along the length of the busbar), we can calculate the experienced voltage drop by the current to get to a certain point in the electrode using:

$$\Delta U_i = l \cdot I_i \cdot \frac{\rho}{A} \quad (4.26)$$

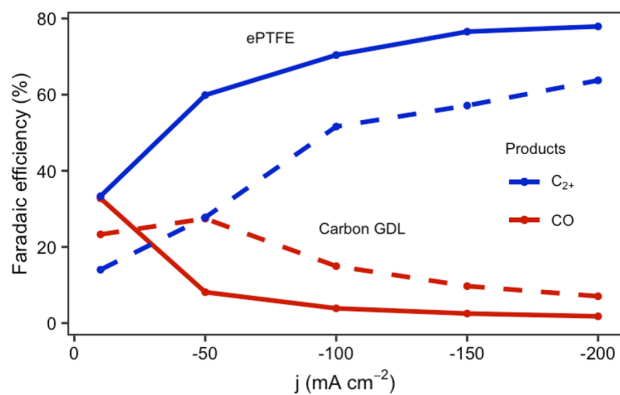
where l is the distance from the current collector, I the current passing through the segment, ρ the approximate resistivity of the copper busbar ($1.724 \cdot 10^{-6} \text{ } \Omega \text{ cm}$, see

Supplementary Table 4.A.3) and A the cross-sectional area of a busbar. The total voltage drop is then:

$$\Delta U_T = \sum \Delta U_i \quad (4.27)$$

As shown in Fig 4.A.21, the voltage drop from the exterior current collector to the center of the small and large electrodes can then be maintained as 80 mV with a reasonable busbar scaling. Reducing busbar spacing and cross-hatching are added ways to reduce voltage drop and/or the required busbar diameters further.

Supplementary Figures



4

Figure 4.A.1: Product distribution at increasing current densities for a 200 nm Cu catalyst layer on a carbon GDL (Sigracet® 38BB) and a 500 nm layer on an ePTFE electrode (Sterlitech® Aspire QL822).

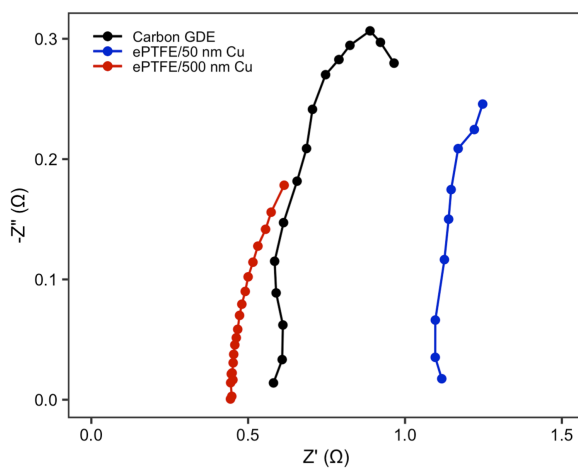


Figure 4.A.2: High-frequency segments of EIS measurements performed on the three compared electrodes, at a current density of -50 mA cm^{-2} and 1M KOH as the electrolyte.

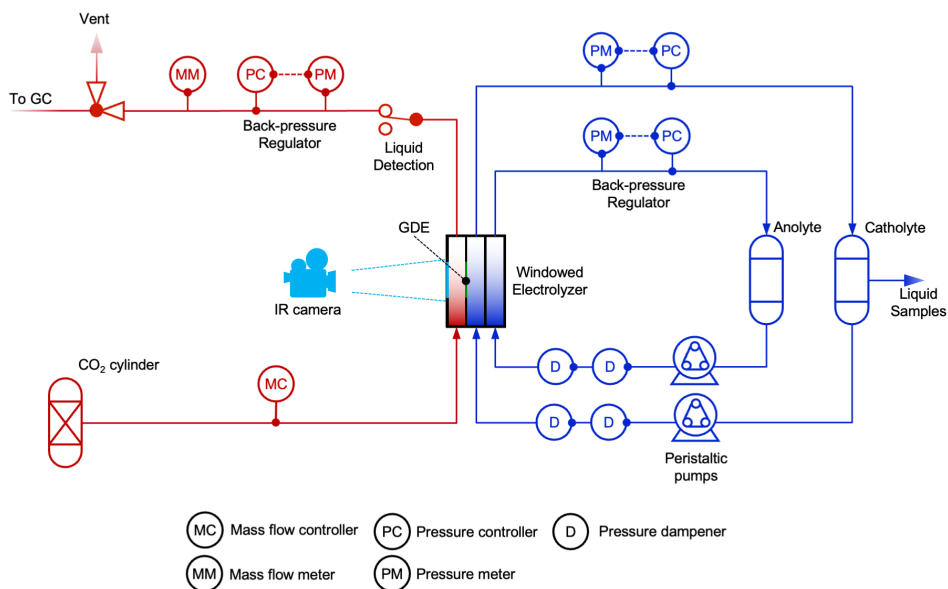


Figure 4.A.3: Process flow-diagram of the electrochemical testing setup used.

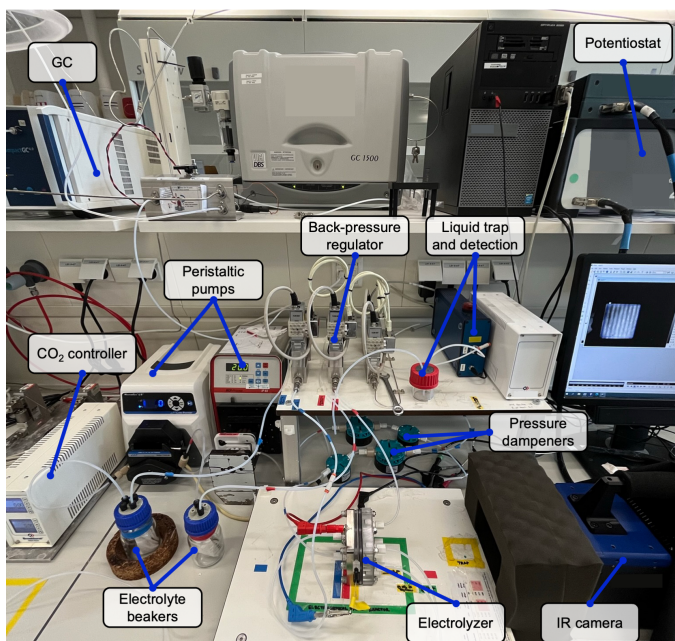


Figure 4.A.4: Picture of the electrochemical testing bench used.

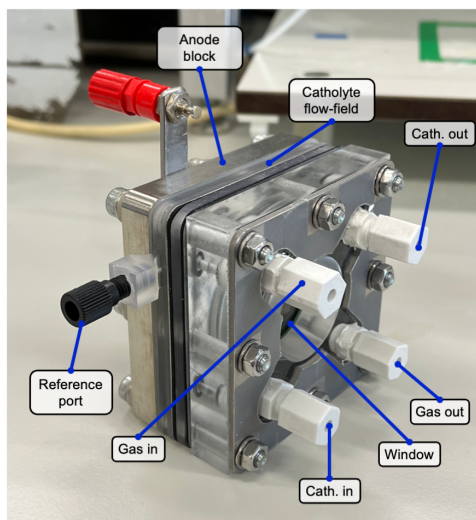


Figure 4.A.5: State-of-the-art windowed electrolyzer used in the electrochemical characterization of the different cathodes. The assembly consists of a titanium anode block (with integrated flow-field), a catholyte flow-field (3D-printed), a gas chamber (3D-printed) and a window end-block (milled, PMMA) with a stainless-steel pressing plate.

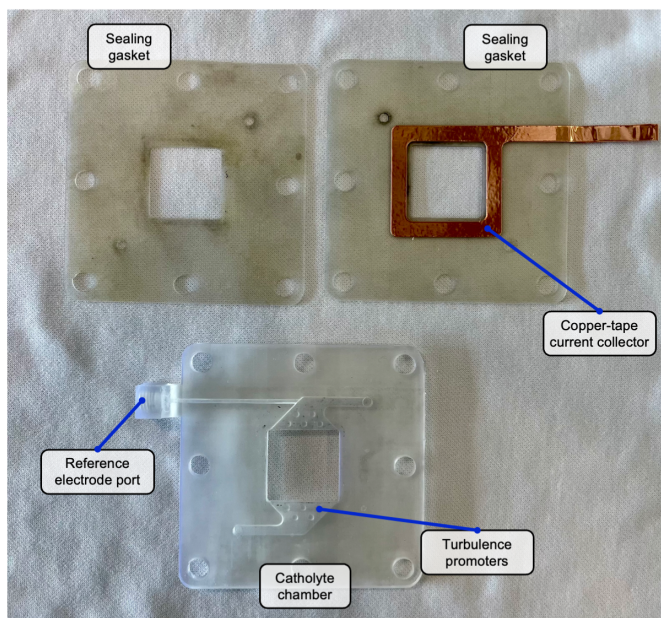


Figure 4.A.6: Assembly around the cathode, consisting of a 3D-printed catholyte chamber with reference-electrode port and turbulence promoters, a sealing gasket ($\delta = 500 \mu\text{m}$, silicone) with an edge-current collector (pressed to the silicone at 10 bar) and a sealing gasket ($\delta = 250 \mu\text{m}$, silicone).

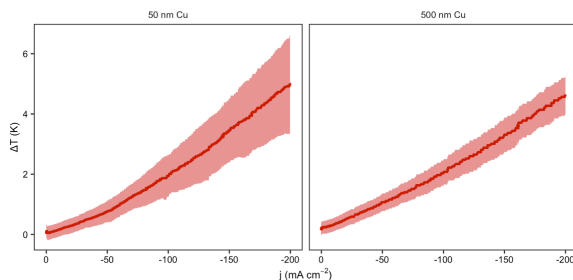


Figure 4.A.7: Average (bold) and standard-deviation (shaded) temperature increase on 50 nm and 500 nm Cu ePTFE electrodes under increasing cathodic polarization.

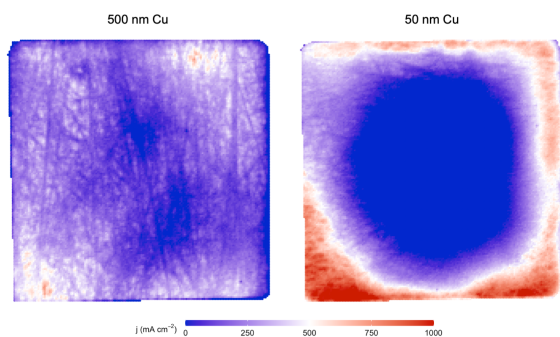


Figure 4.A.8: Corrected local current densities based on the relative temperature increase per pixel for a 50 nm and a 500 nm Cu ePTFE electrode at -200 mA cm^{-2} .

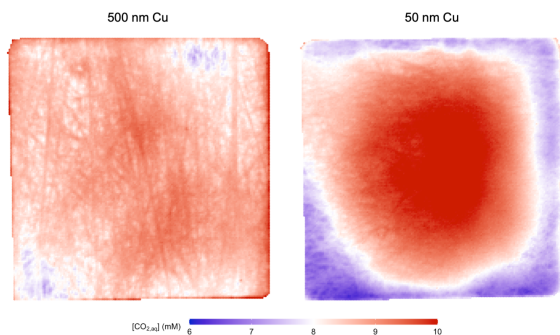


Figure 4.A.9: Corrected local concentration of dissolved CO₂ at the gas-liquid interface, based on the measured temperature per pixel for a 50 nm and a 500 nm Cu ePTFE electrode at an average j of -200 mA cm^{-2} . Salting-out effects were calculated using interpolated ion-concentrations resulting from the model described in the Supplementary Text.

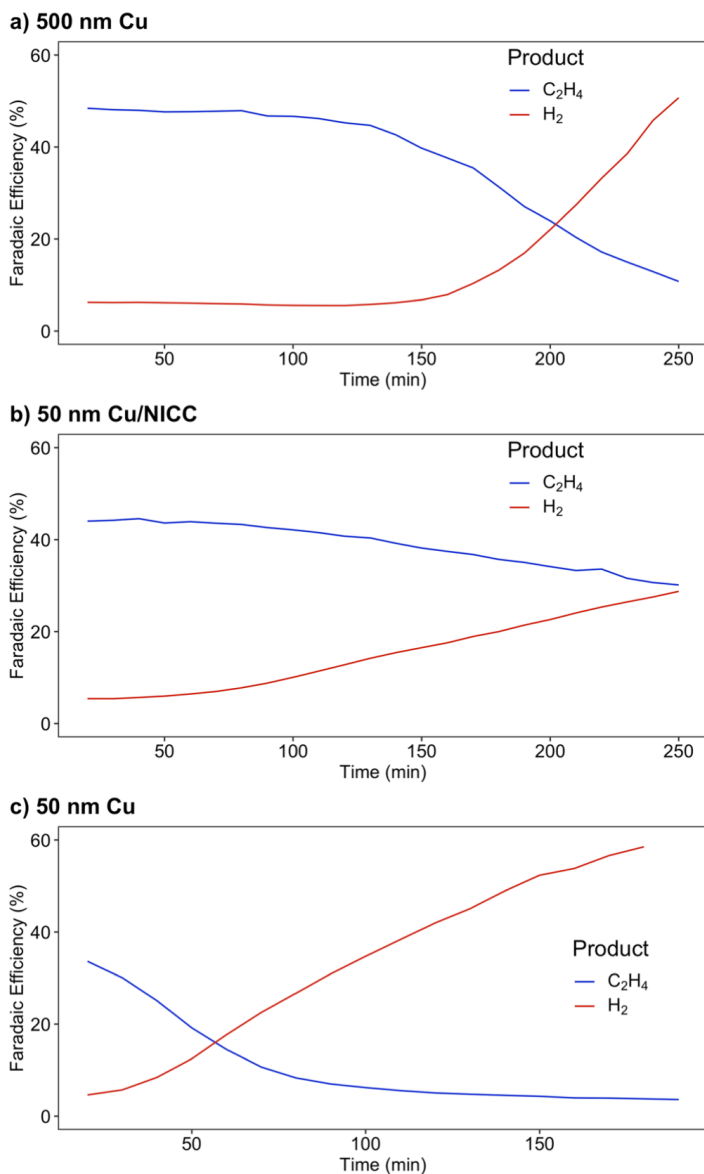


Figure 4.A.10: Long-term faradaic efficiencies towards ethylene and hydrogen of a 500 nm Cu ePTFE electrode, a 50 nm Cu/NICC and a 50 nm Cu design, at constant potential (~ -0.55 V vs. RHE)

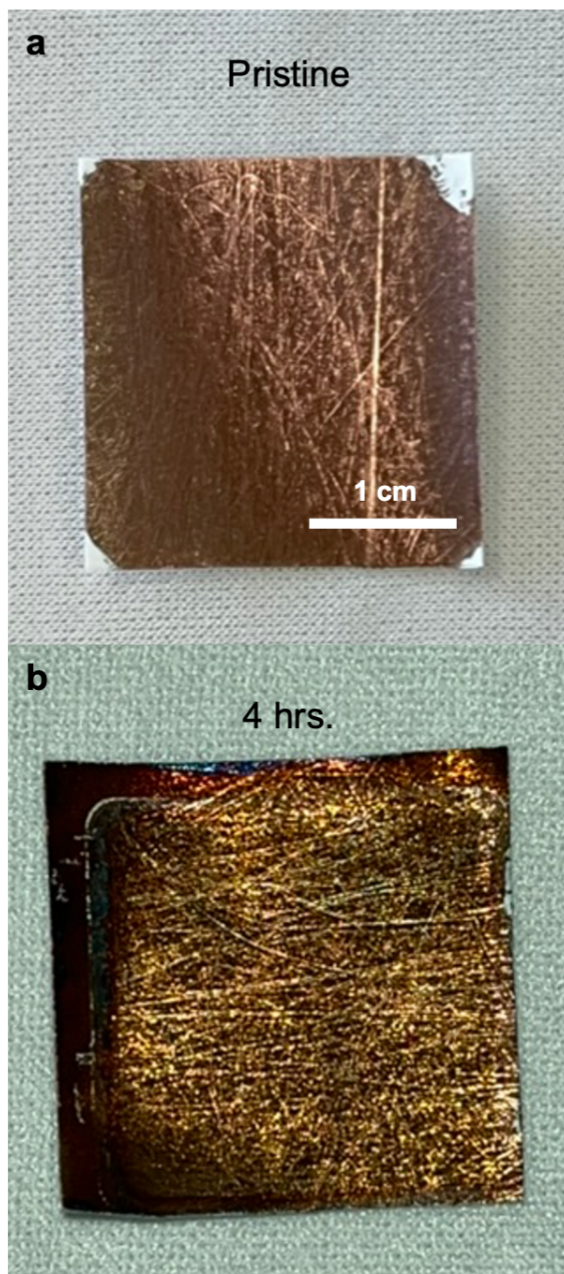


Figure 4.A.11: (a) As-prepared 500 nm Cu ePTFE electrode, and (b) after 4 hrs. of electrolysis at ~ -0.55 V vs. RHE

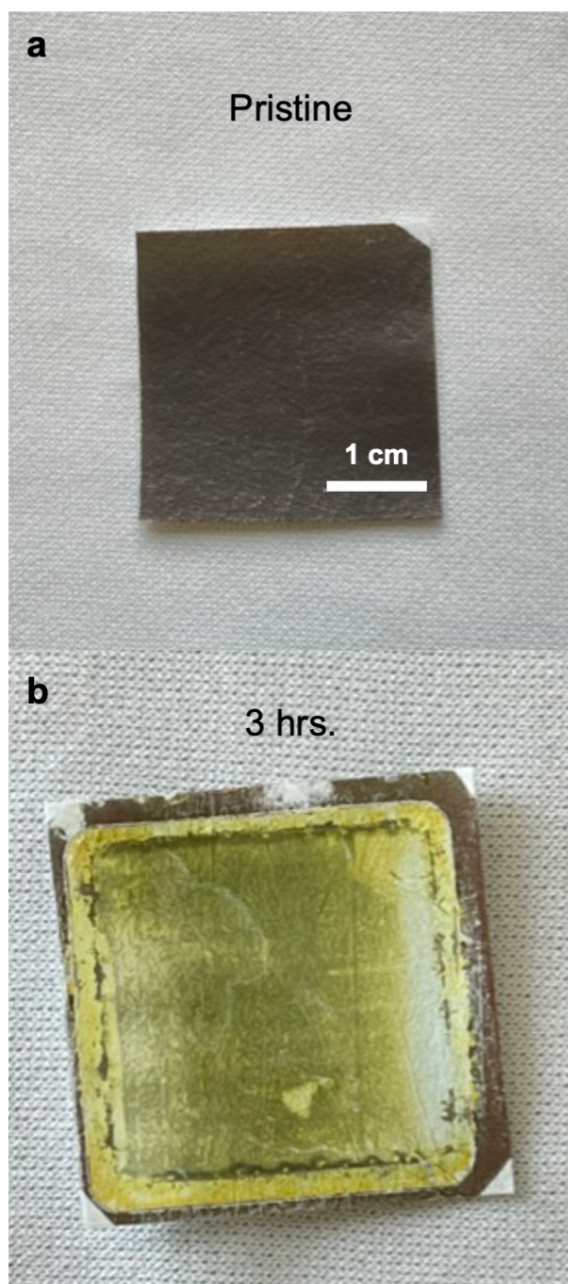


Figure 4.A.12: (a) As-prepared 50 nm Cu ePTFE electrode, and (b) state of a 50 nm Cu sample after 3 hrs. of electrolysis at ~ -0.55 V vs. RHE.

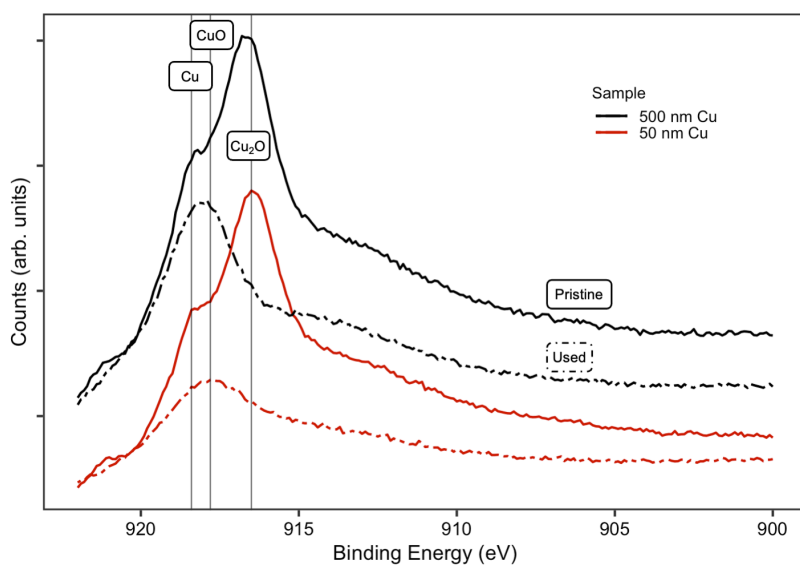


Figure 4.A.13: Cu-LMM XPS scans of pristine and used samples of each thickness. The used 500 nm Cu scan shows a convolution of Cu and CuO peaks, whereas that convolution is much weaker for the 50 nm Cu used sample. The metallic copper shoulder is evident for both pristine samples.

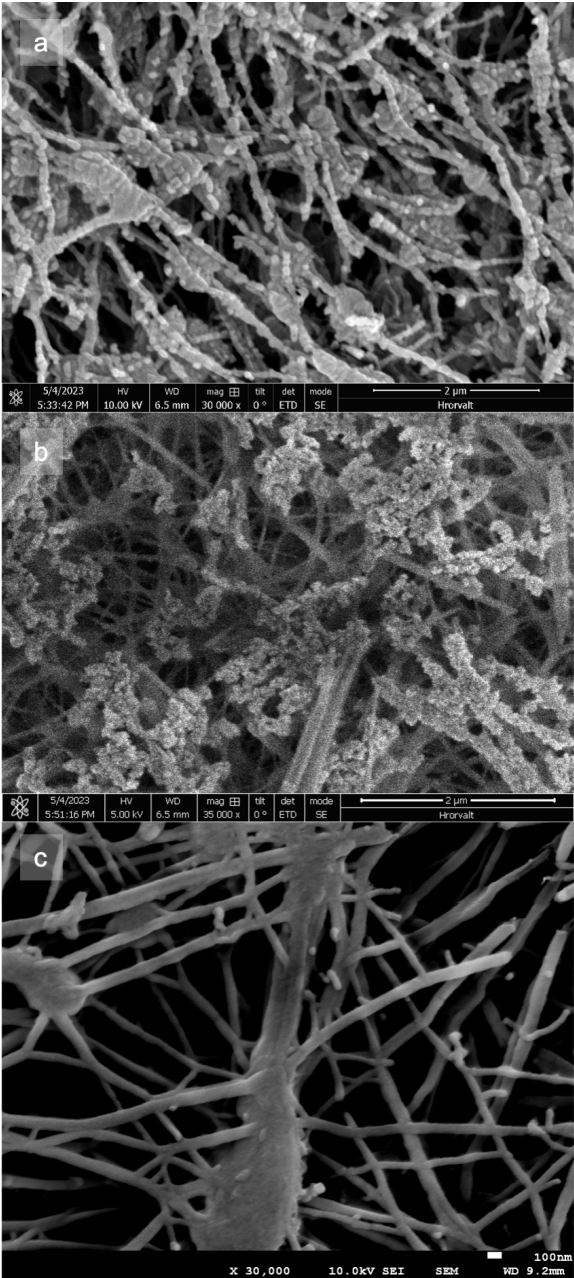


Figure 4.A.14: (a) SEM imaging of as-prepared 50 nm Cu ePTFE electrode, (b) state of a 50 nm Cu electrode after prolonged (~2 h) electrolysis at increasing current densities and (c) state of a bare spot of ePTFE after prolonged (~2 h) electrolysis.

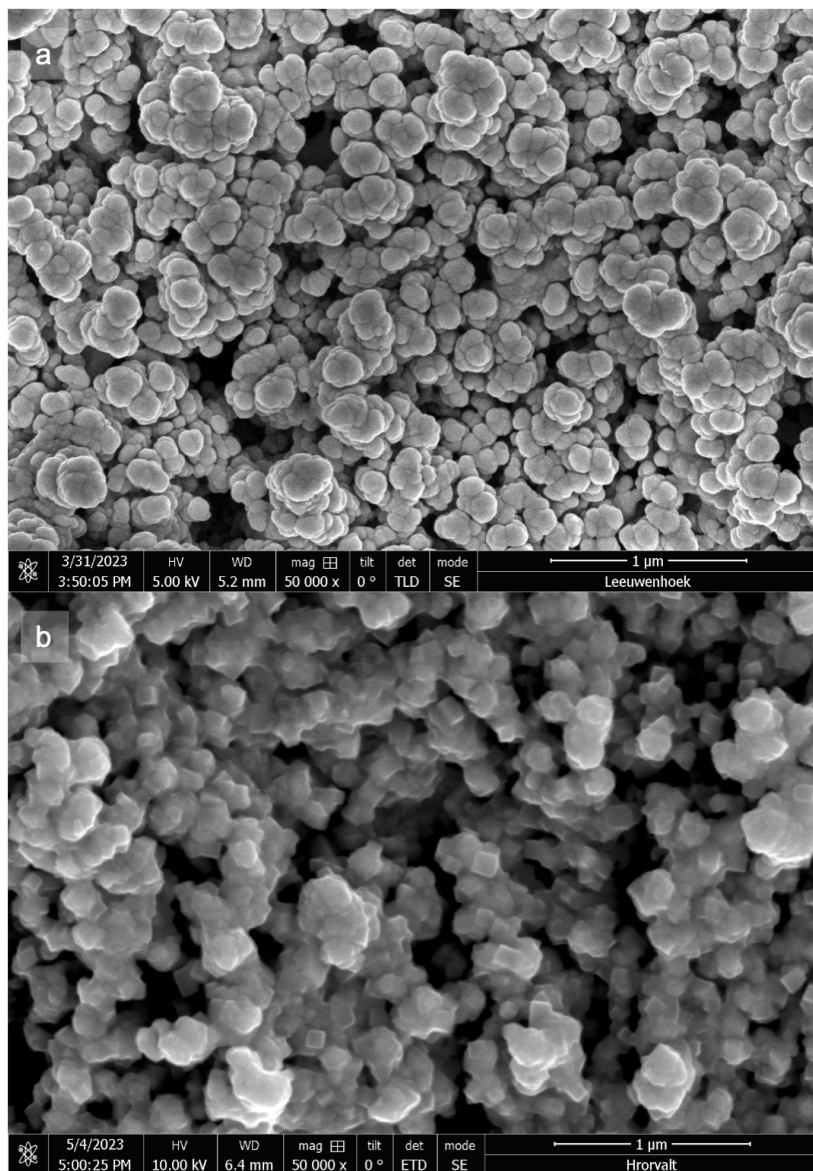


Figure 4.A.15: (a) SEM imaging of as-prepared 200 nm Cu + Sigracet 3BB electrode, and (b) after prolonged (~2 h) electrolysis at increasing current densities from -50 to -200 mA cm⁻².

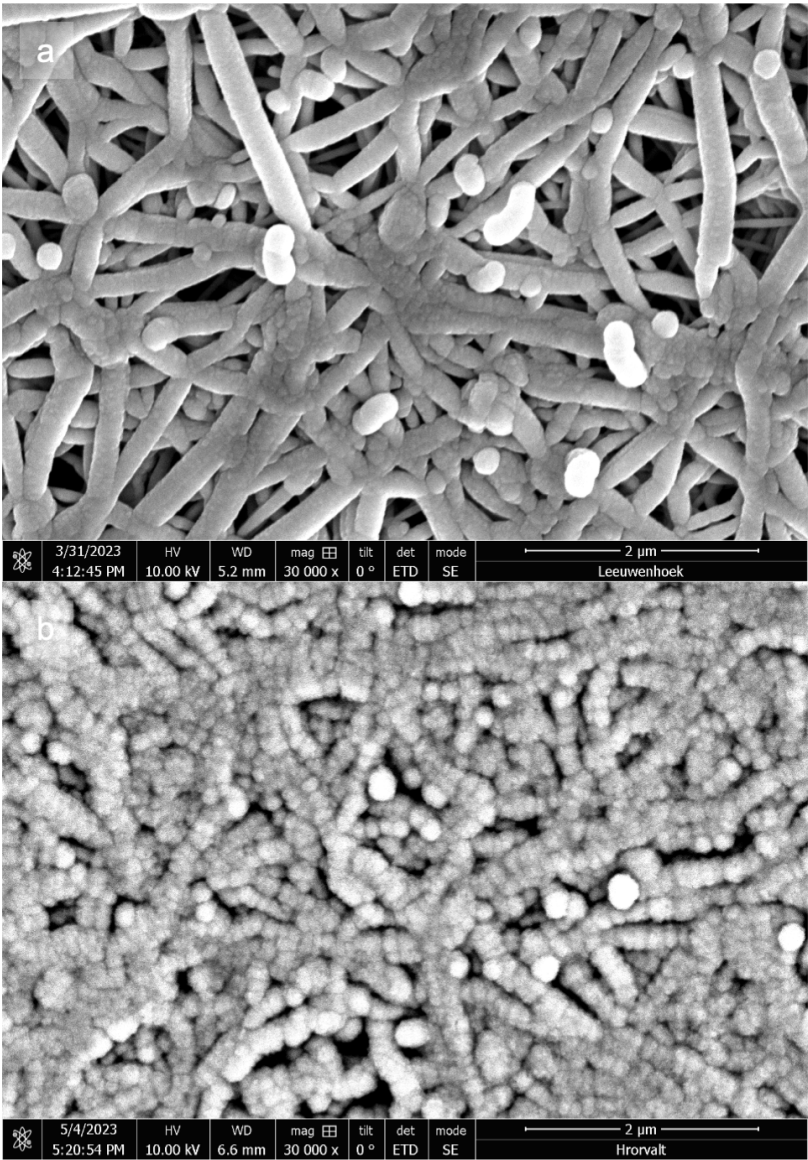


Figure 4.A.16: (a) SEM imaging of as-prepared 500 nm Cu ePTFE electrode, and (b) after prolonged (~2 h) electrolysis at increasing current densities from -50 to -200 mA cm⁻².

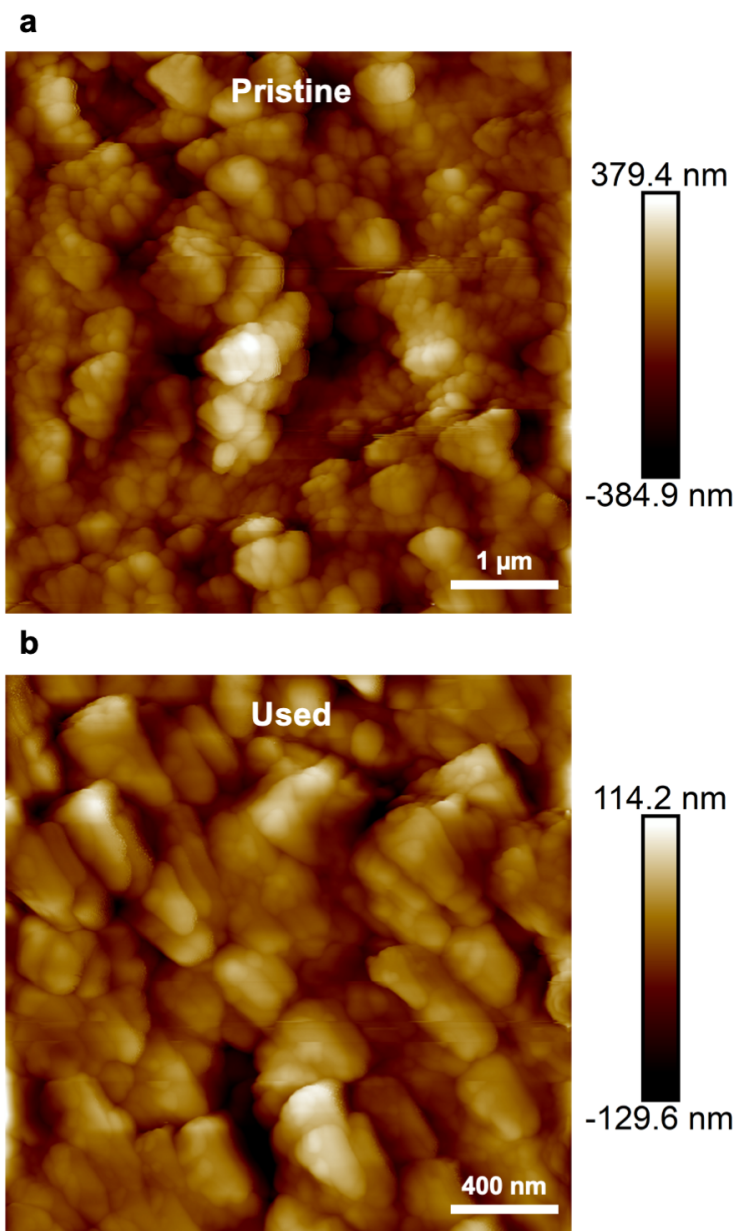


Figure 4.A.17: AFM surface imaging of (a) as-prepared 200 nm Cu on Sigracet 38BB, and (b) state of the 200 nm Cu layer after prolonged (~2 h) electrolysis at increasing current densities.

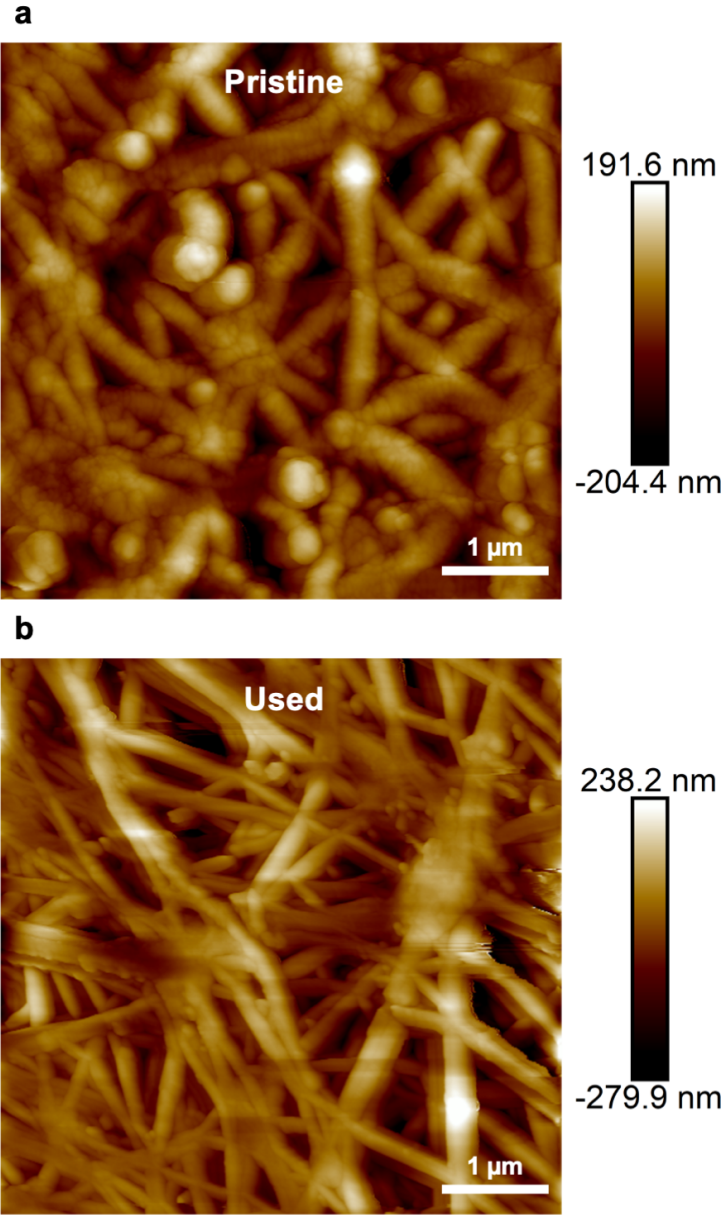


Figure 4.A.18: AFM surface imaging of (a) as-prepared 50 nm Cu on ePTFE, and (b) state of the same layer after prolonged (~2 h) electrolysis at increasing current densities.

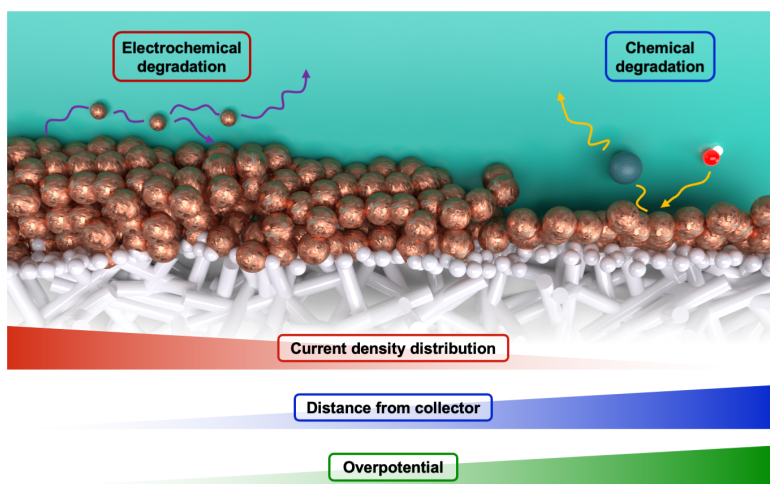


Figure 4.A.19: Sketched deterioration mechanisms for sputtered copper catalyst layers on PTFE GDLs. Areas far from the current collector are progressively electrically isolated and experience chemical corrosion to soluble hydroxides. Areas close to the current collector experience cathodic corrosion resulting in restructuring of the catalyst nanoparticles.

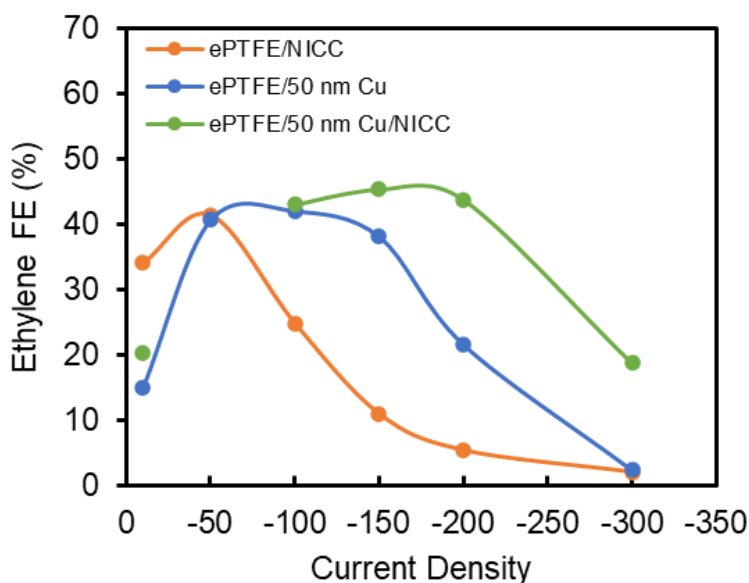


Figure 4.A.20: Comparative ethylene Faradaic efficiency for different electrodes including: (1) ePTFE and a 1 μ m busbar layer (NICC), (2) ePTFE + 50 nm Cu layer, (3) ePTFE + 50 nm Cu layer + a 1 μ m busbar layer (NICC)

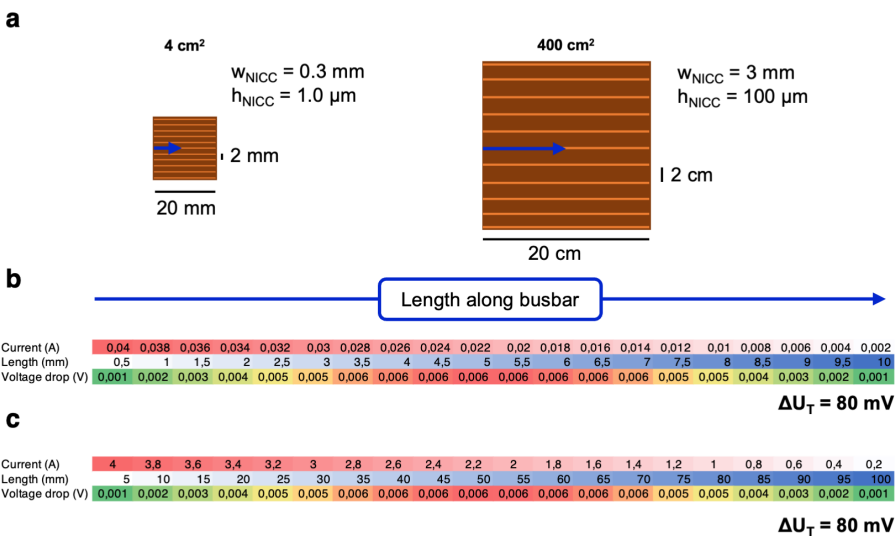


Figure 4.A.21: (a) Sketches for NICC designs on 4 cm² and 400 cm² electrodes with detailed NICC dimensions. (b) The maximum voltage drop along the busbars for a current density of 200 mA cm⁻² in a 4 cm² electrode as detailed in (a), and (c) a 400 cm² electrode with a NICC design as in (a).

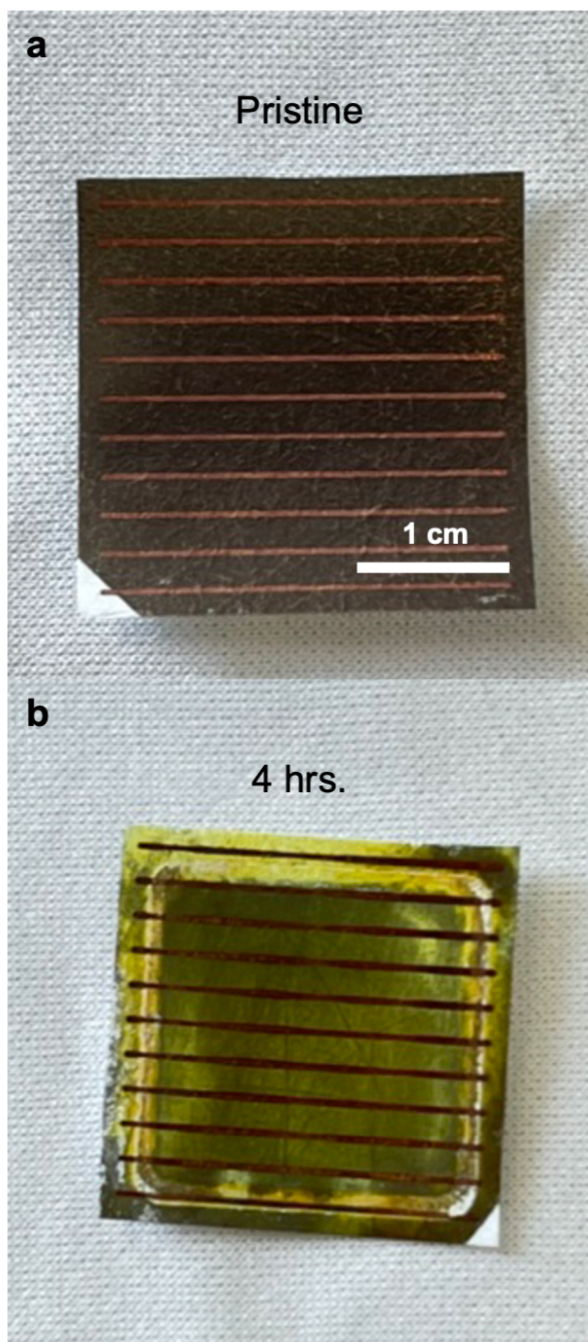


Figure 4.A.22: (a) As-prepared 50 nm Cu/NICC ePTFE electrode, and (b) state of a NICC electrode after 4 hrs. of electrolysis at ~ -0.55 V vs. RHE

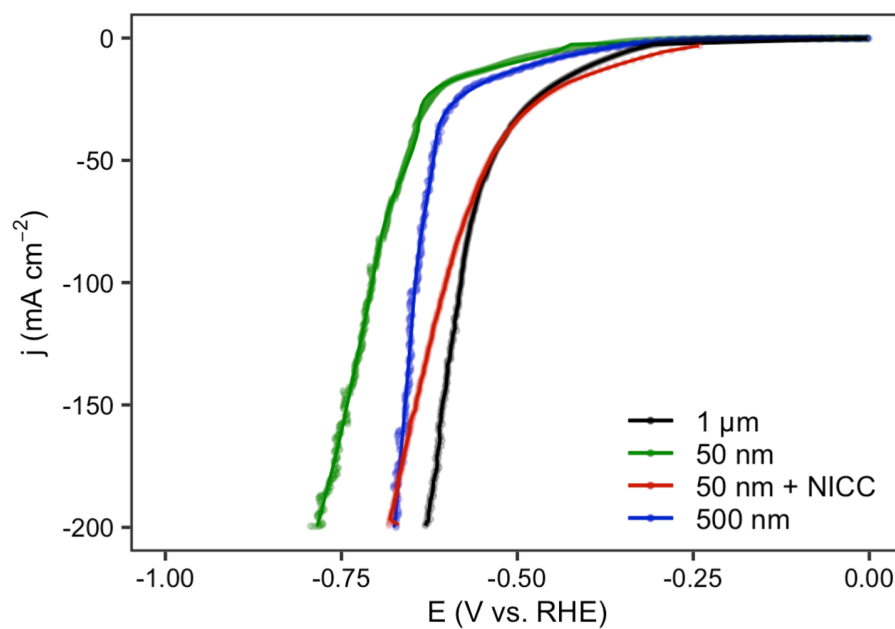


Figure 4.A.23: Polarization curves at -5 mV s^{-1} of 1 μm , 500 nm, 50 nm and 50 nm Cu/NICC electrodes.

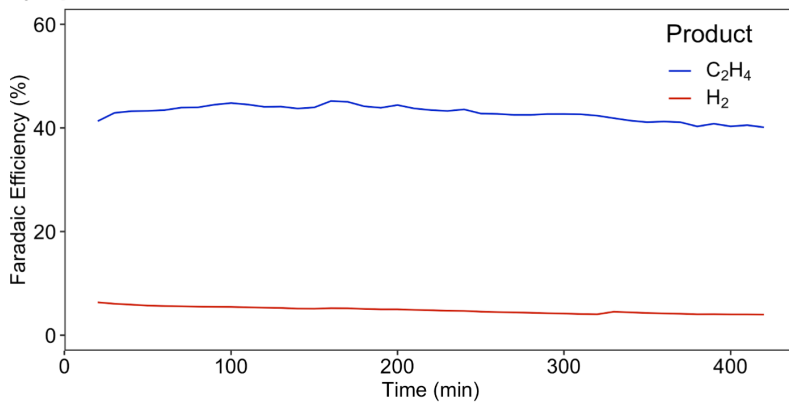
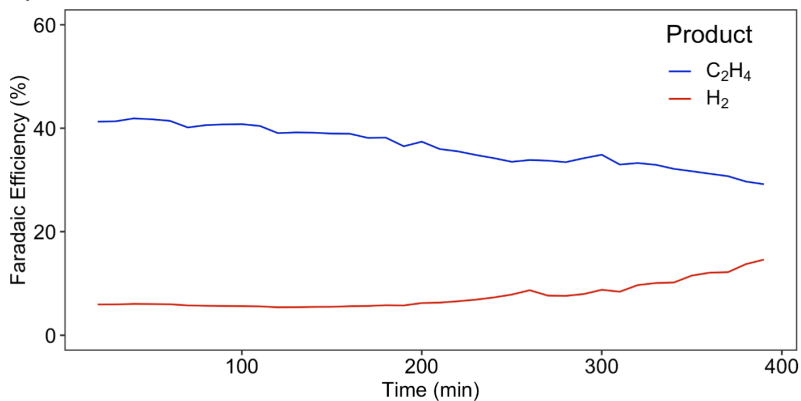
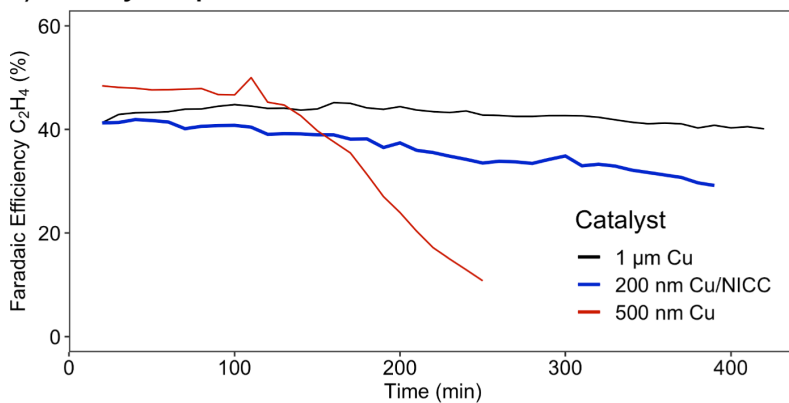
a) 1 μm Cu**b) 200 nm Cu/NICC****c) Stability comparison**

Figure 4.A.24: Long-term faradaic efficiencies towards ethylene and hydrogen of (a) 1 μm Cu ePTFE electrode, (b) 200 nm Cu/NICC electrode, and (c) comparison of stability towards ethylene at constant potential (~ -0.6 V vs. RHE).

Supplementary Tables

Table 4.A.3: 2-electrode probe resistances measured for a 50 nm and a 1 μm Cu layers.

Cu layer thickness	$R_{path,1cm}$ ($\text{m}\Omega\cdot\text{cm}$)
50 nm	1.47
1 μm	0.17

Table 4.A.4: Selectivities for a 1 μ m, 500 nm and 50 nm catalyst layers sputtered on ePTFE GDEs, and of a 200 nm Cu layer on a carbonous electrode (Sigracet 38BB). Data taken at increased current densities. FE's of liquid products are corrected and approximated to resting electrolyte volume at time of acquisition.

	j [mA cm ⁻²]	Methane [CH ₄]	Formate [HCOO ⁻]	Ethylene [C ₂ H ₄]	Ethanol [C ₂ H ₅ OH]	Acetate [CH ₃ COO ⁻]	Propanol [CH ₃ H ₇ OH]	Acetaldehyde [C ₂ H ₄ O]			
								C ₁	C ₂₊	H ₂	
1 μm Cu	- 10	0.00	22.1	9.65	0.48	2.62	0.11	0.00	22.1	12.9	8.73
	- 50	0.00	10.8	33.5	13.0	0.57	6.83	0.00	10.8	53.9	8.42
	- 100	0.00	7.35	43.5	14.2	0.95	6.07	0.00	7.35	64.7	5.83
	- 150	0.00	7.92	46.5	25.3	1.38	9.22	7.85	7.92	90.3	4.45
	- 200	0.00	6.26	48.3	31.0	2.61	8.62	7.07	6.26	97.6	3.87
	- 300	0.00	5.13	47.9	32.3	3.27	6.80	8.51	5.29	98.8	4.87
500 nm Cu	- 10	1.11	16.0	17.8	15.0	7.40	0.13	0.14	17.1	40.5	16.1
	- 50	0.20	5.79	40.4	14.8	1.30	9.03	2.91	5.99	68.5	9.92
	- 100	0.30	4.70	45.5	23.5	2.19	6.79	3.58	5.00	81.5	6.50
	- 150	0.30	3.98	45.2	30.9	2.35	8.46	3.99	4.27	90.9	5.70
	- 200	0.33	3.59	45.8	33.5	2.97	6.97	3.63	3.91	92.8	6.05
	- 300	4.85	3.00	29.8	43.5	6.79	5.42	4.32	7.84	89.8	18.5
50 nm Cu	- 10	0.42	16.3	15.1	0.71	8.30	0.11	0.12	16.7	24.3	21.2
	- 50	4.64	5.08	40.7	14.9	2.57	5.59	6.39	9.72	70.1	6.83
	- 100	6.59	4.66	42.1	19.5	5.76	4.11	6.36	11.3	77.8	4.73
	- 150	13.3	3.99	38.2	24.4	7.90	4.49	6.47	17.3	81.5	6.42
	- 200	31.6	4.61	21.7	21.6	9.26	2.72	4.76	36.2	60.0	17.2
	- 300	29.4	4.90	2.46	13.4	5.12	2.83	3.63	34.3	27.5	30.8
200 nm Cu/C	- 10	0.15	30.8	2.59	11.8	6.41	0.11	0.12	31.0	19.8	28.6
	- 50	2.48	9.05	20.6	5.90	0.87	3.25	0.12	11.5	31.3	13.5
	- 100	4.15	8.79	32.3	17.2	2.32	4.86	3.59	12.9	61.2	9.13
	- 150	4.15	5.81	36.2	19.2	2.90	5.19	2.97	12.7	67.3	7.70
	- 200	5.13	5.99	37.2	25.6	4.25	4.76	4.06	11.1	76.5	7.98
	- 300	6.45	4.00	24.4	25.4	5.80	3.74	2.83	10.5	62.3	9.36

Table 4.A.5: Selectivity for a uniform 50 nm Cu catalyst layers sputtered on an ePTFE GDEs, of a 1 μ m NiCC pattern sputtered on a bare GDE and of a 50 nm Cu/NiCC electrode. Data taken at increased current densities.

	j [mA cm ⁻²]	Methane [CH ₄]	Ethylene [C ₂ H ₄]	Hydrogen [H ₂]	Carbon Monoxide [CO]	Propane [C ₃ H ₈]	Gas products
Bare/NiCC	- 10	0.00	34.1	4.15	20.3	0.50	59.1
	- 50	0.72	41.5	3.76	4.18	0.57	50.7
	- 100	6.23	24.9	25.2	0.86	0.12	57.4
	- 150	9.10	11.0	54.5	0.33	0.03	75.0
	- 200	5.09	5.42	69.6	0.26	0.02	80.4
	- 300	1.19	2.05	71.9	0.24	0.01	75.4
50 nm Cu	- 10	0.42	15.1	21.2	35.7	0.37	72.8
	- 50	4.64	40.7	6.83	8.93	0.60	61.7
	- 100	6.59	42.1	4.73	5.06	0.58	59.0
	- 150	13.3	38.2	6.42	1.65	0.38	60.0
	- 200	31.6	21.7	17.2	0.62	0.17	71.3
	- 300	29.4	2.46	30.8	0.09	0.03	62.8
50 nm Cu/NiCC	- 10	0.39	20.4	8.98	25.7	0.36	55.8
	- 100	3.04	43.1	5.48	9.32	0.42	61.3
	- 150	3.26	45.4	4.47	6.45	0.77	60.4
	- 200	5.63	43.9	4.57	4.29	0.54	58.9
	- 300	27.5	18.8	20.54	6.59	0.10	73.6

Table 4.A.6: Faradaic efficiencies towards ethylene, hydrogen, and carbon monoxide of the architectures compared in Figure 4.4. All data is taken at around -0.55 V vs. RHE using the setup described previously.

t [min]	500 nm Cu			50 nm Cu/NICC			50 nm Cu		
	FE C ₂ H ₄ [%]	FE H ₂ [%]	FE CO [%]	FE C ₂ H ₄ [%]	FE H ₂ [%]	FE CO [%]	FE C ₂ H ₄ [%]	FE H ₂ [%]	FE CO [%]
10	48,42	6,26	4,36	44,03	5,42	5,92	33,62	4,62	12,90
20	48,11	6,21	4,17	44,21	5,41	5,99	30,06	5,72	13,48
30	47,97	6,25	4,38	44,57	5,67	5,85	25,08	8,43	14,37
40	47,64	6,17	4,54	43,62	5,97	5,37	19,18	12,47	14,99
50	47,67	6,09	4,65	43,90	6,44	4,97	14,49	17,70	15,43
60	47,77	5,98	4,75	43,58	6,98	4,58	10,68	22,53	15,46
70	47,89	5,90	4,86	43,30	7,78	4,31	8,31	26,72	15,14
80	46,73	5,68	4,85	42,62	8,79	4,12	7,00	30,94	15,11
90	46,67	5,60	4,83	42,12	10,06	4,10	6,22	34,73	14,76
100	46,17	5,57	4,86	41,52	11,42	4,03	5,56	38,37	14,18
110	45,26	5,56	4,90	40,75	12,79	3,94	5,06	41,98	13,73
120	44,70	5,80	4,97	40,38	14,20	3,90	4,77	45,07	13,04
130	42,63	6,17	5,01	39,20	15,43	3,81	4,54	48,92	12,68
140	39,75	6,78	4,87	38,16	16,51	4,13	4,32	52,33	12,12
150	37,60	7,90	4,91	37,44	17,58	4,04	3,98	53,81	11,40
160	35,46	10,34	5,17	36,78	18,94	4,03	3,92	56,62	11,04
170	31,33	13,21	5,27	35,71	20,00	3,94	3,77	58,51	10,48
180	27,03	16,93	5,23	35,05	21,41	3,93	3,62	60,50	10,06
190	23,94	22,04	5,04	34,14	22,62	3,91	-	-	-
200	20,36	27,39	4,74	33,29	24,06	3,89	-	-	-
210	17,16	33,20	4,37	33,59	25,33	4,05	-	-	-
220	14,98	38,57	3,94	31,59	26,46	3,90	-	-	-
230	12,90	45,76	3,61	30,68	27,53	3,89	-	-	-
240	10,77	50,70	3,18	30,15	28,75	3,89	-	-	-

5

A GUIDE TO ASSEMBLY AND
OPERATION OF CO₂ ELECTROLYZERS

5

“Consciously or unconsciously everyone writes as a partisan.”

— George Orwell,
in *Homage to Catalonia* (1938)

The rapid advancement in the development of CO₂ electrolyzers has triggered the adoption of novel architectures to achieve industrial-rate metrics. Integration of gas-diffusion electrodes, membrane-electrode assemblies and other advanced configurations have brought by rapid expansion towards ampere-level production rates. The reality of CO₂ electrolysis in basic environments, however, brings additional challenges that need to be accounted for, like salt deposition, reactant dissolution and flooding of porous media. Improper accounting of the complex reality of the electrode’s vicinity during this reaction can skew results and misrepresent performance of innovations. In this chapter we present a guide with observations and methodologies based on our lab’s experience. In addition, we include an equipment list, technique overview and troubleshooting guide to help advance novel researchers in their first steps into the field.

5.1 Introduction

The electrochemical reduction of CO₂ is increasingly seen as a viable means of producing carbon-based fuels and feedstocks due to the rapid advancement of cost-linked performance metrics within the past decade. These rapid advancements have also uncovered many fundamental and applied challenges (e.g. salt formation, CO₂ utilization), which researchers have been systematically overcoming through various ingenuities at the catalyst, configuration, and operational levels.[2, 3] Consequently, as the technology pushes further into the unknown and closer to commercially interesting performance metrics, the design, assembly, and operation of lab-scale CO₂ electrolyzers must be regimented. In fact, such regulation is now necessary just to achieve the relevant baseline data needed to demonstrate new performance advancements. While many research studies report their experimental cells and systems used to generate their novel results, few provide an extensive overview, protocol and system diagram that allows new researchers to reconstruct the entirety of the electrolysis system. Groups or new researchers entering the CO₂ electrolysis research field must then either design systems themselves or incorporate pieces of information from a wide variety of sources.

In 2019 our research group provided an “introductory guide” to the assembly and operation of gas-diffusion electrodes for electrochemical CO₂ reduction that acted as a starting point for researchers to shift from aqueous-fed reactants in H-cells to gas-fed reactants using gas-diffusion layers.[4] At the time, we discussed the operational intricacies of rudimentary flow cells utilized at the time. The guide included cell assembly and operational details in the form of pictures and videos. In the past few years, however, substantial advancements have been made in the research field with regards to lab protocols, equipment, and product measurements that warrants an updated guide. Further, the previous guide did not discuss zero-gap membrane electrode assemblies (MEAs) in detail, which have now achieved widespread adoption in CO₂ electrolysis due to their cell simplicity and reduced ohmic losses. We then believe that the field would benefit from an updated “advanced guide” to the assembly and operation of gas-diffusion layers systems for the electrochemical reduction of CO₂.

In this chapter, we present a comprehensive insight into our lab’s materials, equipment, protocols, and methodology with the aim of providing a solid basis for further developments in the field. Additionally, we provide an in-depth start-up guide in our supporting information and video tutorials of assembly, start-up procedures and operation. The aim of this Viewpoint is to facilitate access to the CO₂-electrolysis field to accelerate advancements.

In the following section we provide an elaborate description of our cell designs and the use of gas-diffusion layers. We then detail the importance of accurate mea-

surements and discuss our instrumentation setup used to control the electrolysis process. Finally, we provide additional information on analysis techniques and point the reader to detailed resources on various sub-topics.

5.2 Advanced electrolyzer design for CO₂ electrolyzers

5.2.1 Background on the use of gas-diffusion layers

In the push for industrially feasible metrics, the CO₂ electrolysis field has steadily shifted from typical H-cell designs (where the reactant CO₂ is dissolved in the liquid catholyte) to catalysts supported on gas-diffusion electrodes (GDEs). These porous GDE substrates, usually carbon-based, drastically reduce the diffusion pathway for gaseous CO₂ to reach the catalyst, enabling high current densities and higher volumetric activity rates.

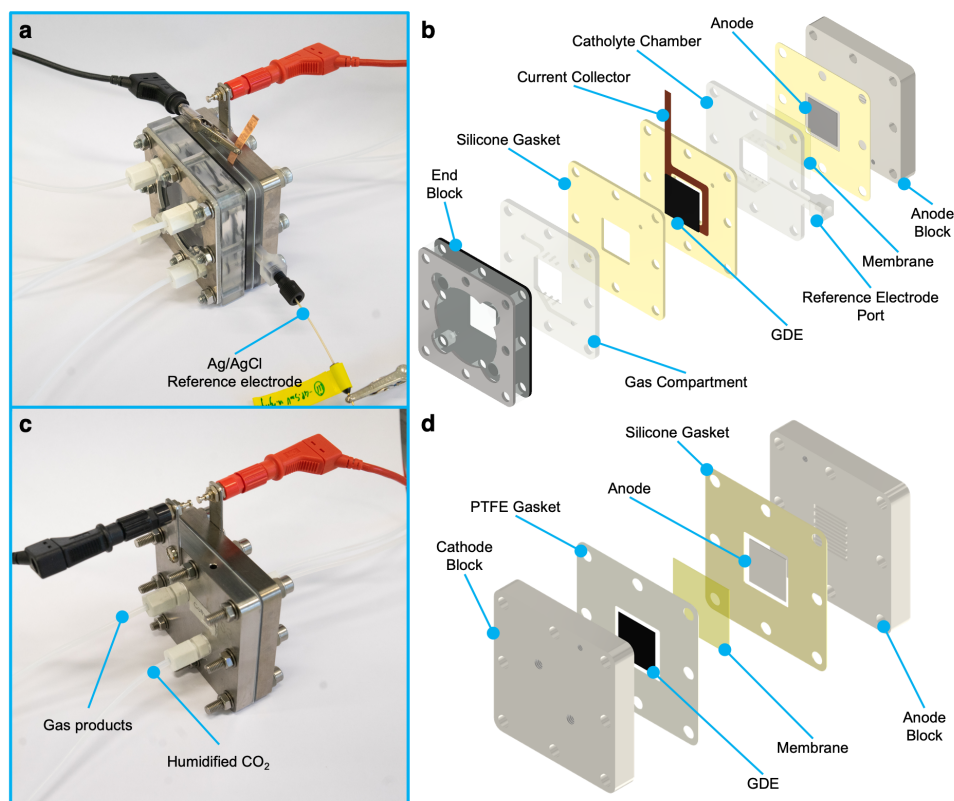


Figure 5.1: Lab-scale electrolyzers for CO₂RR characterization. (a) A flow electrolyzer, based on a commercial anode block and 3D-printed catholyte and gas channels, as assembled, and (b) in exploded view. (c) A commercially available MEA cell, as assembled, and (d) in exploded view.

The use of GDEs with flowing catholytes (Fig. 5.1a and b), however, is not without disadvantages. These systems are prone to flooding due to gas-liquid pressure imbalances, salt pumping and electrowetting[5–7], leading some researchers to adopt gas-diffusion layers fully made of polytetrafluorethylene (PTFE).[8, 9] In an architecture where reducing the diffusion length of CO₂ is key, flooding of GDEs hampers the performance and stability of these systems in the long-term.

An answer to flooding concerns and high ohmic drops in catholytes can be found in MEA cells (Fig. 5.1c and d) where the cathode and anode sandwich an ion exchange membrane. The CO₂ reduction catalyst is then wetted while allowing for efficient CO₂ access from a GDE, and ionic species transport to and from the anode through a membrane. While MEAs reduce the risk of flooding, the low volume of water between the catalyst layer and the membrane increases the relative concentration of carbonate species considerably, which results in noticeable salt precipitation and accumulation, to the point that it can block the gas channels in the cathodic half-cell.

Many of these challenges, however, are resolvable or manageable with proper system design and control strategies. Few resources provide such information. In this viewpoint, we aim to illustrate the effects of stable operation of ancillary equipment of CO₂RR systems at a lab-scale, as well as displaying advances in diagnostic system integration in the test-bench.

5.2.2 Flow-cells and MEA-cells: assembly and operation

In a flow-electrolyzer (FloE), a flowing catholyte along the cathode provides the medium for ions to be transported to the anode chamber. As the electrodes we intend to use for our application are of porous nature, a pressure equilibrium over the cathode is required to confine the electrode in the catholyte chamber and prevent any perspiration and flooding of the GDE, which would result in mass-transport limitations of the reactant CO₂ to the catalyst. The following section discusses the importance and challenges of this pressure regulation in detail.

The FloE design we present in this work is based around a 3D-printed catholyte flow field that accommodates a miniaturized leakless reference electrode (RE), as displayed in Fig. 5.1a and b. 3D printing is an accessible solution to design and manufacture of proprietary flow chambers, which allow for varying thicknesses and flow regimes along the GDE.[10] The inclusion of an RE allows one to operate the cathode at a specific set potential. In complex reaction systems where the applied overpotential determines the product distribution, being able to control the potential the potentiostat applies over the cathode is key to study the nature of the catalyst in detail. A step-by-step guide to assembly of this electrolyzer can be found in Supplementary Movie M1 (see the online version of this publication) and the Supplementary Information.

As most potentiostats reported in literature have a limited compliance voltage, minimizing cell voltage is key to ensuring high current densities can be evaluated at a lab scale. With this insight in mind, a reduction of the anodic and cathodic potentials required is essential. Our design achieves this by, firstly, employing an anode-design identical to that present in MEA cells (namely, a membrane adjacent to the employed anode and a serpentine flow-field through which the anolyte is circulated). Secondly, the thickness of the catholyte chamber is a mere 3 mm, which reduces the overpotential over the cathode chamber considerably when compared to designs prevalent in literature.[9, 11] At the same time, the narrow catholyte channel allows the RE to be placed within 1 mm of the cathode, ensuring accurate control and sensing of the applied overpotential.

The MEA design presented in Fig. 5.1c and d is similar to most reported in literature and is based on commercially available solutions.[12] A titanium anode-block with a milled serpentine channel, and a similar stainless-steel cathode block clamp the membrane-electrode assembly, consisting of a Ni-foam, an anion-exchange membrane, and a GDE-based cathode. A visual and assembly guide of this architecture is included in Supplementary Movie M2. The Supplementary Information includes a step-by-step description of the start-up protocol.

5.3 Lab-scale setup for CO₂ electrolysis

5.3.1 Regulation and measurement of gas and liquid streams

As discussed above, GDE-based FloE and MEA systems require a stable interface at the cathode to operate in a sustainable manner.[13, 14] Control over the inlet flows and pressures of the various gas and liquid channels of the electrolyzer is then essential. Additionally, due to large differences in the inlet to outlet gas flow rates caused by imbalanced CO₂ consumption and product evolution, the flow rate of the CO₂ outlet stream must be measured near or at the point of product quantification to accurately determine gaseous Faradaic efficiencies.[15, 16] Both the stability and product measurement aspects then require substantial balance of plant equipment and calibration to be able to accurately reports traditional CO₂RR metrics. In this section and in the Supplementary Information we discuss these in detail.

Within our test setup we control all gas and liquid pressures in the electrolyzer using a combination of pumps, dampeners, and back pressure regulators (see Fig. 5.2a). The electrolyte, contained in a reservoir, is pumped continuously using a peristaltic pump. Since these pumps cause oscillatory pressure spikes in the stream, we included two dampeners per fluid stream to reduce pulsation amplitudes. The electrolyte then flows through the electrolyzer and exits towards a back-pressure regulator (BPR). The BPR consists of a pressure meter coupled to a controller (a valve) that regulates the pressure of the stream in real-time through a proprietary

software application. The combined pump, pressure dampener and BPR limit liquid pressure oscillations of the electrolyte channels considerably, especially at elevated pressures, as can be seen in Fig. 5.2b. A thorough overview and operation guide can be found in the Supplementary Information, as well as supplementary movies in the original published version.

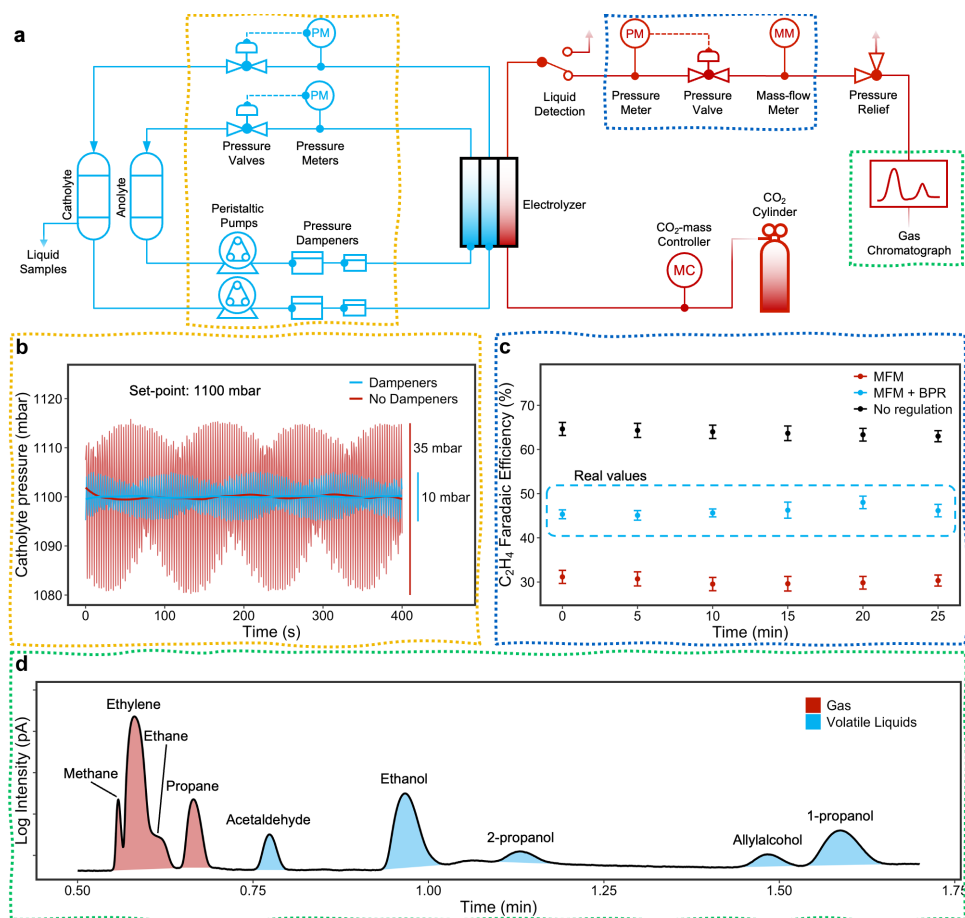


Figure 5.2: A reliable setup for studies on CO₂-electrolysis devices. (a) The process-flow diagram of a flow-cell setup, based on dampened liquid channels, a back-pressure regulator (BPR), and inline GC. (b) The inclusion of dampeners in the fluid channels helps reduce the impact of the peristaltic pumps' pressure spikes. (c) Not regulating and measuring the exit-flow rate results in overestimation of Faradaic efficiencies, as shown in black. On the other hand, just measuring the exit flow rate results in underestimation, as gas leaks to the catholyte compartment (in red). CO₂ electrolysis requires a BPR and mass-flow meter (MFM) that both regulate the pressure difference over the GDE and measure the product flow rate (in blue). (d) Gas chromatography is an adequate method for estimating Faradaic efficiencies of volatile liquid products, as are those of copper catalysts.

A similar pressure-regulation device is also required in the gas-channel of our setup (Fig. 5.2a). When combined the gas and liquid BPR's allow for the absolute and differential pressures of each channel to be regulated, preventing unnecessary gas-liquid crossover across the GDE during operation. Without differential pressure control of the gas-liquid channel, periodic gas penetration into the liquid channel is particularly problematic as it results in periodic perturbations in the gas flow rate, hindering accurate product quantification. Gas crossover across the GDE into the liquid phase will occur at extremely small gas overpressures, thus requiring a liquid overpressure between 10-30 mbar to be set for flowing catholyte systems. Such pressure control is less important for MEA systems due to the polymer membrane blocking direct gas crossover.

A final critical measurement component is a mass flow meter (MFM) or nitrogen bleed into the gas chromatograph (GC) to measure the real flow rate leaving the electrochemical cell. In both neutral-pH and alkaline CO₂ electrolyzers substantial gaseous CO₂ is consumed by abundant hydroxide by-products of electrolysis, causing outlet flow rates to be lower than inputted values. Further, hydrogen evolution can increase flow rates while multi-carbon products consume 2 (or more) mols of CO₂ per 1 mol of gas evolved. These factors then require the outlet gas stream to be accurately measured and recorded. When using a mass flow meter, which is typically calibrated for a specific gas, the measured outlet flow then also must be corrected by the gas composition determined by the GC (see Appendix).[17]

In Fig. 5.2c we briefly highlight the need for both a gas-phase BPR and measurement of the gas flow rate (either via a mass flow meter or a nitrogen bleed to the gas chromatograph). Here we can see three sets of measured data for CO₂RR on sputtered Cu electrodes in 1M KHCO₃. In the black data points the ethylene Faradaic efficiency appears overrepresented due to the use of the inlet flow rate of CO₂ instead of the outlet gas flow rate in the calculation. Further, the red data shows that when a MFM is used without a BPR, gas crossover into the liquid phase results in an underrepresentation of the formed products. Lastly, a combined implementation of an MFM and a BPR system shows the true measured ethylene faradaic efficiency close to the true values (Fig. 5.2c, in blue). We provide, in the Supplementary Information and Movie M3, start-up protocols that are followed to ensure gas-liquid balances, proper pressure regulation, and cell start-up. This combined approach to measuring and regulating the effluent streams removes one of the major pitfalls in catalyst evaluation in the CO₂ electrolysis field.[18]

5.3.2 Integration of in-line diagnostic systems

Key performance metrics of CO₂RR systems in literature include, amongst many, energy and faradaic efficiency towards products, single-pass conversion rate of

CO₂ and long-term stability and selectivity of the cathode.[19] A big part of these metrics revolves around identification and quantification of the species present in the effluent product stream of the electrolyzer. Ensuring that the measurement of all products is as accurate and speedy as possible is then crucial for reporting the performance of CO₂RR electrolyzers.[20] Since products of the electrolyzer can either be gaseous (e.g. carbon monoxide, methane, ethylene) or liquid (e.g. formate, ethanol, acetate), each stream requires separate analysis methods.

Gaseous products are commonly analyzed using gas-chromatograph (GC).[21] This technique separates a gas stream and analyzes its composition as a function of its residence time in separation columns (see the Supporting Information for a detailed description). Whereas some reports in literature involve a manual injection of effluent gas into the GC,[22, 23] our setup has an automatic injection method that periodically collects samples from the gas stream leaving the electrolyzer. This allows us to screen the species in the outlet gas every 5 minutes without margin for human or mechanical error during injection. Recent reports have shown the advantage of using infrared-based detection methods, which increase the scanning frequency and avoid typical shortcomings of GC's, like sensitivity to liquid and salt accumulation.[24, 25]

For the analysis of liquid products, we use high-performance liquid chromatography (HPLC), which uses a system similar to a GC to separate liquid species in an acidic carrying solvent (see Appendix). This allows us to separate most CO₂RR products, even for complex catalysts as copper.[26] The relative tolerance to basic solutions ($\text{pH} \leq 13$, approximately) makes this a more intuitive and accessible method than nuclear-magnetic resonance (NMR), more prevalent in the field,[27–29] which requires extensive sample preparation and cleaning of analysis tubes. Most of these liquid products have a high-enough volatility to be detected in the gaseous stream (see Fig. 5.2d). While saturation times for these products are noticeably higher than those of their gaseous counterparts, signaling using the GC is an adequate proxy for quick assessment of the performance of a cathode (see the Supplementary Information).

Identification of the reactant for a specific product made with low concentrations is best carried out by using labeled CO₂ (C13-based dioxide) to ensure the product is not a result of contamination and is in fact coming from gaseous CO₂. [30] Gas-chromatography systems, however, do not possess sufficient resolution to separate labeled isotopes in products. Instead, combined use of GC and mass-spectrometry (MS) systems is common practice in the field.[31] Alternatively, on-line electrochemical mass spectrometry (OLEMS) provides a flexible architecture that is capable of identifying gas-fraction products of CO₂RR at a high refresh-rate.[32–35]

5.3.3 Additional detailed resources for various measurement aspects

Beyond the information provided here, several other articles have performed various deep dives in advanced measurements and characterization, which we would like to point the reader to. For example, near-unity product analysis and full carbon balances can be extremely challenging in MEA and flowing electrolyzers. While we have highlighted some best practices here, even more advanced methods exist to, for example, (i) separately quantify C12 versus C13 products and hard to detect formaldehyde,[36] (ii) fully-quantify liquid products that can vaporize into the gas stream or crossover to the anode,[37] (iii) accurately measure the potential-drops over every component in a zero-gap MEA electrolyzer,[38] (iv) segmenting a flow field to observe geometric product distributions,[39] and (v) analyzing the kinetics of CO₂-electrolysis in an advanced reactor design using electrochemical impedance spectroscopy (EIS).[40]

In summary, this Viewpoint presents a comprehensive look into our lab-scale operation and analysis protocols of CO₂-electrolyzers. Setups and observations made in the study of these electrolyzers are not trivial and not one-to-one translatable from prior knowledge in other electrochemical fields like water electrolysis and hydrogen fuel-cells. By highlighting our advances in cell-design, process-flow implementation and control, and product quantification, we aim to provide a solid starting base for anyone looking to contribute to the scientific advancement of this field. This document should then become a stepping-stone for anyone without prior experience in the electrochemical conversion of CO₂.

References

- [1] Hugo-Pieter Iglesias Van Montfort, Siddhartha Subramanian, Erdem Irtem, Mark Sassenburg, Mengran Li, Jesse Kok, Joost Middelkoop, and Thomas Burdyny. An Advanced Guide to Assembly and Operation of CO₂ Electrolyzers. *ACS Energy Letters*, 8(10):4156–4161, October 2023.
- [2] Danielle A. Salvatore, David M. Weekes, Jingfu He, Kevan E. Dettelbach, Yuguang C. Li, Thomas E. Mallouk, and Curtis P. Berlinguette. Electrolysis of Gaseous CO₂ to CO in a Flow Cell with a Bipolar Membrane. *ACS Energy Letters*, 3(1):149–154, January 2018.
- [3] Kailun Yang, Mengran Li, Siddhartha Subramanian, Marijn A. Blommaert, Wilson A. Smith, and Thomas Burdyny. Cation-Driven Increases of CO₂ Utilization in a Bipolar Membrane Electrode Assembly for CO₂ Electrolysis. *ACS Energy Letters*, 6(12):4291–4298, December 2021.
- [4] Kai Liu, Wilson A Smith, and Thomas Burdyny. Introductory Guide to Assembling and Operating Gas Diffusion Electrodes for Electrochemical CO₂ Reduction. *ACS Energy Letters*, 2019.
- [5] Lorenz M. Baumgartner, Christel I. Koopman, Antoni Forner-Cuenca, and David A. Vermaas. Narrow Pressure Stability Window of Gas Diffusion Electrodes Limits the Scale-Up of CO₂ Electrolyzers. *ACS Sustainable Chemistry & Engineering*, 10(14):4683–4693, April 2022.
- [6] Lorenz M. Baumgartner, Christel I. Koopman, Antoni Forner-Cuenca, and David A. Vermaas. When Flooding Is Not Catastrophic – Woven Gas Diffusion Electrodes Enable Stable CO₂ Electrolysis. *ACS Applied Energy Materials*, 5(12):15125–15135, December 2022.
- [7] Jae-Hun Kim, Jae-Hyoung Lee, Ali Mirzaei, Hyoun Woo Kim, Boon Teoh Tan, Ping Wu, and Sang Sub Kim. Electrowetting-on-dielectric characteristics of ZnO nanorods. *Scientific Reports*, 10(1):14194, August 2020.
- [8] Cao Thang Dinh, Thomas Burdyny, Golam Kibria, Ali Seifitokaldani, Christine M Gabardo, F Pelayo García De Arquer, Amirreza Kiani, Jonathan P Edwards, Phil De Luna, Oleksandr S Bushuyev, Chengqin Zou, Rafael Quintero-Bermudez, Yuanjie Pang, David Sinton, and Edward H Sargent. CO₂ electroreduction to ethylene via hydroxide-mediated copper catalysis at an abrupt interface. *Science*, 360:783–787, 2018.
- [9] F. Pelayo García de Arquer, Cao Thang Dinh, Adnan Ozden, Joshua Wicks, Christopher McCallum, Ahmad R Kirmani, Dae Hyun Nam, Christine

- Gabardo, Ali Seifitokaldani, Xue Wang, Yuguang C Li, Fengwang Li, Jonathan Edwards, Lee J Richter, Steven J Thorpe, David Sinton, and Edward H Sargent. CO₂ electrolysis to multicarbon products at activities greater than 1 A cm⁻². *Science*, 367:661–666, 2020.
- [10] Daniel Corral, Jeremy T. Feaster, Sadaf Sobhani, Joshua R. DeOtte, Dong Un Lee, Andrew A. Wong, Julie Hamilton, Victor A. Beck, Amitava Sarkar, Christopher Hahn, Thomas F. Jaramillo, Sarah E. Baker, and Eric B. Duoss. Advanced manufacturing for electrosynthesis of fuels and chemicals from CO₂. *Energy & Environmental Science*, 14(5):3064–3074, 2021.
- [11] Armin Löwe, Carolin Rieg, Tim Hierlemann, Nicolas Salas, Dennis Kopljär, Norbert Wagner, and Elias Klemm. Influence of Temperature on the Performance of Gas Diffusion Electrodes in the CO₂ Reduction Reaction. *ChemElectroChem*, 6(17):4497–4506, September 2019.
- [12] Jerry J. Kaczur, Hongzhou Yang, Zengcai Liu, Syed D. Sajjad, and Richard I. Masel. Carbon Dioxide and Water Electrolysis Using New Alkaline Stable Anion Membranes. *Frontiers in Chemistry*, 6:263, July 2018.
- [13] Wanyu Deng, Lei Zhang, Lulu Li, Sai Chen, Congling Hu, Zhi-Jian Zhao, Tuo Wang, and Jinlong Gong. Crucial Role of Surface Hydroxyls on the Activity and Stability in Electrochemical CO₂ Reduction. *Journal of the American Chemical Society*, 141(7):2911–2915, February 2019.
- [14] Yi Xu, Jonathan P. Edwards, Shijie Liu, Rui Kai Miao, Jianan Erick Huang, Christine M. Gabardo, Colin P. O’Brien, Jun Li, Edward H. Sargent, and David Sinton. Self-Cleaning CO₂ Reduction Systems: Unsteady Electrochemical Forcing Enables Stability. *ACS Energy Letters*, 6(2):809–815, February 2021.
- [15] Ming Ma, Ezra L. Clark, Kasper T. Therkildsen, Sebastian Dalsgaard, Ib Chorkendorff, and Brian Seger. Insights into the carbon balance for CO₂ electroreduction on Cu using gas diffusion electrode reactor designs. *Energy & Environmental Science*, 13(3):977–985, 2020.
- [16] Zhuang-Zhuang Niu, Li-Ping Chi, Ren Liu, Zhi Chen, and Min-Rui Gao. Rigorous assessment of CO₂ electroreduction products in a flow cell. *Energy & Environmental Science*, 14(8):4169–4176, 2021.
- [17] Siddhartha Subramanian, Joost Middelkoop, and Thomas Burdyny. Spatial reactant distribution in CO₂ electrolysis: balancing CO₂ utilization and faradaic efficiency. *Sustainable Energy & Fuels*, 5(23):6040–6048, 2021.

- [18] Ying Chuan Tan, Wei Kang Quek, Beomil Kim, Sigit Sugiarto, Jihun Oh, and Dan Kai. Pitfalls and Protocols: Evaluating Catalysts for CO₂ Reduction in Electrolyzers Based on Gas Diffusion Electrodes. *ACS Energy Letters*, 7(6):2012–2023, June 2022.
- [19] David Wakerley, Sarah Lamaison, Joshua Wicks, Auston Clemens, Jeremy Feaster, Daniel Corral, Shaffiq A. Jaffer, Amitava Sarkar, Marc Fontecave, Eric B. Duoss, Sarah Baker, Edward H. Sargent, Thomas F. Jaramillo, and Christopher Hahn. Gas diffusion electrodes, reactor designs and key metrics of low-temperature CO₂ electrolyzers. *Nature Energy*, 7(2):130–143, February 2022. Number: 2 Publisher: Nature Publishing Group.
- [20] Brian Seger, Marc Robert, and Feng Jiao. Best practices for electrochemical reduction of carbon dioxide. *Nature Sustainability*, 6(3):236–238, January 2023.
- [21] Justus S. Diercks, Bernhard Pribyl-Kranewitter, Juan Herranz, Piyush Chauhan, Antoine Faisnel, and Thomas J. Schmidt. An Online Gas Chromatography Cell Setup for Accurate CO₂-Electroreduction Product Quantification. *Journal of The Electrochemical Society*, 168(6):064504, June 2021.
- [22] F. Pelayo García De Arquer, Oleksandr S. Bushuyev, Phil De Luna, Cao-Thang Dinh, Ali Seifitokaldani, Makhosud I. Saidaminov, Chih-Shan Tan, Li Na Quan, Andrew Proppe, Md. Golam Kibria, Shana O. Kelley, David Sinton, and Edward H. Sargent. 2D Metal Oxyhalide-Derived Catalysts for Efficient CO₂ Electroreduction. *Advanced Materials*, 30(38):1802858, September 2018.
- [23] Jianan Erick Huang, Fengwang Li, Adnan Ozden, Armin Sedighian Rasouli, F. Pelayo García De Arquer, Shijie Liu, Shuzhen Zhang, Mingchuan Luo, Xue Wang, Yanwei Lum, Yi Xu, Koen Bertens, Rui Kai Miao, Cao-Thang Dinh, David Sinton, and Edward H. Sargent. CO₂ electrolysis to multicarbon products in strong acid. *Science*, 372(6546):1074–1078, June 2021.
- [24] Angelika A. Samu, Attila Kormányos, Egon Kecsenovity, Norbert Szilágyi, Balázs Endrődi, and Csaba Janáky. Intermittent Operation of CO₂ Electrolyzers at Industrially Relevant Current Densities. *ACS Energy Letters*, 7(5):1859–1861, May 2022.
- [25] Angelika Anita Samu, Imre Szenti, Ákos Kukovecz, Balázs Endrődi, and Csaba Janáky. Systematic screening of gas diffusion layers for high performance CO₂ electrolysis. *Communications Chemistry*, 6(1):41, February 2023.

- [26] Mark Sassenburg, Reinier de Rooij, Nathan T. Nesbitt, Recep Kas, Sanjana Chandrashekar, Nienke J. Firet, Kailun Yang, Kai Liu, Marijn A. Blommaert, Martin Kolen, Davide Ripepi, Wilson A. Smith, and Thomas Burdyny. Characterizing CO₂ Reduction Catalysts on Gas Diffusion Electrodes: Comparing Activity, Selectivity, and Stability of Transition Metal Catalysts. *ACS Applied Energy Materials*, 5(5):5983–5994, May 2022. Publisher: American Chemical Society.
- [27] Thao T. H. Hoang, Sumit Verma, Sichao Ma, Tim T. Fister, Janis Timoshenko, Anatoly I. Frenkel, Paul J. A. Kenis, and Andrew A. Gewirth. Nanoporous Copper–Silver Alloys by Additive-Controlled Electrodeposition for the Selective Electroreduction of CO₂ to Ethylene and Ethanol. *Journal of the American Chemical Society*, 140(17):5791–5797, May 2018.
- [28] Carlos G. Morales-Guio, Etosha R. Cave, Stephanie A. Nitopi, Jeremy T. Feaster, Lei Wang, Kendra P. Kuhl, Ariel Jackson, Natalie C. Johnson, David N. Abram, Toru Hatsukade, Christopher Hahn, and Thomas F. Jaramillo. Improved CO₂ reduction activity towards C₂₊ alcohols on a tandem gold on copper electrocatalyst. *Nature Catalysis*, 1(10):764–771, October 2018.
- [29] Tianyu Zhang, Justin C. Bui, Zhengyuan Li, Alexis T. Bell, Adam Z. Weber, and Jingjie Wu. Highly selective and productive reduction of carbon dioxide to multicarbon products via in situ CO management using segmented tandem electrodes. *Nature Catalysis*, 5(3):202–211, March 2022.
- [30] Xingli Wang, Jorge Ferreira de Araújo, Wen Ju, Alexander Bagger, Henrike Schmies, Stefanie Köhl, Jan Rossmeisl, and Peter Strasser. Mechanistic reaction pathways of enhanced ethylene yields during electroreduction of CO₂–CO co-feeds on Cu and Cu-tandem electrocatalysts. *Nature Nanotechnology*, 14(11):1063–1070, November 2019.
- [31] Chong Liu, Shannon N. Nangle, Brendan C. Colón, Pamela A. Silver, and Daniel G. Nocera. ¹³C-Labeling the carbon-fixation pathway of a highly efficient artificial photosynthetic system. *Faraday Discussions*, 198:529–537, 2017.
- [32] Recep Kas, Ruud Kortlever, Alexander Milbrat, Marc T. M. Koper, Guido Mul, and Jonas Baltrusaitis. Electrochemical CO₂ reduction on Cu₂O-derived copper nanoparticles: controlling the catalytic selectivity of hydrocarbons. *Phys. Chem. Chem. Phys.*, 16(24):12194–12201, 2014.
- [33] Jing Shen, Ruud Kortlever, Recep Kas, Yuvraj Y. Birdja, Oscar Diaz-Morales, Youngkook Kwon, Isis Ledezma-Yanez, Klaas Jan P. Schouten, Guido Mul,

and Marc T. M. Koper. Electrocatalytic reduction of carbon dioxide to carbon monoxide and methane at an immobilized cobalt protoporphyrin. *Nature Communications*, 6(1):8177, September 2015.

- [34] Naoto Todoroki, Hiroto Tsurumaki, Hiroki Tei, Tomohiro Mochizuki, and Toshimasa Wadayama. Online Electrochemical Mass Spectrometry Combined with the Rotating Disk Electrode Method for Direct Observations of Potential-Dependent Molecular Behaviors in the Electrode Surface Vicinity. *Journal of The Electrochemical Society*, 167(10):106503, January 2020.
- [35] Guohui Zhang, Youxin Cui, and Anthony Kucernak. Real-Time In Situ Monitoring of CO₂ Electroreduction in the Liquid and Gas Phases by Coupled Mass Spectrometry and Localized Electrochemistry. *ACS Catalysis*, 12(10):6180–6190, May 2022.
- 5 [36] Tamal Chatterjee, Etienne Boutin, and Marc Robert. Manifesto for the routine use of NMR for the liquid product analysis of aqueous CO₂ reduction: from comprehensive chemical shift data to formaldehyde quantification in water. *Dalton Transactions*, 49(14):4257–4265, 2020.
- [37] Jie Zhang, Wen Luo, and Andreas Züttel. Crossover of liquid products from electrochemical CO₂ reduction through gas diffusion electrode and anion exchange membrane. *Journal of Catalysis*, 385:140–145, May 2020.
- [38] Kentaro U. Hansen, Luke H. Cherniack, and Feng Jiao. Voltage Loss Diagnosis in CO₂ Electrolyzers Using Five-Electrode Technique. *ACS Energy Letters*, 7(12):4504–4511, December 2022.
- [39] Hunter Simonson, Walter Ellis Klein, Danielle Henckel, Sumit Verma, K. C. Neyerlin, and Wilson A. Smith. Direct Measurement of Electrochemical Selectivity Gradients over a 25 cm² Copper Gas Diffusion Electrode. *ACS Energy Letters*, pages 3811–3819, August 2023.
- [40] Fabian Bienen, Dennis Kopljar, Armin Löwe, Simon Geiger, Norbert Wagner, Elias Klemm, and Kaspar Andreas Friedrich. Revealing Mechanistic Processes in Gas-Diffusion Electrodes During CO₂ Reduction via Impedance Spectroscopy. *ACS Sustainable Chemistry & Engineering*, 8(36):13759–13768, September 2020.
- [41] Bronkhorst®. FLUIDAT® on the Net, mass flow and physical properties calculations.

- [42] D. Ambrose, J.H. Ellender, C.H.S. Sprake, and R. Townsend. Thermodynamic properties of organic oxygen compounds XLV. The vapour pressure of acetic acid. *The Journal of Chemical Thermodynamics*, 9(8):735–741, August 1977.
- [43] J. Zielkiewicz, P. Oracz, and S. Warycha. Total vapour pressure measurements and excess Gibbs energies for the binary systems methanol + ethanol, ethanol + 2-propanol, benzene + cyclohexane, benzene + carbon tetrachloride and benzene + ethanol at 303.15 and 313.15 K. *Fluid Phase Equilibria*, 58(1-2):191–209, January 1990.
- [44] Shaun M. Alia, Kimberly S. Reeves, Jefferey S. Baxter, and David A. Cullen. The Impact of Ink and Spray Variables on Catalyst Layer Properties, Electrolyzer Performance, and Electrolyzer Durability. *Journal of The Electrochemical Society*, 167(14):144512, November 2020.
- [45] Nicholas C. Speller, Giorgio Gianini Morbioli, Michael E. Cato, Thomas P. Cantrell, Erin M. Leydon, Britney E. Schmidt, and Amanda M. Stockton. Cutting edge microfluidics: Xurography and a microwave. *Sensors and Actuators B: Chemical*, 291:250–256, July 2019.
- [46] Yurena Seguí Femenias, Ueli Angst, Francesco Caruso, and Bernhard Elsener. Ag/AgCl ion-selective electrodes in neutral and alkaline environments containing interfering ions. *Materials and Structures*, 49(7):2637–2651, July 2016.
- [47] Fabian Bienen, Dennis Kopljär, Simon Geiger, Norbert Wagner, and Kaspar Andreas Friedrich. Investigation of CO₂ Electrolysis on Tin Foil by Electrochemical Impedance Spectroscopy. *ACS Sustainable Chemistry & Engineering*, 8(13):5192–5199, April 2020.
- [48] Abdulhai H. Faqeeh and Mark D. Symes. A standard electrolyzer test cell design for evaluating catalysts and cell components for anion exchange membrane water electrolysis. *Electrochimica Acta*, 444:142030, March 2023.
- [49] B Clément. The Backflush, what is it for, how does it work ?, April 2021.
- [50] Ho-Young Jung, Sheng-Yang Huang, Prabhu Ganesan, and Branko N. Popov. Performance of gold-coated titanium bipolar plates in unitized regenerative fuel cell operation. *Journal of Power Sources*, 194(2):972–975, December 2009.

APPENDIX

Equipment guide for CO₂ electrolysis at a lab-scale

Gas supply

In our setup, CO₂ is supplied from a Linde 5N (i.e., 99.999% purity) CO₂ cylinder. This cylinder is connected to a 2-step reducer, that depressurizes the stream from the bottle's internal pressure to ~5.5 bar, the pressure required by the mass-flow controller (MFC). This 2-step reducer avoids excessive fluctuations in gas-pressure, which might destabilize the pressure equilibrium over the gas-diffusion electrode.

The MFC regulates the gas flow-rate to the cell and is calibrated using CO₂. The controller in our setup is a Bronkhorst® EL-FLOW Select F-201CV, rated to a maximum of 50 sccm, coupled to a Bronkhorst® E-8501 digital readout.

In absence of further pressure regulation in the gas-stream, a manometer may be included between the MFC and the inlet, which helps in controlling the resistance to flow caused by the in-line diagnostic systems downstream, as well as the electrolyzer itself. Additionally, when operating an MEA-electrolyzer, humidification of the stream is required to avoid drying out the membrane. To achieve this, the gas is flowed through a GL-45 thread bottle containing Milli-Q® water (Duran® 4-port GL45 connection with HPLC screwcaps and silicone sealing). This bottle has a gas inlet submerged in the water phase, and an outlet floating above it. The whole is made air-tight by using screwcaps, as shown in Fig. 5.A.1.

If the formation of salt crystals increases the pressure in the system to a point high enough, the humidification device can push the liquid back to the mass-flow controller. To avoid this, a reflux trap can be placed between the outlet of the MFC and the humidification device.

Electrochemical cells

The electrochemical cells reported and displayed in this work are (partially) based on commercially available designs manufactured by Dioxide Materials® (Research Grade 5 cm² Hardware for Carbon Dioxide Electrolysis, see Fig. 5.A.2). The zero-gap membrane electrode assembly setup essentially employs the two endplates (titanium for the anode and stainless steel for the cathode) with a simple two-gasket assembly in-between.

The flow-cell electrolyzer requires adaptations to this design to fit a flowing catholyte compartment and a gas chamber). For this purpose, we 3D printed a catholyte and a gas-chamber with fluid conduction paths that fit the above-mentioned anode block. This allows us to use a transparent PMMA end-block on the gas side, which enables optical tracking of electrode flooding and perspiration of electrolyte.

Current collection in this more complex design is, however, a point of attention. Most carbonous electrodes are sufficiently electrically conductive that a milled stainless-steel plate is sufficient. Exposure to cathodic potentials at this half-cell

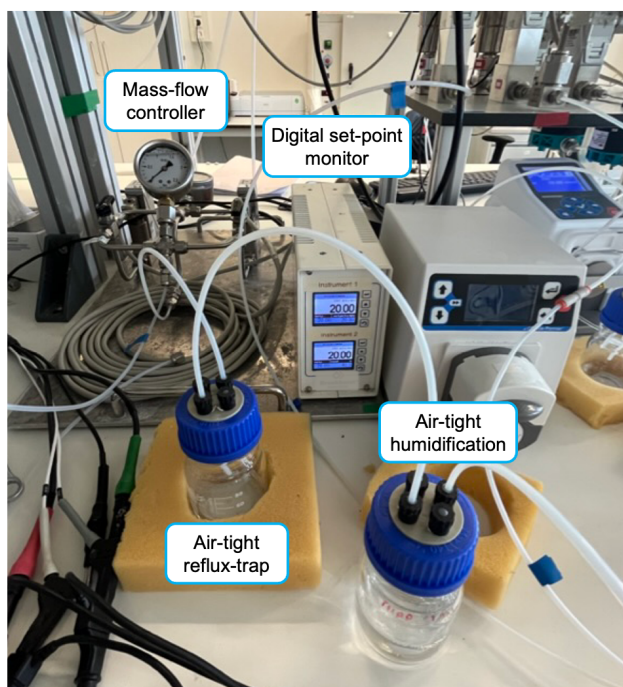


Figure 5.A.1: Complete gas-inlet setup.

prevents oxidation of this plate. For other non-conductive electrode supports, like expanded polytetrafluoroethylene (ePTFE), front contact is needed. In this case we use a precision-cut copper-tape current collector on a 0.5 mm silicone gasket. This is insulated from the electrolyte by the small silicone strip between the hole and the tape and has proven to not intervene in the reaction.

An overview of all mentioned parts can be found in Figure 5.A.2.

In general, the two designs consist of the following components, grouped by place in the depth-direction of the electrolyzer starting from the anode block:

A. Zero-gap MEA:

1. Anode end-block (with isolated bolts)
2. Silicone gasket (~ 0.5 mm) and the anode
3. Membrane
4. PTFE gasket (~ 0.25 mm) and the cathode
5. Cathode end-block
6. Nuts

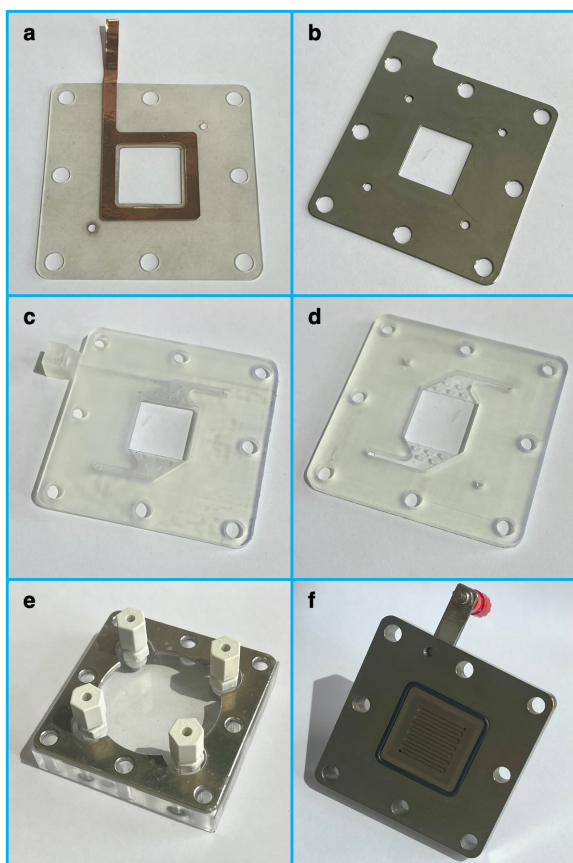


Figure 5.A.2: Main component parts of the described electrolyzer designs. (a) Silicone gasket with front-contact current collector, (b) stainless-steel current collector, (c) 3D-printed (SLA process) catholyte flow channel with turbulence promoters, (d) 3D-printed (idem) gas flow chamber, (e) PMMA-milled end-block with aluminum pressing-plate, and (f) titanium end-block.

B. Flow-cell electrolyzer:

1. Anode end-block
2. Silicone gasket (~ 0.5 mm) and the anode
3. Membrane
4. Silicone gasket (~ 0.25 to 0.5 mm)
5. Cathode flow-field
6. Silicone gasket (~ 0.25 to 0.5 mm)
7. Cathode
8. Current collector

5

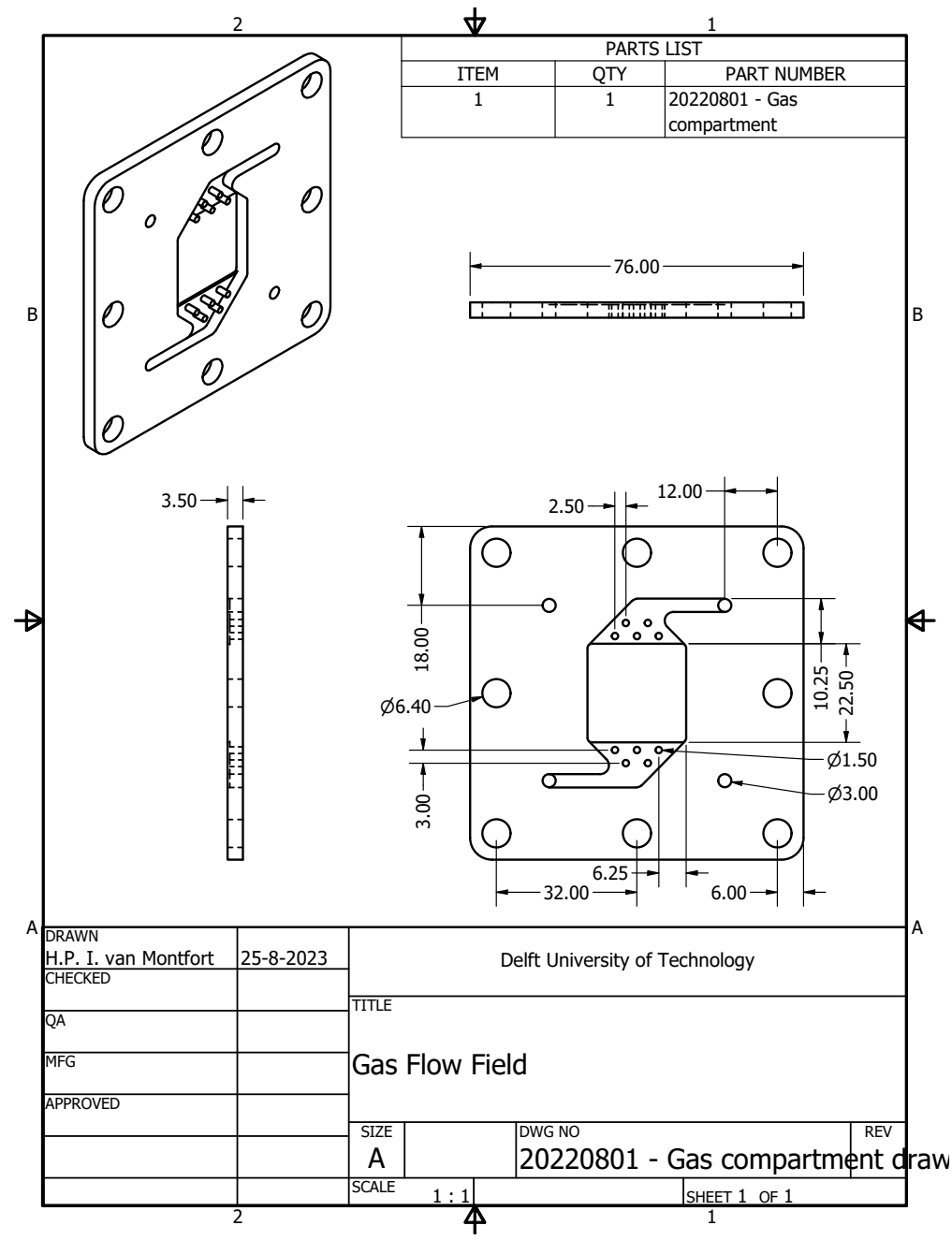


Figure 5.A.4: Technical drawing of the 3D-printable gas flow field.

9. Silicone gasket (~ 0.25 to 0.5 mm)
10. Gas-chamber
11. Viton® gasket (0.5 mm)
12. PMMA end-block
13. Pressing plate
14. Nuts

For illustrative purposes, we have recorded the assembly procedures for each design, included in the original publication. The 3D-printed flow fields are included in the next two pages (Figs. 5.A.3 and 5.A.4). The designs for gaskets and the gas/liquid end-block can easily be derived from these two parts.

Back-pressure regulator (BPR)

Each fluid channel exiting from the electrolyzer has a back-pressure regulator in our setup. These controllers are designed to maintain a set-point pressure and ensure a stable operation of the system. To achieve this, a pressure sensor is coupled to a syringe valve, and the couple is controlled through a commercial controller. The specification for each channel can be seen in Table 5.A.1.

5

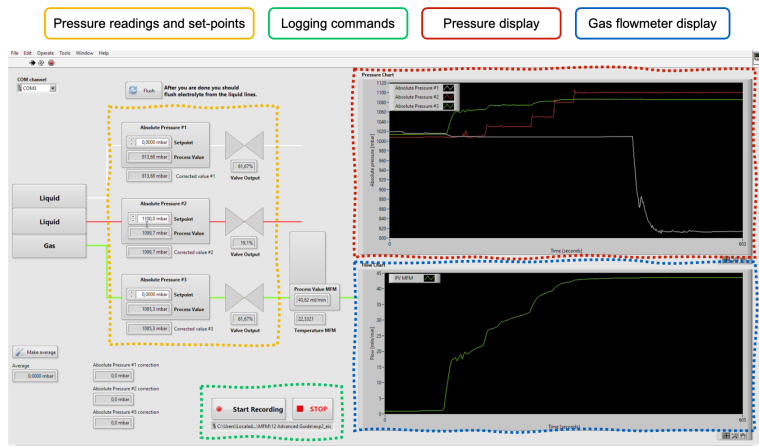


Figure 5.A.5: Back-pressure regulator control software UI written in LabView.

The entire system is operated through a proprietary LabView interface (see Fig. 5.A.5) that allows for real-time monitoring, using set-points for each stream independently, and recording data to a local file. A picture of the setup can be seen in Fig. 5.A.6.

Table 5.A.1: Component list of bench-scale back-pressure regulator

Channel	Purpose	Item	Specs	Indications
ALL	Controller	Bronkhorst® E-8501R	-	-
	Alarm System	See the dedicated section		
Anolyte	Pressure measurement	Bronkhorst® EL-PRESS P-502C	2.5 bar, 25 °C	Rinse thoroughly with Milli-Q water after operation with opened valves
	Pressure regulation	Bronkhorst® C5I-ITU	1 to 2.5 bar, 50 sccm H ₂ O	
	Pressure measurement	Bronkhorst® EL-PRESS P-502C	2.5 bar, 25 °C	
Catholyte	Pressure regulation	Bronkhorst® C5I-ITU	1 to 2.5 bar, 50 sccm H ₂ O	Avoid penetration of electrolyte and prevent accumulation of salts height
	Mass-flow measurement	Bronkhorst® F-101D	1.5 bar, 100 sccm CO ₂	
	Pressure regulation	Bronkhorst® P-702CV	1 to 2.5 bar, 100 sccm CO ₂	

5

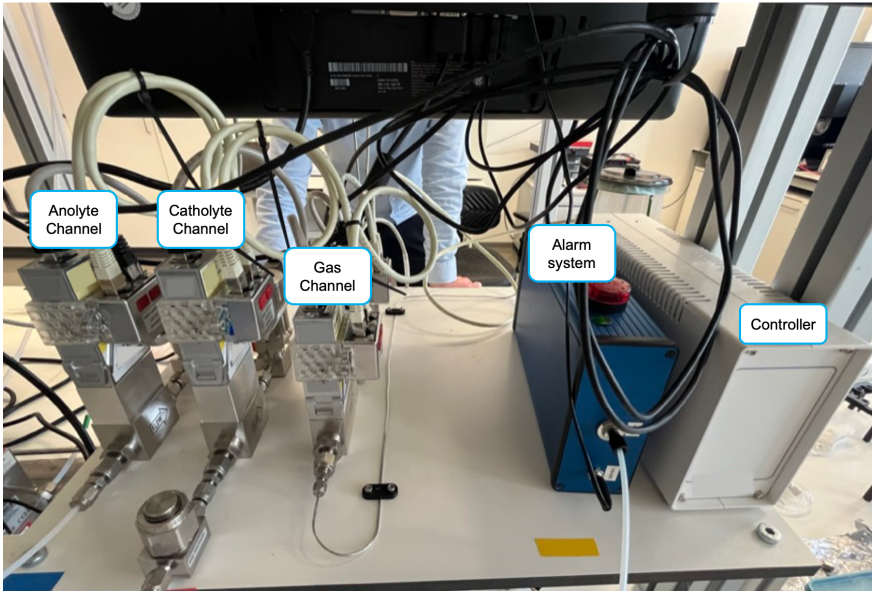
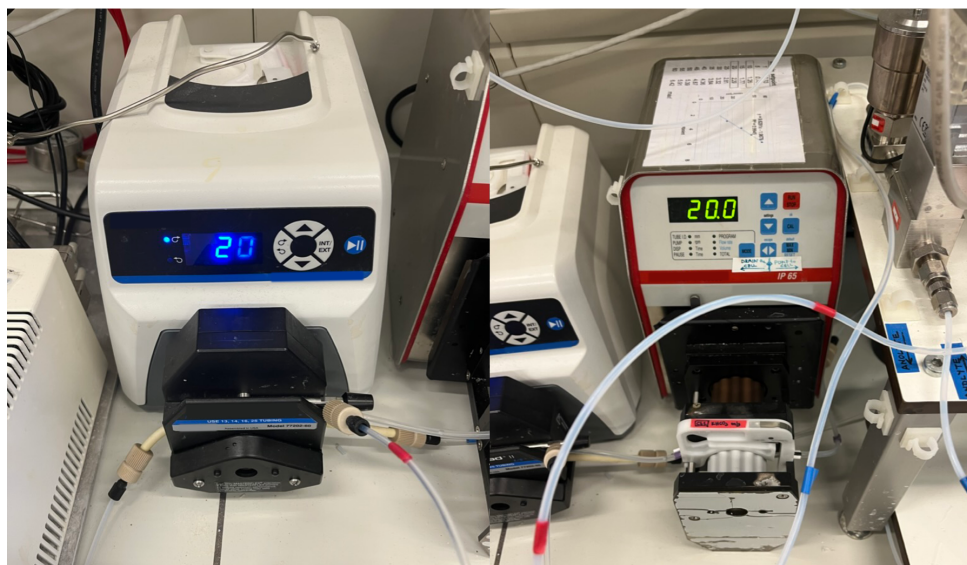


Figure 5.A.6: Bench-scale back-pressure regulator.

Peristaltic pumps and cabling

An array of options is available to create the fluid flow needed for the operation of both the MEA and the flow electrolyzer. Due to the corrosive nature of most electrolytes used in literature, however, a peristaltic pump offers the most versatile solution that is resistant to basic electrolytes. In addition to this, the peristaltic pumps we describe have a very wide operational range (from about 0.2 sccm cm⁻²

to 20 sccm cm^{-2}). These pumps function by rotating a set of rollers mounted on an axis, compressing and decompressing a flexible tubing, mimicking the peristaltic movement of an esophagus (hence the name), see Fig. 5.A.7.



5

Figure 5.A.7: Two examples of peristaltic pumps used in the setup.

The choice of cabling should rely on compatibility with both the flexible tubing of the pumps and the fittings of the cell/BPR system. In our case, 1/8-inch OD translucent tubing allows us to connect to the Cole-Parmer fittings of the cell, the Swagelok fittings of the BPR, the IDEX® P-767 tubing adapters and the fittings of the screwcaps of electrolyte beakers, providing a universal solution.

Pressure dampeners

The oscillatory movement of the peristaltic pump causes pressure spikes and drops in the electrolyte channels. These oscillations can cause flooding through penetration, bulging of the GDE or deformation of the membrane if the pressure in the liquid channel is high enough. To dampen this effect, the setup includes two pressure dampeners for each electrolyte channel (see Fig. 5.A.8).

The dampeners (KNF® FDP 1.10 and 1.06) are arranged from big to small (maximum allowed pressure of 60 mWg and 20 mWg, respectively) in the direction from the pump to the electrolyzer. Their inclusion results in a noticeable reduction in oscillation of liquid pressure (see Fig. 5.2 in the main text).



Figure 5.A.8: Pressure dampeners, screwed to the bottom of the BPR-setup.

5

Liquid-trap and alarm system

Perspirations, flooding, and outright puncture of the GDE can result in the escape of electrolyte to the downstream of the gas circuit. Irruption of liquid in the gas chromatography system further down the line causes serious malfunction of this device, leading to liquid and salt (carbonates formed in the alkaline electrolyte) in the columns. Since this often results in servicing of the GC being required, it is of high importance to avoid liquid entry to the highest degree possible. For this purpose, our setup has a two-step security system.

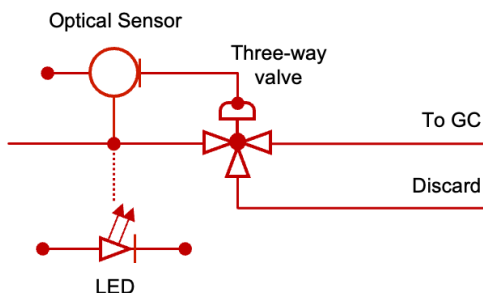


Figure 5.A.9: Working scheme of the alarm system for fluid detection in the gas stream.

On one hand, a liquid trap (GL45 40 mL Duran flask with a hermetic septum-lid) is an air-tight enclosure with an inlet and outlet, where possible liquid is

accumulated. This is placed right after the electrolyzer, like the humidification device shown before (see Fig. 5.A.1).

Further down the line, an alarm-box device based on a laser system detects whether any droplets travel through the gas channel towards the GC. This system diverts, upon trigger, the gas- stream to a purge and requires a reset afterwards, so any perspiration will result in the experiment being stopped, as no product detection is possible afterwards.

The feedback loop in this system, which we dubbed as ‘blue box’ (due to the color of its enclosure) is based on a photo-diode detector (TT Electronics OCB350L0-62Z) that detects changes in refractance inside a transparent tube. When a liquid mass passes through this detector, it actuates on a three-way valve, that diverts the flow to a discard channel (see Fig. 5.A.9). To alert the operator, the system sounds an alarm until it is reset in case of flooding. It only directs gas to the GC if connected to the power and can only be reset manually after opening the device.

5

Pressure relief-valve

Since the circuitry in the GC has an inherent pressure drop attached to it, the injections are noticeable on the mass-flow meter readings. These injections cause pressure spikes that may be detrimental for the integrity of the GDE upstream in flow- cells.

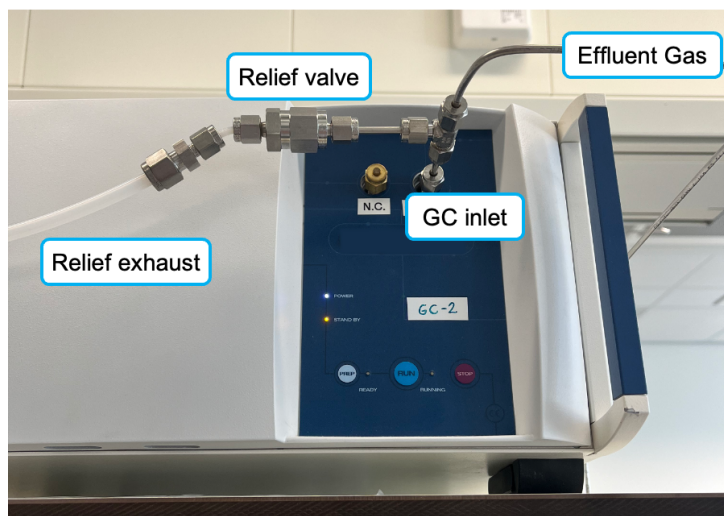


Figure 5.A.10: Relief-valve before the GC inlet.

To avoid a pressure spike, we have included a pressure-relief valve before the inlet of the GC injection intake. These pressure relief-valves (see Fig. 5.A.10) avoid an exaggerated pressure spike on the gas channel, acting as a downstream damp-

ener to the effluent stream from the electrolyzer. We employ, depending on the gas flow-rate, either a 1 psi or a 5 psi relief-valve. The exhaust of this valve is directly routed to the gas vent.

Gas chromatography (GC)

Description

Gas chromatography is a powerful tool to analyze the composition of a gas product-stream. By placing a gas-chromatograph (GC) in-line in our setup, we can continuously monitor the species in the effluent streams of our electrolyzers. The device we employ is a Compact GC 4.0, by Global Analyser Solutions™. A comprehensive specification of columns, detectors and oven settings can be found in Table S2.

Our chromatograph includes three different detectors, in two separate column ovens. The first detector is a flame-ionization detector (FID). In this detector, the analyte is conducted through an ionization flame. The change in signal induced, combined with the retention time, gives information on the kind and concentration of each hydrocarbon species. The other two detectors are thermal conductivity detectors (TCDs) employed to detect, respectively, carbon monoxide and hydrogen. In these detectors, a stream's thermal conductivity is compared to a reference. The TCD – CO channel uses He as carrier gas, which has similar thermal conductivity to H₂ and therefore makes H₂ poorly detectable. Similarly, the TCD – H₂ channel uses Ar as a carrier gas, which has similar thermal conductivity to CO and is unable to accurately detect CO.

Table 5.A.2: Specifications of the detailed gas-chromatography device.

Detector	Oven	Oven Temp. [°C]	Column	Carrier gas	Injector Temp. [°C]	Injection pressure [kPa]	Detector Temp. [°C]	Reference
FID	A	65	RTX-1 5μm (RESTEK)	He	80	70	150	H2:Air (35:350 sccm)
TCD-CO	B	45	CP-molsieve 5A 30μm (Agilent)	He	80	70	110	He (1 sccm)
TCD-H2	B	45	CP-molsieve 5A 30μm (Agilent)	Ar	80	75	110	Ar (1 sccm)

A high throughput product detection using GC requires, on one hand, a short injection time. A limiting factor for an injection's duration is, in most cases, the long time required for the FID channel to distinguish different species. By sacrificing resolution in the ethylene/ethane peaks (allowing them to partially overlap), we reduced the required time for the FID channel down to a theoretical ~1.5 min. Another limitation is the accumulation of CO₂ in the TCD-CO detector's column due to the polarity of the packed molecular sieve column. This causes shifts in the baseline (as can be seen in Fig. 5.A.11). To reduce this effect, we included a back-

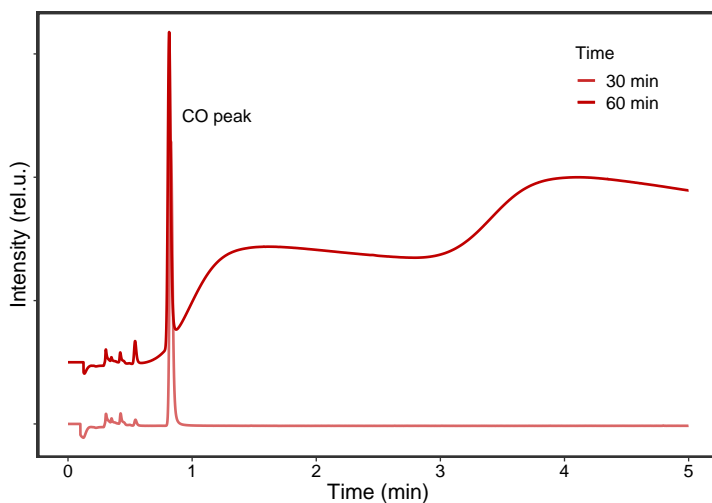


Figure 5.A.11: Accumulation of CO₂ and its effect on the CO-detector signal (baseline shifted for illustrative purpose).

flush procedure in the GC's routine, which evacuates as much gas as possible in the shortest amount of time. This results in a total injection duration of 5 min., which allows us to reliably analyze product composition 12 times per hour.

Calibration

To assign each signal to a species, calibration is needed. For high current-density CO₂RR setups, the calibration bottles should have a high concentration of possible product species (1-5 vol%, or 10,000-50,000 ppm, see Fig. 5.A.12). For low current densities, lower concentrations may be used. To representatively simulate a typical product stream, the balance gas employed may be CO₂ itself. It is also important to calibrate at a representative flow-rate (which also shortens the saturation time of the stream, so that calibration duration is limited). An overview of the concentrations and flow-rate settings we use in our calibration procedures can be found in Table S3. In this table, the set-point for a CO₂-calibrated MFC is displayed as well. After connecting the calibration stream to the GC, the procedure requires two blank injections to saturate the sample-chamber. After this, we run four injections per bottle, and use the average peak-value of each species for the calibration. Calibration streams should be ordered such that concentration of relevant species is ascending (see Table S3). This reduces saturation time in the sample-chamber (since it is easier to saturate a gas recipient than to flush it).

As our mass-flow controller (MFC) is calibrated for CO₂, the set-points during calibration need to be adjusted according to the composition of each gas-stream.

For this, we compensate using a conversion factor based on the heat capacity of each gas species. The equivalent flow-rate then equals:

$$\phi_{sp} = \phi_r \cdot \left(\sum_n^i x_i \cdot C_i \right)^{-1} \quad (5.1)$$

where ϕ_{sp} is the required set-point, ϕ_r is the real flow-rate, x_i the molar fraction of the gas and C_i the conversion factor of each species.[41]

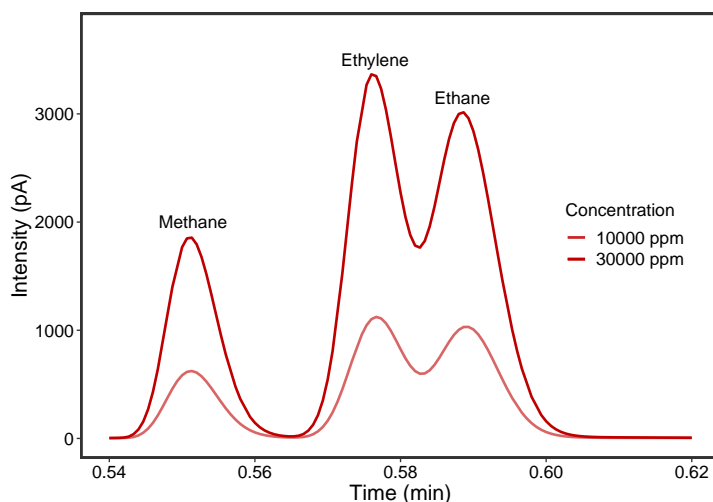


Figure 5.A.12: Calibration curves for light hydrocarbons using the FID-detector for high concentrations.

Table 5.A.3: Concentration of species in calibration gases and MFC set-point for flow-rates equivalent to 20 sccm of CO₂.

Bottle	Balance gas	Conversion factor	ϕ_v [sccm]	[H ₂] (ppm)	[O ₂] (ppm)	[CO] (ppm)	[CH ₄] (ppm)	[C ₂ H ₄] (ppm)	[C ₂ H ₆] (ppm)	[C ₃ H ₈] (ppm)
1	Ar	1.400	10.57	100	0	25	10	10	10	0
2	He	1.409	10.51	200	0	100	200	100	100	20
3	He	1.403	10.55	1000	0	1000	1000	500	500	100
4	N ₂	0.998	14.83	1000	1000	1000	1000	1000	1000	0
5	N ₂	0.990	14.94	10,000	0	10,000	10,000	10,000	0	0
6	N ₂	0.972	15.23	30,000	0	30,000	30,000	30,000	0	0

Before each calibration is carried out, a so-called bake-out of the column ovens is required. By elevating the temperature (in our case, higher than 120 °C but not surpassing the design specifications of 150 °C), residual species present in the column are evacuated. This is especially the case for carbon-monoxide, which

tends to strongly attach to the separators in the column. This results in its signal ‘creeping’ to lower residence time values over time. Given enough time, this leads to CO overlapping with methane signals in the TCD detector. Exit valves must be open during bake-out, and the device should be given a proper amount of time to evacuate the residues. In our case, this results in a bake-out of 48 to 72 h.

Quantification

Upon detection by the GC, the device calculates a concentration value by extrapolating the area of each peak based on the calibration. This concentration can then be transformed to a faradaic efficiency (or: how many of the supplied electrons to the system are used for the catalysis of a certain product) by the following equation:

$$FE_{\%} = \phi_v \cdot \frac{z_i c_i F}{i} \cdot 100 \quad (5.2)$$

where ϕ_v is the volumetric flow-rate leaving the electrolyzer, z_i the number of electrons involved in the reaction towards product i , c_i the concentration of said product, F is the Faraday constant, and i the current applied on the cathode.

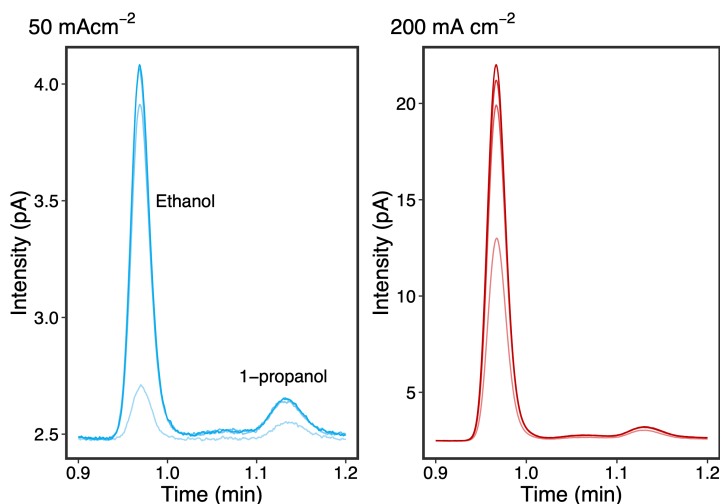


Figure 5.A.13: Peak intensity of vapor-phase ethanol and 1-propanol in the FID chromatographs at -50 and -200 mA cm^{-2} .

Some products of CO_2 -electrolysis are liquid-phase compounds with a high vapor-pressure, such as ethanol, propanol, and acetate.[42, 43] This means that, in theory, they could be detected by the FID sensor in the GC. In practice, however, the saturation times of these alcohols last multiple injections, especially at

Table 5.A.4: Comparison of calculated FE for ethanol through GC and HPLC results on a copper GDE.

Current density [mA cm ⁻²]	Injection	GC FE [%]	HPLC FE [%]
-50	1	1.50	14.8
	2	10.4	
	3	11.5	
	4	11.5	
-200	1	17.4	33.5
	2	28.6	
	3	30.8	
	4	32.1	

5

higher current densities (see Fig. 5.A.13). A saturation time of 2-3 injections is considerably high, and results in a loss of resolution of time effects. The effects of this delay are illustrated in Table 5.A.4, where GC results are compared to liquid chromatography for the same experiments.

On top of this, alcohols tend to strongly attach to the Molsieve in the GC's separation columns, which means a rest signal is preserved through multiple runs. This is only suppressed by baking-out the columns at high temperatures (> 120 °C) and recalibrating the system, as explained before.

Using GC to detect alcohols and other volatile products is, nonetheless, a valid way of monitoring and preemptively assessing the selectivity of a certain catalyst towards these products. Actual faradaic efficiency values calculated after a couple of injections do not substantially differ from high-resolution HPLC calculations (see Table 5.A.4).

High-Performance Liquid Chromatography (HPLC)

Description

Several catalysts for CO₂RR are known to produce liquid-phase products. Copper, for example, generates several oxygenate hydrocarbons (like ethanol, acetate and propanol), whereas tin generates formate, mainly.[26] These products can be detected using high performance liquid chromatography (HPLC) by extracting liquid samples from the catholyte and anolyte reservoirs during operation.

An HPLC device (in our setup, an Agilent Technologies 1260 Infinity II HPLC, see Fig.5.A.14) functions similarly to a GC. A liquid sample of electrolyte is injected to a mobile phase (0.05 M H₂SO₄), which protonates the sample and leads the sample through the 300 mm heated Hi-Plex H column (T = 50 °C, P ~ 36 bar). This column consists of micron-sized Si beads with functional C18 chains that retain



Figure 5.A.14: Agilent Technologies 1260 Infinity II HPLC setup.

molecules for a specific duration of time. Smaller molecules tend to move through the column quicker (formic acid takes, for example, 17 mins.) while larger carbon chains can take much longer (1-propanol, 32 mins.). The separated mixture goes through the Variable Wavelength Detector (VWD, dual wavelength: 210 nm and 280 nm) that measures a change in the optical transmission of specific wavelengths, detecting acids and aldehydes. In the case of CO₂ reduction, formic acid, acetic acid, and acetaldehyde are of interest. Secondly, the Refractive Index Detector (RID, T = 40 °C) is used to detect alcohols, primarily ethanol and 1-propanol.

Calibration

The main products of interest here (formic acid, acetic acid, acetaldehyde, ethanol and 1 propanol) are calibrated at 8 levels between 10 and 5000 ppm, to have a broad testing range with high confidence ($R^2 > 99.9\%$ for all components). For this, we make fresh standard-solutions with the desired concentrations for each calibration. Before each calibration, a sample of Milli-Q water ($R \geq 18 \text{ M}\Omega$) is injected to flush the column of remaining analytes and impurities and set an analytical baseline.

Quantification

Quantification of each product's concentration is calculated similarly to GC results. After having obtained the concentration value for each sample, the faradaic efficiency of each product can be calculated with:

$$FE_{\%} = V \cdot \frac{z_i c_i^{\text{eff}} F}{C} \cdot 100 \quad (5.3)$$

where V is the total volume of the electrolyte at the time the sample was taken, z_i the number of electrons involved in the reaction towards product i , c_i^{eff} the effective concentration increase of said product (the concentration increase compared to the last sample taken), F is the Faraday constant, and C the charge passed through the cathode in the studied interval of the experiment.

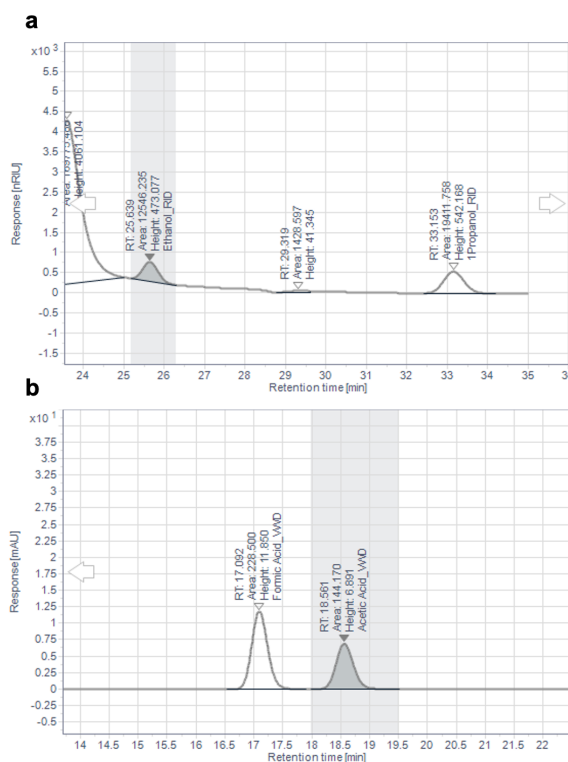


Figure 5.A.15: HPLC chromatographs. (a) RID-detector for oxygenate hydrocarbons, and (b) VWD-detector for carboxylic species.

To quantify each peak properly, a pure Milli-Q sample is analyzed before every sequence. This provides a baseline that can be subtracted from consequent measurements. Usage of a Milli-Q sample before the run also purges the column from any residual analytes.

It is important to realize that, as liquid samples are taken in batch mode and analyzed afterwards, the FE calculation is slightly different than that of the GC.

Here, we employ an effective concentration change. This value is obtained by subtracting the previously measured concentration of product *i* from the following samples to obtain the change of concentration over a period.

Another consideration in performing HPLC for CO₂RR systems is the need to avoid high concentration of ions in the solution. Most CO₂RR experiments employ highly alkaline solutions (e.g. 1M KOH) as the electrolyte. Since the mobile phase of the HPLC is highly acidic, this may result in precipitation of salts in the column. Additionally, a high concentration of bicarbonate species may interfere with the ethanol signals, resulting in low-quality analyses (see Fig. 5.A.15a). To avoid this, samples of high-concentration electrolytes must be diluted before quantification using Milli-Q water. For our setup, the highest threshold to avoid bicarbonate-ethanol interference is 1 M of bicarbonate in the sample.

Nuclear Magnetic Resonance (NMR)

Another commonly used technique for quantification of liquid products from CO₂ electrolysis is proton nuclear magnetic resonance spectroscopy (1H NMR). Here, hydrogen protons in a molecule are excited using a constant magnetic field and an oscillating weak magnetic field to produce electromagnetic signals.

1H NMR acquisition parameters

To improve the signal as much as possible, two parameters can be adjusted:

- 1. Number of scans** The signal to noise ratio is proportional to the square root of the number of scans, so a higher number of scans results in a better signal.
- 2. Relaxation delay (d1-time)** The relaxation delay should be set to at least 5 times the highest T1 value amongst all sample species. The T1 value is a chemical species property: it's the time necessary for each compound to relax back to its equilibrium state after a magnetic pulse has been applied. Hence, picking a too low d1-value can result in a loss of response.

Quantification

To perform H-NMR successfully, one should consider that:

1. An internal standard is necessary to calculate concentrations of compounds
2. The internal standard must be soluble in the electrolyte and NMR solution and should not decay over time
3. Its chemical signal must be unique and stable, not overlapping with other signals

4. Suggested internal standards are maleic acid and DMSO
5. Spectrum must be in a good phase and with a proper baseline

A very appropriate internal standard is maleic acid. This compound is soluble in most deuterated solvents and has comparatively a much lower number of protons (2) compared to DMSO (6). Its chemical shift is around 5.8 ppm, which does not interfere with any CO₂RR product peak, such as formate, ethanol, and acetate.

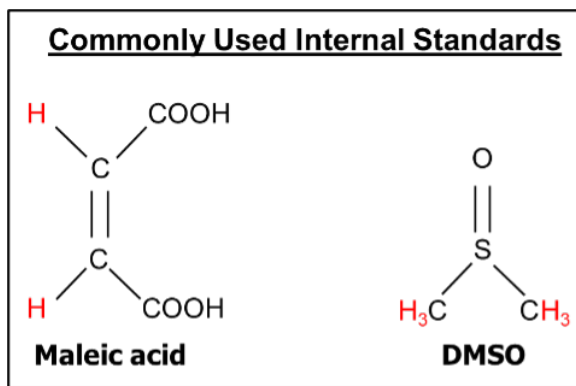


Figure 5.A.16: Protons in maleic acid (left) and DMSO (right).

The concentration of a specific compound can then be calculated as follows:

1. Integrate the maleic acid peak
2. Adjust the integrated value to 2 (the number of protons in maleic acid)
3. Integrate the rest of the products accordingly, each of them normalized to the number of protons present

The molar concentration is then:

$$c_i = \frac{i_i}{i_{std}} \frac{n_{std}}{n_i} c_{std} \quad (5.4)$$

where i_i and i_{std} are the integrals of the compound and the internal standard, respectively, and n_i and n_{std} the number of protons in each of them. Faradaic efficiencies are calculated identically to as described in the HPLC section.

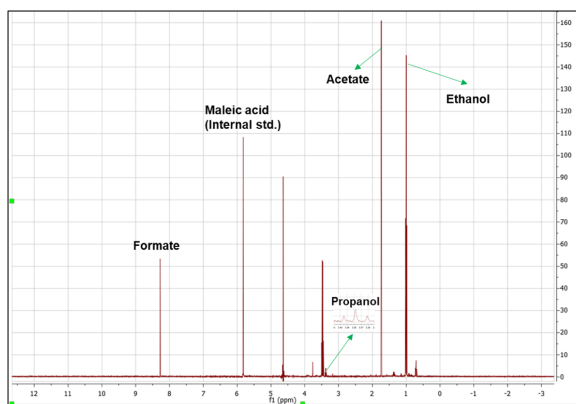


Figure 5.A.17: ^1H -NMR spectrum of liquid products from CO_2RR for a Cu-based MEA electrolyzer.

Sample preparation

To prepare the samples for analysis:

1. Prepare a stock solution of internal standard by dissolving 0.046 g of maleic acid in 10mL of D_2O (40 mM)
2. Fill an NMR tube with 550 μL of the sample electrolyte, followed by 40 μL of the maleic acid dilution and 10 μL of D_2O .
3. Shake the tube gently to mix the solvents
4. Apply water suppression technique during the measurement to suppress H_2O -peaks

Materials and Methods

This section details the preparation, storage, and usage methods of all necessary materials for experiments involving the detailed electrolyzers in the main manuscript.

Preparation of materials

Certain materials require special attention during design, preparation, and assembly of the electrolyzer experiments. This section describes our handling and storage procedures.

Electrodes

Most reported electrodes in literature consist of a carbon gas-diffusion layer and a carbon-bonded PTFE layer (the micro-porous layer). These can be acquired as sheets of various formats (commonly roughly a DIN A4). We cut these sheets to the desired format on reticulated cutting mats using a scalpel. Special care is needed in not touching the surface directly – placing sacrificial papers on both sides of the electrode prevents excessive contamination.

We then deposit catalyst layers by either automated spray deposition[44] (by a CZ Robotics® CNC Airbrush) or DC Magnetron sputtering (AJA International Inc.). As some catalysts oxidize in contact with air, we store freshly produced GDE's in a glovebox system (< 0.1 ppm for both O₂ and H₂O). These are only retrieved when assembling the electrolyzer, guaranteeing their conservation.

After running, and to avoid the accumulation of salts on the catalyst surface post-mortem, we clean the electrodes by immersion in Milli-Q water repeatedly and with care. The glovebox also serves for long-term storage.

Membranes

Most membranes used in CO₂RR experiments are anion-exchange membranes (as OH⁻ is the charge-carrying anion in most cases). These membranes are usually delivered and stored in a wet state. It is important to maintain wetting of these membranes during storage and operation, as they plasticize and defunctionalize when upon drying.

These membranes (like Sustainion® X37-50) come packed between two PP back-ers. They can easily be cut using the reticulated cutting mat and the scalpel. It is important that after cutting the membranes be separated from the backers to activate properly. The best way to differentiate the membrane from a backer is its reaction to wetting: the membrane will curl on itself, while the backer will show no reaction.

Activation should follow the manufacturer's guidelines. For Sustainion's, for example, this involves sustained storage during 24 h in a 1M KOH solution, rinsing and long-term storage in a fresh 1M KOH solution.

Membranes may be reused after usage in a flow cell electrolyzer if optically free of defects or debris. The compression pressure in zero-gap assemblies usually imprints catalyst layer residues on the membrane, rendering them unusable for further experiments.

Gaskets

Materials for gaskets should be flexible and elastic enough to withstand deformation over time. For this, we use mainly silicone, EPDM/Viton® or PTFE gaskets. Attention should be paid to their thickness: upon compressing the electrolyzer, they should leave no gaps between the constituent parts, ensuring equal compression over the entire active area.

While hand-cutting gaskets is a viable method for initial experimentation, we recommend mechanized solutions, like a knife plotter.[45] These devices translate a path design to a perfectly cut gasket, which improves device stability and avoids leakage.

Reference electrodes

Excluding complex state-of-the-art designs,[38] reference electrodes are used in a flow cell electrolyzer to monitor the voltage drop between the electrolyte and the cathode. Given the constricted dimensions of the catholyte flowing plate, the reference electrodes must be of a very small diameter. We accomplish this by employing so-called leak-less electrodes.

For relative low pH values (i.e., bicarbonate electrolytes), a leak-less Ag/AgCl suffices. These electrodes require no long-term maintenance other than rinsing after usage and storage in saturated chloride solutions. They are also suitable for usage in ionic liquids. We use a variety of Ag/AgCl electrodes, like eDAQ®'s ET072-1. Although they are stable, they should be periodically monitored to ensure their readings are still stable. This is easily done by employing a standard reference electrode as a counter electrode in an open circuit setup. Connecting the leak-less electrode to the working-sense channel of the electrode and the standard electrode to the reference channel gives an insight of the stability of potential reading of the leak-less electrode.

On the other hand, when using high pH electrolytes, where Ag/AgCl electrodes have been proven to be unstable,[46] we recommend usage of a leak-less RHE electrode (Gaskatel® Mini- HydroFlex). These use a small replaceable hydrogen cell to supply the Pd-Pt electrode inside. These replaceable hydrogen supplies have a shelf-life of 12 months and must therefore be eventually replaced. The advantage of using these electrodes is that potentiostat readings are already vs. RHE, which simplifies data treatment and reduces conversion errors regarding pH gradients in the cell.

Assembly of the electrolyzers

Assembly of a flow-cell electrolyzer

1. Start with the anode-block with the screws in place. To improve reproducibility, a 3D-printed block with the same dimensions as the block and holes for the screw-tops can be printed (see movies in the original publication).
2. Place the anode gasket and the anode in their place.
3. Place, on top of this, the membrane. If you use wet membranes, make sure it is evenly spread over the anode and no creases are visible.
4. Place the membrane gasket on top. Make sure there are no droplets between the gaskets: upon pressing, droplets can form liquid channels that open a leakage pathway.
5. If assembling a flow-cell, place the catholyte channel on top of the gasket. Make sure you insert the reference electrode and tighten its screw before circulating the electrolyte. Place a gasket on top of the catholyte channel.
6. If assembling a flow-cell, place the cathode GDE on the opening, making sure it is well centered.
7. If assembling a flow-cell, place a current collector to the back of the electrode. Place, on top of this current collector, another gasket, and the gas-chamber. On top of the gas-chamber, place another gasket, and finally the end-block. If your end-block is brittle, use a compression plate and screw everything hand-tight.
8. Place the electrolyzer upright on the desk and screw, crosswise and with a torque screwdriver, all the bolts tight. Our electrolyzer operates best after screwing at a 1.5 to 2 N·m torque force. Take care of not damaging the reference electrode if this is already in place.

Assembly of a zero-gap MEA electrolyzer

1. Start with the anode-block with the bolts in place. To improve reproducibility, a 3D-printed block with the same dimensions as the block and holes for the screw-tops can be printed (see movies in the original publication).
2. Place the anode gasket and the anode porous transport layer (PTL) in their place.

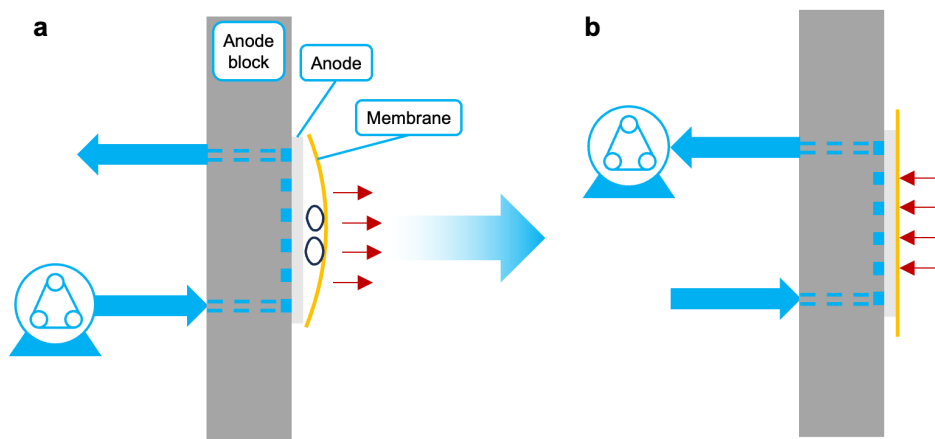


Figure 5.A.18: Pump placement influences the stability of the anode-membrane interface in flow cells. (a) Forward-pumping at high current densities can result in bubble accumulation and bulging of the membrane. (b) Sucking the electrolyte through the compartment avoids these complications.

3. Place, on top of this, the membrane. If you use wet membranes, make sure it is evenly spread over the anode and no creases are visible.
4. Place the membrane gasket on top. Make sure there are no droplets between the gaskets: upon pressing, droplets can form liquid channels that open a leakage pathway.
5. Place the cathode PTL or electrode on top of the membrane, making sure it is perfectly centered so the entire gas-channel is covered by the macro-porous layer of the electrode.
6. Place the end-block on top, screw all the bolts hand-tight.
7. Place the electrolyzer upright on the desk and screw, crosswise and with a torque screwdriver, all the bolts tight. Our MEA electrolyzer operates best after screwing at a 2 N·m torque force.

Start-up routines

In this section we will walk through both the start-up of the fluid streams and the diagnostic electrochemical techniques we recommend running before an experiment.

Starting the flow

In a flow-cell electrolyzer it is key to maintain separation of the three chambers and avoid contact of the membrane and the electrode, be it due to elasticity of the membrane or under- pressure in the catholyte compartment. Therefore, upon assembly of the electrolyzer and connection to the fluid loops:

1. Start the gas-flow into the system. It is preferable to do so instants before hooking the cell up so the upstream cabling is saturated with CO₂. Monitor the gas-flow using your mass-flow meter (MFM).
2. Start the catholyte pump, at a low flow-rate. Track the advancement of the catholyte through the cabling and play close attention to the progress of the liquid. Upon entry of the catholyte to the cell, track the evolution of gas-flow to the MFM, this should go up, as less gas can cross over to the catholyte stream.
3. Increase the pressure on the catholyte stream until it avoids crossover of gas- bubbles. Indications of this are the flow-rate of gas to the MFM reaching saturation **and** the absence of bubbles in the effluent catholyte stream. To avoid sudden breakthrough of electrolyte through the gas-diffusion electrode, increase its pressure in small steps of 10-20 mbar. Give the gas stream enough time to saturate. **REMINDER:** due to dissolution of CO₂ in alkaline media, the effluent gas stream to the GC may not be the same as the inlet pressure upon rest. This depends on the alkalinity of your electrolyte. E.g., our setup reads ~ 43 sccm at the MFM when feeding 50 sccm of CO₂ to a 20 sccm 1M KOH flowing electrolyte.
4. When the gas-catholyte interface is stable, turn on the anolyte flow. Watch the cell for any possible leakages. The pressure in your anolyte compartment should remain smaller than that of the catholyte compartment, to make sure the membrane remains flat with the anode and does not bulge inside the catholyte chamber.
5. **OPTIONAL:** In addition to above steps, you might consider changing the pumping direction of your anolyte stream. Reason for this is: at high current densities, oxygen gas formation at the anode might accumulate and bulge (or even rupture) the membrane. This means the pressure in your anolyte chamber will increase gradually during the experiment and destabilize your system. To avoid this, circulate your anolyte stream using the peristaltic pump to 'suck' out electrolyte from the upper outlet. This will avoid major bubble accumulation and provide the anolyte chamber with a convenient

under-pressure that keeps the membrane flat with the anode. A graphical scheme of this can be found in Fig. 5.A.18.

6. If your catalyst is prone to corrosion in the electrolyte's pH or ionic species, start reducing currents as soon as possible to avoid excessive degradation. The flowing nature of the catholyte in this cell can dissolve and damage your catalyst interface.

As the MEA design is simpler, its startup is also quicker. In this case:

1. Start the gas-flow before assembling the system. As we are humidifying the inlet gas-stream, we want both the humidification and the reflux trap to be fully saturated with CO_2 the moment we connect the gas-stream.
2. Connect the electrolyzer to both anolyte and gas fluid streams. You should see an immediate increase of gas flow in the MFM, as gas crossover to the anolyte stream is blocked by the polymeric membrane in this case. A flow lower than the inlet is still normal due to the CO_2 buffering effect.
3. Start the electrolyte pump. As gas evolution in the anode chamber is less probable in this case (i.e., the MEA is clamped between two rigid blocks), the pump location is less influential.
4. Consider the sensitivity of your catalyst in starting cathodic currents to stabilize it. Corrosion in open circuit can influence its performance on the long run.

Diagnostic electrochemical routines

A set of electrochemical routines can be run after assembly of the electrolyzer to quickly assess the functionality of the system at an early stage. Such diagnostic techniques are a quick way of avoiding running long-term experiments on faulty systems. They can also be integrated in a long-term test to study the stability and evolution of cells or catalysts.

Electrochemical Impedance Spectroscopy (EIS) EIS imposes an alternating current (AC) on the DC signal to obtain a frequency response of the system. This enables a separation of the factors affecting the resistance and capacitance of the electrical circuit studied (in this case, the electrochemical cell).

This signal can be applied at open circuit (no applied potential), or in so-called potentiostat (at a fixed cell potential, PEIS) and galvanostatic (at a fixed current, GEIS) modes. A typical closed-circuit electrolyzer will result in a defined semi-circular plot (see Fig. 5.A.19a). An open or defect system, e.g., due to a pierced

membrane in an MEA electrolyzer, results in different readings (Fig. 5.A.19b). This is, then, a quick way to diagnose the viability of an electrolyzer from the early start of an experiment. More resources on the interpretation and parameter settings of EIS routines are available elsewhere.[47, 48]

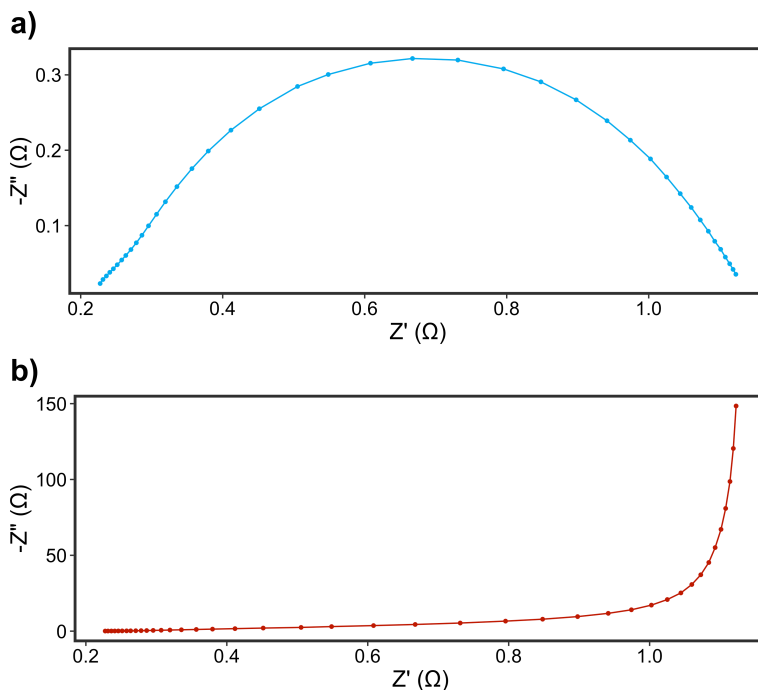


Figure 5.A.19: Nyquist plots of (a) a zero-gap MEA with a functioning membrane, and (b) a zero-gap MEA with a pierced membrane.

Double-layer Capacitance Another way to study the stability evolution in gas-diffusion electrodes is doing a double layer capacitance. This functions as follows: by performing cyclic voltammetries in the charging region of the catalyst at increasing current densities, the capacitance effect can be mapped. This is an indication of, for example, catalyst degradation and flooding of the porous electrode. Plotting the charging current vs. the scan-speed, one obtains a linear relation, the slope of which is the double-layer capacitance of the electrode. These measurements are best performed before and after an experiment to quickly map the effects of the test on the electrode. The scans and linearization are depicted in Fig. 5.A.20.

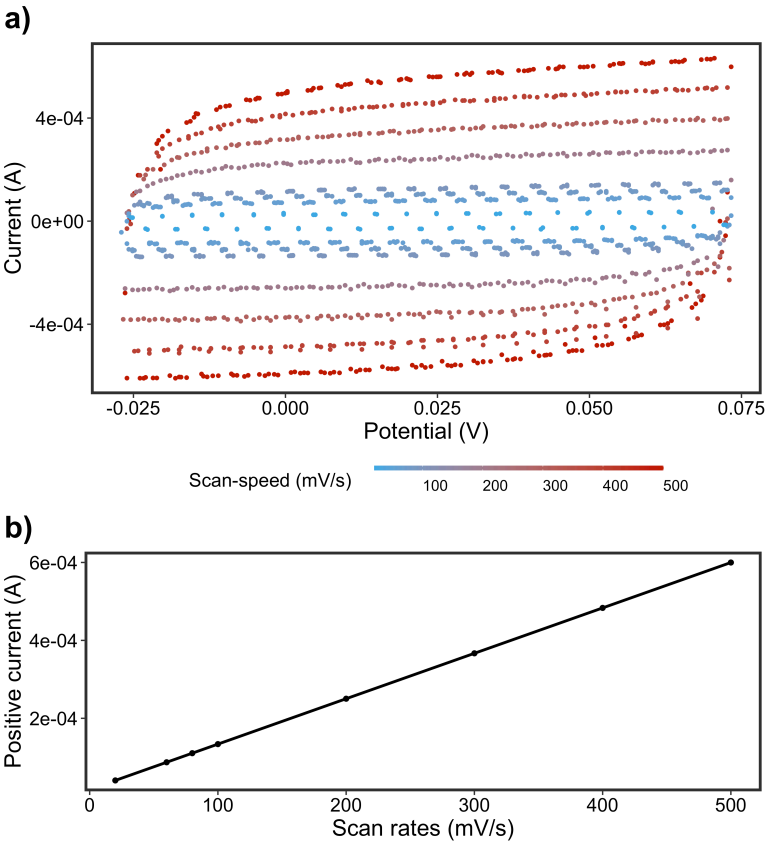


Figure 5.A.20: (a) Scanning the charging region at increasing scan-speeds, and (b) linearization of currents to obtain the capacitance of an electrode (the slope).

Troubleshooting guide

After testing and operating CO₂ electrolyzers for extended periods of time, certain phenomena occur with frequency. For starters in the field, these might present themselves as enigmas to solve. This guide is a compendium of frequently occurring mishaps and their best fixes and solutions, grouped by source of observation.

Potentiostat

1. Potential

a. Values too high

i. Too many bubbles

Stagnant and large bubbles may block the ionic pathway in the cell. Try:

- Increasing the flowrate of the electrolyte
- Increasing the pressure in the electrolyte compartment

ii. Crossover of gas to the catholyte compartment

Due to a pressure imbalance over the GDE between the gas- and liquid-compartment, gas crosses over to the catholyte. This shields a part of the electrode, decreasing the total active catalyst area. Try:

- Increasing the flowrate of the electrolyte
- Increasing the pressure in the electrolyte compartment

iii. Electrolyte not properly prepared

An electrolyte that is not conductive enough will result in a higher ohmic loss over the electrolyzer, raising the potential in fixed-current experiments. Check and make sure your calculations are correct and the concentrations high enough.

iv. Membrane not functionalized properly

A membrane that has not been functionalized/activated properly is less conductive and causes a higher cell potential. Check the specifications of the manufacturer and adhere to these. If this does not help, contact your supplier.

Some membranes are packaged between spacers. These are usually non-conductive sheets of polyethylene. Make sure you are using the polymeric membranes and not the spacers in your experiment. Spacers usually feel like a foil, while (wet) membranes usually curl and stick to themselves if out of the storing solution.

b. Values too low

i. Short-circuit of the cell

If a short-circuit is present, the electrical circuit will possibly close before the potential of reaction is reached. Search for sources of shorting, where anodic and cathodic half-cells come in direct electrical contact. For membrane-electrode assemblies, this is usually a perforation in the membrane. Make sure the clamping torque you apply when assembling the cell is not too high and diagnose the resistance of the system using a 2-electrode mode electrochemical impedance spectroscopy (EIS) measurement. Membrane puncture can also be diagnosed by monitoring cell potential at low reduction currents. A punctured membrane will show extremely low cell potentials for these currents (lower than the reaction's thermodynamic potentials).

ii. Electrode flooded

A flooded GDE resorts to hydrogen evolution. This may affect the potential values in a fixed-current experiment. Restart the experiment with a new electrode and make sure the pressure-drop over the GDE (between the catholyte and gas compartments) is not too big.

iii. Compliance voltage reached

Potentiostats have a maximum potential difference they can apply between the working and counter electrodes. If a high-enough current density is reached, some potentiostats resort to balancing the applied potential on the counter-electrode to artificially reach the demanded current density. This is especially true for unoptimized anodic catalysts, like plain nickel mesh.

Check your total cell potential during the experiment with an open-circuit multimeter and compare to the specifications of the potentiostat. A common strategy to avoid this problem is using smaller active areas that require a lower total applied current to achieve a specific current density.

c. Values drifting during measurement**i. Unstable Reference Electrode**

Reference electrodes may degrade over time. Some reference electrodes, like Ag/AgCl, are not stable in alkaline conditions for long timespans. Make sure to store the reference electrodes according to manufacturer's indications. If you suspect a reference electrode (RE) has degraded, check its potential reading against another RE under open circuit using the sense and reference connections of your potentiostat.

ii. Electrolyte depleting or changing conductivity

Electrolytes can degrade over time, for example due to CO₂ buffering in alkaline media. To avoid this, refresh your electrolyte in time and use an appropriate volume (e.g., for running at -200 mA cm^{-2} for $t \sim 1$ h, a volume of around 100 mL of 1M KOH is recommended).

If you are unsure whether your electrolyte is stable, perform routine pH or conductivity measurements.

iii. Catalyst deactivated

Most electrocatalysts degrade over time. While noble metals display a long stability, some popular CO₂RR catalysts like copper have very poor stability. To avoid excessive deactivation, apply one of the following strategies: either increase the catalyst loading on your cathode, or decrease the maximum current density you apply.

5

2. Current

a. Values too noisy

i. Gas-bubbles in the catholyte compartment

Nucleation of gas products in the catholyte channel, as well as crossover of reactant gas, interfere with the electric field on the cathode and can shield the reference electrode intermittently. Increase the flow rate to improve evacuation and increase the pressure on the catholyte channel to reduce bubble size.

ii. Gas-bubbles in the anolyte compartment

Similar to the catholyte channel bubbles. In semi-MEA designs, where the membrane is pressed on the anode but not on the cathode, this might result in bulging. This can lead to the membrane sticking to the cathode and altering the activity on the catalyst.

To avoid this, ensure you fill first the catholyte compartment on startup and maintain a higher pressure on the catholyte channel than on the anolyte.

3. Resistance

a. Reading too noisy

i. Unstable Reference Electrode

Unstable reference electrodes produce noisy and unreliable readings during an EIS measurement. Check your reference electrode's potential drifting with a second one and replace if needed.

ii. IF in 2-electrode mode

Noisy or irregular results might indicate a rupture in the ionic pathway, i.e., a short-circuit. Check your assembly again and make sure every component is functioning as should. In an MEA assembly this probably indicates a rupture in your membrane.

iii. IF in 3-electrode mode

In 3 electrode mode, noisy signals are usually due to direct contact of the current collector with the catholyte, or insufficient contact of the cathode with the current collector. An increased gas crossover to the catholyte can also result in noisy signals.

b. Values too high

This means the electric circuit is posing a resistance to the transfer of ions. This can have multiple causes. The electrolyte can possibly be depleted or not well prepared. Contact between the cathode and its current collector or the anode and the end block might be compromised, resulting in a higher contact resistance. Finally, the membrane might not be activated properly. In addition to this last point: most membranes are packaged between translucent spacers. It is important to separate these from the membranes before activating, as identifying them correctly afterwards can be hard. If you have doubts whether the membrane is really a membrane or just a plastic spacer, try to wet the membrane and see if it curls. If it does, it is a membrane.

c. Values too low

This points to insufficient resistance to the transport of ions/electrons in your system. Make sure your membrane is unharmed and that there's no electrolyte spilling/leakage through the gaskets.

Back-pressure Regulator**1. Pressure****a. Increasing values (liquid channels)**

In a closed circuit where product gasses accumulate, pressure is going to increase. For long-term experiments, allow for periodic venting of the catholyte and the anolyte loops. Since the anolyte compartment is usually not relevant in terms of product quantification it can be left open, so oxygen/other gaseous products don't accumulate. Accumulation of oxygen in OER configurations at high current densities can affect the physical stability of the membrane, bloating it and even ripping it. To avoid

this in long-term experiments, it is best to configure the anolyte loop in such a way that the peristaltic pump ‘sucks’ the electrolyte through the chamber, rather than pumping it.

The problem is altogether less impactful if the pressure of the catholyte is raised enough, so that product gasses in this chamber evacuate to the gas-chamber immediately.

b. Increasing values (gas channel)

For gas channels, increasing pressure values usually point to an obstruction in the pathway of the gas. In CO₂ electrolyzers this is most commonly salt precipitation. In MEAs, salt is going to quickly accumulate between the cathode and the flow-field of the cathodic current collector. Flow cell electrolyzers generally do not suffer from such large and rapid salt accumulations.

Salt may also deposit downstream in the piping of the gas-stream leading to the BPR or the GC. While it is usually possible to detect salt visually, accumulation inside the devices might need bypassing them to assess the pressure drop the gas-flow experiences. If this is large, the device has probably accumulated too much salt and needs rinsing.

In case a device needs rinsing, follow manufacturer instructions or contact the reseller for indications. Cabling can readily be cleaned with Milli-Q-water and left overnight to dry.

c. Variable readings

Fluctuating readings in the liquid loops indicate that gas crossover or severe H₂-production is taking place. As the masses of gas move past the pressure controller, the device struggles with the mass of the passing fluids.

In case of the gas channel, a fluctuation in readings might point to a leakage in the electrolyzer. To fix this, please read the recommendations under the next point.

d. Values do not reach set-point

If pressure values are not able to reach the set-point, the first possible cause is your set-point is out of reach for your pressure controller. If this is not the case, your set-up probably leaks.

Liquid leaks are readily found. If that is not the case, consider running water with a dye in both loops. This will however mean you have to terminate the experiment.

Gas leaks can be detected using soapy water. When applied to the possible site of leakage, the gas escaping will form bubbles that indicate the locations. If this does not yield results, immerse the electrolyzer in a Milli-Q bath and locate the origin point of gas bubbles escaping from the system (**WARNING:** disconnect your electrolyzer from the potentiostat before performing this operation).

2. Flow measurement

a. Reading differs from set-point

In this case, gas is probably leaking. This might be a leak from the setup to open air, on the one hand, or within the system, on the other. In case of the first, check all the tubing and the electrolyzer with soapy water. The gas leakage will form bubbles indicating the site of the leak. In case of the second, gas is flowing from the gas chamber to the catholyte due to a pressure imbalance. Correct the pressures and check the total gas flow. This leakage might be due to electrode porosity or incorrect assembly of the system. If the latter is the case, disassemble the electrolyzer and locate the fault.

b. No flow

In case of a reading of 0 sccm, the gas is probably not entering the electrolyzer due to a leak upstream. Make sure all tubes are connected and the CO₂ bottle is not empty.

c. Noisy signal

In case of a periodic signal, check the frequency of the signal and look for correlations for bubble movement along the outlet tubing. Also, peristaltic pumps may wear down the rollers and/or the tubing due to misalignment or external damage, which may need inspection.

In case of a non-periodic signal, check for gas breakthrough, electrode flooding and electrode salting, all of which require disassembling of the electrolyzer for inspection.

Gas Chromatograph

1. Disturbances to signal

a. No signal detected

If the acquired signal shows no peaks of produced gas but the potentiostat reads normal figures, the gas products might not be reaching the GC. Make sure the pressure on your gas stream is higher than the back-pressure (intrinsic pressure) of the GC inlet system. This can be checked by circulating inert gas and checking the pressure reading on your BPR without any regulation.

Remember that a certain saturation time in the injection chamber of the GC is needed before the actual concentrations are read. For our system saturation time is between 5 and 10 minutes, for example.

b. Baseline of peaks shifting

The accumulation of certain species (e.g., H₂O and CO₂) in the columns of the GC can result in the shifting of the baseline. This can interfere with the concentration calculation. To prevent this, allow your GC enough time between injections and, if possible, program a back-flush procedure.^[49] Our system presents very little baseline shifting starting at 5 minutes between injections.

c. CO peak's retention time decreases

Progressive binding of a chemical to the column can decrease its retention time. This is the case for CO, whose peak gradually 'drifts' to lower retention times. In the TCD column this can lead to overlap with other peaks, like methane and oxygen.

The way to avoid this is to regularly 'bake out' columns before calibration. This procedure involves raising the column oven's temperature high enough that fouling species are baked out, while the venting valve is open. Normally, a bake out of 72h (over the weekend) before calibration is enough to bring back retention times to their usual figures.

d. Unknown peak appears

The appearance of an unknown peak can be the consequence of two reasons: firstly, the production of a species that the GC was not calibrated for. If you have a suspicion of which species this could be, calibrate your

device (this can also be after an experiment) to a standard concentration of this species and calculate its concentration.

Secondly, a too short injection time. If the residence time of a species is longer than the total time of the injection you allow, it will show up in consecutive scans, as it will leave the column system towards the sensor after the second measurement has started. To avoid this: allow long injection times during your calibration so you are certain all gaseous species get separated and no cross-contamination of samples arises.

2. Quantification

a. Unexpected high concentration

In an automated reporting method, unrealistic high concentrations can be reported occasionally. This is almost exclusively due to peak integration errors due to a shifting baseline (in the TCD channels). Adjust the baseline for each peak manually to correct these integrations.

b. Missing faradaic efficiency

If after integration of the peaks and concentration calculation your products don't add up to 100%, first revise your volumetric flow used in the calculation. This needs to be corrected to the real flow to present real values (see Figure 5.2). If you are still missing products, consider the possibility of a liquid product being formed. Collect liquid samples and analyze these using HPLC or NMR (see the equipment guide for more information).

Electrolyzer

1. Leakage of fluids

a. Leakage of liquid electrolyte

Leakage of liquid electrolyte, either from the catholyte or the anolyte compartment, might be due to several reasons. The most likely of these occurs during assembly: if the gaskets are still wet, these droplets will open leakage 'pathways' upon compressing the cell together (remember liquids are almost incompressible, contrary to the gaskets).

Other causes might be, for example, a sudden pressure increase in the electrolyzer. In this case, check your tubing for obstructions or the electrolyzer itself for accumulation of salts.

Fittings might be a source of leakage if they do not seal properly. Place a slim Teflon tape on your NPT screws and cut Viton (or rubber) sealings for M5 screws (these compress with a ferrule very easily).

b. Leakage of gas

Check the ‘values not reaching set point’ under the BPR guide. Identify the leakage and replace components where needed. In case of MEA usage, make sure there is no hole in the membrane through which the gas at overpressure could penetrate.

2. Corrosion and material stability

a. Corrosion of end-block

Although end-blocks are usually manufactured using corrosion resistant materials (titanium for the anode and stainless steel for the cathode), experimenting with product conditions might expose them to voltages outside their stability windows. A common issue is the oxidation of the titanium end-block after being exposed to spike currents. A strategy to avoid affecting the conductivity of your anode is to plate the flow-field with a conductive, corrosion-resistant material (i.e., gold or platinum) using physical deposition or electroplating methods.[50]

b. Corrosion of current-collector

If the current collector in a flow-cell setup shows signs of discoloration or staining after disassembling the cell, it has most probably been in contact with the electrolyte. This means it has probably interfered with the reaction studied. Engineer your systems in such a way that electrolyte is properly sealed. For our flow-cell, for example, a strip of 1 mm of silicone between the electrolyte gap and the current collector is enough to seal the cathode after assembly.

c. Anode stability

When using common materials for the anode, like nickel foam, corrosion might occur when applying extreme anodic voltages. This is visible on the anode in the form of black corrosive stains. Nickel is, however, reusable after this phenomenon. Storage overnight in a highly alkaline solution (e.g. 1M KOH) should reduce staining. This process can be accelerated with heating.

6

REFLECTION & OUTLOOK

“A poc a poc i bona lletra.”

— Catalan proverb

This dissertation started by highlighting the rationale behind CO₂ electrolysis and its main shortcomings: i) poor utilization and loss of CO₂ at the electrode, ii) salt precipitation, and iii) flooding of the porous medium that supports the cathode. While work presented in this document does not provide an immediate relief to these issues, it presents a novel perspective and methodology to study spatial effects in CO₂ electrolyzers. Advancing our understanding of spatial differences in CO₂RR is a crucial step in scaling up the systems we design towards an industrial scale. Of all spatial variable metrics, electrochemical activity has long been overlooked and assumed to be evenly distributed across the small, lab-scale devices most often reported. Within this thesis we show that even in small systems an assumption of spatial uniformity is invalid. Thus, while assessing reproducibility and consistency over a surface is a focus generally observed at later stages of development when a technology is targeted for scale-up and long-term usage, we demonstrate that this timeline needs accelerating. In this lies the first realization: CO₂RR is reaching maturity and feasibility at a rapid pace, making development and marketization of this technology in the next 20 years more a reality than a dream.

6

In our approach towards a better understanding of the spatial metrics, we coupled the generation of heat at the backbone of a gas diffusion layer to the local activity at the catalyst interface. To do so, we engineered a proprietary cell design with an infrared transparent window that allowed recording using an infrared camera. The beauty of this solution is that it provides an intuitive insight of local activity, which allows to monitor its distribution and evolution in real time. While the solution presented in this work employs a high-resolution, high frame-rate camera that might not be accessible to a wide audience, usage of lower quality sensors (with the caveat of poorer resolution) is still possible. This makes the solution fit for quick diagnostic tests of lab-scale and large-scale electrolyzers.

Utilizing this platform has provided us with many a novel insight, that directly challenges assumptions long upheld in the CO₂RR field. As a first example, the probed local temperatures at the backbone of the GDL are of the order of >10 K higher than the assumed room temperatures when operating at industrially relevant current conditions. This observation has consequences on multiple levels: the local heating increase could directly impact kinetics of the reaction on a noticeable level, challenging all modeling and simulation work performed to date. On a system engineering level, design of CO₂ electrolyzers should take extensive temperature-control solutions to operate in a stack configuration. A second challenged assumption is the influence of flow regimes on activity distribution in the electrolyzers: even at ~2 cm² electrodes, entrance effects result in accumulation zones. These observations result in the need to adapt lab-scale systems to ensure homogeneity over the surface, and the accounting for interface temperatures in

simulations exercises.

Our technique turned out to be a reliable way to detect the current density distribution. While most GDL used in literature are conductive, ePTFE ones are not. The field employed these layers in the assumption that the catalyst layer was conductive enough, whereas our detection system showed serious conductivity deficiencies for thin catalyst layers. What also merits notice is the influence the local current density can have on locally dissolved CO_2 : using our thermographs and a reaction-diffusion model we showed a variance of up to 2x in the concentration of CO_2 , which can have a great influence in the selectivity of catalysts, as it alters local conditions noticeably. In designing a solution to this problem, we turned to the field of photovoltaics, applying a busbar electrode that acted as a highway for electrons to spread more evenly over the catalyst. In this lies another insight: innovating in the field of CO_2RR will often require shifting focus from traditional sources of inspiration, like fuel cells and water electrolyzers, to new areas as complexities in our systems are simply not foreseen in traditional focus areas.

While other unwanted side-effects in CO_2 electrolysis were not a direct focus of works presented in this dissertation, IR thermography still holds promise in delivering quantifiable insights results regarding, for example, flooding of cathodes and salt formation at the GDL backbone. As these phenomena result in observable accumulation of elements with different emissivities, they result in observable artifacts in recorded thermographs. The real-time measurement nature of our architecture allows then for a coupling of these developments to electrochemical (potential and current density) and physical (pressures of electrolyte and gas-streams and their flow-rates) magnitudes. With this, it is foreseeable that further knowledge can be gained in the realms of operation and control of CO_2 electrolyzers, which for now are a blind-spot in literature. Furthermore, IR thermography seems a scalable option for quick diagnostic testing in manufacture of industrial scale electrodes, be it for CO_2RR or other electrocatalytic applications.

With the assembly and operation guide, we aimed to provide a solid, attainable basis of what we believe is essential to ensure reproducibility and comparability in our field. When testing systems on a lab-scale, thorough accounting of relevant metrics is crucial for honest reporting of results. A robust cell architecture needs to be combined with proper flow regulation and stabilization, together with in-line analysis systems to scope the selectivity of the catalyst in operando. The attractiveness and pull-factor the CO_2RR field has on scientists (mainly due to funding reasons) results in an ever-growing number of publications, most of which are unclear in setup and analysis techniques. With it, a beginning researcher has a thorough overview on what he needs and how data is collected.

The nature of this publication is at the same time the evidence of its greatest

shortcoming in current dissemination platforms. In a rapidly evolving field, novel insights should be incorporated as soon as possible to the praxis of as many reports as possible. Producing such guide articles every other year seems a solution with low durability. Instead, a platform of knowledge exchange, rapidly accessible to many at low (or no) cost seems desirable. While intelligent use of social media and outreach through conferences and workshops are a valid (and effective) option, these require a considerable amount of dedication, that mounts on the already extensive list of responsibilities of a researcher in the current funding system.

Outlook of CO₂ electrolysis

The cliché of any outlook section in low technology-readiness level dissertations is a statement along the lines of ‘looking forward to the upscaling and industrialization of said technology in coming years, hopefully sooner than later.’ The reality of CO₂ electrolysis is, nevertheless, that we are witnessing these developments in real-time, which stems positively in regards of real-world impact of this technique.

Some major hurdles need to be overcome, however. Realizing a meter-scale electrolyzer seems easy, especially considering advances booked in adjacent fields like fuel cells and electrolyzers. The reality is stubborn, nonetheless, and any initiative that aims at these scales must implement some kind of mitigation solution to the inherent shortcomings of CO₂RR systems. While we scientists tend to search for ‘beautiful’ solutions that circumvent a problem altogether, we might have to settle on ‘engineering’ solutions for the time being (and possibly forever). An example of this kind of solutions is the on and off cycling of a CO₂ electrolyzer to avoid salt accumulation at the cathode. While this results in a loss of operational time, it is an effective manner of combatting physical degradation of our systems. Again, not beautiful, but effective.

Another major focal point involves the usage of earth-abundant materials. CO₂RR technologies will probably suffer the ever-increasing prices of highly active but scarce materials like iridium. Designing systems that shift from these materials towards more commonly occurring ones holds promise in keeping the capital investment needed for deployment of this technology within reasonable bounds. Many of these solutions will probably result in slightly higher operational expenses, in the form of higher voltage, for example, but these can be compensated by the ever-decreasing prices of renewable electricity sources.

The shift to bigger scales imposes a set of constraints difficult to test in labs. An example of such is the stability of the catalyst on our electrodes. Our field has yet to wade into defining standardized degradation testing routines, and that is probably a focus to turn to after we have addressed inherent stability of some metal catalysts. In this regard, the next big challenge to tackle is the erratic behavior of copper under cathodic conditions. Maintaining the selectivity towards high-value

hydrocarbons like ethylene is key in guaranteeing integration of CO₂ electrolyzers in the massive carbon value-chain that drives our economy. Whoever succeeds in stabilizing copper for 20,000 hours at commercially relevant current densities will be sitting on a gold mine.

Operation of stacked electrolyzers opens a broad horizon of process conditions that the field has not yet anticipated. The increased temperature, and more importantly, its uneven distribution in the stack might hamper efficiency and lifetime of these devices. Disparity of CO₂ utilization might shift selectivities of catalysts, and disparate humidity might affect the stability of membranes. These effects, however, are sadly of little interest for the field as of now. A shift in focus towards these gaps is of utmost importance if we aspire to see CO₂ electrolysis as a viable alternative to the usage of fossil fuels.

SUMMARY

The shift towards a carbon-neutral economy represents a considerable challenge in the search of sustainable carbon-sources. The electrolysis of CO₂ presents an attractive, direct pathway to produce sustainable fuels using only CO₂, water, and electricity. The rapid shift towards high reaction rates and industrially relevant process conditions in just a few short years has opened new research directions towards understanding the intricacy of the complex interfaces involved in this reaction. The two key enabling technologies: gas-diffusion electrodes and membrane electrode assemblies, have greatly increased efficiency metrics of CO₂ electrolyzers, but many questions on the homogeneity and activity of these electrodes remain unanswered.

In the early resurgence of CO₂ electrolysis as a research field in the early 2010's, most developments involved intense catalyst studies, but treated the electrolyzers themselves as black boxes. Synthesis of these catalysts was coupled to device-averaged metrics like faradaic efficiency, with no further insight in spatial effects. While, recently, this spatially uneven distribution has gained more attention, devices to properly scope inequalities inside an electrolyzer are still scarce and difficult to operate. A joint effort of modelling and experimental testing of varying conditions are key to furthering understanding of CO₂ electrolyzers.

Within this thesis it is emphasized that in scaling up an electrolyzer, the distribution of current across the electrode is of utmost importance to guarantee comparable reaction conditions over the entire device. Realizing that cathodic electrolysis reactions inevitably result in a development of heat, we engineered an infrared thermography system to monitor the temperature of the backbone of gas-diffusion electrodes. The heat conductivity and thinness of these electrodes allowed for a thermographic image of the back-side to be translated to an activity map at the catalyst's side. Using this system on a small-scale three chamber electrolyzer, we demonstrate its working principle and possible applications as detection method for catalyst layer defects, catalyst activity and the influence of flow-patterns.

The regular flooding of carbonous gas-diffusion electrodes has pushed the CO₂-RR field towards using super-hydrophobic expanded polytetrafluoroethylene (ePTFE) electrodes. The main difference of these electrodes with their carbonous counterparts is, besides their improved hydrophobicity, the non-conductive character of their backbone. Using infrared thermography, we demonstrate the limits this imposes on catalyst layers, where thin layers display a massively uneven current

distribution. Inspired by the design of photovoltaic panels, we design an improved front-contact current collector that improves activity distribution and stability of the catalyst.

Finally, we compiled the know-how developed in our lab in the last 4 years. Operation of high current-density systems using gas-diffusion electrodes requires pressure and flow control over the chambers of the electrolyzer. Accounting for products using their real rates is of key importance to reliably report the performance of a catalyst. With the work presented, we aim to enable novel researchers' quick entrance in the field, overcoming common barriers like delving in supporting information and appendices of highly cited publications.

SAMENVATTING

De transitie naar een koolstof-neutrale economie is een aanzienlijke uitdaging in de zoektocht naar duurzame koolstofbronnen. De elektrolyse van CO_2 doet zich voor als een aantrekkelijk pad om duurzame brandstoffen te produceren uit CO_2 , water en stroom. In de afgelopen jaren is de aandacht in dit veld verschoven naar hoge reactiesnelheden en industrieel-relevante procesomstandigheden. Dit heeft geleid tot nieuwe onderzoeksrichtingen die zich richten op een beter begrip van de complexiteit in faseovergangen die in zo'n systeem voorkomen. Het gebruik van zogenoemde gasdiffusie elektrodes en membraan-elektrode assemblies heeft de efficiëntie van CO_2 elektrolysecellen enorm vooruitgeholpen, maar er zijn nog veel vragen te beantwoorden over de homogeniteit van condities rondom deze elektrodes.

De initiële focus van dit studieveld rond 2010 richtte zich op de ontwikkeling en studie van katalysatoren alsof het zwarte dozen betrof. De effectiviteit van deze katalysatoren werd daardoor gekoppeld aan apparaat-gemiddelde grootheden, zoals faradaïsche efficiëntie, met verder geen enkel ruimtelijk inzicht. Ondanks de stijging in aandacht voor ruimtelijk inzicht, zijn apparaten die inhomogeniteiten in een elektrolysecel kunnen vaststellen schaars en complex in het gebruik. Een gecombineerde aanpak hiervan, door middel van modelleren en experimenten, is cruciaal om het begrip over CO_2 elektrolysecellen te vergroten.

Deze dissertatie legt de nadruk op de observatie dat, bij het opschalen van elektrolysecellen, de verdeling van stroomsterkte over het oppervlak van de elektrode van groot belang is om de vergelijkbaarheid van procescondities te garanderen. Toen we ons realiseerden dat een kathodische elektrochemische reactie een inherente warmteontwikkeling met zich meebrengt, ontwikkelden we een infrarood thermografisch systeem om de temperatuur van de achterkant van gasdiffusie elektrodes te volgen. De warmtegeleiding en beperkte dikte van deze elektrodes maakt het mogelijk om deze temperaturen te vertalen naar elektrochemische activiteit aan de kant van de katalysator. Gebruikmakend van een kleine-schaal elektrolysecel met drie compartimenten, demonstreren we de kracht van dit systeem bij de detectie van defecten op de katalysator laag, de detectie van activiteit en de effecten van stromingspatronen.

Het regelmatig overstromen van koolstof-gebaseerde elektrodes heeft het studieveld aangedreven om super-hydrofobische polytetrafluoroethyleen (ePTFE) te gebruiken. Het voornaamste verschil tussen deze elektrodes en koolstof-gebaseerde

opties is, naast het afstoten van water, het isolerend karakter van dit alternatief. Door middel van ons infrarood thermografisch systeem laten we zien wat de invloed is van de dikte van de katalysator-laag op de stroomverdeling, die extreem inhomogeen blijkt te zijn bij heel dunne lagen. Geïnspireerd door de manier waarop de elektrische spanning verdeeld wordt in fotonvoltaïsche panelen, ontwerpen en demonstreren we een verbeterde frontale stroom-collector die de activiteitsverdeling verbetert en de stabiliteit van de katalysator verlengt.

Tenslotte bundelden we de kennis die ons lab ontwikkeld heeft in de afgelopen 4 jaar. Gebruik van hoge stroomdichtheid-systemen met gasdiffusie elektrodes vereist controle over druk en stroomsnelheid over alle compartimenten van de elektrolysecel. Rekenen aan de snelheid van productvorming vereist tevens geïntegreerde analysesystemen. Met dit werk proberen we een snelle introductie te geven aan beginnende onderzoekers door barrières, zoals het doorspitten van appendices in vaak geciteerde artikelen, weg te nemen.

ACKNOWLEDGMENTS

The feeling will not be strange to a lot of people in this chapter. You get a new book in hands, wonder how they designed the cover, and leaf through directly to the acknowledgements. Partly because you're timidly curious what they wrote about you, but mostly because in the end we all know this was not an individual endeavor. And, while these lines roll off my keyboard, I must think of Ortega y Gasset's famous line: "*yo soy yo y mis circunstancias*" (I am I and my circumstances). In my case, the circumstances were far more than extraordinary. A great deal, if not all of the merit lays on the excellent people I have had the luck to come across in my journey. These lines are for you, dear friend, colleague, reader.

There was but one possible start to my acknowledgements. **Tom**, I feel I owe it to the reader to paint a sketch of how I got to join the group. After flunking my first interview, you called me up and summoned me to Belvédère, there was some money left and maybe we could make something work. I must admit I do not recall much besides four Leffe Blonds and a fleeting discussion about American politics – fast-forward 4 years and then some, and here we are. Tom, there is something in you I have not yet seen in other scientists. It's an interesting mix of youthful curiosity, mature sternness and baffling creativity. A very big part of who I am today I owe to you, and that's a debt I'll have to carry forever. To my questions you always had answers – albeit often new questions that intrigued me and fueled the patience this job requires. I have been lucky to be a part of this little thing you have going, our lab, and witness it grow and mature. I would like to think my wishes for success were needed, but we both know you don't need them – whatever you do, I'm sure it will be for good. This book is as much yours as it is mine, thank you for everything.

Bernard, door toeval (of niet) was jij een *basso continuo* in mijn opleiding. Van colleges thermodynamica, lab practica bij Petra, bachelor en master scripties bij Wilson, je was er op de achtergrond, als vaderlijk figuur en wijze raadgever deze bijzondere groep wetenschappers. Toen Tom me vertelde dat je de rol van promotor op je zou nemen was ik meteen gerustgesteld – met jou zou het wel lukken. Ik heb niet alleen tegen jou opgekeken, maar ook tegen je studenten; ik heb zelden wetenschappers van zo'n niveau gezien, en dat is ongetwijfeld mede door jouw toedoen. Bij jou kon ik altijd terecht met de meta-kwesties – moest ik me hier of daar op focussen, wat wil ik later met mijn leven, hoe pak ik het

leerproces aan... Er kwam altijd wijze raad uit. Dankjewel voor het mede mogelijk maken van de afgelopen vier jaren.

Klop klop **Joost en Herman**, hebben jullie iets om *onmogelijke handeling*?. ‘Oh, ja hoor!’ was dan altijd het antwoord. Het grootste verschil tussen MECS en de rest van de faculteit is dat wij feitelijk genieten van de allerbeste technici. Niks is teveel gevraagd, alles is mogelijk, ook al komt het niet goed uit. Veel van het werk in dit boekje was onmogelijk geweest zonder jullie hulp, waar ik altijd dankbaar voor zal blijven.

During the four years it took me to complete this book I enjoyed the warmth and homey feeling of the **MECS** section (oh, to enjoy the *gezelligheid* of our coffee breaks). I joined fully convinced, after having completed my master’s thesis two years before. I witnessed professors, postdocs, PhD’s and students come and go, as if that was something external to me, safe as I felt in our group. And then, suddenly, it was my turn. In addition to everyone I already mentioned: **Fokko, Hans, Wilson, Lars, Roos, Erdem, Maryam, Aaron, Kailun, Anirudh, Kai, Mark, Marijn, Diana, Giorgio, Sid, Jesse, Jasper, Gerard, Henri, Elena, Nikita, Davide, Dylan, Peter, Mark, Pranav, Robin, Martin, Santosh, Vineesh, Julia...** To be honest, the list is very, very long. There are, however, a couple of people I’d like to thank in detail. **Sid**, you snatched my job, but we luckily ended up working together. You were always the smart one; you read and cared for literature as I was frying electrodes in the lab. I have seldom encountered someone with so much knowledge, patience and perseverance, never change. **Erdem**, I think sharing an office during my first two years was the best thing that could have happened to me. Science is as much reading as it is discussing, and in you I found someone to explain my nonsense to. Thank you deeply. **Sanjana**: I have two recurring nightmares. The one is about failing my ATP exam, which is a standard one for any Process Engineering graduate – the other is switching on the FTIR and seeing a flatline. The thing is, that paper we worked on, it was one of the most enjoyable ones, even though it took us a good 10 months to get the data. All that’s because I went in for a lab-mate and instead got a friend. Thank you for being awesome. I wish you and **Tushar** all the best in life. **Maryam** and **Aaron**, from a very early stage you involved me in your projects, which was crucial for me to carry on everything written down in this book. I am forever in your debt. **Recep**, it’s been a while, but you are a big part of the reason I decided to embark in this journey. Thank you for teaching me, there’s a sea of knowledge and patience in you. **Jorrit**, samen uit, samen thuis, toch? De TA sessie’s voor ATP in dat eerste jaar waren onwijs gezellig. Ik weet zeker dat, wat je ook besluit te doen, je dat zal rocken zoals je altijd doet.

I owe gratitude as well to my students: you tested my patience at times, and my abilities as a supervisor full-time. **Herman, Michiel, Zhi Wei, Timo** and

Charley, thank you for being part of my journey!

Aan mijn negen lange jaren als orkestlid van het Delftsch Studenten Muziek Gezelschap “Apollo” ben ik veel mooie momenten, maar misschien nog belangrijker, vele vriendschappen verschuldigd. De ‘oude garde’ die me bij de hand meenam naar de eerste Maandagborrels, **Danilo, Philip, Catha, Jurriaan, Jan en Annette**; mijn lieve ‘ir-kwartet’-genoten **Geerte, Matthijs en Roemer**; mijn bestuursgenoten **Beryl, Lianne, Jonathan en Arthur**, en alle mensen die ik sindsdien al musicerend heb leren kennen: we *moeten* er zijn.

Aan de heren (in mijn hoofd nog altijd *jongens*) van clubje Solide: deze is voor jullie. **Alexander, Casper, Coen, Felix, Jasper, Lout, Luciën, Maarten, Marc, Marten, Niek, Olivier, Patrick, Peter, Reinier, Rogier, Steven en Thijs**, soms kijk ik terug op dat najaar van 2013 waarin we elkaar leerden kennen, en dan kan ik niet anders dan heel trots op ons allemaal zijn. Met lichte bewondering, ook, over hoe we levend uit India en Zuid-Korea zijn gekomen (en vooral dat we elkaar niet gaandeweg afgemaakt hebben). Op nog vele mooie jaren samen.

Zittend op de bank met laaiende hoofdpijn van weer een iets té leuke avond is de enige manier om iemand echt te leren kennen. En wat heb ik geboft met mijn huisgenoten, zowel in Delft als in Den Haag. Met de bockjes van De Gouden Bock, **Tom, Reinier, Steven, Maarten, Olivier, Coen, Bram, Elon, Karel, Mark, Jugo, Berend, Tex, Max en Sam** heb ik een veredelde bunker met riantte tuin gedeeld, naast spontaan verbrijzelende deuren, mot met de burens, een wasmachine met ingebouwde Haydn-symfonie en naar rato iets te veel mijn-bezoekjes. Aan de Tunnel mocht ik vervolgens genieten van de rust en vrede van het Zeeheldenkwartier in theorie, De Bieb en De Paap in de praktijk. **Philip, Danilo, Jurriaan, Jan, Jaap, Pieter, Jesse, Tom, Mark, Edvard, Robert, Robert, Wieger, David, Jochem, Joe en Max**, ik had eerlijk gezegd niet helemaal door dat de lijst inmiddels zo lang was, maar ik had met niemand anders Sloos’ spaarrekening willen spekken.

Als de casa, a la bona gent amb qui vaig deixar enrere la nostra ciutat per fer-nos via entre la jungla que és el fer-se gran. I que, malgrat el temps i la distància, segueixen a la meva vida. **Maria**, sempre has sigut una font insaciable d’energia i alegria. Em comforta saber que res ha canviat, i que, passi el que passi, ho afrontaràs tot amb un somriure d’orella a orella. No vull ni arribar a pensar el que hauria sigut de mi si no t’hagués tingut d’amiga. **Uri i Robert**, retrobar-nos sempre ha estat com tornar a casa després d’un dia molt (i molt) llarg. Res em fa més feliç que haver compartit alts i baixos amb vosaltres, i saber que, sense importar quan i com, ens tornem a veure com si res hagués passat. A tots tres, gràcies de tot cor; perquè quan la gent em pregunta què trobo a faltar de casa, la resposta sempre ha estat i sempre serà: vosaltres. I Girona una micona, també.

I, arribats a aquest punt, és obvi que faltava reconèixer l’immens paper que ha




tingut la meva família en ser qui sóc. **Pap, Mam, Daan**, no sé què és exactament el que ens fa ser com som, però quelcom devem fer bé. Serà el popurri de llengües a taula, o les frases inacabades perquè tampoc cal pronunciar el que se sobreentén. Casa-casa només n'hi ha una, i potser ara és a Fornells, però sempre serà on sigueu vosaltres. Us estimo.


H.P.

The Hague, March 2024


LIST OF PUBLICATIONS

Journal Articles

13. **IGLESIAS VAN MONTFORT, H.P.**, HOLOVANOV, V., KOK, J., PINILLA-SÁNCHEZ, A., GARCÍA DE ARQUER, F. P., AND BURDYN, T. High-throughput screening of catalysts for CO₂ electrolysis using infrared thermography. *In preparation* (2024)
12. IRTEM, E., **IGLESIAS VAN MONTFORT, H.P.**, LI, M., ABDINEJAD, M., MIDDELKOOP, J., AND BURDYN, T. Influencing intermediates during electroreduction of CO₂ in a flow-cell electrolyzer using scavenging agents. *In preparation* (2024)
11. SASSENBURG, M., **IGLESIAS VAN MONTFORT, H.P.**, KOLOBOV, N., SMITH, W. A., AND BURDYN, T. Bulk layering effects of Ag and Cu in tandem CO₂ electrolysis to adjust C₂₊ selectivity. *Submitted* (2024)
10.  SUBRAMANIAN, S., **IGLESIAS VAN MONTFORT, H.P.**, AND BURDYN, T. Going beyond one dimension: how spatial effects define CO₂ electrolysis systems. *Under review* (2024)
9. LI, M., LEES, E. W., WEN, J., SUBRAMANIAN, S., YANG, K., BUI, J. C., **IGLESIAS VAN MONTFORT, H.P.**, ABDINEJAD, M., MIDDELKOOP, J., STRASSER, P., WEBER, A., BELL, A. T., AND BURDYN, T. Local ionic transport enables stable PGM-free bipolar membrane electrode assembly. *Under review* (2024)
8. SUBRAMANIAN, S., KOK, J., GHOLKAR, P., KUMAR, A. S., **IGLESIAS VAN MONTFORT, H.P.**, KORTLEVER, R., URAKAWA, A., DAM, B., AND BURDYN, T. CO residence time modulates multi-carbon formation rates in a zero-gap Cu based CO₂ electrolyzer. *Under review* (2024)
7.  **IGLESIAS VAN MONTFORT, H.P.**, LI, M., IRTEM, E., ABDINEJAD, M., WU, Y., PAL, S. K., SASSENBURG, M., RIPEPI, D., SUBRAMANIAN, S., BIEMOLT, J., RUFFORD, T. E., AND BURDYN, T. Non-invasive current collectors for improved current-density distribution during CO₂ electrolysis on super-hydrophobic electrodes. *Nature Communications* 14, 1 (Oct. 2023), 6579
6.  **IGLESIAS VAN MONTFORT, H.P.**, SUBRAMANIAN, S., IRTEM, E., SASSENBURG, M., LI, M., KOK, J., MIDDELKOOP, J., AND BURDYN, T. An advanced guide to assembly and operation of CO₂ electrolyzers. *ACS Energy Letters* 8, 10 (Oct. 2023), 4156–4161

5. ABDINEJAD, M., YUAN, T., TANG, K., DUANGDANGCHOTE, S., FARZI, A., **IGLESIAS VAN MONTFORT, H.P.**, LI, M., MIDDELKOOP, J., WOLFF, M., SEIFITOKALDANI, A., VOZNYI, O., AND BURDYN, T. Electoreduction of Carbon Dioxide to Acetate using Heterogenized Hydrophilic Manganese Porphyrins. *Chemistry – A European Journal* 29, 14 (Dec. 2022), 202203977
4. LI, M., IRTEM, E., **IGLESIAS VAN MONTFORT, H.P.**, ABDINEJAD, M., AND BURDYN, T. Energy comparison of sequential and integrated CO₂ capture and electrochemical conversion. *Nature Communications* 13, 1 (Sept. 2022), 5398
3.  **IGLESIAS VAN MONTFORT, H.P.**, AND BURDYN, T. Mapping Spatial and Temporal Electrochemical Activity of Water and CO₂ Electrolysis on Gas-Diffusion Electrodes Using Infrared Thermography. *ACS Energy Letters* 7, 8 (Aug. 2022), 2410–2419
2. CHANDRASHEKAR, S., **IGLESIAS VAN MONTFORT, H.P.**, BOHRA, D., FILONENKO, G., GEERLINGS, H., BURDYN, T., AND SMITH, W. A. Investigating the role of potassium cations during electrochemical CO₂ reduction. *Nanoscale* 14, 38 (August 2022), 14185–14190
1. ABDINEJAD, M., IRTEM, E., FARZI, A., SASSENBURG, M., SUBRAMANIAN, S., **IGLESIAS VAN MONTFORT, H.P.**, RIPEPI, D., LI, M., MIDDELKOOP, J., SEIFITOKALDANI, A., AND BURDYN, T. CO₂ Electrolysis via Surface-Engineering Electrografted Pyridines on Silver Catalysts. *ACS Catalysis* 12, 13 (July 2022), 7862–7876

Patents

1.  **IGLESIAS VAN MONTFORT, H.P.**, AND BURDYN, T.E. Plane-resolved activity mapping at a gas-diffusion electrode through infrared thermography. *Dutch Patent Office*, WO2023009003A1 (Feb. 2023)

CURRICULUM VITÆ

Hugo-Pieter Iglesias van Montfort

2024 - Present	Senior Battery Scientist Ore Energy B.V., Amsterdam (The Netherlands)
2020 - 2024	PhD in Chemical Engineering <i>Dissertation:</i> Mapping Spatial Effects in CO ₂ Electrolysis <i>Promoters:</i> Prof. dr. B. Dam & Dr. T. Burdyny Delft University of Technology, Delft (The Netherlands)
2019 - 2020	Improvement Consultant Tata Steel Europe, Ltd., IJmuiden (The Netherlands)
2016 - 2018	MSc in Chemical Engineering <i>Specialization:</i> Process Technology <i>Thesis:</i> The formation of ethane on copper electrodes during electrochemical CO ₂ reduction – <i>an in situ approach</i> Delft University of Technology, Delft (The Netherlands)
2017	Plant Improvement Intern Royal DSM, N.V., León (Spain)
2012 - 2016	BSc in Molecular Sciences and Technology <i>Major:</i> Chemical Technology <i>Minor:</i> Economy, Law and Philosophy in Technology Delft University of Technology, Delft (The Netherlands)
2006 - 2012	Cum laude Baccalaureate in Sciences and Technology Institut Montilivi, Girona (Catalonia)
2006 - 2012	Professional Degree in Music, unfinished Aula Musical, Girona (Catalonia)
30/12/1994	Date of birth in Girona, Catalonia